technische universität
dortmund

Department
of Physics

A thesis submitted for the academic degree
Doctor rerum naturalium (Dr. rer. nat.)

Capsule Rheology and Machine Learning

Felix Sebastian Kratz

submitted in July 2024

AG Kierfeld
Department of Physics
Technische Universität Dortmund

Abstract

Capsules and their properties have provoked an increasing interest in several fields of the sciences and industry. In the sciences, several relevant biological system are modeled as a liquid core encapsulated by a skin of some sort, e.g. red blood cells. In industry, capsules are usually used the other way around – not to model nature, but rather to design for functionality, e.g. in medical application or the food industry. Given their ubiquitous application, we discuss and investigate the solution of shape equations for freely pendant droplets, capsules and derive a method to incorporate viscous dissipation for time dependent deformation sequences. These theoretical investigations are supplemented with a novel numerical framework which allows us to solve the shape equations, fit them to experimental images, and therefore infer information from experiments. We apply the theoretical and numerical insights gained during the course of this work to investigate the properties of complex interfaces, such as multi-layer systems.

While an individual capsule has interesting applications, the reality often is that a capsule can not be isolated from other capsules or some constraining boundaries. We therefore investigate – for the first time in literature – the contact problem of a pressurized, bending-stiff, adhesive, elastic capsule under an external force both with a solid wall and with another capsule of this kind. The resulting shape equations give us access to the shape-parameter diagram and allow us to understand the contact problem without performing any experiment. We rather integrate the shape equations numerically and find the solutions nature realizes, together with all relevant derived quantities, such as the contact force. Additionally, we design a meta-material (theoretically) from an elastic capsule unit-cell by extending the contact theory to a columnar structure.

Several problems encountered in physics, especially in inverse problems, can be considered ill-conditioned. An ill-conditioned problem reacts sensitive to perturbations of the input data and usually needs to be regularized or otherwise constrained to produce stable predictions or results. In this thesis we explore the potential of machine learning approaches for exactly this task. With liquid droplet and elastic capsule shape fitting, as well as traction force microscopy, as example problems, we convincingly show that machine learning approaches for these ill-conditioned problems are suitable and outperform conventional methods by orders of magnitude in speed, allowing for a entirely new applications.

Contents

List of Recurring Symbols

s	Arc length coordinate, Fig. 1.1	p. 3
Ψ	Arc angle coordinate, Fig. 1.1	p. 3
κ_ϕ	Circumferential curvature of the interface, Eqn. (1.2)	p. 4
κ_s	Meridional curvature of the interface, Eqn. (1.2)	p. 4
a	Width of the capillary, Eqn. (1.3)	p. 4
γ	Surface tension of the interface, Eqn. (1.4)	p. 5
$\Delta\rho$	Density contrast to the surrounding medium, Eqn. (1.4)	p. 5
g	Gravitational acceleration close to the ground ($\sim 9.81\,\mathrm{m/s^2}$), Eqn. (1.4)	p. 5
p_L	The pressure difference at the apex of the reference droplet, Eqn. (1.5)	p. 6
δn	Shape variation normal to the interface, Eqn. (1.6)	p. 6
δt	Shape variation tangential to the interface, Eqn. (1.6)	p. 6
$\tilde{p}_L$	Dimensionless apex pressure of the reference droplet, Fig. 1.3	p. 7
$\Delta\tilde{\rho}$	Dimensionless density contrast, Fig. 1.3	p. 7
Ω	Bulge and neck count of the shape, Eqn. (1.11)	p. 8
A_0	Undeformed surface area, Eqn. (1.12)	p. 9
L_0	Undeformed total arc length of the interface, Eqn. (1.12)	p. 9
w_{S_0}	Surface energy density with respect to the undeformed surface area, Eqn. (1.12)	p. 9
s_0	Undeformed arc length coordinate, Eqn. (1.12)	p. 9
r_0	Undeformed radial component, Eqn. (1.12)	p. 9
p_a	Pressure at the apex of the non-reference shape, Eqn. (1.12)	p. 9
λ_s	Meridional stretch ratio, Eqn. (1.12)	p. 9
λ_ϕ	Circumferential stretch ratio, Eqn. (1.12)	p. 9
τ_s	Meridional surface stress, Eqn. (1.16)	p. 10
τ_ϕ	Circumferential surface stress, Eqn. (1.16)	p. 10
$\underline{\underline{C}}$	three dimensional right-Cauchy-Green tensor, Eqn. (1.19)	p. 11
$\underline{\underline{\mathcal{C}}}$	two dimensional right-Cauchy-Green tensor, Eqn. (1.19)	p. 11
H	Thickness of the interface material, Eqn. (1.19)	p. 11
$k_\mathrm{B}T$	Thermal energy scale, Eqn. (1.19)	p. 11
Y_M	Mooney-Rivlin elastic modulus, Eqn. (1.22)	p. 13
Ψ_M	Second Mooney-Rivlin elastic constant, Eqn. (1.22)	p. 13
Y_2D	Two dimensional Young's modulus, Eqn. (1.23)	p. 13
ν_2D	Two dimensional Poisson's ratio, Eqn. (1.23)	p. 13
ν_3D	Three dimensional Poisson's ratio, in text	p. 13
λ_A	Area stretch ratio, Fig. 1.4	p. 14
Q	Non-dimensional stress-strain anisotropy measure, Eqn. (1.25)	p. 17
$\vec{\tau}$	Surface stress vector with respect to undeformed coordinates, Eqn. (1.34)	p. 22
$\vec{\epsilon}$	Surface strain vector, Eqn. (1.34)	p. 22
$\dot{J}_{ij}(t)$	Components of the relaxation function derivative tensor, Eqn. (1.42)	p. 24

η	Surface viscosity of the Kelvin-Voigt model, Eqn. (1.43)	p. 24
σ	Standard deviation of a Gaussian distribution, Eqn. (2.2)	p. 29
MAE	Mean absolute error, Eqn. (2.2)	p. 29
E_{Gibbs}	Gibbs fluid elastic modulus, Fig. 3.2	p. 42
A_{ref}	Reference area, technically equivalent to A_0, but conceptually different, Fig. 3.3	p. 44
RMSE	Rooted mean square error, Fig. 3.5	p. 45
γ_{ref}	Surface tension of the respective reference shape, emphasizes that they may be different in an individual figure, Fig. 3.7	p. 45
G_{2D}	Two dimensional shear modulus, Fig. 3.10	p. 51
$\Delta\gamma_{\text{wall}}$	Surface tension difference between wall-surrounding and wall-capsule, Eqn. (4.1)	p. 56
l_0	Position of the contact detachment in undeformed arc-length coordinates, Eqn. (4.1)	p. 56
f	External force applied to the contacting system, Eqn. (4.1)	p. 56
q	Transverse shear stress due to bending forces, Eqn. (4.18)	p. 60
Γ	Surface tension ratio between upper and lower contact reference shape, Eqn. (4.68)	p. 74
$\tilde{\gamma}_c^{u,d}$	Relative contact surface tension contribution, Eqn. (4.76)	p. 76
R_0	Reference shape radius of curvature at the apex, Fig. 4.16	p. 87
$\vec{u}$	Displacement field, Eqn. (5.1)	p. 100
$\vec{n}$	Surface normal vector, Eqn. (5.2)	p. 100
$\underline{\underline{\sigma}}$	Stress tensor, Eqn. (5.2)	p. 100
$\vec{t}$	Traction vector, Eqn. (5.2)	p. 100
$\mathbf{G}(x, y, z)$	Three dimensional Greens tensor, Eqn. (5.4)	p. 101
$\mathbf{G}(x, y)$	Two dimensional Greens tensor, Eqn. (5.6)	p. 101
DDA	Deviation of Traction Direction at Adhesions, Eqn. (5.14)	p. 111
DTMB	Deviation of Traction Magnitude in the Background, Eqn. (5.15)	p. 112
DTMA	Deviation of Traction Magnitude at Adhesions, Eqn. (5.16)	p. 112
ADTMA	Absolute Deviation of Traction Magnitude at Adhesions, Eqn. (5.17)	p. 112
SNR	Signal to noise ratio, Eqn. (5.18)	p. 113
DMA	Deviation of the Maximum traction at Adhesions, Eqn. (5.19)	p. 113
K_s	Meridional bending strain, Eqn. (A.23)	p. 129
K_ϕ	Circumferential bending strain, Eqn. (A.23)	p. 129
m_s	Meridional bending moment, Eqn. (A.28)	p. 129
m_ϕ	Circumferential bending moment, Eqn. (A.28)	p. 129

Introduction and motivation

Interfaces between two or more phases are ubiquitously found in nature. They are fundamental for the function of cells [1], [2], transport processes [3], [4] and the respiratory system [5], [6], only to name a few – life could not exist without them.

Interfaces are in-fact so common that their properties are intuitive to most humans, without a deeper understanding of the underlying physics. For example, when using a straw to drink from a container, we intuitively exploit the surface tension of the liquid in combination with an under-pressure generated by our mouth to draw the liquid up the straw, overcoming the gravitational pull exerted onto the liquid. This is a complicated process from a physicist's point-of-view, but considered trivial, or obvious, from the perspective of the person intuitively enjoying a tasty beverage. While it is implausible that a deeper theoretical understanding of the underlying physics would improve the straw-drinking-technique of a human, it is indeed very likely that we are able to provide insight for the straw manufacturer. Parameters such as the straw width, material, height are all accessible in a theoretical description of the system. Moreover, unleashing the analytic tool-set of a physicist allows us to identify and prove optimal parameters and stability thresholds for a set of carefully selected and agree-able assumptions.

What makes the physics of fluids and interfaces challenging is that on a microscopic level there are a multitude of effects at play. For example, a microscopic description of the liquid-air interface needs to account for the complex interactions between the vast number of liquid and air molecules. For example, there are electrostatic interactions induced by the charge distribution in the liquid and air molecules, leading to a plethora of effects such as hydrogen bonds or van-der-Waals interactions. Properly retaining all of the microscopic detail in a description of the liquid-air-interface is thus simply not feasible. We can, however, similar to the approach of Ludwig Boltzmann to thermodynamics, define macro-observables, describing the system accurately on a macro-scale, while coarsening the description such that individual molecule interaction is not relevant. The property that emerges from such approach is exactly the surface tension of the interface, as commonly denoted by the symbol γ. It sufficiently captures the manifestations of the microscopic effects and provides a suitable proxy to describe the system on a macro-scale. The first theoretical treatment of the interface between fluids goes back to Thomas Young in 1805 [7]. Combined with the work of Pierre-Simon Laplace in 1806 and James Clerk Maxwell in 1830 [8] a breakthrough in the theoretical description of static interfaces is achieved as the Young-Laplace-equation, which connects the pressure difference across the interface with the radii of curvature and the surface tension – i.e. connects the geometry of the interface with the forces acting on it via an algebraic equation, as we will rediscover in the following chapter.

For some applications, such as oxygen transport through the body [1] or drug delivery, the properties of simple liquid-liquid interfaces are exhausted by the required specifications [1], [9]–[11]. Luckily, there are ways to further enhance these interfaces, for example, to allow for larger deformations or reduce/increase adhesion. What we will be focusing on in this thesis is the use of interfacial skins produced at the interface of two phases for exactly these means.

There are several ways to produce interfacial skins, a popularly known approach is to pre-manufacture an elastic skin and retroactively fill it with one phase, while keeping it embedded in another phase – just like a balloon for a birthday party. While the theory presented in this thesis also describes interfacial skins produced this way, we want to focus on a particular *reference* geometry of the elastic skin, i.e. a particular geometry of the skin where no elastic stresses are

[1] Red blood cells (erythrocytes) in particular.

present. The reference geometry of the elastic skin is essentially arbitrary, however, a common technique in experiments is to let the skin form on an already existing interface, e.g. a droplet [12]–[15]. The general idea is that transport processes from the bulk to the interface are able to accumulate enough polymeric material at the interface to start a cross-linking process. Over time, or with the right external stimulus, such as light exposure [16], a skin develops at the interface. This makes the reference geometry of the interfacial skin akin to the liquid-liquid interface shape, such that it is possible to accurately tune the response to external loads by modifying the structure of the cross-linked network, while maintaining the same reference geometry.

Of course, we will use a model system for the cross-linked interfacial network, as an accurate simulation of such network on the length scale of a single polymer would be too resource intensive. Instead, we reduce the complexity of our description by providing a suitable approximation and are then able to fully describe the interface via an algebraic *constitutive law*, connecting the applied stress with a deformation response. The free parameters appearing in the constitutive laws are the elastic and viscoelastic effective moduli of the interfacial skin. The full theoretical treatment of the problem is presented in Chap. 1. Determining the constitutive parameters from an experiment purely by shape analysis is discussed in Chap. 2. Finally, we demonstrate our approach in-action for two experiments graciously provided to us by our collaborators from the groups of W. Drenckhan and F. Mugele in Chap. 3, where we are able to make quantitative statements about the nature of the experimental system.

Furthermore, we will provide a detailed discussion of the contact behavior between interfacial skins, e.g. two air balloons pressed together, in Chap. 4.

Finally, we investigate novel approaches for the determination of the constitutive parameters from pendant droplets and capsules using machine learning. This is a classic inverse problem, where we have access to the solution of a set of ordinary differential equations and want to determine the respective control parameters of the problem from this solution. We show that machine learning can accelerate these inverse problems tremendously in Chap. 5.

Additionally, we investigate another elastic inverse problem, which has a distinctly different nature. Here, we want to determine cell forces [2] from deformation information in a linear elastic substrate with known material parameters. The challenge encountered here stems from the fact that this problem is mathematically ill-conditioned, once noise enters the displacement field. We show that machine learning is able to outperform conventional approaches by orders of magnitude in any metric in Chap. 5.

[2] More accurately, we want to determine the cell tractions.

1 Axisymmetric interfaces attached to capillaries

In this section we want to study the properties of interfaces between two phases which have a particular symmetry. Namely, we want to limit our view to axi-symmetric interfaces, where the shape of the interface is symmetric with respect to a rotation about the symmetry-axis [1].

Keeping axi-symmetry allows us to describe the interfacial geometry without resorting to finite element methods, as the entire interface is uniquely determined by a single arc C (see the black outline in Fig. 1.1 as an example). A rotation of the arc C about the axis of symmetry then reveals the entire interfacial geometry. This reduces the effective interface geometry from a two dimensional manifold embedded in three dimensional space to a one dimensional line segment embedded in two dimensional space [2]. We will be able to generate a set of first order ordinary differential equations, which entirely characterize the shape of the interface – the shape equations. Importantly, this will be possible for arbitrarily complex interfaces, as long as the symmetry of the problem is preserved. The following sections are determined to derive exactly these shape equations for interfaces ranging from purely liquid to interfaces with complex viscoelastic properties.

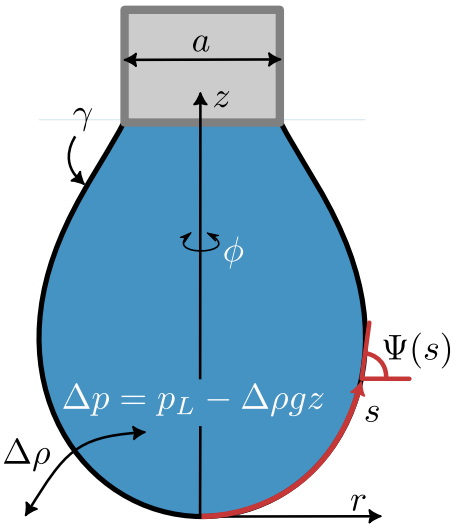

Figure 1.1: Visualisation of an axi-symmetric droplet suspended from a capillary, parametrized in arc length coordinates s and Ψ. The pressure difference across the interface Δp is proportional to the mean local curvature.

Furthermore, we want to study such interfaces in a state, where they are attached to a capillary in this section. This geometry is mainly motivated by the fact that it is easily attainable and alterable in an experiment [12]–[15], [17]. The geometry of the capillary will, however, merely enter as a boundary condition[3], such that the theory presented here can also be used to study interfaces in other axi-symmetric geometries, for example closed interfaces as studied in Ref. [18] in the context of buckling instabilities, or as in Ref. [14] in the context of capsules at liquid-liquid interfaces and in Ref. [19] for capsules in a magnetic field. Importantly, this also means, that some experimental aspects of the capillary are not fully accounted for. For example, if the interface is not pinned at the capillary, but is able to freely slide along the capillary wall, additional balance equations at the capillary arise [4]. While this geometry seems simple, the experimental realization of such a geometry is severely complex [12]. Here, we will not discuss the immense effort required to properly prepare and manufacture the capillary for experiments using this geometry, and rather limit ourselves to the theoretical description of such systems, where we assume ideal conditions. More detailed information about the experiment preparation of capillaries can be found in the experiment literature [12], [20]–[22].

[1] Without loss of generality, we always choose the z-axis as the axis of symmetry for all of our considerations.

[2] From the mathematical description point-of-view the radial component r of the cylindrical coordinates is independent from the angle of rotation about the cylindrical axis ϕ.

[3] Mathematically, the capillary attachment is only a boundary condition. However, enforcing this boundary condition yields several non-trivial effects, such as stress concentration around the capillary.

[4] Because the radial and vertical variations at the capillary no longer vanish trivially.

One particularly convenient parametrization of the arc C is found as the arc-length parametrization, where the parametrization parameter of the curve C is chosen to be the integrated arc length s, as shown in Fig. 1.1. At any arc length s, the tangent of the arc has an angle Ψ relative to a reference tangent. We will always measure Ψ with respect to the r-axis, as seen in Fig. 1.1. Knowledge of the function $\Psi(s)$ at every arc length s along the arc C is sufficient to construct the entire interface geometry. This is obvious once we construct the coordinate transformation to cylindrical coordinates (r, z) as

$$\frac{\mathrm{d}r}{\mathrm{d}s} = \cos\Psi, \text{ and } \frac{\mathrm{d}z}{\mathrm{d}s} = \sin\Psi. \tag{1.1}$$

Our efforts will thus be aimed at determining the function $\Psi(s)$, or a derivative of this function. We use Eqns. (1.1) in the following to transform from arc-length coordinates to cylindrical coordinates. In a sense, Eqns. (1.1) are the first two shape equations present for any of our problems and arise purely from the coordinate transformation, we thus call them the *geometric shape equations* in the following.

The two principal curvatures of the interface are the circumferential and meridional curvatures as defined purely by geometry

$$\kappa_\phi = \sin\Psi/r \text{ , and } \kappa_s = \mathrm{d}\Psi/\mathrm{d}s\,. \tag{1.2}$$

While the meridional curvature measures the inverse radius of curvature along the arc-length coordinate s, the circumferential curvature measures the inverse radius of curvature of the direction orthogonal to the arc. Finally, the appropriate [5] geometric boundary conditions for an interface attached to a capillary with diameter a are given by

$$r(s=0) = z(s=0) = 0 \text{ and } r(s=L) = \frac{a}{2}\,, \tag{1.3}$$

where L is the total length of the arc C. The boundary conditions at $s = 0$ describe the apex of the interface, where the radius, the arc angle and the height are fixed to zero. Finally, the last boundary condition in Eqns. (1.3) at $s = L$ describes the attachment to the capillary. The boundary conditions Eqns. (1.3) will be universally used for all further problems where we attach an interface to a capillary. Altough the connection to the capillary might still be accompanied by additional boundary/ initial conditions stemming from material response functions, as we will discuss. These prerequisites set the stage for the discussion of actual interfaces, where the physical properties of the interface will dictate the interface shape via additional shape equations, finally yielding the function $\Psi(s)$. Determining the shape equations, dictated by the interface properties, requires us to use the appropriate mathematical tools along with the laws of nature. While there are many (mostly equivalent) ways to derive those shape equations, we will discuss the derivation in terms of variational calculus, simply because of its elegance. While the shape equations for liquid and elastic interfaces are known in literature [8], [18], [23], we want to provide a complete derivation here for completeness sake and as a pre-requisite for the derivation of the shape equations for the contact problem in Chap. 4. An overview of the mathematical framework of calculus of variations required for the discussion of the problems encountered during this thesis is provided in the Appendix A.1.

We start our discussion with a simple case, where the interface only has a constant surface tension and then progressively generalize the theory until we arrive at the time-dependent shape equations of visco-elastic capsules.

[5] Appropriate in the sense that the boundary conditions for the *apex* of the interface should eliminate the translational degrees of freedom in the z coordinate and fix the rotational axis to be the z-axis. The missing boundary condition for $\Psi(s = 0)$ is actually not trivial and must emerge from the variation/force balance at the apex, hence it is not yet listed here, although we will show that $\Psi(s = 0) = 0$ is recovered in most cases.

1.1 Liquid interfaces

> **Notice** – A full discussion of the shape space of liquid droplets can be found in the author's master thesis and the author's publication [24]. The discussion presented here extends those results for inverted gravity ($\Delta\tilde{\rho} < 0$). This is a relevant pre-requisite for the contact problem discussed in Chap. 4.

At liquid-liquid interfaces two distinct phases meet. Due to the change in the interaction potential across the interface, an energetic penalty proportional to an infinitesimal interface area patch is incurred. The proportionality constant of this energetic penalty is called *surface tension* and denoted by γ. It is not universal, but differs for every set of two phases. The effective surface tension at any point of the interface can account for several different physical effects, which all generate/inhibit an energy penalty proportional to the surface area patch $\mathrm{d}A$, such as an energy difference between cohesion and adhesion, surfactant concentration, material density inhomogeneities and more. Effectively, the surface tension encountered at the interface is a force per length, which acts tangential to the interface, in order to reduce the interface area and subsumes several microscopic effects. In the following, we will not discuss non-uniform surface tensions and area dependent surface tensions, although it would be possible to generalize the following description to exactly these cases, e.g. we could imagine that the surfactant concentration is affected by gravity, i.e. $\gamma = \gamma(z)$, or directly dependent on the surface area of the interface A, over which a fixed number of surface active molecules spreads uniformly [6] and thereby modifies the surfactant concentration. An effective elastic response to area changes based on the redistribution of surfactants could also be described as a Gibbs elasticity, as detailed in Ref. [25].

In order to derive the shape equation for $\Psi(s)$, we can choose between several equivalent approaches. As we have shown in Ref. [24], balancing all forces acting on a horizontal slice of the liquid droplet is sufficient to derive the required shape equation. Here, however, we perform the first variation of the free energy in order to obtain the shape equations, because we can reuse the derivation for several later chapters [7].

Thus, we express the energy for a purely liquid droplet with uniform surface tension γ at the interface with surface area A, uniformly loaded with gravitational acceleration g along the z-axis [8] as

$$E = \int \mathrm{d}A\,\gamma + \int \mathrm{d}V\,\Delta\rho g z \tag{1.4}$$

where the first term is the energetic penalty of the interface, while the second term is the gravitational potential energy of the fluid with density contrast to the surrounding medium $\Delta\rho$. The influence of small perturbations of the gravity-capillary alignment is studied phenomenologically in Ref. [17] and motivated by the general sensitivity of axisymmetric solutions to perturbations in the control parameters, as we show in Ref. [24]. It is vital to keep the intrinsic limitation of assuming axi-symmetry for the resulting extremal shape equations in mind.

The trivial solution, minimizing the energy functional Eqn. (1.4), is obviously given as a droplet with no surface and no volume, as then $E = 0$. This solution is of course not the desired one. Hence we want to employ an additional constraint, namely, we want to prescribe the volume of the droplet and only allow solutions with this volume, i.e. we want to search for the optimal surface geometry at a given internal volume. To achieve this we perform a Legendre transformation of Eqn. (1.4) with the conjugate pair of the prescribed volume V and its Lagrange multiplier, which

[6] Because of Marangoni flow of the surfactants at the interface.
[7] Specifically, the variational approach will come in really useful in the discussion of contacting elastic interfaces.
[8] The axis of gravity *must* coincide with the symmetry axis chosen in our parametrization.

is the pressure difference between inside and outside of the drop $p_L = \Delta p(s=0)$, measured at the apex of the drop at $s = 0$.

We want to emphasize the actual interpretation of the Lagrange multiplier p_L – the gradient of the inner energy of the droplet E produces forces, which drive the droplet into the minimum of the inner energy E. The global minimum of the inner energy E has no surface area and no volume. By performing the Legendre transformation from E to a modified energy $F = E - Vp_L$, we modify the energetic landscape in such a way that the extremum of the function F is achieved at a particular volume V of the droplet [9] given the appropriate choice of Lagrange multiplier p_L. In terms of a force balance, this means that the conjugate parameter p_L counteracts the contraction of the droplet due to the gradient in the inner energy E and thus indeed quantifies an over-pressure inside of the droplet. The pressure p_L thus gives a measure of the slope of the inner energy E with respect to volume changes. If the sign of the pressure p_L is positive, the system is forced (by the volume constraint) into a state which could reduce the inner energy E by a decrease in volume V [10]. If, however, the pressure is negative [11] the inner energy is forced into a state, from which it could (without the volume constraint) reduce its inner energy E by increasing the volume.

We finally arrive at the appropriate functional we want to subject to extremization as

$$F = \int \mathrm{d}A\,\gamma + \int \mathrm{d}V\,\Delta\rho g z - \int \mathrm{d}V p_L = \pi \int_0^L \mathrm{d}s \left\{ 2r\gamma - \underbrace{(p_L - \Delta\rho g z)}_{p(z)}\, r^2 \sin\Psi \right\} , \tag{1.5}$$

where we parametrize the drop in arc length parametrization and write out the area and volume elements in terms of the infinitesimal arc length element $\mathrm{d}s$, such that $\mathrm{d}A = \mathrm{d}s\, 2\pi r$ and $\mathrm{d}V = \mathrm{d}s\, \pi r^2 \sin\Psi$.

As formally derived in the Appendix A.1.1, we can determine the shapes which are realized in nature from the energy functional Eqn. (1.5) by analysing the first variation of the functional. These extremal solutions are a super-set of the solutions with minimum overall energy F. As also discussed in the Appendix A.1, the Euler-Lagrange equations are a conceptualization of the results obtained from the first variation. It is important to properly discuss all resulting boundary terms, as they are easily forgotten when simply applying the Euler-Lagrange equations to a functional such as Eqn. (1.5). For the purpose of a later derivation (namely for the contact problem in Chap. 4) we want to make use of a particular choice of an explicit shape variation. Hence we will not use the Euler-Lagrange formalism here.

Specifically, we want to subject the shape of the droplet to normal and tangential variations δn and δt. Those geometric shape variations can be expressed in terms of the more attainable geometric variations in r and z components through the purely geometric relations [18], [26], as depicted in Fig. 1.2:

$$\begin{aligned} \delta r &= \sin\Psi\delta n + \cos\Psi\delta t\ , \quad & \delta n &= \sin\Psi\delta r - \cos\Psi\delta z \\ \delta z &= \sin\Psi\delta t - \cos\Psi\delta n\ , \quad & \delta t &= \cos\Psi\delta r + \sin\Psi\delta z \end{aligned} \tag{1.6}$$

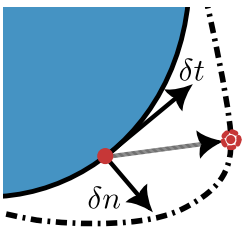

Figure 1.2: Normal and tangential shape variations.

with the defining geometric relation $\mathrm{d}s^2 = \mathrm{d}r^2 + \mathrm{d}z^2$. Conceptually, we are allowing two independent functions $\delta n(s)$ and $\delta t(s)$ to deform the shape everywhere along the

[9] In the following, we will refer to this as "volume control".

[10] The positive pressure p_L means that the inner energy E produces contractive forces, which need to be countered by the Lagrange multiplier p_L.

[11] The pressure can not be negative for a liquid droplet, but it can be negative for elastic shells, where we will reuse these considerations.

arc. The shape variations need to respect the geometric requirements, e.g. the clamping at the capillary, and must conserve a continuous shape, such that $\delta r(s)$ and $\delta z(s)$ must be continuous at every point of the solution.

Finally, when properly performing the variation of Eqn. (1.5), we arrive at the resulting extremal identity:

$$\delta F/\pi = \left[2r\gamma\delta t - p(z)r^2\delta z\right]_0^L + \int_0^L \mathrm{d}s \left\{2\delta n \left[\gamma\left(\sin\Psi + r\frac{\mathrm{d}\Psi}{\mathrm{d}s}\right) - p(z)r\right]\right\} . \tag{1.7}$$

The variations δn and δt are arbitrary for the points $s \in (0, L)$, hence if we demand that $\delta F = 0$, we can directly conclude how the arc angle Ψ changes along the arc s on the domain $(0, L)$, which is the well known *Young-Laplace* equation [7], [8]:

$$p(z) = p_L - \Delta\rho g z = \gamma\left(\frac{\sin\Psi}{r} + \frac{\mathrm{d}\Psi}{\mathrm{d}s}\right) = \gamma\left(\kappa_\phi + \kappa_s\right) . \tag{1.8}$$

The boundary terms encountered at $s = L$ in Eqn. (1.7) are zero, because the variations δn and δt are zero at $s = L$ [12]. The total height of the droplet is free, such that the variation at $s = 0$ is only partially clamped. The droplet has to connect to itself, such that $r(s = 0) = 0$, where $\delta r(s = 0) = 0$ in order to not rip the droplet open at the apex. However, $\delta z(s = 0) \neq 0$ in general [13], such that another equation arises at the apex of the drop, where we find

$$2\gamma \sin\Psi(s = 0) = p_L r(s = 0) . \tag{1.9}$$

Eqn. (1.9) gives access to the curvature at the apex of the droplet and hence the missing initial condition for $\Psi(s = 0)$. Because $r(s = 0) = 0$, we immediately recover $\Psi(s = 0) = 0$. Furthermore, Eqn. (1.9) is otherwise equivalent to the Young-Laplace Eqn. (1.8), once we enforce isotropy at the apex with $\kappa_\phi(s = 0) = \kappa_s(s = 0)$. In principle, the length L in Eqn. (1.5) is allowed to vary as well, however, the variation of the length L yields no additional equation, because the transversality condition at the apex yields $2\gamma r(s = 0) = 0$, which is always fulfilled by our boundary condition, imposed by symmetry, $r(s = 0) = 0$ [14]

A first integral of the Young-Laplace equation Eqn. (1.8) can easily be found by utilizing Noethers theorem (see Appendix A.1.4 for an overview of the results and implications) as the resultant of the conserved quantity belonging to the translational invariance in the z-coordinate, which gives exactly the force balance in z-direction:

$$2\pi r\gamma \sin\Psi - p(z)r^2 = \Delta\rho g \int \mathrm{d}V. \tag{1.10}$$

The force balance Eqn. (1.10) states that the surface tension forces along the circumference of the drop act against the internal pressure and self weight of the drop. This is exactly the force balance used in our derivation of the Young-Laplace equation in Ref. [24].

Even though the energetic constituents are so simple, we find a complex and rich shape space even for purely liquid droplets.

[12] They are zero at $s = L$, because the shape is clamped to the capillary here, which forbids any variations of the normal and tangential components.

[13] Our parametrization places the apex at $s = 0$ with $r = z = 0$, however, the droplet is actually suspended from the capillary, such that it is in order to not clamp the vertical variation $\delta z(s = 0)$ here.

[14] The transversality condition gives an equation at $s = 0$, because the endpoint at the apex of the drop is the one that is free and not the one at the capillary.

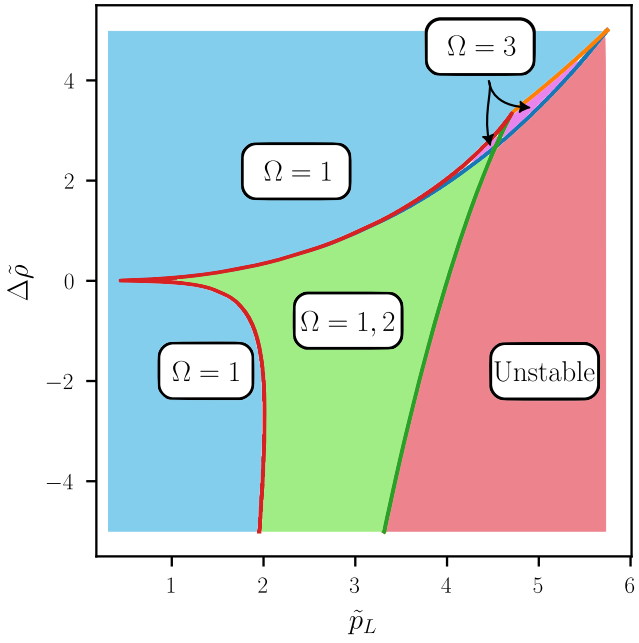

Figure 1.3: The shape space of liquid droplets contains several characteristic regions. The blue shaded area where $\Omega = 1$ is the region, where only shallow droplets can exist. These droplets have no neck or bulge and present the most stable configuration for the liquid droplets because they are stable both with volume and pressure control, as we have shown in Ref. [24]. The solutions with $\Omega = 1$ extend further to the green shaded area, where $\Omega = 1, 2$. In this region, however, also shapes of class 2 are available as solutions to the shape equations. Shapes with $\Omega = 2$ are only stable when subjected to volume control and unstable otherwise. Stable solutions of class $\Omega = 3$ (under volume control only) are also found in a small region (pink shaded region), which is bounded by the maximum volume line (blue line) towards higher pressures.

The three shape equations, retrieved for the shapes of purely liquid droplets, expose three dimensionless control parameters – the dimensionless pressure difference $\tilde{p}_L \equiv p_L a/\gamma$, the dimensionless density contrast $\Delta\tilde{\rho} \equiv \Delta\rho a^2/\gamma$ and the shape class Ω. The shape class Ω appears, because the shape equations have multiple solutions for a prescribed boundary condition $r(L) = a/2$ and it is defined to count the number of bulges and necks of the shape, as we introduce in Ref. [24]:

$$\Omega \equiv 1 + \#\text{necks} + \#\text{bulges}\,. \tag{1.11}$$

A neck can be found exactly at each local minimum of the function $r(s)$, and a bulge can be found at each local maximum of the function $r(s)$. Because the function $r(s)$ is continuous, it is guaranteed that the shape class Ω properly classifies all possible shapes.

Finally, we can attain a parameter diagram of the liquid droplet shape space by choosing the continuous control parameters (i.e. $\tilde{p}_L$ and $\Delta\tilde{\rho}$) as the respective axis of the parameter space and by coloring the associated allowed discrete values of Ω, as shown in Fig. 1.3. Possible solutions found in this parameter diagram include shapes from various shape classes. Shapes of class $\Omega = 1$ (blue and green regions of Fig. 1.3) correspond to shallow spherical caps and are always stable because $\mathrm{d}p_L/\mathrm{d}V > 0$ [24]. These solutions are ultimately limited in volume, since, by definition, no bulge or neck is possible along the entire shape. The shape transition $\Omega = 1 \to 2$ (green line at the right boundary of the $\Omega = 1, 2$ region in Fig. 1.3) is accompanied by an inversion of the pressure-volume slope $\mathrm{d}p_L/\mathrm{d}V < 0$ as we show in Ref. [24]. This also means that shapes from class $\Omega = 2$ can only be stable if the volume is directly controlled, while they are always unstable if the pressure is controlled [24]. Some specific solutions of class $\Omega = 3$ are stable (see Fig. 1.3 pink regions) when controlling the volume, those are rarely subjected to experiments however, because of their sensitivity to pressure and density fluctuations [24] and collapse. All further solution classes $\Omega > 3$ are always unstable and are not realized in nature [24].

The solutions found for $\Delta\tilde{\rho} < 0$ only contain shapes with shape classes $\Omega = 1$ and $\Omega = 2$, as can be seen in Fig. 1.3. We can understand this by realizing that the transition from $\Omega = 2 \to 3$ would require a neck to appear along the shape, however, a neck can not be stable with the gravitational force acting to compress the shape against the capillary. This fact becomes obvious when consulting the force balance Eqn. (1.10).

1.2 Elastic interfaces

The next generalization from the Young-Laplace equation (while keeping strict axisymmetry) is to allow for anisotropic and in-homogeneous stress contributions at the interface, i.e. we allow stretching of the interface material with a certain prescribed stress response to the stretching load – a constitutive law.

We will now re-discover the results from literature [14], [15], [23] and derive the appropriate shape equations for such elastic skin from a variational calculation. We will later re-use this derivation for the elastic contact problem in Chap. 4, which is why it is included here.

For now, we want to assume that the stretching of the material does not dissipate energy, however, we will in a later section (see Sec. 1.3) consider materials which dissipate energy during deformation. With the assumption of a conservative material, it is possible to define a surface energy density of the interface w_{S_0}, measured relative to the *undeformed* surface area A_0 of the interface

$$F = \int \mathrm{d}A_0\, w_{S_0} - \int \mathrm{d}V(p_a - \Delta\rho g z) = \pi \int_0^{L_0} \mathrm{d}s_0 \left\{ 2r_0 w_{S_0} - \lambda_s r^2 \sin\Psi (p_a - \Delta\rho g z) \right\}, \quad (1.12)$$

where the volumetric term constitutes the gravitational potential energy and the volume constraint enforced by the Lagrange multiplier p_a. While p_a also quantifies the pressure at the apex of the capsule, just as p_L, it is only equal to the pressure of the reference liquid droplet p_L, if the deformation of the capsule is zero. Hence, we need to differentiate between the apex pressure of the (deformed) capsule p_a and the pressure of the reference liquid droplet p_L. The transformations from undeformed coordinates (s_0, r_0, z_0) to deformed coordinates (s, r, z) are given by the two stretching ratios $\lambda_s \equiv \mathrm{d}s/\mathrm{d}s_0$ and $\lambda_\phi = r/r_0$, with $\mathrm{d}z^2 = \lambda_s^2 \mathrm{d}s_0^2 - \lambda_\phi^2 \mathrm{d}r_0^2$. A deformed element of the surface area is thus given by $\mathrm{d}A = \lambda_s \lambda_\phi \mathrm{d}A_0$. Additionally, we have a well defined reference arc length $L_0 = \int \mathrm{d}s_0$, which is fixed. Thus, if we are able to express the functional in terms of the undeformed arc-length coordinate s_0, we will have a simple variational problem with fixed endpoints on our hands (exactly as described in Appendix A.1.1). Using the stretches λ_s and λ_ϕ allows us to express the functional as such that we obtain the r.h.s of Eqn. (1.12), just as in the literature [18].

At this point we are able to perform the variation, once we specify on which parameters the surface energy density shall depend. We will neglect bending effects for now, which makes the surface energy density a function exclusively of the surface stretches λ_s and λ_ϕ. Including bending effects is as simple as respecting that the surface energy density should additionally depend on the bending strains, we detail this in the Appendix A.2.1.

As before, we perform a partial integration for all terms with variations of geometric derivatives and use Eqn. (1.6) to express all encountered variations via the normal and tangential shape variations, finally resulting in

$$\begin{aligned} \delta F = \pi \left[2\frac{r}{\lambda_\phi} \frac{\partial w_{S_0}}{\partial \lambda_s} \delta t - (p_a - \Delta\rho g z) r^2 \delta z \right]_0^L \\ + 2\pi \int_0^L \mathrm{d}s\, r \Bigg\{ \delta n \left[-(p_a - \Delta\rho g z) + \frac{1}{\lambda_\phi} \frac{\partial w_{S_0}}{\partial \lambda_s} \frac{\mathrm{d}\Psi}{\mathrm{d}s} + \frac{\sin\Psi}{r} \frac{1}{\lambda_s} \frac{\partial w_{S_0}}{\partial \lambda_\phi} \right] \\ + \delta t \left[-\frac{1}{\lambda_\phi} \frac{\mathrm{d}}{\mathrm{d}s} \frac{\partial w_{S_0}}{\partial \lambda_s} + \frac{\cos\Psi}{r} \frac{1}{\lambda_s} \frac{\partial w_{S_0}}{\partial \lambda_\phi} \right] \Bigg\}, \end{aligned} \quad (1.13)$$

which is the result also obtained in Refs. [15], [18], [27]. From Eqn. (1.13) we can extract two extremal properties of the shape, which give the slope of the arc angle along the shape as a function

of the pressure, stretches and the derivatives of the surface energy density with respect to the stretches, as well as the slope of the surface energy change in meridional direction:

$$p(z) = p_a - \Delta\rho g z = \frac{1}{\lambda_\phi}\frac{\partial w_{S_0}}{\partial \lambda_s}\frac{\mathrm{d}\Psi}{\mathrm{d}s} + \frac{\sin\Psi}{r}\frac{1}{\lambda_s}\frac{\partial w_{S_0}}{\partial \lambda_\phi} = \tau_s\kappa_s + \tau_\phi\kappa_\phi \tag{1.14}$$

$$\frac{1}{\lambda_\phi}\frac{\mathrm{d}}{\mathrm{d}s}\frac{\partial w_{S_0}}{\partial \lambda_s} = \frac{\cos\Psi}{r}\frac{1}{\lambda_s}\frac{\partial w_{S_0}}{\partial \lambda_\phi} \Rightarrow \frac{\mathrm{d}\tau_s}{\mathrm{d}s} = \frac{\cos\Psi}{r}(\tau_\phi - \tau_s)\,. \tag{1.15}$$

these are exactly the force balance conditions with meridional and circumferential surface stresses defined as [15], [18], [28]:

$$\tau_{s,\phi}\lambda_{\phi,s} = \partial w_{S_0}/\partial\lambda_{s,\phi}\,. \tag{1.16}$$

We will show in a later section that the definition Eqn. (1.16) is not sufficient to discuss viscelasticity and instead provide a derivation where $\tau_{s,\phi}$ are purely defined by the geometric line forces. The resulting relation between surface stresses $\tau_{s,\phi}$, the surface curvatures $\kappa_{s,\phi}$ and the pressure $p(z)$ reduces to the Young-Laplace equation for $\tau_s = \tau_\phi = \gamma$.

All boundary terms obtained from Eqn. (1.13) at $s = 0$ and $s = L$ vanish. The boundary terms at $s = L$ vanish because the interface is geometrically clamped to the capillary, such that neither tangential, nor normal variations are allowed, and thus $\delta t(s = L) = \delta n(s = L) = \delta z(s = L) = 0$. The total height of the capsule is still allowed to be varied at the apex, such that $\delta z(s = 0) \neq 0$ in general, however because $r(s = 0) = 0$, this terms vanishes as well. Finally, the tangential variation at $\delta t(s = 0)$ is disallowed, as it would violate the parametrization. Note that the boundary terms appearing in Eqn. (1.13) will be essential for the discussion of the solutions of the respective broken functional in the contact problem discussed later in Chap. 4. There, these boundary terms will generate the Weierstrass-Erdmann conditions (see Appendix A.1.3 for a derivation of those conditions) at the contact point of the two elastic skins.

What is still missing in our description of the elastic interface is the exact mapping between surface stretches and surface strains. In the fully elastic case, where the elastic potential energy is well defined, we are looking for an elastic surface energy density capturing all of the important effects of the elastic deformation of the interface at least to leading order. The choice of constitutive law, or surface energy density, is not trivial, since there are numerous approximations that have to be made specifically for the material which is to be described.

1.2.1 Elastic Constitutive Laws

We want to start by assuming that our interface material consists of a cross-linked polymeric chain network. These kinds of polymeric networks can form at the interface when sufficient material accumulates and a polymerisation reaction is engaged. Typically, this is done by means of a chemical reaction or irradiation [16]. Consequently, we first want to discuss a single freely-jointed polymer chain with N monomers, each of length b, as a simple as possible material model. The polymer resists stretching because of the entropic penalty generated by the reduced configurational degrees of freedom in the stretched state. In the limit where we have many monomers $N \gg 1$, the probability distribution $P(R_p)$ of end-to-end vectors $\vec{R}_p$ of a single polymer chain is guaranteed to be Gaussian, simply because of the central limit theorem. Furthermore, due to entropic effects – or equivalently averaged dynamical effects [29] – we expect an energetic penalty for an extension of the polymer. Thus

$$P(R_p) = \left(\frac{2\pi\langle R_p^2\rangle}{d}\right)^{-d/2}\exp\left(-\frac{d}{2}\frac{R_p^2}{\langle R_p^2\rangle}\right) \tag{1.17}$$

is the relevant probability distribution in d dimensions [30] ($d = 3$ here, despite the polymeric membrane being flat, as we will argue later), as long as the assumption of uncorrelated monomers holds, i.e. as long as the stretching of the chain is not too strong.

We immediately find that the associated free energy difference between an undeformed configuration $\mathrm{d}\vec{R}_{p,0}$ and a deformed configuration $\mathrm{d}\vec{R}_p$ is given by

$$\Delta F = \frac{d k_B T}{2\langle R_p^2 \rangle} \left(R_p^2 - R_{p,0}^2 \right) , \tag{1.18}$$

where the mapping between the undeformed and deformed configurations is defined as the *deformation gradient tensor* $\underline{\underline{F}}$ with $\mathrm{d}\vec{R}_p \equiv \underline{\underline{F}} \mathrm{d}\vec{R}_{0,p}$. The free energy difference Eqn. (1.18) is that of an entropic spring which has a quadratic energy penalty for extension, just as an ideal classical spring and is the simplest consideration for polymeric elasticity.

Defining stretching ratios λ_i along the principal directions $\vec{e}_i$ is possible by utilizing projections of the deformation gradient tensor $\lambda_i = \sqrt{\vec{e}_i \cdot \underline{\underline{F}}^{\mathrm{T}} \underline{\underline{F}} \cdot \vec{e}_i}$, where $\underline{\underline{C}} \equiv \underline{\underline{F}}^{\mathrm{T}} \underline{\underline{F}}$ is the *right-Cauchy-Green tensor* with eigenvalues λ_i^2 and eigenvectors $\vec{e}_i$. With the stretches λ_i^2 we are able to rewrite Eqn. (1.18) and assume a very simple polymer material, where single polymers are used independently to construct a polymeric *phantom* network with isotropic polymer density [31]. The total surface energy density $w_{S_0} = \mathrm{d}F/\mathrm{d}A_0$ for a region of the network containing N_p polymers is thus

$$w_{S_0} = \frac{k_B T}{2\langle R_p^2 \rangle A_0} \sum_{n=1}^{N_p} \sum_{i=1}^{d} \left(\lambda_{i,n}^2 - 1 \right) R_{i,n,0}^2 \approx H \rho_p \frac{k_B T}{2\langle R_p^2 \rangle} \frac{\langle R_0^2 \rangle}{d} \left(\langle \mathrm{Tr}\, \underline{\underline{C}} \rangle - d \right) , \tag{1.19}$$

where we enforced isotropy by demanding $\langle R_{i,n,0}^2 \rangle = \langle R_0^2 \rangle / d$ and define the polymer density as $\rho_p = N_p / V_0$ and the skin thickness as H. Finally, we find that the proportionality constant found in Eqn. (1.19) is the elastic modulus $E \propto H k_B T$.

Additionally, the fluid-skin interfaces on both sides of the interface generate surface tensions between outer fluid and the skin γ_o and inner fluid and the skin γ_i, leading to an additional energy cost $\Delta F_\gamma = \int \mathrm{d}A \, (\gamma_o + \gamma_i) = \int \mathrm{d}A_0 \, \gamma \sqrt{\det \underline{\underline{\mathcal{C}}}}$ [15], where we abbreviate $\gamma = \gamma_o + \gamma_i$ and introduce $\underline{\underline{\mathcal{C}}} \equiv \underline{\underline{C}}^{2D}$ as the 2D right Cauchy-Green tensor. The 2D right Cauchy-Green tensor is a 2x2 matrix with eigenvalues λ_1^2 and λ_2^2. The third dimension, i.e. the thickness, is integrated out and the eigenvalue λ_3^2 of the 3D right Cauchy-Green tensor is implicitly constructed by an additional constraint for the invariants of the 3D Cauchy-Green tensor $\underline{\underline{C}}$. Typically, 3D incompressibility is used as such an additional constraint [32], where $\det \underline{\underline{C}} = 1$.

Importantly, only accounting for constant surface tension contributions is a significant simplification. For complex interfaces other fluid effects, such as the self assembly of substructures at the interface, as seen in vesicles [33], introduce additional non-trivial energetic contributions depending on e.g. the mean curvature $(\kappa_s + \kappa_\phi)/2$ or the Gaussian curvature $\kappa_s \kappa_\phi$ of the interface. These interfaces might be poorly characterised by a purely surface tension based surface energy. Whether or not these effects are relevant for the *reference shape* can be determined experimentally by assuming a purely surface tension based surface energy functional and fitting the associated shapes to an experimental deformation series of the reference interface. Should this fit have a significant shape residual, the aforementioned effects could play a significant role in the deformation of the final deformed shapes sequence as well. Even if the reference interface is not indicative of such effects,

[15] The root determinant of $\underline{\underline{\mathcal{C}}}$ is exactly the change in surface area $\sqrt{\det \underline{\underline{\mathcal{C}}}} = \mathrm{d}A/\mathrm{d}A_0 = \lambda_1 \lambda_2$, and thus indeed the relevant quantity to scale the surface tension energy contribution.

they might still be present in the final interface if the microscopic interface elasticity can not be approximated as an effective entropic spring. A first correction to this is a dissipative component, which makes the surface forces non-conservative. We will generalize the theory to such dissipative contributions in Sec. 1.3.

The total surface energy density for our polymeric skin is thus given by linear superposition of the elastic stretching energy and the surface tension energy $w_{S_0} = E\left(\operatorname{Tr}\underline{\underline{C}} - d\right)/2 + \gamma\sqrt{\det\underline{\underline{\mathcal{C}}}}$. It captures the polymeric resistance to stretching as well as the tendency to minimize surface area due to the interfacial tension. In principle, it would be possible that the surface tension γ additionally depends on the stretching of the skin, since, e.g. there could be a fixed number of surfactants attached to the interface. As the skin expands the surface area density of surfactants is reduced and the surface tension contribution changes accordingly, giving an additional *fluid elasticity*, also often called Gibbs elasticity in the literature [25], leading to the substitution $\gamma = \gamma_0 + G\ln(A/A_0)$. The Gibbs modulus is given by $G = \partial\gamma/\partial\ln(A)$ [34]. Since we want to first investigate the most simple model system, we will not consider this case in the following, however, it could be added to the model in the future, should there be experiment evidence that this makes the description more consistent.

If the skin is thin with respect to the tangential dimensions $H \ll \sqrt{A}$ but thick with respect to the average range of a single polymer $H \gg \sqrt{\langle R_p^2\rangle}$ the dimension d in Eqn. (1.19), which is the relevant dimension that the single *polymers* have available for their movement, needs to be $d = 3$, even though we still have a macroscopically flat skin. Thus the appropriate surface energy density in this case is given by $w_{S_0} = E\left(\operatorname{Tr}\underline{\underline{\mathcal{C}}} + C_{33} - 3\right)/2 + \gamma\sqrt{\det\underline{\underline{\mathcal{C}}}}$ with C_{33} being the third diagonal element of the right Cauchy-Green tensor. If we express C_{33} via the incompressibility condition $\det\underline{\underline{C}} = \det\underline{\underline{\mathcal{C}}}\, C_{33} = 1$ we immediately recover $w_{S_0} = E\left(\operatorname{Tr}\underline{\underline{\mathcal{C}}} - 3 + 1/\det\underline{\underline{\mathcal{C}}}\right)/2 + \gamma\sqrt{\det\underline{\underline{\mathcal{C}}}}$ which is exactly the surface energy density of a neo-Hookean skin with added surface tension energy cost [32].

We can extract the Cauchy surface stresses $\tau_{s,\phi}$ (force per *deformed* length) in meridional and circumferential direction from the energy per *undeformed* surface area w_{S_0} via [15], [18]

$$\tau_{s,\phi} = \frac{1}{\lambda_{\phi,s}}\frac{\partial w_S}{\partial\lambda_{s,\phi}} = E\left(\frac{\lambda_{s,\phi}}{\lambda_{\phi,s}} - \frac{1}{\lambda_s^3\lambda_\phi^3}\right) + \gamma\,. \tag{1.20}$$

Since all the constitutive laws must be invariant with respect to the frame of reference, it is clear that only the invariants of $\underline{\underline{C}}$ may appear in the deformation energy, i.e. $\operatorname{Tr}\underline{\underline{C}}$, $\operatorname{Tr}\left(\operatorname{cof}\underline{\underline{C}}\right)$[16] and $\det\underline{\underline{C}}$, which is the case for our simple as possible polymeric deformation energy Eqn. (1.19).

A phenomenological generalization of the theory is thus to include further combinations of the invariants. Including the unused third invariant $\operatorname{Tr}\left(\operatorname{cof}\underline{\underline{C}}\right)$ as an additive contribution to Eqn. (1.19) reveals another well-known material model

$$w_{S_0}^{\mathrm{M}} = \frac{E}{2}\left(\operatorname{Tr}\underline{\underline{\mathcal{C}}} + \frac{1}{\det\underline{\underline{\mathcal{C}}}} - 3\right) + B\left(\det\underline{\underline{\mathcal{C}}} + \frac{\operatorname{Tr}\underline{\underline{\mathcal{C}}}}{\det\underline{\underline{\mathcal{C}}}}\right) + \gamma\sqrt{\det\underline{\underline{\mathcal{C}}}}\,, \tag{1.21}$$

which is the *Mooney-Rivlin* material model [35], [36], yielding the surface stresses:

$$\tau_{s,\phi} = \frac{Y_M}{3}\left(\frac{\lambda_{s,\phi}}{\lambda_{\phi,s}} - \frac{1}{\lambda_{s,\phi}^3\lambda_{\phi,s}^3}\right)\left[\Psi_M + \lambda_{\phi,s}^2(1-\Psi_M)\right] + \gamma\,, \tag{1.22}$$

[16] $\operatorname{Tr}\left(\operatorname{cof}\underline{\underline{C}}\right) \equiv \left(\operatorname{Tr}\left(\underline{\underline{C}}\right)^2 - \operatorname{Tr}\left(\underline{\underline{C}}^2\right)\right)/2$

with $3E \equiv Y_M \Psi_M$ and $3B \equiv 2Y_M(1-\Psi_M)$. We can immediately see that for $\Psi_M = 1$, the Mooney-Rivlin law Eqn. (1.22) reduces to the neo-Hookean law Eqn. (1.20). The new contribution constructed from the invariant $\mathrm{Tr}\left(\mathrm{cof}\underline{\underline{C}}\right)$ allows us to change the structural coupling of the principle directions, to get an intuitive understanding of this, it is adequate to write out Eqn. (1.21) to quadratic order for small strains $\lambda_{s,\phi} \sim 1$:

$$w_{S_0}^{\mathrm{M}} \approx \frac{Y_{2D}}{2(1-\nu_{2D}^2)}\left((\lambda_s-1)^2+(\lambda_\phi-1)^2\right)+\frac{\nu_{2D}Y_{2D}}{1-\nu_{2D}^2}(\lambda_s-1)(\lambda_\phi-1)+\gamma\sqrt{\det\underline{\underline{\mathcal{C}}}}+\text{const.}\,, \tag{1.23}$$

where we introduced the two dimensional Young's modulus Y_{2D} and two dimensional Poisson's ratio ν_{2D} with $Y_{2D}/2(1-\nu_{2D}^2) = 4E+5B$ and $\nu_{2D}Y_{2D}/(1-\nu_{2D}^2) = 4(E+B)$. We can directly see that the neo-Hookean limit of $B=0$ gives a fixed $\nu_{2D} = 1/2$ and only the third invariant $\mathrm{Tr}\left(\mathrm{cof}\underline{\underline{C}}\right)$ allows for materials deviating from this Poisson's ratio. Values for $\nu_{2\mathrm{D}}$ may be in the interval $(-1,1)$, which is a larger interval than that of the three dimensional Poisson's ratio $\nu_{3\mathrm{D}} \in (-1,1/2)$ [37]. We note that three dimensional material incompressibility demands $\nu_{3\mathrm{D}} = 1/2$ for isotropic materials, simply because a stress applied along the 1-axis induces a volumetric change $\mathrm{d}V = \mathrm{d}V_0\lambda_1\lambda_2\lambda_3$, such that $\lambda_1\lambda_2\lambda_3 = \lambda_1^{1-2\nu_{3\mathrm{D}}} = 1$ [17] if $\mathrm{d}V = \mathrm{d}V_0$ [18] and thus $\nu_{3\mathrm{D}} = 1/2$. However, if the material is not isotropic, the incompressibility constraint may also be achieved by a material with $1-\nu_{3\mathrm{D}}^{ij}-\nu_{3\mathrm{D}}^{ik} = 0$ for $(i\neq j, k\neq i, j\neq k) \in \{1,2,3\}^3$ especially, in the case of in-plane isotropy, we have a single Poisson's ratio $\nu_{2\mathrm{D}}$ for all in-plane deformations, which is arbitrary, while the out-of-plane Poisson's ratio is chosen such that the incompressibility constraint is fulfilled. Thus, incompressibility with in-plane material isotropy does *not* generally yield $\nu_{2\mathrm{D}} = 1/2$, such that we keep the two dimensional Poisson's ratio as a parameter in all further considerations to quantify the effects of out-of-plane anisotropy.

We generate the surface stresses from Eqn. (1.23) with the same procedure as before to get

$$\tau_{s,\phi} = \frac{Y_{2D}}{1-\nu_{2D}^2}\frac{1}{\lambda_{\phi,s}}\left(\lambda_{s,\phi}-1+\nu_{2D}(\lambda_{\phi,s}-1)\right)+\gamma\,, \tag{1.24}$$

which is called the *non-linear Hooke* material model in the literature [14], [15]. This is the elastic material model used in all further considerations unless stated otherwise. Furthermore, we want to consider the unstressed/reference configuration of the elastic problem as the shape that fulfills $\lambda_s(s) = \lambda_\phi(s) = 1\,,\ \forall s \in [0,L]$ and is thus equivalent to the shape of a liquid drop with $\tau_s(s) = \tau_\phi(s) = \gamma\,,\ \forall s \in [0,L]$ along the contour.

[17] Because of the definition $\nu_{3\mathrm{D}} \equiv \mathrm{d}(\lambda_{2,3}-1)/\mathrm{d}(\lambda_1-1)$.
[18] Incompressibility demands constant volume if there is no volumetric sink.

1.2.2 Anisotropic deformation contributions

The main difference between a liquid interface and an elastic interface is the anisotropy and inhomogeniety of the surface stresses. Close to the reference shape, however, these anisotropic and inhomogeneous surface stress contributions necessarily vanish. We want to understand the origins and manifestations of the surface stress anisotropy and inhomogenity in the case where no gravitational forces act on a capsule suspended from a capillary, i.e. $\Delta\tilde{\rho} = 0$ and $r(s = L) = a/2$. The liquid reference shape must then be a perfect spherical cap. All deviations from a spherical shape during the deformation of the pendant capsule are a result of anisotropic and inhomogeneous surface stresses. A rough approximation of the capsule shape in the limit of small deformations $\lambda_s \sim \lambda_\phi \sim 1$ is thus still a spherical cap. We want to discuss when the spherical approximation is appropriate, and when it breaks apart in the following. We start our investigation by introducing the relevant dimensionless quantities. The influence of the elastic skin in relation to the surface tension is measured as $\tilde{K}_{2D} \equiv K_{2D}/\gamma$ and the change in the surface area is expressed as the area stretch $\lambda_A \equiv A/A_0$. Now, we are able to measure the anisotropy in terms of different measures and as a function of the relevant dimensionless parameters in Fig. 1.4. In the case of fully isotropic deformation, corresponding to a spherical sector shape, the deviation of the mean stretch ratio along the contour $\langle \lambda_s/\lambda_\phi \rangle - 1$ (Fig. 1.4 a,b) and the standard deviation of the meridional and circumferential stretches $\mathrm{std}_s(\lambda_{s,\phi})$ (Fig. 1.4c,d) are both zero. Since we neglect gravitational effects, it is clear that the unstressed shape of the capsule at $\lambda_A = 1$ *must* be a spherical sector. The stretched shape will be anisotropically stressed, in general, because of the boundary condition imposed by the attachment at the capillary. We can find, however, another particular stretch, where the *stressed* shape is approximately spherical. This is reached at the critical stretch $\lambda_{A,c}$ at which $\tilde{p} = 0$. The force balance for every point on the capsule requires that the pressure force cancels the tension force. For $\tilde{p} = 0$, we therefore have $\tau_s = \tau_\phi = 0$ on the entire surface, i.e. the surface is stress-free everywhere at this critical stretch. Since $\tau_s = \tau_\phi = 0$ implies $\lambda_{s,c} = \lambda_{\phi,c} = (1 + \gamma/E)^{-1/6}$ [19] and thus isotropic stretching, the shape at this point is again correctly described by a perfect sphere. However, it is not possible to reach this exact shape with the clamping at the capillary. This is obvious when considering that $\lambda_\phi(s = L) = 1$ must be satisfied due to the capillary, which is why we can not actually reach this point in Fig. 1.4 but can get arbitrarily close to it, concentrating the anisotropy in a smaller and smaller region around the capillary.

If the stretch is further decreased to $\lambda_A < \lambda_{A,c}$ both $\tau_s < 0$ and $\tau_\phi < 0$ will become compressive and buckling or wrinkling instabilities of the capsule may occur [15], [37].

For stretch values other than $\lambda_A = 1$, the resulting shape is non-spherical, because of the anisotropy ($\lambda_s \neq \lambda_\phi$) introduced by the boundary condition at the capillary. This can clearly be seen in Fig. 1.4a,b. For inflated shapes $\lambda_A > 1$, we find $\langle \lambda_s/\lambda_\phi \rangle - 1 > 0$ indicating that stretching is biased towards meridional deformations resulting in slightly prolate shapes, whereas for deflated shapes $\lambda_A < 1$, $\langle \lambda_s/\lambda_\phi \rangle - 1 < 0$ and circumferential deformations are preferred, resulting in slightly oblate shapes. The mean anisotropy increases upon inflation before decreasing again at much higher stretches (see the insets in Fig. 1.4a,b for a wider deformation range), when the influence of the capillary becomes again negligible.

[19] For the neo-Hookean elastic surface stresses as defined in Eqn. (1.20).

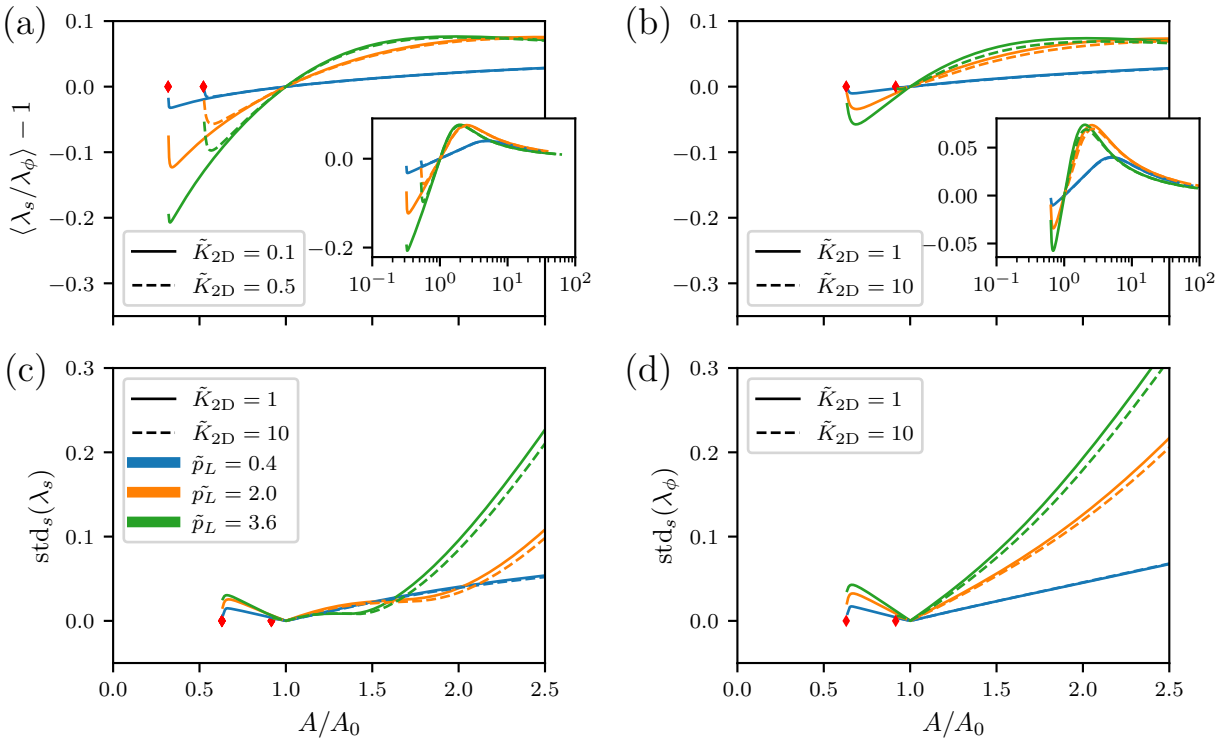

Figure 1.4: Characterization of the stretch anisotropy and the stretch inhomogeneity. (a,b) The mean ratio of meridional and circumferential stretches $\langle \lambda_s/\lambda_\phi \rangle - 1$ along the contour characterizes stretch anisotropy and is shown for (a) $\tilde{K}_{2D} \leq 0.5$ and (b) $\tilde{K}_{2D} > 0.5$. The standard deviations of (c) meridional stretches λ_s and (d) circumferential stretches λ_ϕ along the contour characterize the inhomogeneity of stretches. We show the critical stretches $\lambda_{A,c}$ as red diamonds in (a-d).

Furthermore, the standard deviation of the stretches along the contour $\mathrm{std}_s(\lambda_s)$ and $\mathrm{std}_s(\lambda_\phi)$ shown in Fig. 1.4c,d characterizes the inhomogeneity of the stretches along the contour. A standard deviation of $\mathrm{std}_s(\lambda_s) = \mathrm{std}_s(\lambda_\phi) = 0$ corresponds to a spherical sector. The meridional and circumferential stretches of an inflated capsule are isotropic at the apex with $\lambda_s(s=0) = \lambda_\phi(s=0) \propto \lambda_A^{1/2}$. At the capillary, the attachment condition mandates $\lambda_\phi^{\mathrm{cap}} = 1$ while λ_s^{cap} increases with λ_A, which introduces anisotropy and inhomogeneity into the problem with meridional stresses accumulating at the capillary. The spherical approximation will hold well for shapes where the stretches are approximately *homogeneous* over a large arc length, corresponding to a small standard deviation of the stretches, and *isotropic*, corresponding to a mean stretch along the contour $\langle \lambda_s/\lambda_\phi \rangle$ close to unity. This is fulfilled at the two spherical configurations $\lambda_A = 1$ and approximately close to $\lambda_{A,c}$. The spherical configuration with $\lambda_{A,c}$ appears to be highly sensitive, and small changes in λ_A lead to large deviations in the anisotropy (and inhomogeneity). It is interesting to note that at small deformations around $\lambda_A = 1$, the anisotropy evolution depends only on $\tilde{p}_L$ and not on $\tilde{K}_{2D}$.

We argue that the evolution of the anisotropy and inhomogeneity can be grasped by considering that the capillary acts similar to a rigid inclusion in a stretched elastic skin as both enforce the absence of circumferential stretching ($\lambda_\phi = 1$) at their boundary. A rigid inclusion in a stretched elastic skin is known to concentrate the meridional stresses creating anisotropy and inhomogeneity, similar to the stress concentration around a crack tip. For flat skins, a rigid inclusion is a classic problem that was studied for neo-Hookean skins by Wong and Shield [38]. For the capsule we have a curved geometry, which gives rise to an even more pronounced increase of anisotropy around the

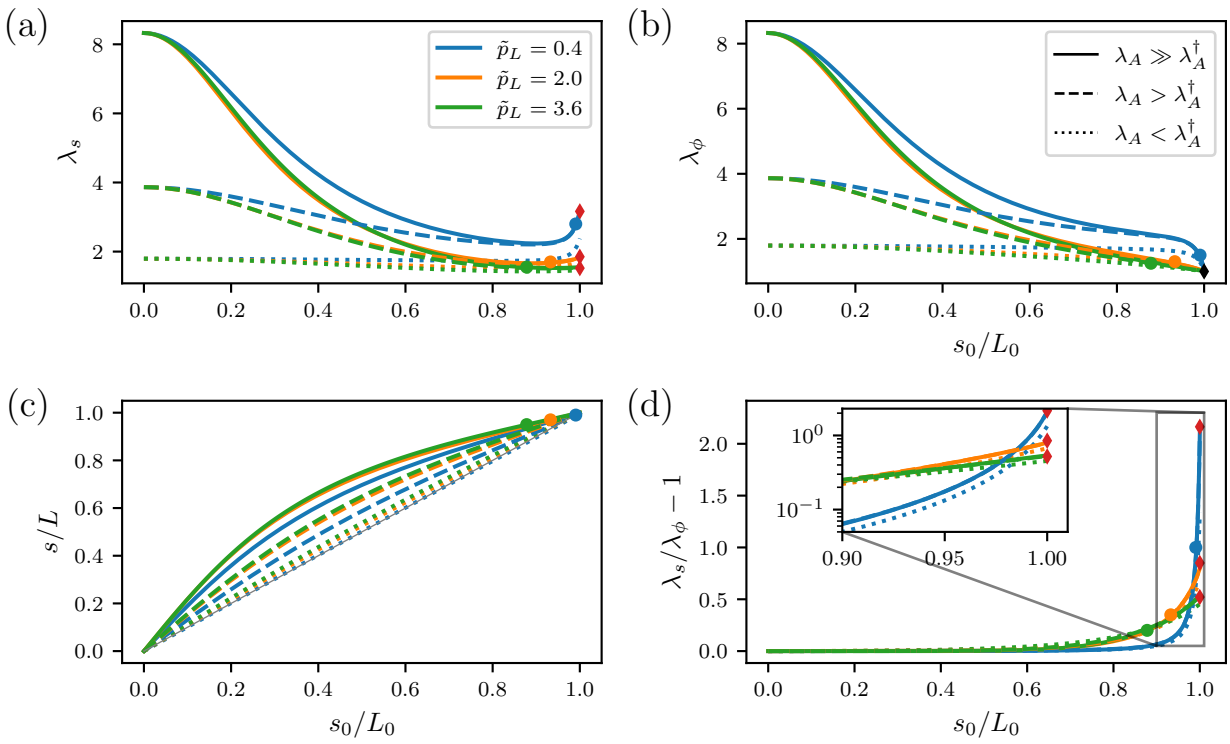

Figure 1.5: Stretch anisotropy of capsule shapes with $K_{2D} = 10\gamma$ for three values of $\tilde{p}_L$ for each of three area stretches $\lambda_A \gg \lambda_A^\dagger$, $\lambda_A > \lambda_A^\dagger$, and $\lambda_A < \lambda_A^\dagger$ (see also Fig. 1.6 for a definition of the characteristic area stretch $\lambda_A^\dagger$). (a,b) Stretch ratios λ_s and λ_ϕ as a function of the undeformed arc length s_0/L_0 along the contour. While λ_ϕ is approaching the undeformed value of 1 at the capillary ($s_0/L_0 = 1$), λ_s rises at the capillary. (c) shows that the deformed arc length s considerably deviates from the undeformed arc length s_0 along the contour. (d) The resulting stretch anisotropy $\lambda_s/\lambda_\phi - 1$ is localized at the capillary. The size of the anisotropy zone around the capillary can be characterized by an exponential decay arc length s_0^*, which is calculated from the logarithmic derivative of $\lambda_s/\lambda_\phi - 1$ at the capillary for the solid lines and shown as colored dots in all plots (a-d). We also show the maximal stretch at the capillary from Eqn. (1.26) as red diamonds in (a) and (d).

capillary.

We see clear evidence of the increased anisotropy around the capillary in the numerical solutions to the full anisotropic shape equations as shown in Fig. 1.5. In Fig. 1.5 a,b,c, we show the stretch ratios λ_s and λ_ϕ and the redistribution of arc length along the contour of inflated capsules. These results show the rise of meridional stretch close to the capillary. Fig. 1.5 d reveals that the resulting stretch anisotropy $\lambda_s/\lambda_\phi - 1$ is localized at the capillary and that it decays exponentially over a characteristic arc length s_0^* away from the capillary. Here, s_0 is the arc length of the undeformed reference shape (the spherical droplet), which is related to the arc length s of the deformed shape by the meridional stretch ratio, $\mathrm{d}s/\mathrm{d}s_0 = \lambda_s$. We use the logarithmic derivative of $\lambda_s/\lambda_\phi - 1$ to numerically determine the size s_0^* of the zone of increased anisotropy around the capillary.

We propose that the relative meridional extent of the anisotropy zone along the *deformed* capsule contour provides a non-dimensional number Q, which is suitable to characterize the importance of elastic anisotropy effects in the regime $K_{2D} > \gamma$, where elastic energies dominate. We thus define $Q \equiv s^*/L$, where s^* is the meridional length of the anisotropy region measured in terms of the *deformed* arc length, while L is the total arc length of the deformed capsule contour. For $K_{2D} < \gamma$, elastic energies are small compared to droplet surface tension such that also elastic anisotropy

becomes less important.

In order to evaluate the anisotropy parameter Q, we use the general relation $\mathrm{d}s/\mathrm{d}s_0 = \lambda_s$ between deformed and undeformed arc length at the capillary and $L \sim \pi R_0 \lambda_A^{1/2}$ for the total arc length L in the limit $\tilde{p}_L \ll 4$ to obtain

$$Q \equiv \frac{s^*}{L} \sim \frac{s_0^* \lambda_s^{\mathrm{cap}}}{L} \sim \frac{s_0^* \lambda_s^{\mathrm{cap}}}{\pi R_0} \lambda_A^{-1/2} \tag{1.25}$$

where λ_s^{cap} is the meridional stretch at the capillary and R_0 the radius of curvature of the reference liquid droplet. To make further progress, we derive relations for the size s_0^* of the anisotropy zone and the stretch ratio λ_s^{cap} at the capillary from numerical results shown in Fig. 1.6.

Because the maximal stretch anisotropy is found at the capillary and $\lambda_\phi = 1$ at the capillary, the meridional stretch at the capillary actually equals the maximal stretch anisotropy, $\max\left(\frac{\lambda_s}{\lambda_\phi}\right) = \lambda_s^{\mathrm{cap}}$. While in the case of flat skins the maximal anisotropy $\lambda_s^{\mathrm{cap}} \propto \lambda_s(s=\infty)$ is proportional to the radial stretch at infinity [38], our numerical results for curved capsules indicate that λ_s^{cap} first increases upon inflation $\lambda_A > 1$ but saturates for highly inflated capsules with area stretches λ_A exceeding a fairly well-defined value $\lambda_A^\dagger$, as shown in Fig. 1.6a for the case of $K_{2\mathrm{D}} = 10\gamma$. Further numerical analysis of the saturation value as performed in Fig. 1.6b allows us to quantify the saturation value as

$$\max\left(\frac{\lambda_s}{\lambda_\phi}\right) \approx \lambda_s^{\mathrm{cap}} \equiv \mathrm{const}\, \tilde{p}_L^{-1/3} \tag{1.26}$$

with const ≈ 0.93 in the regime $K_{2\mathrm{D}} > \gamma$. This saturation value is solely determined by the geometrical parameter $\tilde{p}_L$ of the undeformed shape, which demonstrates that the saturation is induced by droplet curvature. We also find $\lambda_A^\dagger \sim (\lambda_s^{\mathrm{cap}})^{3/2}$ for the area stretch, where saturation of the maximal anisotropy sets in. The maximal anisotropy given in Eqn. (1.26) diverges in the limit $\tilde{p}_L \approx 0$, which seems counter-intuitive at first, because the spherical approximation works best for exactly this limit. This issue will be resolved below. Let us quantify the size s_0^* of the anisotropy zone around the capillary. From Fig. 1.6c, we find a conservative bound

$$s_0^* \leq \frac{a}{4}. \tag{1.27}$$

This relation reveals that the size of the stretch anisotropy zone is set by the geometry parameter $\tilde{p}_L$ of the reference state rather than the elastic compression modulus $K_{2\mathrm{D}}$.

Using Eqn. (1.27) for s_0^* and the saturation value given in Eqn. (1.26) for λ_s^{cap} in Eqn. (1.25), we obtain $Q \propto \tilde{p}_L^{2/3}/\lambda_A^{1/2}$ for the anisotropy parameter Q for highly inflated capsules $\lambda_A > \lambda_A^\dagger$. This parameter remains small for $\tilde{p}_L \ll 4$ indicating that we can neglect anisotropy effects in this limit.

At smaller deformations $1 < \lambda_A < \lambda_A^\dagger$, where saturation of the capillary anisotropy has not yet set in, we numerically find that the maximal stretch anisotropy scales with $\log(\lambda_A)$ (see Fig. 1.6a), giving

$$Q = 4\tilde{p}_L \frac{\lambda_s^{\mathrm{cap}} - 1}{3\pi \log(\lambda_s^{\mathrm{cap}})} \frac{\log(\lambda_A)}{\lambda_A^{1/2}}, \tag{1.28}$$

where we again use the saturation value λ_s^{cap} from Eqn. (1.26).

We obtain a full contour plot of the anisotropy parameter Q in Fig. 1.6d by joining the results in the two regimes ($\lambda_A > \lambda_A^\dagger$ and $\lambda_A < \lambda_A^\dagger$) with a smooth interpolating function. This plot confirms that

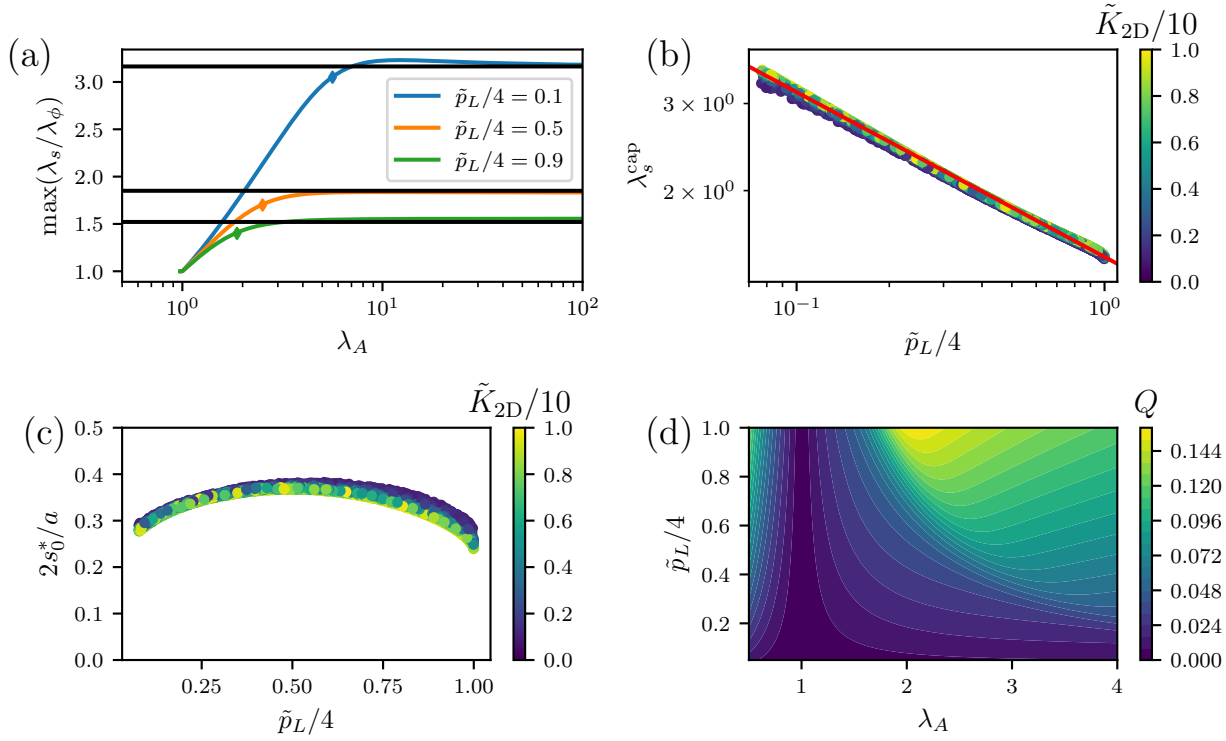

Figure 1.6: Analysis of the anisotropy zone and the anisotropy parameter Q from numerical solutions of the anisotropic shape equations. (c) The size of the anisotropy zone s_0^* is roughly constant giving rise to the bound Eqn. (1.27). (b) The saturation value is mainly determined by the dimensionless reference pressure $\tilde{p}_L$, see Eqn. (1.26). (a) As a function of the area stretch λ_A, the maximum anisotropy saturates at large deformations beyond a value $\lambda_A^\dagger$ (results for $\tilde{K}_{2D} = 10$ shown as colored diamonds). (d) Contour plot of the non-dimensional anisotropy parameter Q according to Eqn. (1.25). Stretch anisotropy effects are negligible for $Q \ll 1$.

Q is small ($Q \ll 1$) for shapes where the spherical approximation works best. In particular, we find that we can neglect anisotropy effects ($Q \ll 1$) in the limit $\tilde{p}_L \ll 1$, resolving the counter-intuitive behaviour of the maximal anisotropy. We emphasize the fact that Eqn. (1.28) only depends on $\tilde{p}_L$ and λ_A and *not* on K_{2D}, as long as $K_{2D} > \gamma$. This indicates that stretch anisotropy is mainly governed by geometry rather than by elastic energy contributions. As already pointed out above, elastic contributions and, thus, also elastic anisotropy effects become increasingly irrelevant for $K_{2D} < \gamma$, where surface tension dominates and the shape resembles a spherical liquid droplet. The regions $\lambda_A > \lambda_A^\dagger$ and $\lambda_A < \lambda_A^\dagger$ differ markedly in their functional dependence on λ_A. This results in a maximum of the parameter Q for area stretches $\lambda_A \sim \lambda_A^\dagger \propto \tilde{p}_L^{-1/2}$ at a fixed value of $\tilde{p}_L$. This, in turn, indicates that stretch anisotropy is most relevant for these intermediate area stretches.

The possibility of approximating the capsule shape by a spherical sector over a wide range of parameters is an important piece of information for experimentalists since it means that approximate analytical expressions relying on the assumption of isotropic and homogeneous stresses can be used in certain scenarios to reliably quantify the elastocapillary properties of capsule interfaces over a reasonably wide range of elastocapillary numbers.

1.3 Viscoelastic interfaces

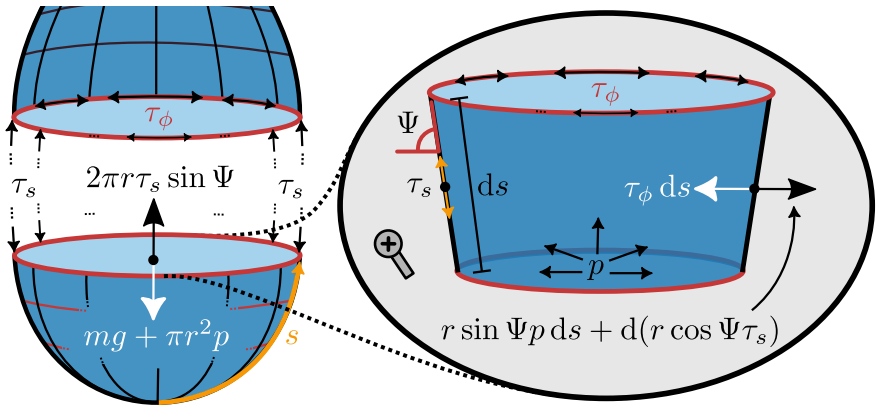

Figure 1.7: We can formulate the forces appearing in the elastic capsule skin through simple geometric arguments. We slice the capsule horizontally (left), pull it appart slightly (for visual purposes) and find the forces acting on this slice in both vertical (left) and horizonal (right) direction. This allows us to introduce non-conservative surface stresses.

Next, we want to explore viscous, or *dissipative*, effects encountered during the deformation of a pendant capsule. Microscopically, energy dissipation can happen in many places of our model, we want to consider only the case where the polymers are "sticky" and create drag in the polymer matrix by interacting with the other polymers.

For conservative elastic capsules, we are able to write down an elastic energy density w_{S_0}, which is a potential of the elastic forces. Now, however, we want to include non-conservative forces, such that an energy density does not exist. This also means, that we are not able to generate the shape equations from the first variation of the free energy as shown in Sec. 1.2. Rather, we need to operate one level lower and formulate the appropriate force balance from which we are able to derive the shape equations containing non-conservative forces.

We want to preserve the assumption of axi-symmetry, such that our viscoelastic solution shapes shall only have scalar accelerations in the radial direction $\ddot{r}$ and along the axis of symmetry $\ddot{z}$. All other accelerations are disallowed for axi-symmetric solutions, i.e. accelerations which have components pointing out of the plane of projection of our parametrization. This means that an interface patch of mass $\mathrm{d}m$ is accelerated with an acceleration $\vec{a}$ by all acting forces $\vec{F}$ due to Newtons law: $\vec{a} = \mathrm{d}\vec{F}/\mathrm{d}m$. Importantly, the inertial corrections are proportional to the mass of the interface element, which scales with the thickness of the skin H and its mass density ρ, such that we find $\mathrm{d}m = \mathrm{d}A\, H\rho = 2\pi\,\mathrm{d}s\, H\rho r$.

If we project Newtons law onto the axis of symmetry (i.e. the z-axis), we can isolate the vertical acceleration $\ddot{z}$ together with the forces acting in the vertical direction

$$2\pi\rho r H\ddot{z} = \frac{\mathrm{d}}{\mathrm{d}s}\left(2\pi r\tau_s \sin\Psi - \pi r^2 p - \pi\Delta\rho g\int_0^z \mathrm{d}z'\, r^2\right), \tag{1.29}$$

where the first term on the r.h.s. of Eqn. (1.29) is the force generated by the surface stress acting vertically, the second term is the force generated by the internal pressure p, finally, the third term is the force due to the self weight of the segment below height z. This is exactly the same argument we made in Ref. [24] to derive the vertical force balance of a pendant droplet. All forces acting on the horizontal slice of the capsule are shown in Fig. 1.7. Importantly, the force per length τ_s is no longer required to be conservative because we now consider the appropriate force balance instead of the variation of the free energy, allowing us to include dissipative constitutive properties in the surface stress τ_s. This approach is similar to that provided in Ref. [24] for liquid droplets. Note, however, that already at this point an assumption is made for the dynamics of the fluid inside and outside of the capsule – the relaxation time-scale of the hydrodynamic flow inside

and outside of the capsule is much faster than any other time-scale in the system. In the case where the liquid flow field produces significant corrections, which is not the case for e.g. water and air [39], the full hydrodynamic equations for the inner and outer liquid need to be evaluated for the specific dynamic boundary conditions, in order to acquire an appropriate time-dependent pressure term p acting on the interfacial skin. We will not include these hydrodynamic effects here, hence assuming that the fluid flow in the surrounding phases is negligible on the time scale of the deformation of the interfacial skin. In Ref. [40] a drop is studied in an external flow field, which conceptually involves similar steps towards including the self-induced flow around and inside of a pendant capsule. Further studies for elastic capsules in an external flow field are readily available [11], [41]–[44] and could be used to adopt the present approach.

With some basic calculus, we are able to reduce Eqn. (1.29) to

$$\rho H \ddot{z} = \cos\Psi \left[-p + \tau_s \kappa_s + \kappa_\phi \left(\tau_s + \frac{\mathrm{d}\tau_s}{\mathrm{d}s} \frac{r}{\cos\Psi} \right) \right] , \tag{1.30}$$

which, for the static case, i.e. $\ddot{z} = 0$, reduces to a combination of the shape equations found in Sec. 1.2 and [15].

The second force balance we need to consider is that in radial direction, where the accompanying acceleration is $\ddot{r}$. We start by considering a horizontal hoop with a height of the arc-length section $\mathrm{d}s$ (see Fig. 1.7). The force in radial direction, caused by the pressure difference is simply the pressure times the patch area, projected onto the r-axis $\mathrm{d}F_r^p = \mathrm{d}s\, r \sin\Psi p$. The force in radial direction, caused by the meridional surface stress τ_s is obviously given by $F_r^{\tau_s} = r\cos\Psi\tau_s$ and the force contribution of the circumferential line tension τ_ϕ is the total inwards pointing force due to the stress on the hoop $\mathrm{d}F_r^{\tau_\phi} = -\mathrm{d}s\,\tau_\phi$. Combining all relevant contributions finally gives the radial acceleration

$$\rho H \ddot{r} = \sin\Psi p + \frac{1}{r}\frac{\mathrm{d}}{\mathrm{d}s}\left(r\cos\Psi\tau_s\right) - \frac{\tau_\phi}{r} , \tag{1.31}$$

We can input Eqn. (1.30) into Eqn. (1.31) to find a more convenient equation with a specific geometric acceleration arising naturally

$$\rho H (\cos\Psi\ddot{r} + \sin\Psi\ddot{z}) = -\frac{\cos\Psi}{r}(\tau_\phi - \tau_s) + \frac{\mathrm{d}\tau_s}{\mathrm{d}s} , \tag{1.32}$$

where $\cos\Psi\ddot{r} + \sin\Psi\ddot{z}$ is exactly the tangential acceleration of the interface.

We are able to infer the normal acceleration of the interface from simple geometric considerations as well

$$\rho H (\sin\Psi\ddot{r} - \cos\Psi\ddot{z}) = p - \tau_s\kappa_s - \tau_\phi\kappa_\phi . \tag{1.33}$$

If the deformation is quasi-static, where we have slow deformations and thus $\ddot{r} \sim \ddot{z} \sim 0$, Eqn. (1.32) can be identified with the static shape equation Eqn. (1.15) and Eqn. (1.33) becomes equivalent to the static generalized Young-Laplace equation Eqn. (1.14), as it should be.

This discussion allows us to use the new set of shape equations Eqn. (1.33) and Eqn. (1.32) to confidently introduce dissipative and hence non-conservative surface stress contributions into our model. By extension, we are interested in the temporal evolution of the shape on the time scale of the dissipative relaxation. We have to consider three time scales in our discussion [20]. We have the

[20] The two additional time scales, the relaxation of the fluid flow in the inner and outer phase result, not included – they should be small compared to all other time scales cases.

time scale of the stimulus t_d, e.g. that of an external driving force, and the time scale of the energy dissipation, over which the viscous stresses relax t_r. The third time scale is the characteristic time scale produced by Eqns. (1.33) and (1.32) as $t_i = a\sqrt{\rho H/\gamma}$, and is the inertial time scale. If the time scale of the external stimulus is much larger than the inertial time scale $t_d \gg t_i$, we are able to neglect the l.h.s of Eqn. (1.33) and Eqn. (1.32), giving the quasi-static case.

Should the dissipative relaxation time scale t_r be sufficiently small in comparison to the deformation time scale $t_r \ll t_d$, where the deformation time scale is also large enough to not cause inertial corrections $t_d \gg t_i$, the temporal shape evolution will be purely elastic to first order. If, however, the dissipative relaxation time scales are on the same order of magnitude as the deformation time scale $t_r \sim t_d$, we need to account for the corrections applied to the dynamics by the viscous effects. This does not mean that inertial effects play a relevant role yet, because it is still possible that $t_d \sim t_r \gg t_i$. Finally, if all time scales are of the same order of magnitude $t_d \sim t_r \sim t_i$, we need to solve the full equations (1.32) and (1.33) in order to predict the shape evolution accurately. For all of our purposes, we will assume $t_d \sim t_r \gg t_i$, such that inertial corrections can be neglected safely and only viscous dissipation is accounted for.

Introducing non-conservative surface stresses without the present discussion is not consistent, since the original equations where derived from a free energy, where dissipative surface stresses are generally disallowed.

1.3.1 Viscoelastic constitutive equation

> **Notice** – This section is a continued development of the method first derived in the author's master thesis [45]. Some parts of this section are reproduced with modifications from the author's master thesis [45].

We want to connect this discussion directly to that of the constitutive material model discussion in Sec. 1.2.1, such that we again consider a polymeric skin. Now however, we want to consider possible origins of viscosity.

If the polymers of the interfacial skin are sticky in the sense that polymers generate drag with other polymers and the surrounding medium, while sliding through the polymer network, while otherwise preserving the overall integrity of the cross-linked polymer matrix, we have a case where, on short time scales, the polymer matrix is an effective fluid. The monomer beads have to pass through this effective fluid and generate viscous drag while doing so. This yields a *solid-like* viscoelastic interface, where slow deformations $T \ll \tau$ would give the behavior of a solid elastic skin. A material of this kind would not encour any damage during loading, such that Mullins effect, or the Payne effect are not captured [46].

We could also consider a fundamentally different origin of viscosity, where the polymer matrix has cross-linkings, which persist over a certain characteristic time, such that they are not rigid and can change over the characteristic time. These interfaces would exhibit *fluid-like* behavior, simply because for time scales much larger than the characteristic cross-link lifetime the material will flow like a fluid because all original cross-links have resolved and the new steady-state will eventually settle in to be a solution of the Young-Laplace equation (see Eqn. (1.8)), simply because all elastic and viscous stresses nesseccarilly dissappear over long time-scales. This material would not behave like an elastic capsule for slow deformation rates, simply because the reference shape of the elastic skin changes throughout the deformation.

Here, we will consider only solid-like viscoelasticity, where the elastic reference shape is preserved throughout the entire deformation sequence. Generalizing the present theory to also include

fluid-like viscoelasticity is simple. While many viscoelastic constitutive laws exist in literature [47]–[59] we want to derive the constitutive law for the geometry at hand from first principles while stating all of our assumptions carefully.

We start our consideration by writing the most general stress-strain relationship, with viscoelastic stress vectors $\vec{\tau}$ defined per *undeformed* lengths $\vec{\tau} = (\lambda_\phi \tau_s^{\mathrm{v}}, \lambda_s \tau_\phi^{\mathrm{v}})^{\mathrm{T}}$ and strain vectors $\vec{\epsilon} = (\lambda_s^2 - 1, \lambda_\phi^2 - 1)^{\mathrm{T}}/2 \approx (\lambda_s - 1, \lambda_\phi - 1)^{\mathrm{T}}$, such that

$$\underline{\underline{\hat{\chi}}}\vec{\tau} = \underline{\underline{\hat{\zeta}}}\vec{\epsilon}, \tag{1.34}$$

where $\underline{\underline{\hat{\chi}}}$ and $\underline{\underline{\hat{\zeta}}}$ are arbitrary *tensor operators* acting on the stress and strain vectors respectively. The stresses τ_s^{v} and τ_ϕ^{v} are only the viscoelastic stress resultants, further surface stresses such as a constant surface tension excluded.

Working with Eqn. (1.34) directly is of no immediate benefit, as it is too abstract to be used for inference of physical truths and properties. Consequently, we reduce the abstraction of Eqn. (1.34) by loosing some of the generality, but again, we do this while carefully documenting our assumptions.

The first assumption we want to make is that the constitutive equations do not depend on the entire stress/strain history, but only on the current temporal derivatives of arbitrary order. The differential operators are thus equally not *explicitly* time dependent as the operators only contain temporal derivatives of given order and constant coefficients χ_{ijk} and ζ_{ijk}:

$$\hat{\chi}_{ij} = \sum_{k=0}^{\infty} \chi_{ijk} \frac{\partial^k}{\partial t^k}\,, \qquad\qquad \hat{\zeta}_{ij} = \sum_{k=0}^{\infty} \zeta_{ijk} \frac{\partial^k}{\partial t^k}\,. \tag{1.35}$$

Consequently, we expect that the constitutive equation only characterises viscoelastic capsule deformation behavior to first order in the strains, and to arbitrary order in time [21]. Still, the constitutive equations respect the geometric non-linearities of our problem.

To solve for $\vec{\epsilon}$ Eqn. (1.34) can be transformed via a Carson transform $\mathcal{C}(f(t))(s) \equiv s\mathcal{L}(f(t))(s)$, where $\mathcal{L}$ is the Laplace transform such that

$$\sum_{k=0}^{\infty}\sum_{j=1}^{d} \chi_{ijk} s^k \tilde{\tau}_j = \sum_{m=0}^{\infty}\sum_{n=1}^{d} \zeta_{inm} s^m \tilde{\epsilon}_n\,, \tag{1.36}$$

where we define $p_{ij}(s) \equiv \sum_k \chi_{ijk} s^k$ and $q_{in}(s) \equiv \sum_k \zeta_{ink} s^k$ as the naturally appearing polynomials in the complex variable s. Eqn. (1.36) consists of d equations for d unknown strains, such that we can solve the system of equations. Since we are interested in capsule systems we restrict our investigations to $d = 2$ and solve the system of equations analytically by isolating the two components $\{i, m\}$ explicitly (we demand $i \neq m$, such that these are the two principal stretches in this case). We arrive at an expression for the transformed strains as a function of the transformed stresses

$$\tilde{\epsilon}_i = \sum_j \underbrace{\frac{p_{ij}(s)q_{mm}(s) - q_{im}(s)p_{mj}(s)}{q_{ii}(s)q_{mm}(s) - q_{im}(s)q_{mi}(s)}}_{J_{ij}^*(s)} \tilde{\tau}_j\,, \tag{1.37}$$

where we define the complex matrix $J_{ij}^*(s)$ in terms of the polynomials $\{p_{lr}\}$ and $\{q_{lr}\}$. The functions $J_{ij}^*(s)$ characterize the couplings between stress and strain and, equivalently, define the memory kernels of the material.

[21] If a Taylor expansion exists for both stress and strain.

A next assumption is that the materials we are considering should be *isotropic* [22], meaning that the principal directions are interchangeable and behave the same. Explicitly, this means that the polynomials $\{p_{lr}\}$ and $\{q_{lr}\}$ must be invariant under the renaming of $i \to m$ and $m \to i$ such that $p_{im}(s) = p_{mi}(s)$, $q_{im}(s) = q_{mi}(s)$, $p_{mm}(s) = p_{ii}(s)$, and $q_{mm}(s) = q_{ii}(s)$.

The characteristic response matrix for isotropic materials is thus given as:

$$J^*_{ij}(s) = \frac{q_{ii}(s)p_{ij}(s) - q_{im}(s)p_{mj}(s)}{q^2_{ii}(s) - q^2_{im}(s)}\,. \tag{1.38}$$

A particularly "simple" material can be acquired if we only allow for a scalar memory kernel in an isotropic material, where all relaxation processes have the same relevant time dependency, i.e. we additionally force $p_{ii}(s) = p_{im}(s)/\alpha_{im} \equiv p(s)$ and $q_{ii}(s) = q_{im}(s)/\beta_{im} \equiv q(s)$ where isotropy forces $\alpha_{ii} = \alpha_{mm} \equiv 1$ and $\alpha_{im} = \alpha_{mi} \equiv \alpha$, as well as $\beta_{ii} = \beta_{mm} = 1$ and $\beta_{im} = \beta_{mi} \equiv \beta$.

Such uni-relaxant [23] material matrix can thus be described as

$$J^*_{ii} = \frac{1 - \beta\alpha}{1 - \beta^2}\frac{p(s)}{q(s)}\,, \qquad\qquad J^*_{im} = \frac{\alpha - \beta}{1 - \beta^2}\frac{p(s)}{q(s)} \tag{1.39}$$

where we only retain a single memory kernel, applied to all deformations of the material components. The components of the characteristic response matrix $\underline{\underline{J}}^*$ can still respect for a fixed Poisson's ratio, manifesting as β in Eqns. (1.39), as we will demonstrate later.

For *any* of the characteristic matrices Eqns. (1.37), (1.38) and Eqn. (1.39), we always find a fraction of polynomials. We are hence able to use the partial fraction decomposition to reduce the characteristic matrix to

$$J^*_{ij}(s) = \sum_{k=0}^{\infty} u_{ijk}s^k + \sum_{l=1}^{t_{ij}}\sum_{n=1}^{e_{ijl}} \frac{\kappa_{ijln}}{(s + \omega_{ijl})^n}\,, \tag{1.40}$$

where we are able to separate the polynomial fraction into a polynomial with coefficients u_{ijk} and the $\prod_{l=1}^{t_{ij}} e_{ijl}$ partial fractions for the t_{ij} poles $-\omega_{ijl}$ with degeneracy e_{ijl} and coefficients κ_{ijln}.

Finally, we acquire the temporal stress-strain relationship by applying the inverse Carson transformation $\mathcal{C}^{-1}\left(f(s)\right)(t)$ to both sides of Eqn. (1.37), resulting in

$$\epsilon_i(t) = \sum_j \left\{ J_{ij}(0)\tau_j(t) + \int_0^t \mathrm{d}t'\, \dot{J}_{ij}(t - t')\tau_j(t') \right\}\,, \tag{1.41}$$

which is a generalised version of the *Hereditary integral equation* for linear viscoelasticity [55].

In the following we use the additional physical constraint $J_{ij}(0) = 0$, because we enforce a finite causality latency and request the relaxation functions to be differentiable in $t = 0$, as an instantaneous strain response following a suddenly applied stress could be considered unphysical. We note that the purely elastic material would yield such step in the response function. Of course, this is an idealized concept, because the strain response propagates through the material at the speed of sound in the material – and thus not instantaneously [24].

The real relaxation functions can thus be acquired by directly applying the inverse Laplace transform to Eqn. (1.40) to find:

[22] This means in-plane isotropic in this case. Out-of-plane anisotropy is still possible.

[23] Uni-relaxant because it only has one fundamental relaxation function for all components.

[24] The most conservative upper bound to the propagation speed of the stress through the material is the speed of light.

$$\dot{J}_{ij}(t) = \sum_{k=0}^{\infty} u_{ijk}\delta^{(k)}(t) + \sum_{l=1}^{t_{ij}} \sum_{n=0}^{e_{ijl}-1} \frac{\kappa_{ijnl}}{n!} t^n e^{-t\omega_{ijl}} \,. \tag{1.42}$$

In Eqn. (1.42) we can identify some classes of deformation memory behavior, some of which are to be excluded from our investigation:

- $\omega_{ijl} \in \mathbb{R}$: Dominantly decaying exponentially (for $\omega_{ijl} > 0$, $\omega_{ijl} < 0$ makes memory of long ago deformation exponentially more relevant, which is unphysical.)
- $\omega_{ijl} = ic_{ijl}\,, c_{ijl} \in \mathbb{R}$: Sinusoidal correlation
- $\omega_{ijl} = r_{ijl} + ic_{ijl}\,, \{r_{ijl}, c_{ijl}\} \in \mathbb{R}^2$: Exponentially dampened sinusoidal correlation (again with $r_{ijl} > 0$)
- $u_{ijk} \neq 0$ correlated to the kth derivative of the stresses at t

From those modes we can exclude some for our considerations, because of their implications for the physical realization of the material deformation.

First of all, we expect the correlation between an induced strain and the strain causing stresses to decay monotonically in a passive material, otherwise energy must be dissipated through some time correlated mechanism, which we will not allow. This allows us to specify that $\omega_{ijl} \in \mathbb{R} > 0$ and thus $\kappa_{ijnl} \in \mathbb{R}$. Furthermore, we exclude plastic deformations and instantaneous correlations due to the physical constraint of the finite causality latency, which requests that $u_{ijk} \equiv 0\,, \forall\{i,j,k\}$.

The general viscoelastic capsule material thus has 4 different relaxation functions, each with $\prod_{l=1}^{t_{ij}} e_{ijl}$ relaxation modes. We are able to reduce this to only two relaxation functions in the isotropic case (see Eqn. (1.38)) and only one non-proportional relaxation function in the uni-relaxant case (see Eqn. (1.39)).

1.3.2 Kelvin-Voigt Capsule

A simple as possible uni-relaxant linear viscoelastic model for the pendant capsule skin is the Kelvin-Voigt viscoelastic material. The material may be isotropic, such that $\alpha = 0$ and $\beta = \nu_{2D}$ with an elastic component $\propto Y_{2\mathrm{D}}$ and a dissipative component $\propto \eta$ in parallel, such that

$$\dot{J}_{ii}(t) = \frac{1}{1-\nu_{2D}^2}\frac{1}{\eta}\exp\left(-\frac{Y_{2D}}{\eta}t\right) \text{ and } \dot{J}_{im}(t) = -\nu_{2D}\dot{J}_{ii}(t)\,. \tag{1.43}$$

In differential form this model has the following constitutive law:

$$\tau_{s,\phi} = \frac{1}{\lambda_{\phi,s}}\frac{Y_{2D}}{1-\nu_{2D}^2}(\lambda_s - 1 + \nu_{2D}(\lambda_\phi - 1)) + \frac{1}{\lambda_{\phi,s}}\frac{\eta}{1-\nu_{2D}^2}(\partial_t\lambda_s + \nu_{2D}\partial_t\lambda_\phi) + \gamma\,, \tag{1.44}$$

where it is obvious that the Kelvin-Voigt capsule reduces to a non-linear Hooke model for $\eta = 0$. This is not unexpected, since the generalized viscoelastic constitutive equation, by design, contains elastic contributions up to quadratic precision in the surface energy density, which is exactly the approximation used to derive the non-linear Hookean material model from the Mooney-Rivlin material model (see Sec. 1.2.1). In the differential form Eqn. (1.44), we can appreciate the manifestations of the added viscosity. Namely, it adds a stress proportional to the temporal derivatives of the strain components, which yields in a smoothing of strain responses to abrupt stress loads. The characteristic time-scale of the smoothing is immediately evident from Eqn. (1.43), where it appears naturally as the time-scale of the memory decay and is given as $\eta/Y_{2\mathrm{D}}$.

2 Numerically solving and fitting shape equations

Published material – The theoretical background for shape fitting is reproduced with modifications and permission from the author's publication [13], © 2023 The Authors. Published by American Chemical Society. The present work is a continuation of the work by Sebastian Knoche in Refs. [15], [27] and Jonas Hegemann in Refs. [14], [60].

So far, we have discussed the derivation and properties of various shape equations. We have not, however, gone into any detail on how to actually solve those equations for a given set of control parameters. Solving shape equations numerically in an efficient and timely manner enables iterative shape fitting approaches, which where introduced by Knoche et. al in 2013 for elastic capsules [15] and further improved by Hegemann et. al in 2018 [14]. Even the improved design leaves the method in a state, where it is plagued by problems, such as failure to fit an experimental shape reliably and being comparably slow overall. This renders the resulting open source software *OpenCapsule* interesting, but ultimately too unreliable for use by experimentalists. Many other computational methods are available for the characterization of elastic and viscoelastic response functions, as described in a recent review by Jeansson et al. in Ref. [61]. The aim of this work is to improve the design and fix methodological flaws present in *OpenCapsule* to make it more reliable, faster, more precise, extensible and accessible. Ultimately, a full re-write of the software is required to modernize it and make it easier to use. In this chapter, we will discuss the basics of solving and fitting shape equations with a computer and additionally discuss the design improvements over *OpenCapsule*. Finally, we will present an overview of the new software package and its capabilities.

Mathematically, the present shape equations are classified as sets of ordinary first order differential equations (ODE). In principle, solving ODEs is usually simple and straight forward if approached by off-the-shelf numerical methods such as the Euler-method or Runge-Kutta methods [14], [15]. Upon naively applying these methods to the present systems of ODEs, however, a number of non-trivial challenges and problems manifest. These problems need to be treated with great care. Some of the challenges are of numerical nature, such as numerical precision limitations, numerical singularities, or proper book-keeping of the solution data, while other problems arise from the nature of the problem statement, such as the requirement of fulfilling conditions at multiple boundary points.

Especially if the solutions of the shape equations are subjected to a fitting algorithm, as done previously in [14], [15], several non-trivial challenges arise. The pendant droplet is the most straight forward case to numerically tackle, and numerical fitting routines are both commercially and freely available [17]. The only available package for the numerical fitting for elastic capsules is the open source software *OpenCapsule* [14]. No software currently (to the best of the author's knowledge) performs exact shape fitting for entire deformation sequences, accounting for viscoelastic effects. While Nguyen et al. demonstrate in Ref. [62] that it is possible to determine the viscoelastic properties from compression experiments, their approach is computationally demanding and requires a different experiment setup. The complexity of viscoelastic shape sequence fits is drastically higher than that of a single elastic capsule and will only be feasible and traceable with the novel numerical framework presented in this section.

2.1 Liquid pendant droplets

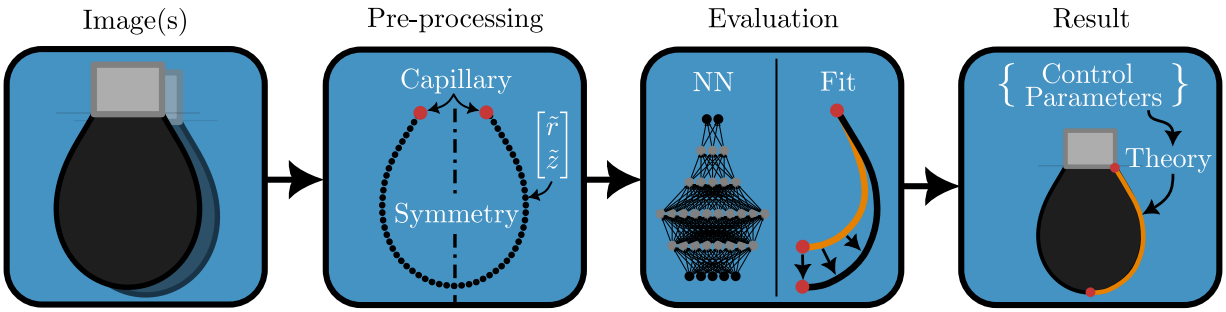

Figure 2.1: A conceptualization of shape fitting. Our input will be experiment images (left). The images are pre-processed into a suitable representation (center left). With this representation we can apply a method of choice to determine the control parameters (center right). In this work, we discuss a neural network (see Sec. 5.1) and a conventional shape fit as an evaluation method (this section). Finally, we attain a control parameter set for the given theory and are able to produce a theory representation of the experiment data (right).

Determining the surface tension from axisymmetric images of droplet profiles is not a new idea [14], [15], [17], [63]–[67]. Liquid pendant droplet shapes are used as the reference geometry for all elastic and viscoelastic capsules we consider in this work. They are thus of great importance for the numerical framework as well. To accurately solve and fit the shape of an elastic or viscoelastic capsule, we need to first make sure that we can determine the respective reference shape accurately. Any error made in determining the liquid reference shape will negatively impact the precision of the elastic and viscoelastic solver and shape fit. Fortunately, solving the shape equations of a liquid drop is well conditioned and can be tackled with a standard Runge-Kutta numerical integration scheme [17], [24]. Additionally, we will discuss how the numerical solution of the inverse problem is implemented. A visual conceptualization of shape fitting in general is given in Fig. 2.1. We will in a later chapter (see Sec. 5.1) discuss how the solution of the inverse problem can be accelerated by several orders of magnitude by utilizing machine learning capabilities of modern computers.

As we have already discussed in Sec. 1.1, the control parameters for the three shape equations (1.1) and Eqn. (1.8) of the liquid droplet problem are given as the set $\{\tilde{p}_L, \Delta\tilde{\rho}, \Omega\}$ [24]. Those can be chosen independently to manipulate the shape of the liquid drop. Note that not all combinations of the control parameters will yield a physical solution, as shown in the parameter diagram Fig. 1.3 presented in Sec. 1.1.

We start the numerical integration from the initial conditions $\tilde{r}(\tilde{s}=0)=0, \tilde{z}(\tilde{s}=0)=0$ and $\Psi(\tilde{s}=0)=0$, where we calculate the derivatives $\tilde{r}'(\tilde{s}=0), \tilde{z}'(\tilde{s}=0)$ and $\Psi'(\tilde{s}=0)$ by evaluating the three shape equations (1.1) and Eqn. (1.8) at $\tilde{s}=0$ [1]. Already at this point we face the first numerical problem. The Young-Laplace equation (1.8) develops a numerical singularity at $\tilde{s}=0$ as we rearrange it for $\Psi'(\tilde{s})$ [24]:

$$\frac{\mathrm{d}\Psi}{\mathrm{d}\tilde{s}} = \tilde{p}_L - \Delta\tilde{\rho}\tilde{z} - \frac{\sin\Psi}{\tilde{r}}\,. \tag{2.1}$$

The problematic term is the circumferential curvature $\kappa_\phi = \sin\Psi/r$, where we find the numerically undefined result "0/0". Of course, there is no actual singularity here, as we can easily show by using the rule of de L' Hôspital [24] or alternatively by symmetry considerations [14], [27]. We

[1] All geometric symbols are non-dimensionalized by the diameter of the capillary a, such that $\tilde{x} \equiv x/a$.

finally find the well defined – and finite – value for the derivative of the arc angle at $s = 0$ as $\mathrm{d}\Psi/\mathrm{d}\tilde{s}(\tilde{s} = 0) = \tilde{p}_L/2$. This result is a manifestation of the required isotropy at the apex of the shape with $\kappa_s(s = 0) = \kappa_\phi(s = 0)$. This limit needs to be implemented manually in the numerical solver and is used while $\tilde{s} < 10^{-8}$ as a replacement for Eqn. (2.1) [2].

Now, we are able to advance the solution by utilizing the derivatives at $\tilde{s} = 0$ to approximate a value for $\tilde{r}(\tilde{h}), \tilde{z}(\tilde{h})$ and $\Psi(\tilde{h})$ at $\tilde{h} > 0$ but $\tilde{h} \ll 1$. More precisely, we advance the solution by utilizing the Runge-Kutta method of order 4, i.e. we evaluate the shape equations four times for each integration step of size $\tilde{h}$ at the arc-lengths $\{\tilde{s}, \tilde{s} + \tilde{h}/2, \tilde{s} + \tilde{h}/2, \tilde{s} + \tilde{h}\}$, where the respective previous estimate for the values of $\tilde{r}, \tilde{z}$ and Ψ are used to calculate the derivatives at the sampling points. Finally, all resulting estimates for $\tilde{r}, \tilde{z}$ and Ψ are averaged with the respective weights $\{1/6, 1/3, 1/3, 1/6\}$ which gives the final estimate for $\tilde{r}(\tilde{s} + \tilde{h}), \tilde{z}(\tilde{s} + \tilde{h})$ and $\Psi(\tilde{s} + \tilde{h})$. Other discrete integration methods, such as the Euler-method could alternatively be used, however, the Runge-Kutta method of order 4 provides a sufficient balance between precision and speed.

As we progress trough the solution of the shape, by chaining the Runge-Kutta integration steps, we detect the necks and bulges of the solution, by searching for minimum and maximum in the radial distance function $\tilde{r}(\tilde{s})$. As we detect a neck or a bulge along the shape we increase the internal neck and bulge counter [3]. Additionally, we search for capillary boundary condition matches, i.e. $\tilde{r} = 1/2$. Obviously, we can not search for $\tilde{r} = 1/2$ directly, but search for a sign change in the function $d = \tilde{r} - 1/2$, which indicates a boundary condition match in the previous integration interval of size $\tilde{h}$. If, and only if, the internal bulge and neck counter matches the bulge and neck count prescribed by the control parameter Ω *and* we detect a boundary condition match, we have found a solution for the given set of control parameters.

To improve the final precision of the liquid reference shape we discard the very last integration step of the N total integration steps performed until now and re-integrate precisely up to the capillary. We achieve this by creating a continuous spline interpolation of the shape and performing a bisection in the range $[(N-1)h, Nh]$, searching for the exact [4] location of the point $\tilde{r}(\tilde{L}) = 1/2$. This search is performed up to the machine precision, as the bisection algorithm is guaranteed to converge in less than $n \leq log_2(h/\epsilon_{\text{double}}) \sim 40$ bisection steps. This optimization yields a better capillary precision and reduces the computation time in comparison to *OpenCapsule*, where the determination of the capillary coordinate is performed by evaluating the boundary deviation at 100-fixed points and choosing the one with the lowest deviation, limiting precision to $\tilde{h}/100$ while taking at worst $n = 100$ steps.

2.1.1 Fitting the shape equations

The objective for shape fitting is to find a set of parameters $\vec{L}^* = (\tilde{p}_L^*, \Delta\tilde{\rho}^*, \Omega^*)^T \in P$ from the admissible parameter space P (see Fig. 1.3), which generates a shape $S_0(\vec{L}^*) : P \to T$ from the possible shapes T [5] which, compared to a predetermined target shape S_0^T [6], minimizes a suitable error metric $\vec{E}(S_0^T, S_0(\vec{L}^*))$, comparing a number $\dim \vec{E}$ of shape coordinates from both shapes:

$$\vec{L}^* = \arg\min_{\vec{L}^*} \left\{ ||\vec{E}(S_0^T, S_0(\vec{L}^*))||^2 \right\} . \tag{2.2}$$

[2] In practical terms $\tilde{s} < 10^{-8}$ applies only for the very first integration step.
[3] This is exactly the discrete control parameter Ω as introduced in Sec. 1.1.
[4] Up to machine precision, meaning $|\tilde{r} - 1/2| \leq 10^{-16}$.
[5] The function S_0 is the mapping from parameter space P to shape space T determined by the shape equations. Thus, only solutions to the shape equations are elements of T.
[6] The target shape is a representation of an experimental image in most cases.

Ideally, if the target shape $S_0^T = S_0(\vec{L}_0^T) \in T$ is a solution to the shape equations, with parameters $\vec{L}_0^T \in P$, the solution of Eqn. (2.2) is $\vec{L}^* = \vec{L}_T$, with $\vec{E}(S_0^T, S_0(\vec{L}^*)) = \vec{0}$.

However, the target shape S_0^T is not necessarily limited to be a member of T. Rather, the target shape can be any arbitrary shape from the super-set $H \supseteq T$. This is the manifestation of the target shapes being experiment data in most cases and thus not exact solutions to the shape equations. We still assume that the experiment shapes follow the shape equations we provide at least up to a certain precision, however, there might be noise or small deviations from the idealized theoretical description. Thus, the target shapes might always be imperfect to a certain degree and thus, we expect $||\vec{E}(S_0^T, S_0(\vec{L}^*))|| > 0$ and $\vec{L}^*$ only being an approximate solution. Ultimately, this means that the precision of the fit is intrinsically limited by the respective experiment errors [7] and we must declare the fit converged at a finite (and positive) target precision $||\vec{E}(S_0^T, S_0(\vec{L}^*))|| < \epsilon$ to eventually halt the algorithm [8].

A prominent iterative numerical approach for solving problems of the kind found in Eqn. (2.2) is the least squares method [68], where an improved guess $\vec{L}_{i+1}$ is achieved by incorporating information about the derivatives in the error-parameter landscape $\mathbf{J}_i^E$ (i.e. the Jacobian matrix) at the current guess $\vec{L}_i$. We apply this to Eqn. (2.2) by writing the Taylor expansion to first order of the error metric at $\vec{L}_i$ with a step $\Delta\vec{L}_i \equiv \vec{L}_{i+1} - \vec{L}_i$

$$\vec{E}(S_0^T, S_0(\vec{L}_{i+1})) \approx \vec{E}(S_0^T, S_0(\vec{L}_i)) + \mathbf{J}_i^E \Delta\vec{L}_i \tag{2.3}$$

and decompose the Jacobian into an orthogonal matrix $\mathbf{Q}_i$ and an upper triangular matrix $\mathbf{R}_i$: $\mathbf{J}_i^E = \mathbf{Q}_i\mathbf{R}_i$. We accordingly rephrase Eqn. (2.2) as

$$\Delta\vec{L} = \arg\min_{\Delta\vec{L}} \left\{ ||\mathbf{Q}_i^T \vec{E}(S_0^T, S_0(\vec{L}_i)) + \mathbf{R}_i \Delta\vec{L}_i||^2 \right\} , \tag{2.4}$$

with the unique solution

$$\Delta\vec{L}_i = -\mathbf{R}_i^{-1}\mathbf{Q}_i^T \vec{E}(S_0^T, S_0(\vec{L}_i)) . \tag{2.5}$$

We use Eqn. (2.5) to update the parameter set in each iteration of the optimization and employ a line-search algorithm to enforce $||\vec{E}(S_0^T, S_0(\vec{L}_{i+1}))|| \leq ||\vec{E}(S_0^T, S_0(\vec{L}_i))||$ by backtracking through $\vec{L}_i + \xi\Delta\vec{L}_i$ with $\xi \in (0, 1)$ till the condition is fulfilled.

Notably, it is possible to find an approximate mapping $\vec{L}^* \sim \vec{S}_0^{-1}(S_0^T)$ with the methods of machine learning, eliminating the need for computationally expensive iterative techniques at the cost of traceability, as we show in Ref. [24] and later in Sec. 5.1, where an estimate for $\vec{S}_0^{-1}$ is found using a feed-forward neural network.

For now, we stick to the iterative numerical approach and calculate the parameter update numerically by solving the shape equations once per continuous parameter in the direct vicinity of the last iteration value $\vec{L}_i$ allowing us to calculate the approximate derivatives in the error-parameter landscape per shape coordinate.

Ultimately, we do not implement the QR-decomposition ourselves, but use the free and open-source software package *Armadillo* because it employs several advanced optimization techniques, while retaining accuracy. The solver function from *Armadillo* is ~ 10 times faster than the custom QR decomposition implemented in *OpenCapsule* utilizing the free and open-source library *GSL*. The optimizations *Armadillo* provides are enabled by combining the entire solver into one function, where intermediate calculations can be shortcut, combined as vector instructions, or entirely reused from previous steps.

[7] Those include, but are not limited to, camera resolution limitations, material inhomogeneities and gravity-capillary misalignment.

[8] We employ a host of other halting criteria because this check alone obviously does not guarantee convergence.

2.1.2 Precision, performance and robustness

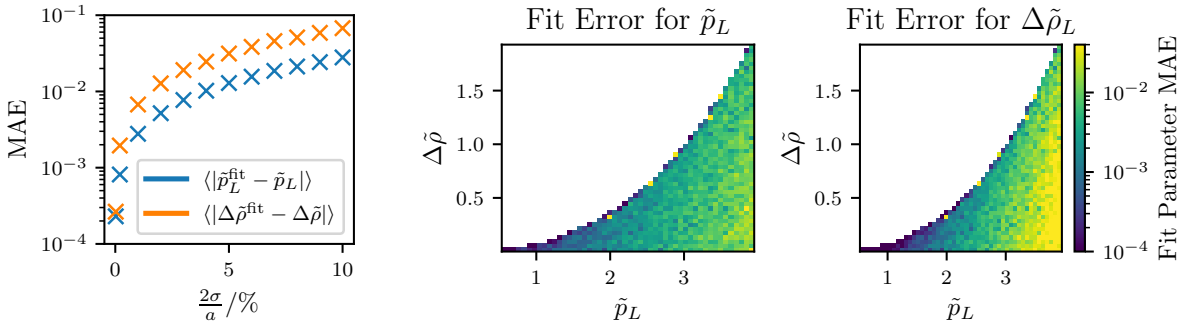

Figure 2.2: The precision of the numerical fit (MAE) shows a low error at low Gaussian noise standard deviation $\sigma \sim 0$ with MAE $\sim 10^{-4}$ (see left), upon increasing the standard deviation of the Gaussian noise σ we observe a quick decline in precision to MAE $\sim 10^{-2}$ at noise standard deviations equivalent to 1% of the capillary radius. The decay in precision for higher noises slows down significantly. A more detailed look at a low noise level (middle, right) reveals the fitting precision correlation in the parameter space.

In order to provide a more complete picture of the capabilities of the solver, we benchmark it with some artificially constructed data. This will benchmark the capability of the method on "perfect" [9] data. To make the evaluation more indicative of actual performance on experiment images, we apply a uniform Gaussian noise with standard deviation σ to the shape coordinates and probe the robustness of the numerical method in Fig. 2.2. The precision for low noise shape data ($2\sigma/a \leq 1\%$) is severely improved over the method used in Ref. [24] and results in mean absolute errors (MAE) in the fit parameters of $\sim 10^{-3}$ (see Fig. 2.2, left). The MAE increases quickly with applied noise and already at $2\sigma/a \sim 3\%$ diminishes to MAE $\sim 10^{-2}$.

We can determine the regions in the parameter space (see Sec. 1.1) where the fit is more accurate by evaluating a 2D histogram of fit errors as a function of the two non-dimensional fit parameters $\tilde{p}_L$ and $\Delta\tilde{\rho}$, as shown in Fig. 2.2 (middle, right). It is to no surprise that the shape fit – especially in the parameter $\Delta\tilde{\rho}$ – is more precise near the top bifurcation boundary for $\Omega = 2 \to 3$, as we have previously shown in Ref. [24] that this bifurcation boundary corresponds roughly to the line of volumetric stability control loss and thus highest shape sensitivity. This investigation also reveals that the fit error is orders of magnitude more precise in specific parts of the shape space than the MAE (averaged over all regions) implies.

Finally, the performance of the method is measured in real-time consumption, as this is the most relevant performance measure in practical applications. We note that the real-time consumption will vary drastically with the hardware executing the code. On an Apple M1 Pro CPU, we achieve ~ 20 fits per second per CPU core, which makes a single fit take ~ 50 ms. This includes fitting both hemispheres of a droplet profile. The time consumed by a fit scales linearly with the noise applied, where at a high noise of $2\sigma/a \sim 10\%$ the time for a single fit is increased on average by 35%, because the gradients in shape-parameter-space get more noisy as well, which increases the iteration steps required to find the minimum of the shape error landscape.

[9] Perfect in the algorithmic sense, because we provide the numerical inverse method with data generated directly from the forward method.

2.2 Elastic capsules

Since we choose the reference shape of the elastic capsule to always match the shape of a purely liquid droplet, we can conveniently reuse the non-dimensionalization of the liquid droplet, i.e. the surface tension γ of the reference droplet as a stress scale, and the capillary diameter a as a length scale. This enables us to write the full set of dimensionless shape equations along with the dimensionless constitutive equations of the non-linear Hooke model as [14], [15]:

$$\frac{\mathrm{d}\tilde{r}}{\mathrm{d}\tilde{s}_0} = \lambda_s \cos\Psi \tag{2.6}$$

$$\frac{\mathrm{d}\tilde{z}}{\mathrm{d}\tilde{s}_0} = \lambda_s \sin\Psi \tag{2.7}$$

$$\frac{\mathrm{d}\Psi}{\mathrm{d}\tilde{s}_0} = \frac{\lambda_s}{\tilde{\tau}_s}\left(\frac{p_a a}{\gamma} - \Delta\tilde{\rho}\tilde{z} - \frac{\sin\Psi}{\tilde{r}}\tilde{\tau}_\phi\right) \tag{2.8}$$

$$\frac{\mathrm{d}\tilde{\tau}_s}{\mathrm{d}\tilde{s}_0} = \lambda_s \frac{\cos\Psi}{\tilde{r}}\left(\tilde{\tau}_\phi - \tilde{\tau}_s\right), \tag{2.9}$$

$$\tilde{\tau}_{s,\phi} = \frac{Y_{2\mathrm{D}}/\gamma}{1-\nu_{2\mathrm{D}}^2}\frac{1}{\lambda_{\phi,s}}\left(\lambda_{s,\phi} - 1 + \nu_{2\mathrm{D}}(\lambda_{\phi,s} - 1)\right) + 1\,. \tag{2.10}$$

The equations (2.6), (2.7), (2.8) and (2.9) are ordinary differential equations of first order and may be integrated by the same numerical method as applied to the shape equations of the liquid droplet (i.e. a Runge-Kutta method of order 4) when combined with the constitutive equations of the non-linear Hookean material model Eqn. (2.10). Just as in the liquid droplet case, there are some inconvenient numerical singularities of type "0 / 0". In addition to the circumferential curvature at the apex $\kappa_\phi(s=0)$ (which was discussed already in Sec. 2.1), we encounter the additional numerical singularity $(\tau_\phi(s=0) - \tau_s(s=0))/r(s=0)$. Which we can, again, recover using the rule of de l'Hôspital to be $(\tau_\phi(s=0) - \tau_s(s=0))/r(s=0) = 0$ [14], [15]. As before, we handle these numerical singularities by manually switching between the analytically calculated limit and the exact equation in the vicinity of the singularity, i.e. $\tilde{s} < 10^{-8}$.

One peculiar problem arises because the actual solution shapes shall end at a predetermined radius, i.e. $r(s=L) = a/2$ is the attachment boundary condition at the capillary, and at a predetermined total length $L = \int_0^{L_0} \mathrm{d}s_0 \lambda_s$. We are thus no longer able to simply integrate to an arbitrary arc-length where the capillary boundary condition is met, as we did in the liquid droplet case, complicating matters significantly. If we ignore the attachment condition, we are able to independently specify the apex stress $\tau_s(s=0)$ and the apex pressure $p_a = p(z=0)$ along with the other control parameters of the problem[10]. Consequently, the solutions will, in general, no longer attach to the capillary at $s = L$, however, there exists a hyperplane of solutions in this larger [11] parameter space of the problem, where the boundary condition at $s = L$ is fulfilled exactly. Thus, we need to limit the acceptable solutions to exactly this hyperplane.

Obviously, the questions now becomes, which of the control parameters is replaced by constraining the acceptable solutions to the hyperplane of solutions that do satisfy the attachment boundary condition and can no longer be chosen freely. This control parameter is implied by the choice of all other control parameters and the boundary conditions at the capillary. In Ref. [14] they choose to eliminate the apex stress $\tau_s(s=0)$ as a control parameter. This, however, is a grave mistake, since it leaves the pressure at the apex p_a as a control parameter for the system, where we have

[10] I.e. the reference shape parameters and the constitutive parameters.
[11] Larger by exactly one dimension, which we need to use to fulfill the boundary condition.

shown previously in Ref. [32] that the apex stress $\tau_s(s = 0)$ is not guaranteed to be unique for a given apex pressure, i.e. multiple apex stresses yield the same apex pressure, while additionally fulfilling all initial and boundary conditions. Thus Ref. [14] eliminate a parameter which is not uniquely determined by the other control parameters, since it intersects the hyperplane multiple times and is thus not an injective parameter of the problem.

The same is not true the other way around – a predetermined apex stress has exactly one corresponding apex pressure p_a for any point that lies on the hyperplane of solutions that satisfy all boundary conditions and thus, eliminating the apex pressure p_a as a control parameter is the only correct choice. This statement is accessible to a simple proof, utilizing the implicit function theorem and that the Jacobian matrix of the solution at the additional boundary constraint is always locally invertible. Not realizing this fact excludes entire solution branches from the numerical integration and makes it ultimately entirely unpredictable, because it is arbitrary which of the matching parameters is selected during the search for a hyperplane intersection, rendering the shape fit built on top of this numerical integration routine intrinsically ill-conditioned and crippled in its capabilities.

Thus, we perform a shooting method in the apex pressure p_a, i.e. we leave the apex stress $\tau_s(s = 0)$ as a control parameter and search for the one and only apex pressure p_a matching the boundary condition $r(s = L) = a/2$, and thereby finding the hyperplane intersection, iteratively. The search for the proper apex pressure p_a is performed with an initial multi-section search to find a valid interval around the reference pressure p_L, followed by a much faster secant method to finally converge to the correct apex pressure. This conceptual improvement together with the new shooting algorithm already improves the shape fitting performance and reliability drastically over *OpenCapsule*.

Now, the shooting method can fail only due to two reasons

- For a given set of control parameters, shooting parameters and initial/boundary conditions, no valid [12]solution exists.
- The shooting parameter required to match the boundary condition for a set of given control parameters and initial/boundary conditions exists, but can not be found by the algorithm.

The first case appears naturally due to physical limitations and is a feature of the equations and thus not a problem in itself, counter-intuitively, however, classifying solutions as invalid (and thus ignoring them in the shooting and fitting method) too aggressively will negatively impact the capabilities of the shooting algorithm. Not all invalid solutions are created equally – we distinguish between the numerically invalid solutions, where a numerical problems leads to an abort of the shape equation integration (e.g. if a variable has the NaN flag set) and the solutions which are physically invalid. The solutions, which are physically invalid but not numerically invalid, are mathematically valid and as such proper solutions of the shape equations. These simply fail to satisfy physicality constraints, such as self-intersecting solutions.

Since we are searching for a zero crossing in the boundary deviation as a function of the shooting parameter, we need to be able to evaluate solutions at as many points of the larger solution space as possible. We reason that all mathematically valid solutions may be used to evaluate the boundary deviation, since the boundary deviation continuously depends on the shooting parameter for all mathematically valid solutions. During the shooting method, we thus include the valid but unphysical solutions to stabilize the method. Only when the solution of the shooting method is still unphysical, we discard it. This further improves the reliability of the shooting method, while retaining correctness.

[12]Valid in the sense that it may not intersects itself, diverge or show geometric discontinuities.

The second case why the shooting method can fail is the one that is critical. Here, an algorithmic limitation is responsible for a failure to generate a physically valid solution. This is exactly the case which needs to be optimized and understood carefully to allow a proper and reliable parameter space exploration, which is an important prerequisite for numerical shape fitting. In the following, we will discuss some of the more important aspects, where we are able to significantly improve the reliability of the shooting method in comparison to *OpenCapsule* and beyond the conceptual improvements already discussed here.

2.2.1 Fitting the shape equations

Conceptually, fitting elastic capsules is similar to fitting liquid droplets. The input to the fit is still a representation of the profile shape (e.g. an image), and the goal still is to find the set of control parameters which produce the shape profiles (see Fig. 2.1). It is thus to no surprise that we are able to reuse a significant amount of work already done for the liquid droplet fit. Being able to properly reuse the important structures of the actual implementation, requires them to be designed with a certain degree of generality in mind. How exactly the design of the software allows us to implement all kinds of fits in a compact and maintainable software package without unnessecarry code duplication will be discussed in a later section (see Sec. 2.4).

Beyond the superficial, conceptual, similarities between the elastic capsule fit and the liquid droplet fit, there are some striking dissimilarities. A first fundamental dissimilarity is the parameter-shape sensitivity. For a liquid droplet, a single high quality profile image suffices to determine all relevant dimensionless control parameters in almost all cases [17], [24]. For elastic capsules, the situation is more involved. It is trivial to produce a scenario, where even the most accurate shape fit will fail to determine all control parameters from a single image. The underlying problem is that only parameters, which produce a force resultant adequate for altering the shape, can be determined by a shape fit. This obvious statement is the reason why a single image of an elastic capsule may not always suffice to recover all control parameters. Take for example the stresses generated from elastic deformations of the interface, those only manifest if there is a deformation away from the elastic reference shape. As long as the capsule is sufficiently close to the reference shape, the elastic stresses are not capable of notably altering the resulting shape – we will not be able to properly fit the elastic control parameters manifesting as elastic stresses if the shape is close to the elastic reference shape. We will study the fitting landscape in the next section in order to make quantitative statements about the fidelity of the elastic fit.

While it is theoretically possible to obtain a fit for a (sufficiently elastically stressed) shape on its own, we can determine a subset of the control parameters already from the liquid reference shape, if we have access to it. From a theoretical point-of-view the reference shape is exactly the shape where no anisotropic and inhomogeneous surface stresses exist. These shapes are guaranteed to be solutions of the Young-Laplace equation. From an experiment point-of-view, determining a proper reference shape is not as straight forward and requires feedback from evaluation methods quantifying the anisotropy and inhomogeneity of the surface stresses [12], [13]. Sometimes the reference shape is only determined during the analysis, by determining the exact point where the Young-Laplace fits[13] start to fail and use this shape as the proper elastic reference, as we show in Ref. [13] and later in Sec. 3.1.

The subset of control parameters for the elastic problem, accessible through the reference shape is, by definition, exactly the reference shape parameter set $\vec{L} = \{\tilde{p}_L, \Delta\tilde{\rho}, \Omega\}$. Along with the reference shape parameters, we obviously also, implicitly, find the elastic reference shape of the capsule. Apart from the reference shape, we can also reuse the parameter $\Delta\tilde{\rho}$, if and only if the

[13] Purely isotropic and homogeneous surface stresses.

total isotropic and homogeneous surface stress does not notably change, the density contrast $\Delta\rho$ does not change, the capillary geometry does not change and the gravitational acceleration does not change, i.e. $\Delta\rho g a^2/\gamma$ must be a constant throughout the entire experiment.

Finally, the fit for an elastic capsule is separated into two parts, we first fit the pendant liquid drop reference shape to get access to the parameters $\vec{L} = \{\tilde{p}_L, \Delta\tilde{\rho}, \Omega\}$. This is done exactly as described in Sec. 2.1.

Second, we fit a sufficiently deformed shape with our elastic theory. The slightly modified problem statement for this is summarized as following. Let $\vec{W}^* = (K^*_{2D}/\gamma, \nu^*_{2D}, \tau^*_s(s=0)/\gamma)^T$ be a parameter vector for the elastic problem modulo the reference degrees of freedom (i.e. $\tilde{p}_L, \Delta\tilde{\rho}, \Omega$) and S_L be a mapping from the elastic parameter space to the elastic shape space with given reference parameters $L \in P$. The parameter set $\vec{W}^*$ is considered to be the best elastic fit for some target shape S^T if it is a solution to

$$\vec{W}^* = \arg\min_{\vec{W}^*} \left\{ ||\vec{E}(S^T, S_L(\vec{W}^*))||^2 \right\} . \tag{2.11}$$

Since Eqn. (2.2) and Eqn. (2.11) are from the same class of problems we solve it by utilising the exact same procedure as discussed for the liquid drop.

Of course, due to the drastically increased complexity of numerically solving the forward problem, we see a significant degradation in performance compared to a liquid droplet fit. However, through meticulous optimization (detailed in Sec. 2.4) the time required for an elastic fit is *only* a factor of 20 slower than the liquid droplet fit (~ 1 fit/second using multiple cores). This makes the present software up to three orders of magnitude faster than *OpenCapsule*, while being drastically more reliable and accurate at the same time.

2.2.2 The fitting landscape

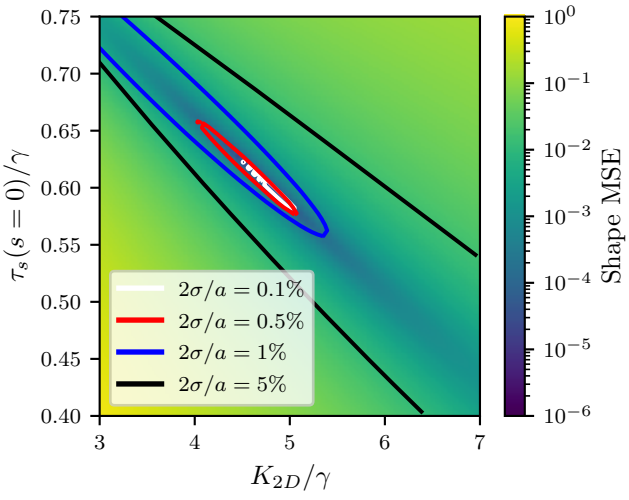

Figure 2.3: An example of the error-parameter landscape encountered during the fit of an elastic capsule. For this visualization we have deactivated the additional parameter ν_{2D} as a fit parameter, which we choose as the actual target parameter $\nu_{2D} = \nu^*_{2D}$. The full error-parameter landscape is three dimensional. The target shape is located at the point of zero shape MSE, while shapes similar to the target shape appear on a straight line. We superpose the numerical target shape with varying degrees of Gaussian noise and sample the shape error in the vicinity of the target shape. Varying the standard deviation σ reveals the size of regions where the error is already close to the best shape error encountered (colored contours).

To better understand the potential shortcomings encountered in the numerical fit, we can probe the fitting landscape by choosing an arbitrary target shape with the parameter set $\vec{W}^*$ and then mesh through the parameters $K_{2D}/\gamma, \tau_s(s=0)/\gamma$ and ν_{2D} while evaluating the error function $||\vec{E}(S^T, S_L(\vec{W}^*))||^2$. For visualization purposes we exclude ν_{2D} from our parameter space exploration and set it to the actual parameter of the target shape $\nu_{2D} = \nu^*_{2D}$.

We color code the error function in Fig. 2.3 for an arbitrarily chosen set of control parameters [14].

[14]The control parameters are: $\tilde{p}_L = 3.7, \Delta\tilde{\rho} = 1, \tilde{K}_{2D} = 4.7, \nu_{2D} = -0.3, \tilde{\tau}_s(\tilde{s}=0) = 0.6$

Interestingly, the region of low shape error seems to be a straight line. We can understand this by assuming an approximately homogeneous stretching and realizing that at the apex of the shape, we achieve a similar stretching $\lambda_s(s=0)$ if

$$\frac{\tau_s(s=0)-\gamma}{K_{2D}} \sim 2(1-1/\lambda_s^*(s=0))\,. \tag{2.12}$$

The slope of the straight line (called *similarity line* in the following) is related to the stretching of the target capsule at the apex $\lambda_s^*(s=0)$. This is also the reason why the slope of the region of low residual shape error does not strongly depend on ν_{2D}. Rather, a change in ν_{2D} will shift the global minimum along the straight line. Interestingly, Eqn. (2.12) predicts that, if the target shape is close to the reference shape $\lambda_s^*(s=0) \sim 1$, we obtain a horizontal line of similar shapes. This result makes sense, as we discussed previously that exactly those shapes are entirely insensitive to the elastic compression modulus K_{2D}. Another notable observation is that the similarity line will have a positive slope for stretched solutions $\lambda_s^*(s=0) > 1$ and a negative slope for compressed shapes $\lambda_s^*(s=0) < 1$. Furthermore, the maximum slope of the similarity line for stretched solutions is encountered for $\lambda_s^*(s=0) \to \infty$ as 2, while for compressed solutions the similarity line gets vertical for $\lambda_s^*(s=0) \to 0$.

This is a valuable insight for our goal of extracting rheological parameters from the deformed shapes, since it allows us to quantify a lower bound for the expected error encountered in the determination of constitutive parameters from deformed shapes. In Fig. 2.3, we compare exact numerical solutions, however, in a realistic experimental setting, we will not have two perfect shapes. Rather, we will have a noisy experimental shape, which we compare to the perfect numerical shapes in order to find the fitting set of theoretical shape parameters. Hence, we always have a natural noise floor, which is superposed onto the perfect shape error shown in Fig. 2.3, eliminating all shape errors lower than the background noise contribution from the line of low error and disallowing a more precise solution for any single shape. The ramifications of this are that the region of indistinct shapes [15] grows larger. We show this in Fig. 2.3, where we disturb the numerically generated target shape's dimensionless coordinates with a uniform Gaussian noise of magnitude σ and use it for the shape error calculation. We highlight the contour lines where the shape error is within $0.1\%, 0.5\%, 1\%$ and 5% of the lowest error encountered for a specific noise amplitude, which gives us an insight into the limitations we face during the fit. It is evident that a high precision fit is required to resolve the constitutive parameters accurately, as the region of indistinct shapes grows rapidly with the precision cut-off of the fit.

Numerical problems may arise if a local minimum exist in between the initial guess and the global minimum. This problem really only materializes once ν_{2D} is included as a parameter. The general sensitivity of ν_{2D} on the target shape is much lower than that of the other two elastic parameters K_{2D} and $\tau_s(s=0)$, however, it causes significant trouble for our numerical fit. The manifestations of this are that we achieve unsuccessful shape fits, where we use unsuccessful in the sense that the "correct" set of parameters was not retrieved. Interestingly, however, when considering a different measure of "success", namely, the shape residual, most of these fits are actually successful. The problem here is that these fits get stuck in a local minimum along the similarity line of low error in Fig. 2.3 with the wrong ν_{2D}, which leads to an inaccurate overall parameter set.

Generally, determining ν_{2D} is ill-conditioned if the shape deformation is approximately isotropic, because then $\lambda_s \sim \lambda_\phi$ and ν_{2D} vanishes entirely from the constitutive equations, only leaving K_{2D} as a constitutive parameter. Inconveniently, this is always the case if the deformation is small, because the reference shape surface stresses are isotropic and homogeneous. Therefore, predicting

[15] Indistinct up to a specific precision.

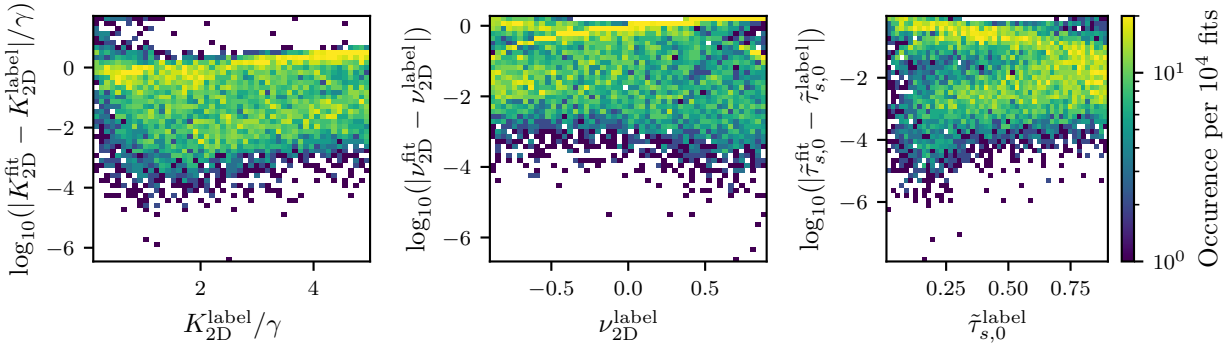

Figure 2.4: The error encountered during the fit spans several orders of magnitude. Fits with a parameter residual of MAE $> 10^{-1}$ are frequently encountered. These fits are not necessarily bad shape matches, as they may lie on the similarity line (see Eqn. (2.12)). The problem in the region MAE $> 10^{-1}$ is in most cases related to an improper initial guess, which we show in a later chapter where the initial guess is supplied by a machine learning approach.

ν_{2D} reliably is only possible for large enough deformations and appropriate initial guesses for the fitting algorithm.

Determining an appropriate initial guess for the shape fit, i.e. the start of the optimization is essentially arbitrary. However, there are better choices than others for the initial guess. An advantageous property for the initial guess is that it should reside in a region of the parameter space, where the gradient components in parameter-shape space are all sufficiently steep. Take for example any initial guess with $\tau_s(s=0) = \gamma$, where it is obvious that this point is located in a region with several slopes in the parameter-shape space being zero [16]. The shape fit would only very slowly depart from the initial guess because of the vanishing gradients in the vicinity of the initial guess. We thus have to avoid this initial guess and instead choose one, where $\tau_s(s=0) < \gamma$, since the slope of the similarity line is more sensitive to $\tau_s(s=0) < \gamma$. Finally, we settle on the (informed, but still arbitrary) initial guess for the fit: $\tilde{K}_{2D} = 2.5, \nu_{2D} = 0.5, \tilde{\tau}_s(\tilde{s}=0) = 0.95$. We will, in a later chapter, discuss a significantly more robust way to provide a proper initial guess for the numeric fit with the help of machine learning (see Sec. 5.2) to again significantly improve the precision, performance and robustness of the fit.

First, we want to evaluate the precision of the numerical fit without applying further machine learning driven optimizations. In Fig. 2.4 we generate 10.000 random shapes [17] by solving the shape equations with the numerical forwards solver. These shapes are superposed with a Gaussian noise ($\sigma = 2\%$) and fed back into the inverse fit. In a sense, this is an idealized scenario for the solver and stands as a "best case" fit performance measure. The results in Fig. 2.4 shows that the fit can produce accurate results, if it is not trapped in a local shape-error minimum, however, compared to the liquid droplet fit – where almost all fits return an adequate parameter set – we see a decrease in robustness and overall precision. We are able to improve the precision and robustness of the numerical fit beyond Fig. 2.4 by carefully selecting a set of fitting parameters which is conditioned better than the present one. Finally, we internally use K_{2D} and $G_{2D} = K_{2D}(1-\nu_{2D})/(1+\nu_{2D})$ as parameters for the fit. A more elaborate investigation of this can be found in the Appendix A.3.1.

[16] The slopes with respect to $\tau_s(s=0)$, K_{2D} and ν_{2D} are all zero at this point.
[17] Uniformly sampled in the parameter range shown on the respective x-axis and with uniformly sampled reference shape parameters from the liquid shapes with $\Omega = 2$.

2.3 Viscoelastic capsules

The next numerical challenge we want to tackle is that, where the shape equations (2.6), (2.7), (2.8) and (2.9) are accompanied by a time dependent constitutive law. In the purely elastic case discussed in Sec. 2.2 a numerical scheme was trivially achieved by analytically solving the constitutive equation in τ_s for λ_s. Here, we will need to make λ_s accessible from the available information as well, but have to consider the much more general constitutive law of a viscoelastic skin, as derived in Sec. 1.3 in the form of Eqn. (1.41).

Here, we choose to explicitly discretize the convolution integral appearing on the r.h.s of the constitutive equation Eqn. (1.41) with a trapezoidal rule on a temporal grid with uniform time step Δt. The time $t = n\Delta t$ is quantized by the time step number n, which is why we use that to refer to the temporal evolution in the following. All other time dependent quantities are also denoted by their respective the time step number. Finally, we apply the discretization

$$\sum_j \int_0^t \mathrm{d}t' \dot{J}_{ij}(t-t')\tau_j^{\mathrm{v}}(t') \to \frac{\Delta t}{2}\sum_j \left(\dot{J}_{ij,n}\tau_{j,0}^{\mathrm{v}} + \dot{J}_{ij,0}\tau_{j,n}^{\mathrm{v}} + 2\mathcal{R}_{ij,n}\right), \text{ with } \mathcal{R}_{ij,n} \equiv \sum_{k=1}^{n-1} \dot{J}_{ij,n-k}\tau_{j,k}^{\mathrm{v}} \tag{2.13}$$

where $R_{ij,n}$ is zero if $n < 2$. The entire memory of the deformation sequence is contained [18] in the terms $R_{ij,n}$, which is why they constitute the history terms.

Applying the discretization Eqn. (2.13) to Eqn. (1.41) and utilizing the previously introduced definition $\tau_1 = \tau_s\lambda_\phi$ and $\tau_2 = \tau_\phi\lambda_s$ we arrive (after some basic calculus) at an expression for $\lambda_{s,n}$:

$$\begin{aligned}\lambda_{s,n} - 1 = \frac{\dot{J}_{s\phi,0}}{\dot{J}_{\phi\phi,0}}(\lambda_{\phi,n}-1) + \frac{\Delta t}{2}\Bigg(&\lambda_{\phi,n}\tau_{s,n}^{\mathrm{v}}\left(\dot{J}_{ss,0} - \frac{\dot{J}_{s\phi,0}}{\dot{J}_{\phi\phi,0}}\dot{J}_{\phi s,0}\right) + \lambda_{\phi,0}\tau_{s,0}^{\mathrm{v}}\left(\dot{J}_{ss,n} - \frac{\dot{J}_{s\phi,0}}{\dot{J}_{\phi\phi,0}}\dot{J}_{\phi s,n}\right)\\ &+\lambda_{s,0}\tau_{\phi,0}^{\mathrm{v}}\left(\dot{J}_{s\phi,n} - \frac{\dot{J}_{s\phi,0}}{\dot{J}_{\phi\phi,0}}\dot{J}_{\phi\phi,n}\right) + 2\left(\mathcal{R}_{ss,n} + \mathcal{R}_{s\phi,n} - \frac{\dot{J}_{s\phi,0}}{\dot{J}_{\phi\phi,0}}(\mathcal{R}_{\phi s,n} + \mathcal{R}_{\phi\phi,n})\right)\Bigg)\end{aligned} \tag{2.14}$$

The final equation, which closes the system of equations, is obtained by solving the constitutive equation for $j = 2$ for $\tau_{\phi,n}$:

$$\begin{aligned}\tau_{\phi,n}^{\mathrm{v}} = \frac{1}{\lambda_{s,n}\Delta t\dot{J}_{\phi\phi,0}}(&2(\lambda_{\phi,n}-1)\\ &-\Delta t(\dot{J}_{\phi s,n}\lambda_{\phi,0}\tau_{s,0}^{\mathrm{v}} + \dot{J}_{\phi s,0}\lambda_{\phi,n}\tau_{s,n}^{\mathrm{v}} + \dot{J}_{\phi\phi,n}\lambda_{s,0}\tau_{\phi,0}^{\mathrm{v}} + 2\mathcal{R}_{\phi s,n} + 2\mathcal{R}_{\phi\phi,n}))\,.\end{aligned} \tag{2.15}$$

In all following considerations, and in the actual simulation code, we will choose that at $n = 0$ or $t = 0$ the capsule is in a configuration with no viscoelastic stresses $\tau_{s,0}^v = \tau_{\phi,0}^v = 0$. This marks the start of the simulation, but including the viscoelastic pre-stress in a simulation is no problem either [19]. An important realization is that the time step Δt *must* be significantly smaller than the viscoelastic relaxation time scale in order for the simulation to be precise.

[18] If the first step is in a reference configuration.
[19] By including all terms from Eqn. (2.14) and Eqn. (2.15) in the simulation software.

2.3.1 Fitting shape sequences

If we wish to fit the parameters of a time-dependent constitutive model to a prescribed shape deformation sequence, we need to generalize several concepts used for the static case in the previous sections. Namely, we still have a set of parameters $\vec{W}^*$ for the viscoelastic response, however, the mapping function from parameter space to shape space is history-, and thus time-, dependent $S_L(\vec{W}, t)$. This means that the problem statement for the inverse problem changes in a subtle way to:

$$\vec{W}^* = \arg\min_{\vec{W}^*} \left\{ \sum_n ||\vec{E}(S_n^T, S_{L,n}(\vec{W}^*, t))||^2 \right\} . \quad (2.16)$$

Still, Eqn. (2.16) is a least-squares problem, which is accessible to the treatment discussed in Sec. 2.1, in certain circumstances.

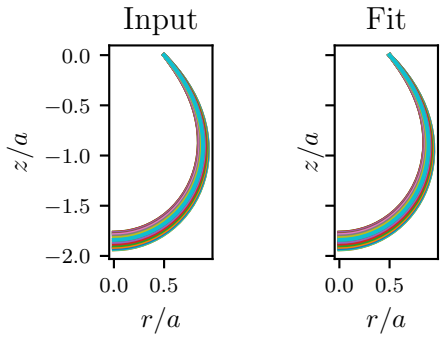

Figure 2.5: We supply an ideal shape sequence (left) to our numerical inverse solver and let it deduce the control parameters purely by shape sequence analysis. The resulting fit (right) is precise with MAE $\sim 10^{-4}$ in the control parameters.

It is important to properly understand which information we actually wrap into $\vec{W}^*$ and if there may be problems with assuming that those properties are static. The obvious parameters that go into $\vec{W}^*$ are the parameters of the constitutive law, i.e. elastic moduli and viscosities [20]. Those can reasonably be assumed to be static. However, for every shape in the sequence, there is an additional degree of freedom we need to properly determine, which is exactly the apex stress in meridional direction $\tau_s(s = 0)$. In extent, we could choose to only provide information about the constitutive parameters and for every shape do an additional, "inner", fitting routine, which determines the best apex stress $\tau_s(s = 0)$ for the given target image and fixed constitutive parameters. This is the most general way to fit a viscoelastic shape sequence, however, it provides a computational challenge. For a shape sequence consisting of N time steps, the complexity for a single "outer" fit iteration is high, because N inner fit iterations for the N apex stresses need to be calculated, making the overall fit untraceably slow.

We thus choose to reduce the generality and assume a sinusoidal oscillation of the applied external stress, which we can use to determine that the apex stress throughout the shape sequence shall also be sinusoidal. The only unknown parameter in this case is the amplitude of the apex stress oscillation throughout the shape sequence, which is, however, a static parameter, we can add to the fit parameter set $\vec{W}$. In the future, with significant technical effort, fitting the apex stresses exactly might be possible, but is out of scope for this work.

In an ideal scenario [21] a viscoelastic shape sequence following the Kelvin-Voigt constutive relationship and consisting of 30 shapes, results in a fit taking $\sim 20\,\mathrm{s}$. We show this fit in Fig. 2.5, where it is evident by visual comparison of the shape sequences (colors indicate temporal evolution) on the left (input) and right (fit) that the fit does work. Of course, we can determine the control parameter deviation, since we have access to the actual ground-truth. The MAE of the control parameters in an ideal scenario (just as shown in Fig. 2.5) is $\sim 10^{-4}$. We want to highlight that this level of performance is only possible through meticulus optimization as well as static and dynamic analysis of the code. Of course, real-world shape sequences will in general take longer than the ideal scenario, because the error-parameter landscape is more treacherous. Additionally, for real-world shape sequences we do not have a ground-truth for the actual control parameters. We will investigate real-world shape sequences in Chap. 3.

[20] Or in terms of the relaxation functions: decay time scale and amplitude.
[21] Ideal meaning that a theory shape sequence is presented as the input to the inverse method.

2.4 CapSol: A highly capable capsule solver with powerful shape fitting capabilities

> **Notice** – This section details the software created by the author. It is a rewrite and significant improvement of the open source software OpenCapsule. The motivation for this new software is that the extension to viscoelastic capsules requires drastically better performance. Additionally, several significant problems exist in OpenCapsule, which make a significant restructuring essential.

In this section we want to highlight the software that enables all of the shape fits presented in Chap. 3 and which also supplies the data presented in Chap. 1 and Chap. 2. An often overlooked, but very important, step towards a well-functioning software is the actual design of the implementation. This point is conceptually different from the pure numerics, since it focuses on ease-of-use, extensibility, re-usability, error mitigation and performance. It is crucial to design the implementation in a way where human error is spotted early and critical functionality is isolated.

The design of the present software – *CapSol* – is guided by object oriented programming (OOP). Using OOP has many benefits over using functional programming in a project such as CapSol. Abstracting the components of the program into compact objects supports minimal code duplication and an overall easier to understand structure. For example, we consider solutions of axi-symmetric shape equations in all of our application cases, hence we abstract the information the *Shape* holds into a structure, where we additionally define a common interface to interact with these information. Any solution of an axi-symmetric shape equation then inherits from the *Shape* class, giving it immediate access to all of its members without any code duplication. Furthermore, the interface of a base class may be purely virtual, forcing the inheriting class to implement those functions, keeping the code consistent and functional across multiple independent sections. Additionally, templating the interfaces with purely virtual functions allows us to implement generalized functions, such as a shape fitting function, without specifying the exact routine or parameters required to generate the solution shapes from the shape equations. The child class then inherits all traits and only implements the functions required by its virtual base class, e.g. the shape equations. This way, all solutions to axi-symmetric shape equations can directly use the shape fitting capabilities when inheriting from the abstract *Shape* class without any further work required.

An example which shows the power of this design is the least squares method, which is employed for the shape fit in all of our applications. This method needs to only be implemented a single time when properly utilizing purely virtual functions, although the shape equations, parameter sets, initial conditions and more may be different for the specific application. For this to work, the least squares method needs to impose a certain interface, which all classes using the method must implement, i.e. a set of purely virtual functions which can be called during the fitting procedure and call out to the specific implementation in the child classes.

This is one of the major optimizations made in the design compared to OpenCapsule, where functional design and object oriented designs are mixed, producing many code duplications. This reduces the maintenance cost of the code and overall code complexity drastically.

2.4.1 Accessing information of other solution shapes

To solve the shape equations, we are required to evaluate properties of solutions of other shapes (such as the reference shape) at points between integration steps. This is purely due to the Runge-Kutta method used for the integration.

The Runge-Kutta method of order four, employed here, requires us to evaluate the shape equations at points $\tilde{s}+\tilde{h}/2$, where we need access to e.g. $\lambda_\phi = r/r_0$. However, r_0 is provided by the reference solution.

One way to account for this is to interpolate these properties using a spline interpolation for the entire integration interval $s \in [0, L]$. The spline can be evaluated at any point inside the interpolation interval, this is exactly what Ref. [14] does to tackle this problem. A drawback of this technique is that creating and evaluating splines is computationally demanding and comparatively slow. Additionally, the interpolation does not actually produce correct intermediate values, because it is only an interpolation, which can induce numerical instability. It turns out that we are able to entirely circumvent using an interpolation technique, while solving the shape equations, by not only saving the results of the integration at all integration steps, but also all results of the intermediate steps performed by the Runge-Kutta algorithm. This requires the integration step size to be the same for all relevant solutions of the shape equations, but replaces a spline with an array and a spline evaluation with a direct memory access. This speeds up the integration process and additionally improves the reliability of the method because we are not using interpolated values, but actual integration values in all of our integrations. A side-effect of this is that it reduces the required minimal integration step-size because the errors made in in-between steps are smaller.

2.4.2 Python API

While C++ is a robust language choice for the computation side, because the language is compiled into raw machine code and thus fast, it is not entirely easy to use from a user/scripting perspective. A common language for scientists is the interpreted language *Python*, possibly because of its simplicity and intuitiveness. There is a way to bridge these two worlds together. Python is able to load static object files and call exported symbols by allowing the instruction pointer to jump into the loaded object machine code. A simple to use abstraction for this is the free and open-source package *pybind11*, which allows us to expose classes and functions from native C++ to a Python module.

Using *pybind11* we are able to fully expose the C++ framework to Python and make it possible to inspect variables, integration results and generate shapes, compute shape fits all from within the comfort of a simple to use Python interface. Additionally, we can use readily available python packages to perform the experiment image preparation before passing it into the shape fitting routine implemented in C++. The shape detection and pre-processing is a technical detail and is delegated to the author's master thesis [45] for the interested reader.

A documentation for the Python API, together with the entire source code, is available at the software repository `https://www.github.com/FelixKratz/CapSol`.

3 Analysis of experimental shape sequences

Notice – None of the experiments discussed in this chapter are performed by the author, they are provided by our collaborators from the groups of W. Drenckhan et al. at the Institut Charles Sadron in Strasbourg, and F. Mugele et al. at the University of Twente. Although the author participated in parts of the experiments performed for Sec. 3.2, he was merely participating as a visiting observer. The author's contribution is the experiment data analysis and interpretation discussed in the following sections.

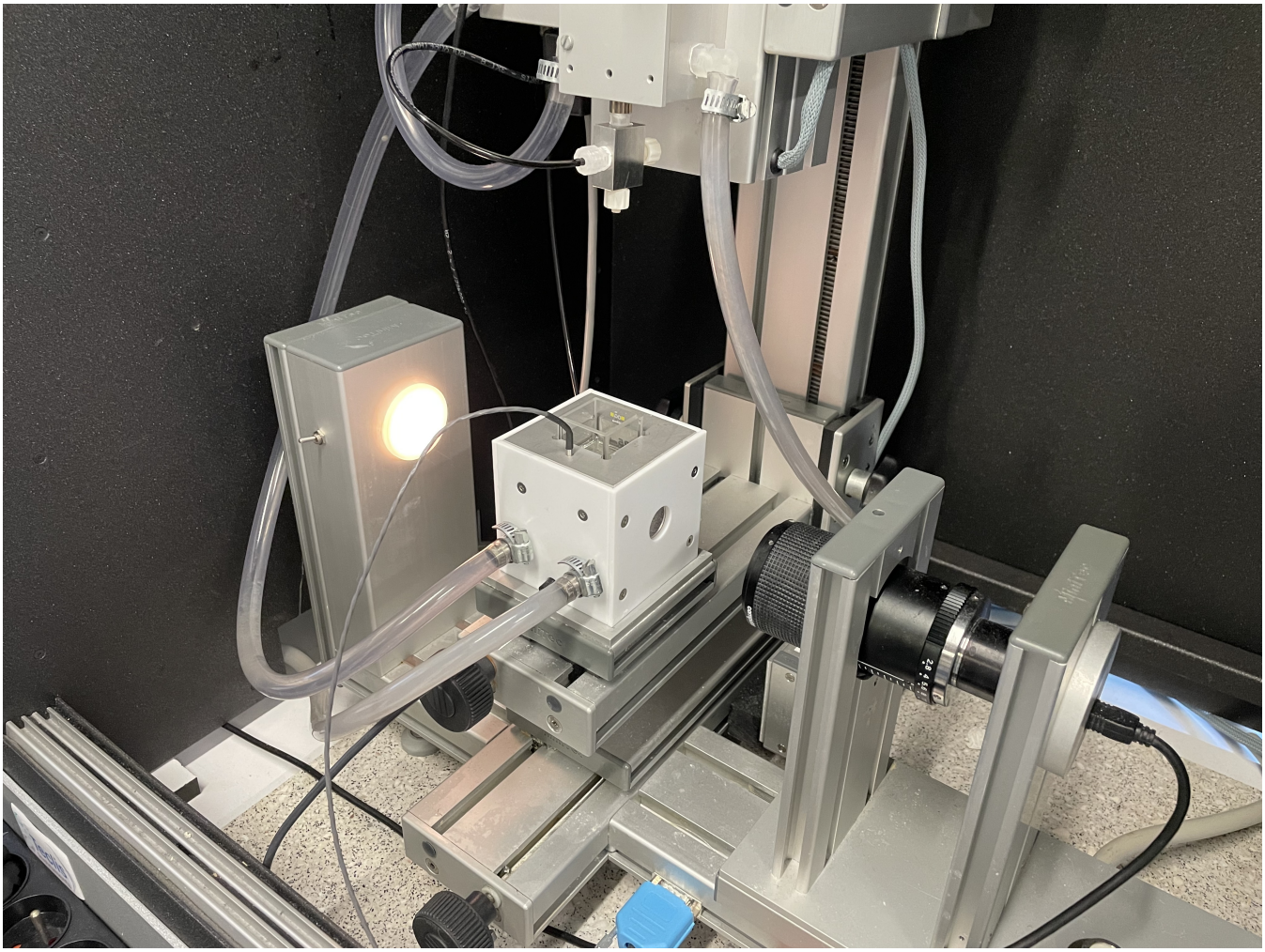

Figure 3.1: An experiment setup for pendant droplet experiments. The image is taken at the laboratory of W. Drenckhan et al. and shows their experiment setup used for the experiments from Sec. 3.2 and Ref. [12]. A camera is pointed at the cuboid experiment cell into which a needle (not seen in the image) is suspended from the top mechanic platform. The experiment is illuminated from the back. The tubing attached to the white cuboid is used to exchange the outer liquid phase and control the polymerisation process of elastic surface layers. It can be used to manufacture multilayer skins and is not generally required for liquid droplet experiments.

Having an exchange between theory and experiment is an integral constituent for the knowledge gain in the natural sciences. While the pure theory aspect of physics may give insight into possible mechanisms of nature, we have no strict axiomatic framework from which it would be possible to derive all inner workings of nature in a formal manner. Rather, any theory about nature's workings needs to be rooted to reality via appropriate experiments. Those experiments should be designed in a way to be able to test assumptions and results derived from them as well as inspire novel theoretical approaches. Ultimately, this is the reason why a theory in the natural sciences is not accessible to a formal proof as seen in pure mathematics, rather, it is only valid as long as none of its assumptions are rejected by an experiment. Although this thesis is primarily a theory based work, in this chapter, the focus will be to apply the theory presented in Chap. 1 and the computational methods presented in Chap. 2 to actual experiments and thereby real, non-idealized, systems. All experiments discussed in this chapter are performed by skilled experimentalists belonging to our collaborators from the groups of W. Drenckhan et al. and F. Mugele et al..

The setup for the pendant drop experiments performed for this section is common in the literature [12], [13], [17], [32]. A drastically simplified description of the experiment setup is given here for completeness sake. A spherical needle is attached to a rigid frame and connected (commonly via tubes) to a liquid reservoir, e.g. a syringe. The liquid reservoir can be controlled to eject or retract fluid through the needle. Creating a proper needle, which does not create additional interactions with the fluid (often achieved by a hydrophobic coating [12]) is one of the many difficult challenges encountered on the experiment side, which we will not discuss here. If experimenting with non-negligible gravitational effects, i.e. $|\Delta\tilde{\rho}| > 0$, the needle needs to be precisely oriented along the axis of gravity to reduce deviations from axi-symmetry as well as possible. The influence of non-axisymmetric shape corrections is discussed qualitatively in Ref. [17] for liquid droplets. Additionally, the interface attached to the needle needs to be presented with proper lighting, such that the outlines of the interface are clearly distinguishable from the background. Usually, the droplet is illuminated from the back, while a digital camera is focused on the front of the droplet, as depicted in Fig. 3.1.

Such experiment can be performed both in a pendant and in a rising geometry. Ultimately, only the sign of the product $g\Delta\rho$ determines the directionality of the effective buoyancy force acting on the droplet, such that a pendant drop experiment $g > 0$ with positive density contrast $\Delta\rho > 0$ is entirely equivalent to a rising drop experiment $g < 0$ with negative (but equal magnitude) density contrast $\Delta\rho < 0$. Only if the combined sign changes, the experiments are not equivalent, as one of them has positive $\Delta\tilde{\rho}$ and the other has negative $\Delta\tilde{\rho}$. All of the present experiments have positive $\Delta\tilde{\rho} > 0$, such that they operate in the positive half space of the parameter space (see Fig. 1.3). A liquid droplet in air at $\sim 1\,\mathrm{bar}$ has a positive $\Delta\tilde{\rho}$ if it is suspended in a pendant geometry. An oil droplet suspended in water has positive $\Delta\tilde{\rho}$ if suspended in a rising geometry.

Additionally, the present experiment shapes are always volume controlled [1] and never pressure controlled. This makes all liquid shapes of class $\Omega = 1, 2$ and some of class $\Omega = 3$ available to the experiment, as detailed in Fig. 1.3. In order to precisely follow a given volumetric deflation sequence of the drop, a software calculates the volume (or equivalently surface area) from the profile of the shape in real-time and performs micro-adjustments through an electric motor which controls the liquid flow rate at the tip of the needle, e.g. by pressing or pulling on a syringe. Notice that the calculation of volume or surface area is not equivalent to the liquid or elastic shape fits in any way. Rather, it only uses the geometry of the profile to calculate the volume and does not solve any shape equations to properly include the force balances – this is what we will do in the following sections.

[1] Sometimes implicitly through a software surface area control mechanism.

3.1 Complex interfaces with liquid-solid phase transitions

Published material – This section is reproduced with modifications and permission from the author's publication [13], © 2023 The Authors. Published by American Chemical Society. All experiments discussed in this section are performed by the group of F. Mugele et al. at the University of Twente.

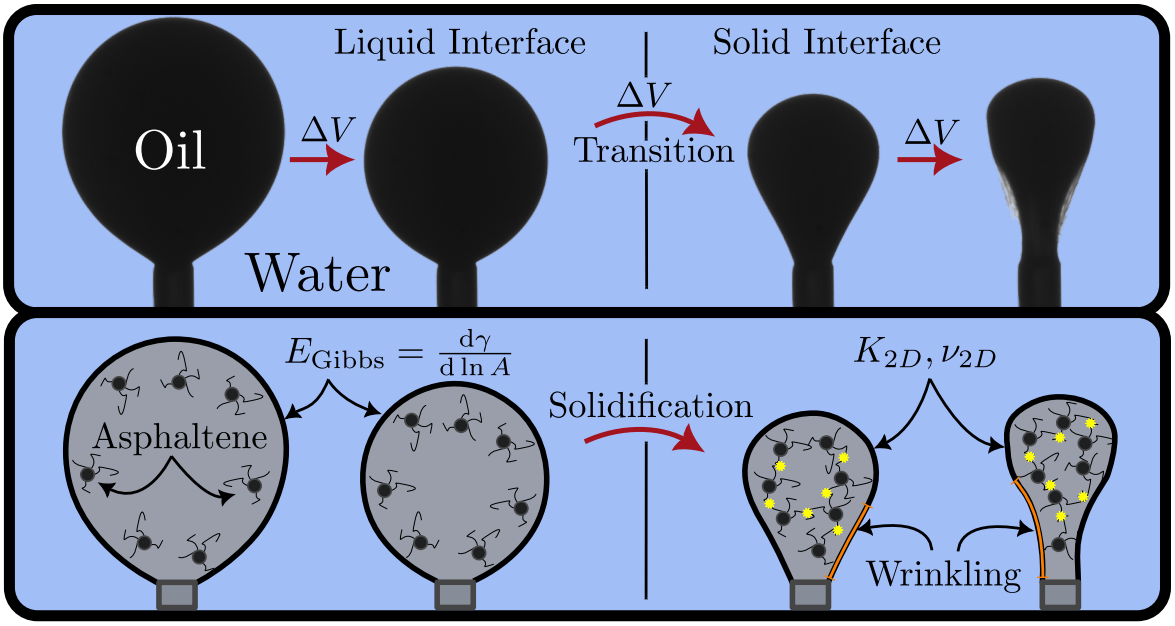

Figure 3.2: The experimental observation (top), where we successively reduce the volume of the oil droplet to find a transition between a liquid-like interface and a solid-like interface. The theoretical description (bottom) shows the devised mechanism of the process, i.e. the solidification process due to a change in the interaction between surface molecules at a certain critical surface area. While the drops are initially well described by a uniform, but temporally varying, surface tension (i.e. a Gibbs-elasticity), this description starts to break down at the critical point, where anisotropies and inhomogeneities in the surface stresses need to be taken into account to appropriately describe the shape sequence.

In all of our previous considerations, the actual interface configuration only entered the discussion in terms of the surface tension γ of the elastic reference shape and in terms of the density contrast $\Delta\rho$ between the phases in the reference configuration. This is the idealized theoretical description used to model the interface properties. From an experimental perspective, however, there are several additional complex processes at interfaces, which need to be considered with care. One such ubiquitous complex interface is the interface between crude oil and water. Here, several *surface active* organic molecules (surfactant molecules) can be found at the interface, which means that they are able to actively migrate at the interface. The effects sufactant molecules have for the interface deformation behavior are multitude. A particularly obvious modification to interface properties driven by surfactants is regularly exploited by most people – scientists and non-scientists alike – when soap is mixed into water in order to reduce the surface tension of oil-water interfaces, emulsifying the oil-water mixture and thus making it possible to rinse the mixture more easily. Other complex interface effects include the accumulation of macroscopic structures at the interface in an aging process, as observed in biological proteins such as hydrophobins [14], industrially used polymers such as PNIPAM [69], and crude-oils [70] used in the energy sector.

These complex structures at the interface can, under certain circumstances, be described as viscoelastic surface layers. The modifications made by the viscoelastic surface layer can be drastic, as discussed from the theoretical perspective in Sec. 1.3. As a result, the microscopic manifestations of such drastic change in theoretical description include, but are not limited to, changes to capillary pressure, surface flow, transport through the interface, stability of emulsions and contact properties (which we will discuss in Chap. 4) [71].

To properly understand these complex systems, we quantify the rheological properties of the interface by utilizing the methods developed in this thesis, i.e. the theory of two dimensional surface viscoelasticity in combination with the numerical shape-fitting backbone. In this section, we will use the interface between crude oil (CRO) and brines containing aqueous salt ions as the *complex* interface subjected to our methods. We note that the methodology employed for this specific system is widely applicable for other complex interfaces, as we will discuss in the following sections.

Such crude oil interfaces occur naturally within oil reservoirs and unnaturally in ocean oil spills. Crude oils contain a diversity of surface-active organic molecules, resulting in a complex interface rheology. The complexity of interfaces between brines and CRO plays a significant role in the recovery process of crude oil from ocean spills and phase separation [72]. The question, which microscopic constituent causes the complexity of the interface is usually answered by: asphaltenes. Asphaltenes are exactly those components of crude oil, which fulfill a set of solubility specifications and are also found in other materials such as coal. The exact specification requires asphaltenes to be soluble in toluene, but insoluble in n-alkanes. This definition dates as far back as to J. Boussingault in 1837 [73]. The amphiphilic nature of asphaltenes in combination with the significant alkane fraction in most CROs leads the asphaltenes to adsorb (often irreversibly) to the oil/brine interface [74], creating macroscopic interface sub-structures. The exact structure of the asphaltene interface layers depends on several factors, including resin content, ionic composition of the brine, hydrogen bonding, temperature, surface history, kinetics, and other factors [75]. A recent review by Moud et al. discusses the importance of various controlling factors in asphaltene layer development at the oil/brine interface [76].

Asphaltene layers grown under a wide variety of conditions show distinct phase transitions when compressed. Both Yarranton et al. [77] and Kabbach et al. [78] qualitatively describe the surface tension versus surface area relationship for these interfaces. A change in Gibbs modulus seems to indicate a "phase change" of the interface during compression. With the assumption that asphaltenes adsorb nearly irreversibly to oil/brine interfaces, the Gibbs elasticity is defined as $E_{\text{Gibbs}} = \mathrm{d}\gamma/\mathrm{d}\ln A$. How reliable the interpretation as a fluid Gibbs-elasticity is remains somewhat elusive for now, as a qualitative comparison of residual error is not performed up till now. Continuing to compress further, induces surface wrinkling and distortion that they attribute to a solid interfacial layer [70], [77]. Measurements of the surface layers, at 2-9 nm thick, seems to suggest that network formation extends into the oil phase [79]. Additionally, interfacial shear rheology and particle tracking has shown that asphaltenes form rigid, heterogeneous films that immobilize particles on the surface [80].

On the other hand, a number of authors have shown that asphaltene-laden interfaces show a unique equation of state (EoS), meaning every interfacial tension corresponds to a unique surface coverage, even independent of external conditions. They also state that the maximum surface coverage aligns well with the average size of a single asphaltene molecule, suggesting a packed, but unaggregated, asphaltene layer [81]–[84]. Others find a single equation of state when the heptane fraction in the solvent is low, but suggest gel formation when the heptane fraction is higher (as it is in natural CRO) perhaps due to adsorption of nanoaggregates to the interface [85]. Some

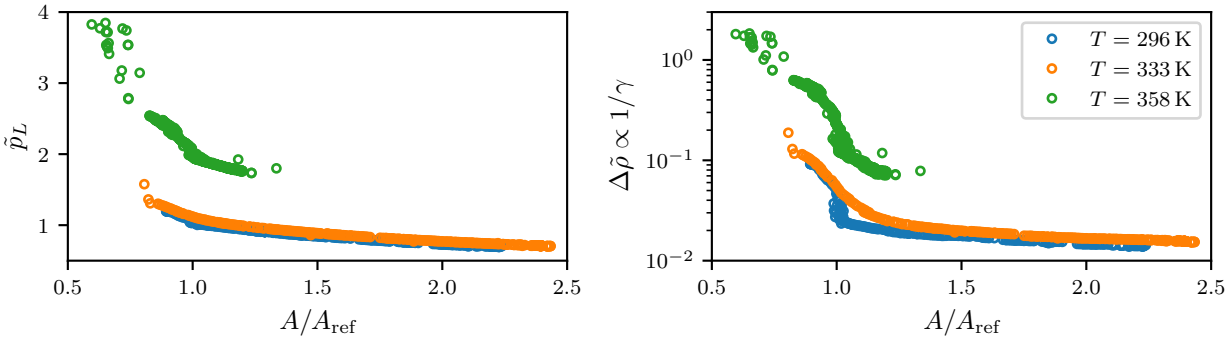

Figure 3.3: The purely liquid shape fits utilizing the Young-Laplace equation (1.8) show non-constant control parameters throughout the entire deformation sequence. The dimensionless pressure $\tilde{p}_L$ (left) is expected to change during the deflation of a liquid droplet, however, the dimensionless density contrast $\Delta\tilde{\rho}$ (right) of a liquid droplet with constant surface tension is not expected to change during a deflation, hinting at an effective fluid viscosity. The non-dimensional control parameter $\Delta\tilde{\rho}$ (right) is the more important one, since we use it to acquire the dimensional surface tension.

authors also propose both an EOS model at lower asphaltene coverage and a solid model at higher coverage [86].

We note that the current research explores the CRO/brine interfacial rheology using techniques such as Gibbs isotherms, which eventually break down as the interface forms a layer which supports anisotropic and inhomogeneous surface stresses[14], [32], [71]. Once the layer has undergone a phase transition to a fully solid interface layer, the surface stresses are no longer compatible with the Young-Laplace equation, and thus fits utilizing it are no longer viable[14], [15], [24], [32], [87]. Previous works have used the onset of Young-Laplace fit errors to describe a potential phase transition, however this method is qualitative [88]. Recently, also the detection of deviations from Laplacian shapes without (computationally intensive) fitting to them has been described [89]. Here, we introduce a new method for quantitative measurements of the elastic compression modulus $K_{2\mathrm{D}}$ and the two dimensional Poisson's ratio $\nu_{2\mathrm{D}}$ of a fully solidified CRO/brine interface. We solve the pendant capsule shape equations of droplets with a true elastic interface using the theoretical description provided in Sec. 1.2 and then fit the resulting shapes to the experimental data.

We find that a phase transition to a truly solid interfaces occurs earlier than discussed in prior work. We determine the exact transition point by comparing the shape fit residuals of a Young-Laplace shape fit compared to a truly elastic shape fit. Furthermore, using this measure, we are able to determine the importance of anisotropic and inhomogeneous surface stress contributions that arise upon sufficient deflation.

The experiments are performed in a rising droplet geometry, with $\Delta\tilde{\rho} > 0$, such that the experiments can be subjected to our numerical machinery described in Chap. 2. The experiment data consists of a series of images taken during the deflation process, as shown in Fig. 3.2 (top).

3.1.1 Fitting the elastic shape equations to the experiment data

We quantify the importance of anisotropic and inhomogeneous surface stresses during the deflation of the drops by comparing the residual fit error of a purely liquid elastic fit with that of a solid elastic theory, including anisotropic and inhomogeneous surface stress contributions. It is important to emphasize that both the purely liquid elastic, as well as the solid elastic interface theories are mere approximations of more complex interfaces – both theories capture entirely different

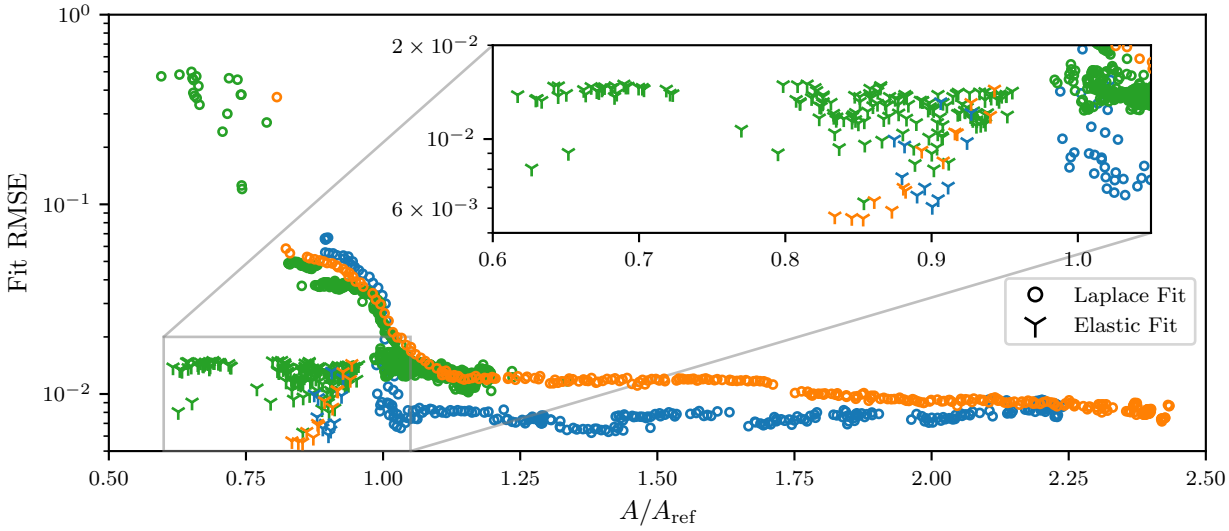

Figure 3.5: We perform two kinds of fits, a purely liquid (Laplace) fit – using Eqn. (1.8) – and an elastic fit, where we use the equations produced in Sec. 1.2. We show the relevant shape fit residual (Fit RMSE) as a function of the relative area compression A/A_{ref}, where A_{ref} is chosen to be the area of the shape after which the shape error for Young-Laplace fits start to drastically increase, as can be seen at $A/A_{\mathrm{ref}} \sim 1$. The secondary increase in fit error (towards errors RMSE $> 10^{-1}$) as seen prominently for the green points at strong area compression $A/A_{\mathrm{ref}} < 0.8$ is of technical nature, since the solution class changes from $\Omega = 2$ to $\Omega = 3$ and our Young-Laplace fit only considers shape class $\Omega = 2$ solutions. The shape error of the elastic fit is detailed in the inset figure and is always lower than the error achieved by a Young-Laplace fit.

physical properties and the experimental system might have characteristics correctly described by either of the theories. Thus, we can only quantify which theory has a smaller residual error to hint at the relative importance of the characteristics contained in each theoretical description.

We start our analysis of the experiment system by fitting the deflation sequences to the purely liquid model using our Young-Laplace fit as described in Sec. 2.1. These fits yield the non-dimensional control parameters of the shape equations, which we show in Fig. 3.3. A first observation is that the dimensionless density contrast $\Delta\tilde{\rho} \equiv \Delta\rho g a^2/\gamma$ is not constant. Since the defining dimensional properties a, g and $\Delta\rho$ are not expected to change during the deflation sequence, the effective dimensional surface tension γ must be the non-constant contribution. In fact, we can calculate the dimensional surface tension γ by inverting the definition of the dimensionless density contrast, as shown in Fig. 3.4. It seems that the slope of the effective surface tension γ as a function of the logarithmic surface area $\log A$ undergoes a significant change at $A/A_{\mathrm{ref}} \sim 1$. This is exactly the reason both Yarranton et al. [77] and Kabbach et al. [78] conclude a change of composition from one fluid surface elasticity $E_{\mathrm{Gibbs}}(A/A_{\mathrm{ref}} > 1) < E^*_{\mathrm{Gibbs}}(A/A_{\mathrm{ref}} < 1)$ towards a stiffer Gibbs modulus E^*_{Gibbs}. However, this is not necessarily the correct conclusion. We compare the shape fit residual error along the entire deflation sequence in Fig. 3.5 (circles) and find a peculiar coincidence of the slope change in Fig. 3.4 at $A/A_{\mathrm{ref}} \sim 1$ and a drastic increase in the shape fit error (RMSE) at $A/A_{\mathrm{ref}} \sim 1$ in Fig. 3.5.

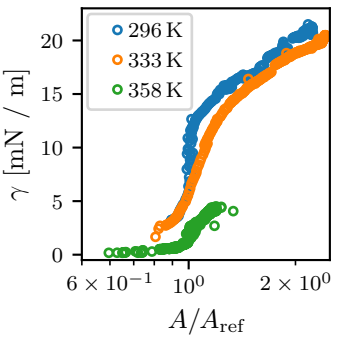

Figure 3.4: The effective surface tension γ, as recovered as the best Young-Laplace fit.

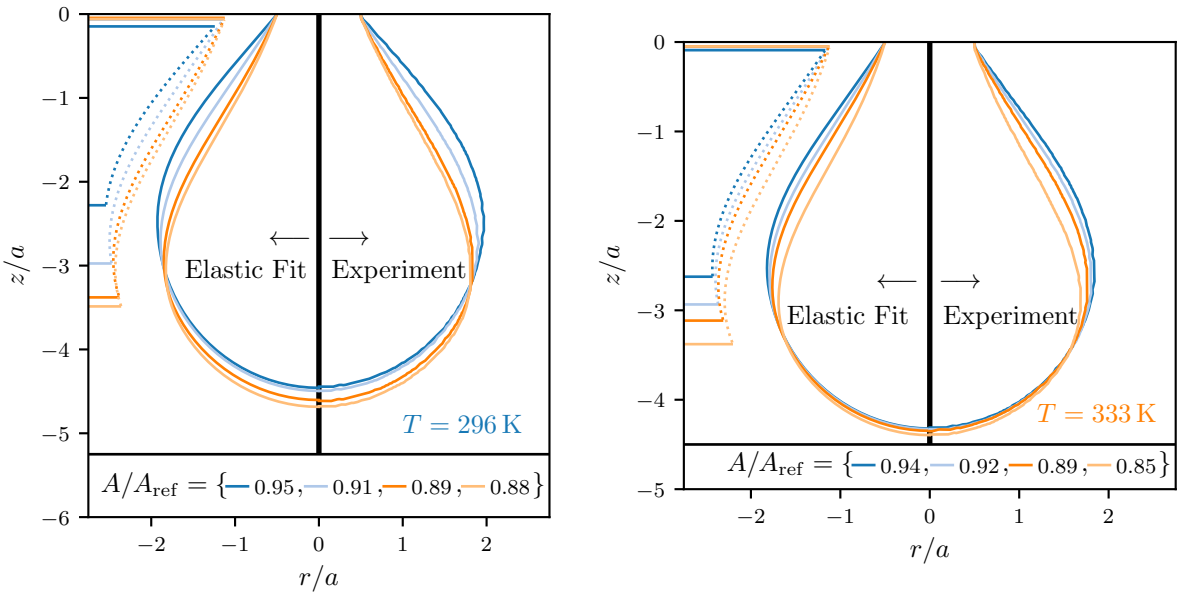

Figure 3.6: We show a visual comparison of the shapes seen in experiments (positive r/a respectively) and the best fitting theory shapes (negative r/a respectively). Additionally, the dotted lines on the left of the theory shapes indicate the effective shape and range of the wrinkled region. Here we only show shapes from the temperatures $T = 296\,\mathrm{K}$ (left) and $T = 333\,\mathrm{K}$ (right). The visual compatibility of theory and experiment shapes is obvious and quantified in Fig. 3.5 for all three experiment temperatures.

The appropriate conclusion thus seems to be that, while the slope of the effective surface tension changes at $A/A_{\mathrm{ref}} \sim 1$, it might not actually be caused by a transition between two fluid elastic phases, but rather by a more fundamental transition to a non-liquid interface morphology. This more fundamental change in constitutive law induces a change in the effective surface tension as the Young-Laplace equation fails to capture the actual shape deformation with enough precision. As soon as the liquid shape fit error starts to increase, the surface stresses become anisotropic and inhomogenous, as we discussed in Sec. 1.2.2 and Ref. [32].

It is evident from Fig. 3.4 that the surface tension of the liquid shapes change even *before* a significant increase in fit error is observed. This is consistent with a fluid elasticity, i.e. a Gibbs elasticity, till the critical deformation is reached. We identify the point at which the liquid shape error starts to rise as the onset of anisotropic and inhomogeneous surface stress contributions, after which the shape of the experimental system might no longer be adequately described by the Young-Laplace equation. The liquid drop shape at this critical deformation can be used as a liquid reference shape for the elastic corrections we apply next, since it is the last shape properly characterized by the Young-Laplace fit and thus by fully homogeneous and isotropic surface stresses.

We achieve significantly better fits with the solid elastic theory, using a reference shape right before the critical deformation, i.e. $A/A_{\mathrm{ref}} \sim 1$. This is evidenced by the significantly decreased fit errors in Fig. 3.5 (as seen in the inset). We also show some of the shape fits created by our solver in Fig. 3.6, where the elastic fit is shown as the left half of the respective plots and the experiment data as the right half of the plots. This grants an intuition of the precision we are able to achieve with our software.

The results of Fig. 3.5 suggests that $A/A_{\mathrm{ref}} = 1$ indeed marks the onset of non-negligible anisotropic and inhomogeneous surface stress contributions, which are taken into account in the solid elastic

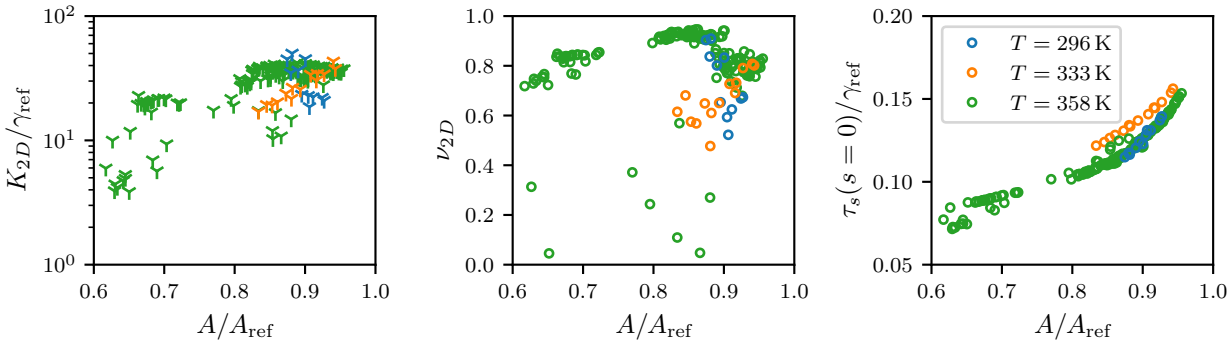

Figure 3.7: The dimensionless elastic control parameters arising from our shape fits are the main result of this section. We note that the reference surface tension γ_{ref} is different for each of the temperature trials, such that the dimensional compression moduli $K_{2\mathrm{D}}/\gamma_{\mathrm{ref}}$ (left) exhibit an additional temperature dependence inherited from the reference surface tension. The dimensional apex stress $\tau_s(s = 0)$ also inherits this additional temperature dependence in addition to the temperature dependence of the dimensionless apex stress (right). All data points depicted in this figure are the result of two independent fits for both hemispheres of the experimental images, weighted by their respective residual error.

theory.

In total we fit the theory to three different experimental shape sequences at three different temperatures $T = \{296\,\mathrm{K}, 333\,\mathrm{K}, 358\,\mathrm{K}\}$ respectively. All values of the elastic control parameters acquired by the fit are shown in Fig. 3.7, here we will only focus on the average values over a respective deformation sequence.

While the experiments fitted with the solid elastic theory show some noise in their respective *dimensionless* compression modulus $K_{2D}/\gamma_{\mathrm{ref}}$ in Fig. 3.7 (left), we see that the dimensionless compression modulus is fairly constant for the three temperatures. The results for the average dimensionless compression moduli are summarized in Tab. 3.1.

For a fully polymeric network interface, we would expect an explicit temperature dependence of $K_{2D} \propto T$, simply because the entropic spring constant scales linearly with temperature, as evident from Eqn. (1.19). A hypothesis for the present results is that the dimensionless compression modulus $K_{2D}/\gamma_{\mathrm{ref}}$ is *not* explicitly dependent on temperature, hinting at a steric interaction as the reason for the large and constant dimensionless compression moduli. This would support the hypothesis that, at a critical area compression $A/A_{\mathrm{ref}} \sim 1$, contact between steric constituents on the interface is established, which counteracts further contraction. Our results in the elastic region are not compatible with the assumption of an entropic temperature scaling with $K_{2D} \propto T$, but it is compatible with a temperature independent dimensionless compression modulus. If we assume the validity of the temperature independent compression modulus hypothesis we can average *all* data points for the dimensionless compression moduli together to get a universal non-dimensional compression modulus $K_{2D}/\gamma_{\mathrm{ref}} = 30.0 \pm 0.7$.

It is important to realize that while the dimensionless compression modulus might show no temperature dependence, the same is not true for the dimensional compression modulus

$$K_{2D} = \frac{K_{2D}}{\gamma_{\mathrm{ref}}}\gamma_{\mathrm{ref}} = \frac{K_{2D}}{\gamma_{\mathrm{ref}}}\frac{\Delta\rho g a^2}{\Delta\tilde{\rho}(A/A_{\mathrm{ref}} = 1)} \tag{3.1}$$

where we have used the definition of the dimensionless density contrast. Thus the dimensional compression modulus is inversely proportional to $\Delta\tilde{\rho}(A/A_{\mathrm{ref}} = 1)$, which is different for each temperature trial, as can be seen in Fig. 3.3.

Temperature	$\langle \mathbf{K_{2D}}/\gamma_{\mathrm{ref}} \rangle$	$\gamma_{\mathrm{ref}}\,(\mathbf{mN/m})$	$\langle \mathbf{K_{2D}} \rangle\,(\mathbf{mN/m})$	$\langle \nu_{2\mathrm{D}} \rangle$
296 K	29 ± 2	7.8	226 ± 16	0.74 ± 0.03
333 K	27 ± 2	6.6	178 ± 13	0.68 ± 0.02
358 K	30 ± 1	2.1	63 ± 2	0.81 ± 0.02

Table 3.1: Results of our elastic capsule fits for drops aged in de-ionised water for half an hour at three temperatures. Here, we show the average non-dimensionalized compression modulus ($K_{2D}/\gamma_{\mathrm{ref}}$), the surface tension of the reference state (γ_{ref}), the average re-dimensionalized compression modulus (K_{2D}), and Poisson's ratio (ν_{2D}).

The surface tension γ_{ref} of the reference shape for the three trials (shown in Tab. 3.1) can be used to re-dimensionalize the dimensionless compression modulus and to give us the dimensional compression moduli (also shown in Tab. 3.1). While the dimensional compression modulus is an order of magnitude larger than the fluid elastic Gibbs modulus, it shows the same qualitative, decreasing trend with temperature. The inconsistency of solid elastic compression modulus measurements with liquid elastic Gibbs elasticities is known in literature [14], [15].

Poisson's ratio seems to not vary drastically with temperature as can be seen in Fig. 3.7 (center). The averaged Poisson's ratios are shown in Tab. 3.1. These resulting data for Poisson's ratio are not compatible with a single constant for the three experiments. If we, regardless of this incompatibility, enforce a constant Poisson's ratio, we arrive at an overall average $\nu_{2D} = 0.79 \pm 0.01$ over all data points. We show the dimensionless apex stresses of the elastic fits in Fig. 3.7 (right) to find that the dimensionless apex stresses behave similar for all three temperatures. We can motivate this finding by remembering that the surface stresses are exclusively controlled via the local stretches $\tau_{s,\phi} = \tau_{s,\phi}(\lambda_s, \lambda_\phi)$, hence at equal area compression, where $\mathrm{d}A = \mathrm{d}A_{\mathrm{ref}}\lambda_s\lambda_\phi$, we expect to find apex stresses similar in magnitude. Thus finding similar dimensionless apex tensions between temperatures is compatible with the claim of temperature independent dimensionless compression moduli, because all temperature dependence is contained in the dimensional $K_{2\mathrm{D}}$.

It is clear from our analysis of CRO droplets that Gibbs isotherm analysis and elastic shape fitting are not equivalent methods for examining the elasticity of those droplets. This highlights the importance of introducing elastic shape fitting for quantitative measurement of the elasticity contributed by solid interfacial layers. These interfaces are extremely complex and, in order to begin to understand their surface structure, we must think critically about the assumptions behind the analysis method we choose to employ. A Gibbs isotherm analysis proves to be useful to identify the characteristic regions, altough mainly as an artifact of a worsened shape residual. It provides accurate fits for $A/A_{\mathrm{ref}} > 1$ and can be used to identify the transition point. In the present analysis, elastic shape fitting reduces the error significantly for $A/A_{\mathrm{ref}} < 1$ suggesting that the CRO interface should be interpreted as solid rather than liquid in this regime. This insight cannot be gained from Gibbs isotherm analysis alone. In addition, the temperature dependence of the measured elastic modulus provides hints about the mechanism of solid interface formation and suggests solidification by steric interactions rather than polymeric network formation. We employ simple elastic constitutive equations; for other complex interfaces more complex constitutive laws might be more appropriate and can be also employed in elastic shape fitting [14].

Although such elastic membranes have been reported in the literature, no quantitative measurements have been made of the solid layer elasticity. Here, we show that quantitative measurements of the surface elasticity in solid regimes are possible using shape-fitting elastometry. Not only does this elastometry allow us to measure the elasticity of the compressed layers, it also gives us clearer insight into where this solid phase transition occurs. This analysis shows that it is likely that the compressed layer becomes solid much earlier in compression than previously assumed.

3.2 Multilayer elasticity and viscoelasticity

Published material – Parts of this sections results are reproduced with modifications and permission from the author's publication [12], © 2024 The Royal Society of Chemistry.

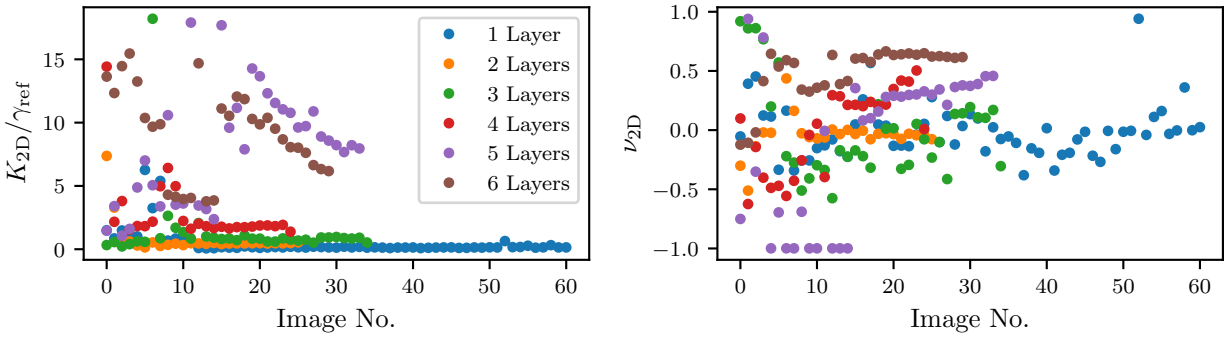

Figure 3.8: The elastic shape fit provides values for the elastic moduli at each point of the deformation sequence (linear volume deflation). Increasing image number corresponds to decreasing volumes. From this data we are able to deduce the dependence of surface elasticity and surface layer count. While the fits all show a low fit error (see Fig. 3.9), we see that the elastic compression modulus seems to rise up until 5 layers are reached (left), thereafter a decrease in compression modulus is observed, hinting at an irreversible change of the skin composition (e.g. a rupture). Already at the fifth layer, the fit gets highly incompatible with a single universal compression modulus for the entire deformation sequence, hinting at a severe restructuring of the interface between the fourth and fifth layer. The Poisson's ratio is noisy (right), but compatible with low values for the initial layers. Upon increase of the layer count, the Poisson's ratio seems to increase as well.

In this section we investigate a system composed of a liquid core and polyelectrolyte multilayers at the interface. This system is interesting due to its relevance to encapsulation applications [90], [91]. We aim to understand the properties of those multilayer system in detail and quantify the viscoelastic response to external stimuli. The polyelectrolyte layers used here (see [12] for details about the experiment) consist of two components, one constructed from NaPSS, and the other from PAH. Interestingly, there is no need for an anchoring layer in this system because NaPSS solidifies at the interface naturally and therefore constitutes sufficient anchoring for successive layers. We employ the shape fitting technique developed in Sec. 2.2 in order to extract the elastic constitutive properties of the multilayer system. First, we want to analyse the shape sequences with our purely elastic constitutive law. We expect this to be appropriate for the first couple of layers, until at some point significant dissipation will become important. We will try to quantify exactly at which count of layers the transition from a quasi-elastic to a fully viscoelastic description becomes relevant. We achieve this by utilizing our viscoelastic theory (see Sec. 1.3) to improve the compatibility of the generated shapes and experiment shapes over the entire deformation sequence.

The results for the elastic shape fit are shown in Fig. 3.8. Because of the intrinsic sensitivity issues at small deformations, the first ~ 10 images can not adequately reflect the elastic constitutive properties, which is why they fluctuate severely. After a sufficient deformation is reached, the shape fit can unleash its power and accurately determine the constitutive properties. We thus average all measured properties starting from the 10th image. Here we find average results contained in Tab. 3.2.

It is evident from Tab. 3.2 that a drastic change in the surface layer morphology takes place between layer four and five, because the compression modulus increases strongly compared to the

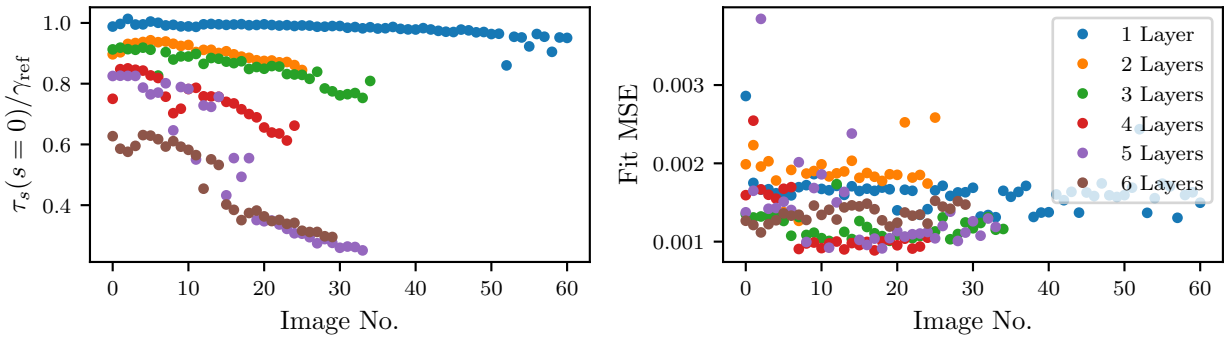

Figure 3.9: During the elastic fit, we need to search for the best matching apex stress $\tau_s(s=0)$. This apex stress should reflect the experimental stimulus of the system. In our case, it is a linear deflation. Additionally, we are able to quantify the fit error by calculating the mean square pixel error between the best fitting theory shape and the experiment shape. All errors encountered during our elastic fit are low at 0.2% average pixel deviation relative to the capillary diameter.

prior gradual evolution. Furthermore, after layer five, the monotonous increase in compression modulus seems to also stop. Rather, adding a sixth layer now *decreases* the compression modulus for the first time. Looking more closely at the evolution of the compression modulus throughout the deformation sequence in Fig. 3.8 (left), we see a qualitative change in the evolution of the compression modulus with deformation appear at layer four and five, indicating an incompatibility of the applied constitutive law appearing here. This further bolsters the theory of a significant change in surface layer morphology. The Poisson's ratio is compatible with a low value around zero for most layers, only for the sixth layer we see a drastic increase in Poisson's ratio. How representative this result is is somewhat elusive for the fifth and sixth layer, as the compression moduli show a strong deformation dependence. Hence, the constitutive model – and all parameters obtained with – might not be adequate for these layers after all. However, the error achieved by the elastic fits stays relatively low at a mean pixel coordinate deviation below 0.2% of the capillary diameter, as seen in Fig. 3.9 (right). Additionally, the apex stress $\tau_s(s=0)$ identified by the elastic fit reflects the experimental stimulus – a linear deflation – well, such that we can confidently state that the fitted constitutive parameters indeed result in precise theoretical reconstructions of the experiment.

Layer Count	1	2	3	4	5	6
$K_{2D}/\gamma_{\mathrm{ref}}$	0.18 ±0.02	0.46 ±0.01	0.88 ±0.06	1.79 ±0.05	9.6 ±0.8	8.4 ±0.7
ν_{2D}	-0.02 ±0.03	-0.04 ±0.01	-0.12 ±0.04	0.21 ±0.05	0.1 ±0.1	0.58 ±0.02

Table 3.2: The average results of the shape sequence fit shown in Fig. 3.8 using a purely elastic constitutive law. The averages are taken starting at the 10th image of the deformation sequence.

We perform another fit, where we exchange one of the fitting parameters to properly quantify a different set of constitutive parameters. Up to now, we only considered K_{2D} and ν_{2D} as the fitting parameter of the elastic constitutive law. However, as discussed in Sec. 1.2 we can use any combination of two compatible parameters to quantify the elastic response of the skin. While these sets of constitutive parameters can always be transformed into another, we do not know whether the fitting method might perform better with one set of parameters or the other [2].

[2]Simply due to the conditioning of the fitting algorithm changing.

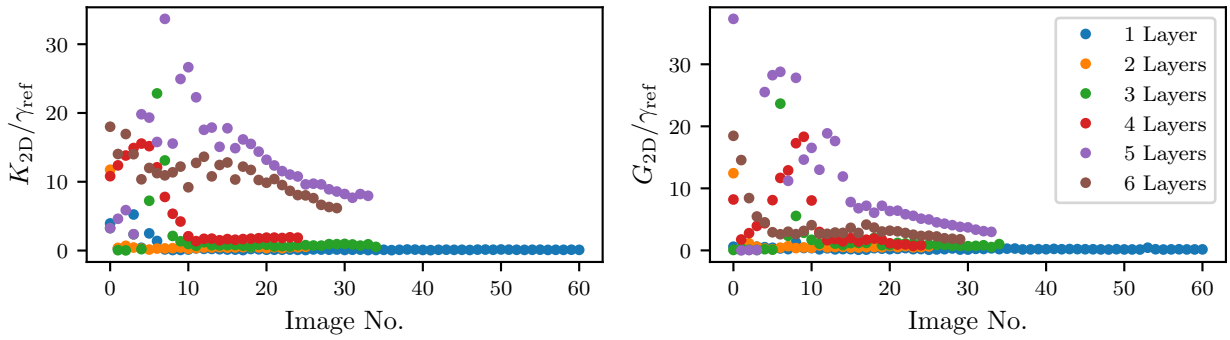

Figure 3.10: We can perform the elastic fit in any combination of compatible elastic parameters. Here we refit the shapes using the compression modulus and the shear modulus to better quantify those parameters. We can see a notable stability improvement in the method compared to Fig. 3.8. The compression modulus (left) still varies greatly in the first ~ 10 images – which we expect – but starts to show a relatively smooth deformation dependence thereafter.

Hence, we perform a new fit in the compression modulus K_{2D}, paired with the shear modulus $G_{2D} = K_{2D}(1-\nu_{2D})/(1+\nu_{2D})$. The results are qualitatively similar as seen in Fig. 3.10. However, it is already visually obvious that the fitted parameters are less noisy, hinting at a better fitting stability with those parameters. This could be caused by the fact that both of these parameters have no upper bound, where Poisson's ratio has a strict upper bound of one, which might hinder the algorithm at properly exploring the parameter landscape. Additionally, the shape equations might be better conditioned with respect to changes in the shear modulus versus Poisson's ratio.

The results obtained for the compression modulus and the shear modulus shown in Fig. 3.10 result in the averaged (from the 10th image) constitutive parameters summarized in Tab. 3.3. The

Layer Count	1	2	3	4	5	6
K_{2D}/γ_{ref}	0.13 ±0.01	0.43 ±0.02	0.78 ±0.03	1.74 ±0.04	13 ±1	9.9 ±0.5
G_{2D}/γ_{ref}	0.21 ±0.01	0.55 ±0.02	1.07 ±0.08	1.95 ±0.44	7 ±1	2.8 ±0.2

Table 3.3: The average results of the shape sequence fit shown in Fig. 3.10 using a purely elastic constitutive law. The averages are taken starting at the 10th image of the deformation sequence.

obtained results for the compression modulus in Tab. 3.3 are compatible with those obtained in Tab. 3.2.

3.2.1 Viscoelastic effects

Next, we allow viscous dissipation and fit an entire sinusoidal shape oscillation sequence to a viscoelastic Kelvin-Voigt model (as discussed in Sec. 1.3). In contrast to methods used in the literature [92], we solve the full time dependent shape equations and fit them to the experimental input. It is important to discuss the potential pitfalls encountered during such a fit. One major problem of the available data is that the resting droplet image is not captured. Thus, the first data point in each shape sequence is captured already *after* the oscillatory stimulus was started. This makes determining the proper, non viscously stressed, shape impossible. However, since the data rate is sufficient, we can still use this image as an approximate reference shape, if we

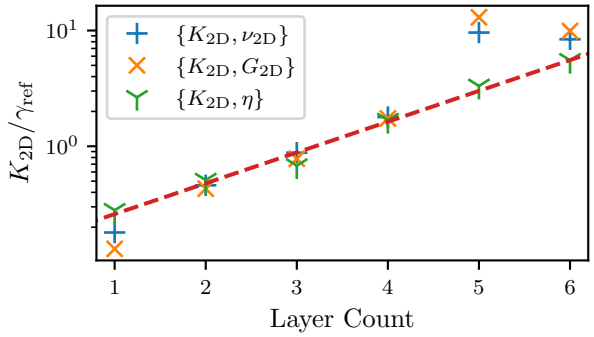

Figure 3.11: We compare the results of several fits performed on the same expermiment system. A purely elastic fit for individual shapes of the sequence in the fitting parameter ensembles $\{K_{2D}, \nu_{2D}\}$ and $\{K_{2D}, G_{2D}\}$ (blue plus and orange cross respectively) gives the indicated averaged results. Additionally, we perform a viscoelastic shape sequence fit for an entire oscillation sequence (green Y). The results coincide for the first few layers but start to drastically diverge for layers five and six. The viscoelastic fit allows us to fit an exponential dependence to the data (red dotted line) with $K_{2D}/\gamma_{ref} \propto 1.85^n$.

assume that the deformation is small during the first frame time. Additionally, the shape data points obtained from the experiment are not equidistantly spaced in time. Rather, the images have (sometimes largely) varying frame-times. This makes the viscoelastic shape fit challenging, because in the numerical implementation, we use a fixed time step. While it would be possible to generate the theory shape sequences at a much finer temporal resolution to match the experiment variations, we avoid doing that for performance reasons. In the end, we fit the shape data assuming a constant time-step and because the actual frame-times are spread symmetrically around an average frame-time, we expect the error we produce by neglecting the precise timing to not be relevant in the long run. This is because the mean-square pixel displacement of the entire shape sequence is minimized during a viscoelastic fit, such that, as long as the error is symmetric, we still achieve a proper result.

In total, each experiment we subject to our analysis contains five sinusoidal cycles. We are able to fit the viscoelastic properties to the entire shape sequence, meaning all five cycles are used in a single fit. This makes the viscoelastic fit use *much* more information than the purely elastic fit and the result is the one that fits the entire data the best, with the constraint that the constitutive parameters are constant throughout the entire deformation sequence. The results obtained from

Layer Count	1	2	3	4	5	6
K_{2D}/γ_{ref}	0.28	0.51	0.68	1.68	3.32	5.53
$\eta\omega/\gamma_{ref}$	0.18	0.25	0.53	0.57	0.86	4.02

Table 3.4: The results of the viscoelastic shape sequence fit using a Kelvin-Voigt model with a dissipation coefficient η and compression modulus K_{2D}. Poisson's ratio is not fitted here, rather it is kept constant at $\nu_{2D} = 0.5$.

the viscoelastic fit, as seen in Tab. 3.4, are qualitatively similar to the results obtained by the purely elastic shape fit in Tab. 3.3. However, the transition between layer four and five is no longer so drastic. Instead, the viscosity of the interface seems to change dramatically between layers five and six. The layer dependence of the compression modulus can be obtained from Fig. 3.11, where it is evident that an exponential dependence is compatible with the results of the viscoelastic shape sequence fits. The data produces a layer dependence for the dimensionless compression modulus as $K_{2D}/\gamma_{ref} \approx (0.14 \pm 0.02) \cdot (1.85 \pm 0.08)^n$, where n is the layer count – for every additional layer n, the compression modulus roughly doubles. Isolating the first three layers, reveals that a linear fit $K_{2D}/\gamma_{ref}(n \leq 3) \approx (0.20 \pm 0.02)n + (0.09 \pm 0.04)$ is compatible with the data as well. However, the exponential fit can be applied even to layers four and five, indicating that the layers may start to grow super-linearly or synergetic effects start to be important.

4 Contact phenomena of complex interfaces

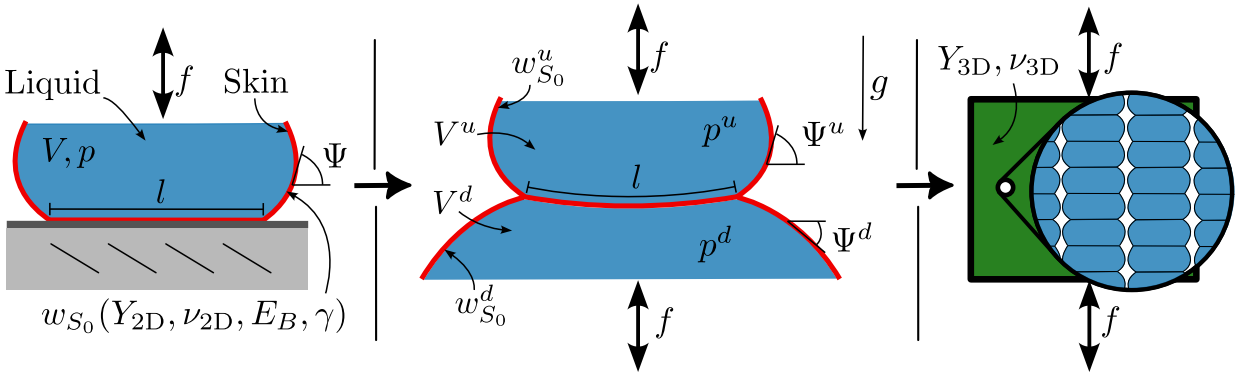

Figure 4.1: We discuss contact phenomena in several geometries. We start from a contact between an elastic capsule and a wall (left). Then, we progress to the contact between two capsules (center). Finally, we discuss the contact of many capsules, which form a three dimensional macrostructure and has bespoke three dimensional elastic moduli (right).

Contact phenomena between soft or elastic bodies are ubiquitous in nature. They are encountered in problems across the scales and include important biological processes, such as cell interactions, as well as medical applications such as drug delivery. An important hallmark in the understanding of contact mechanics is the Hertz-problem, studied and solved by Heinrich Hertz in 1881 [93]. It predicts the contact properties of spherical fully elastic bodies without adhesion or friction. It is still applied in scientific and industrial innovations today and marks the importance of contact problems in general. While the contact between two curved bulk elastic objects is well understood by this theory, the understanding for thin-walled and pressurised elastic objects is still evolving [94]–[96].

The properties of micro-capsules with an elastic interface have received increasing interest in the sciences and in industry, because of their ubiquitous fields of applications. Contacting elastic capsules with certain loads is usually discussed in terms of a point force [97]–[99] or in contact with a rigid wall [96], [100]–[110]. Adhesive membranes, without elasticity, are considered in the literature for various tasks, such as robotic gripping [111] and the membrane-membrane contact properties are frequently discussed [95], [112], [113]. Elastic capsules are theoretically more complex because the elasticity generates a local surface stress depending on deformations relative to a relaxed elastic reference shape. There is very little literature available for the elastic capsule contact problem [94] and the understanding is still evolving.

In this work we want to explore the contact mechanics of two thin walled, pressurised adhesive elastic capsules – with and without bending stiffness – suspended from two opposing capillaries and pressed against each other by an external force, as seen in Fig. 4.1. The theoretical investigation is performed in terms of variational calculus of the appropriate free energy. We differentiate between free-slip and no-slip contact boundary conditions and derive the full set of shape and contact equations independent of the elastic constitutive law. Finally, we integrate the resulting shape equations numerically and analyse the parameter-shape-space and the force-contact-length relationship. As a pre-requisite to the capsule contact problem we investigate the contact between an elastic capsule with and without bending stiffness and a solid wall (see Fig. 4.1 (left)). We also show how the solution of the contact problem could be applied in the material sciences to design elastic capsule meta-materials with peculiar bulk elastic properties, as shown in Fig. 4.1(right).

4.1 Buckling, and why we can ignore it

In the literature there are numerous works which discuss the buckling instability of shells [18], [114]. The common result seemingly is that shells without bending stiffness buckle immediately. We want to discuss why this is *not* generally true and how to instead interpret the results from literature in the limit of vanishing bending stiffness.

The general setup for the discussion of the buckling instability is a shell in some geometry, where we will concentrate on the spherical geometry. The shell has elastic energies proportional to the two dimensional Young's modulus $Y_{2\mathrm{D}}$ and bending stiffness proportional to the bending modulus E_{B}. An isometric compression of the shell will create a cost in stretching energy and bending energy, because the shell is deformed in-plane to reduce the surface area and, additionally, the radius of curvature decreases from the preferred spontaneous curvature. This is an energetic loose-loose scenario (i.e. overall higher total energy). If the bending energy is much smaller than the stretching energy, we arrive at a situation, where the energy can always be decreased from an isometrically compressed solution by creating a mirror inverted cap. This is exactly the result from Pogorelov [114]. In this scenario it is indeed the case that vanishing bending modulus allows the shell to decrease its volume without any energetic cost, simply by creating an appropriately sized mirror inverted dimple. Here we indeed have instantaneous buckling at a volume decrease.

The situation changes, however, once we introduce a constant surface tension contribution, which quantifies the energetic penalty created by the shell being embedded into the surrounding medium. By introducing a constant surface tension we ensure that the shell behaves as the pure liquid enclosed by the skin in contact with the surrounding medium (e.g. water in air) in the limit $Y_{2\mathrm{D}} \to 0$ and $E_{\mathrm{B}} \to 0$, as it should be. Now, however, the energetic situation changes quite fundamentally. An isometric compression of the shell still costs bending and stretching energy. However, the reduction of the interfacial area *reduces* the energetic penalty of embedding the shell into its surrounding medium, simply because the surface area is reduced. This is no longer a situation where it is clear which energetic contribution dictates the shape of the shell. Simplifying the situation and reducing the bending stiffness $E_{\mathrm{B}} \to 0$ we now have a situation, where an isometric compression might actually be favourable from an energetic perspective if the reduction of the surface tension induced interfacial energy $\propto \gamma \Delta A$ outweighs the energetic increase in elastic compressive energy $\propto \Delta \left(\int \mathrm{d}A \, w_{S_0}^{\mathrm{el}} / (\lambda_s \lambda_\phi) \right)$.

Another way to think about this is to realize that in a state without any elastic stresses $\lambda_s = \lambda_\phi = 1$, a constant surface tension contribution yields $\tau_s = \tau_\phi = \gamma$ and thus requires a positive internal pressure p to achieve a force balance. Without surface tension, this pressure is zero in the undeformed state because then also $\tau_s = \tau_\phi = 0$.

We are able to state that, as long as the internal pressure is positive, buckling is generally disallowed. This statement is actually trivial, because the sign of the pressure p quantifies the sign of the slope of the inner energy E (i.e. the surface energy due to stretching, bending and surface tension), with respect to volume changes. This becomes obvious when considering that the pressure p is introduced as a Lagrange multiplier in the Legendre transformation from inner energy E to the volumetrically constrained free energy $F \equiv E - pV$ and thus counters the forces generated by the inner energy in order to drive the shell into the inner energy minimum. Thus, if the pressure p is positive, the inner energy is *reduced* by a reduction in volume and vice versa. Buckling on the other hand is a process, where the system is forced into a configuration which is more unfavourable for the inner energy at decreased volume, which is why the pressure is always negative (or zero) for buckling.

Another way to think about this fact is that a force balance can never be achieved in a mirror-inverted region with positive pressure, because $p = \kappa_s \tau_s + \kappa_\phi \tau_\phi$, where the curvatures are inverted in the mirror-inverted region but the tensions do not change their sign. This is exactly the manifestation of the energetic decrease due to the decreased surface area. As long as the internal pressure is positive, it needs to counteract the net tension along the interface, which acts to further compress the shell. Hence, only at the point where $p = 0$ and as such $\tau_s = \tau_\phi = 0$, the energetic penalty from the elastic compressive energy becomes larger than the energetic benefit due to the surface area reduction. Exactly at this point mirror-inversion buckling is again the energetically favourable solution at a further decrease in volume V.

Additionally, because increasing bending stiffness *delays* the buckling transition (to increasingly negative internal pressures), we can be sure that as long as the internal pressure p is positive, we can not have a buckling transition.

4.2 Contact of a capsule with a solid wall

We want to start our investigation by considering the contact of an elastic capsule and a solid wall of arbitrary (smooth) shape, which is visualized in Fig. 4.2. The scenario is similar to that in an emulsion, investigated by Morse and Witten in Ref. [115], only that we want to derive the exact shape equations for the contact with a wall. The capsule shall have a surface energy per undeformed unit area w_{S_0} and vanishing bending stiffness $E_B = 0$. In a later chapter, we will generalize the derivation to non-zero bending stiffness. Note that $E_B = 0$ is not an exotic case of the problem. When performing the limiting process $E_B \to 0$, the solution will smoothly approach the one for $E_B = 0$. We can understand this fact by considering that the bending stiffness imposes a length scale $R_{\min}$ of smallest radius of curvature allowed. Conversely, if this length scale is small with respect to the characteristic length scale of the problem, i.e. $R_{\min} \ll a$, we encounter a scenario, where the corrections due to the bending energy only have an effective correlation length-scale given by $R_{\min}$ and are thus negligible for the macroscopic solution on the length scale a (which we are interested in). Thus, the limiting process $E_B \to 0$ continuously converges to the case $E_B = 0$ on the macro-scale.

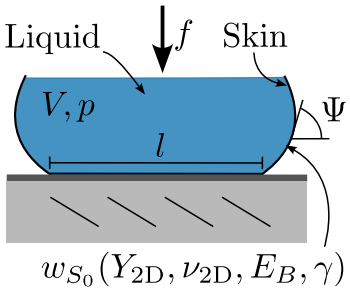

Figure 4.2: A fluid filled, pressurized elastic capsule is pressed against a solid wall with force f and contacts it over a length l.

The capsule shall be in contact with the wall over a total parametric length l and then detach from the wall. The capsule shall be pressed against the wall with a force f. The modifications to the constitutive law of the capsule due to the contact with the wall, e.g. a change in surface tension, are kept as a parameter in the following derivation and can be chosen arbitrarily. The surface energy density in the contact region is marked with an additional superscript to indicate this fact.

The energy functional of the system at hand has two distinct regions, the contact region and the region where the shape is free. Between those regions, discontinuous changes in the Lagrange function can appear. Thus, the energy functional has to be treated as a *broken functional*. We discuss the variational calculus of broken functionals in the Appendix A.1.3 and can simply use the derived formalism here. The broken functional can be written in terms of the undeformed arc

length coordinate s_0, simply by collecting all energetic contributions [1]

$$\begin{aligned} F =& \pi \int_0^{l_0} \mathrm{d}s_0 \underbrace{\left\{ 2r_0 w_{S_0}^c - \left(pr^2 - \frac{f}{\pi} \right) \lambda_s \sin \Psi \right\}}_{\mathcal{L}^c + 2r_0 \lambda_s \lambda_\phi \Delta\gamma_{\mathrm{wall}}} - \pi \int_0^{l_0} \mathrm{d}s_0 2r_0 \lambda_s \lambda_\phi \Delta\gamma_{\mathrm{wall}} \\ &+ \pi \int_{l_0}^{L_0} \mathrm{d}s_0 \underbrace{\left\{ 2r_0 w_{S_0} - \left(pr^2 - \frac{f}{\pi} \right) \lambda_s \sin \Psi \right\}}_{\mathcal{L}^f} . \end{aligned} \tag{4.1}$$

The term $\propto \Delta\gamma_{\mathrm{wall}}$ in Eqn. (4.1) is the surface energy change of the wall due to it being in contact with the interface material versus the surrounding medium. This is the same term encountered in the discussion for capsules absorbed to liquid-liquid interfaces in Ref. [26]. Note that the contribution $\propto \lambda_s \sin \Psi$ is always zero in the contact region if the wall is flat, because then $\sin \Psi \equiv 0$ in the entire contact region. Additionally, the variation of the pressure term $\propto p$ only produces pre-factors to the variation normal to the interface $\propto \delta n$, which is always zero in the contact region to ensure that the variations do not violate the premise of a contact with the wall, such that even in the more general case of a non-flat wall, the pressure term always vanishes from the variation in the contact region – as it should be.

The shape equations in the non-contacting region are equivalent to those found in [14], [15], [26] and those produced in Sec. 1.2. Alternatively and equivalently, we could apply the Euler-Lagrange formalism for broken functionals introduced in the Appendix A.1.3 in the free region to the functions $r, r' \equiv \mathrm{d}r/\mathrm{d}s_0, z$ and $z' \equiv \mathrm{d}z/\mathrm{d}s_0$ to find

$$\frac{\mathrm{d}}{\mathrm{d}s_0} \frac{\partial \mathcal{L}^f}{\partial z'} = \frac{\mathrm{d}}{\mathrm{d}s_0} \left(2r\tau_s \sin \Psi - pr^2 + \frac{f}{\pi} \right) = \frac{\partial \mathcal{L}^f}{\partial z} = z' r^2 \Delta\rho g \,, \tag{4.2}$$

$$\frac{\mathrm{d}}{\mathrm{d}s_0} \frac{\partial \mathcal{L}^f}{\partial r'} = \frac{\mathrm{d}}{\mathrm{d}s_0} \left(2r\tau_s \cos \Psi \right) = \frac{\partial \mathcal{L}^f}{\partial r} = 2\lambda_s \tau_\phi + 2prz' \,. \tag{4.3}$$

The two equations Eqn. (4.3) and Eqn. (4.2) reduce to the shape equations recovered by variations in normal and tangential directions δn and δt given as Eqn. (1.14) and Eqn. (1.15) respectively, however, we can attain some additional information about the system. If we have no gravitational effects, i.e. $\Delta\rho g = 0$ and consequently $p(z) = p = \text{const.}$, the problem becomes translationally invariant in the z-coordinate. As stated in the Noether theorem (see Appendix A.1.4 for more detail), such symmetry entails an associated conserved quantity, simply because variations along this symmetry do not change the energy. The conserved quantity associated with this translation invariance is the quantity $\partial \mathcal{L}^f / \partial z'$. Even with gravity we are able to integrate the Euler-Lagrange equation (4.2) and write

$$f = \pi r^2 p - 2\pi r \tau_s \sin \Psi + \pi \Delta\rho g \int \mathrm{d}z r^2 \,, \tag{4.4}$$

where we identify the last term as the gravitational force due to the self weight of the shape below height z. As such Eqn. (4.4) is exactly the force balance in z-direction and the force required to press the capsule against the wall is given as f and conserved along the entire non-contacting solution region in the case of $\Delta\rho g = 0$. Without external force $f = 0$, this is exactly the generalization of the force balance Eqn. (1.10) as found for liquid droplets and a special case of the viscoelastic capsule force balance in the limit of quasi-static deformations (see Eqn. (1.29)).

The solution for the contacting region is a bit more involved, since the wall sets some constraints for the variations. Here it is no longer possible to freely vary the radial and height coordinates r

[1] Surface energy density w_{S_0}, pressure difference p, external force f and the wall surface energy.

and z. We are able to intuitively understand this fact by realizing that a shape variation in normal direction δn, applied to a surface patch in the contact region, will always create a contradictory shape. Either, the surface patch penetrates the wall after applying the normal variation, or it detaches from the wall, violating the assumption of a contact.

Furthermore, we must take into account the contact coupling between the wall and the material of the capsule. Consider the two simple special cases:

- (slip) The capsule skin can slide frictionless over the surface of the wall.
- (no-slip) The capsule can not slide over the surface of the wall at all.

We will refer to those two conditions as slip and no-slip boundary coupling conditions. In the no-slip case, the capsule can not slide along the wall at any point in time, such that the shape is effectively "glued" to the wall once it comes into contact. This makes the no-slip contact entirely contact history dependent, since it fully determines which undeformed coordinate s_0 of the capsule is in contact with a certain point on the wall, completely dictating the deformation in the contact region. In this case, no evolution equation for the shape is generated by the variations in the contact region, because no variation is allowed, i.e. $\delta r = \delta z = 0$, as also discussed in Ref. [116].

The slip contact coupling is easier to work with, as it makes the current shape entirely independent of the contact history. In this case, it is imperative to limit the variations in the contacting region to those that are tangential to the wall, as normal variations relative to the wall would either violate the premise of a contact, or lead to an unphysical penetration of the wall.

Hence, we perform the variation of the free energy Eqn. (4.1) in terms of normal δn and tangential variations δt and set the normal variation in the contact region to zero $\delta n = 0$. In the contact region we need to take into account the additional contribution generated by the surface energy change of the wall.

Importantly, the variation of the external force term does not contribute to the shape equations in the respective domains, since $f\delta \int_a^b \mathrm{d}s \sin\Psi = f[\delta z]_a^b$ [2]. The only equation we acquire in the contact region is thus

$$\frac{\mathrm{d}\tau_s}{\mathrm{d}s} = \frac{\cos\Psi}{r}(\tau_\phi - \tau_s) \text{ , for } s \in [0, l) \text{ (slip)}, \tag{4.5}$$

where the geometry of the shape is purely controlled by the wall geometry. As such, it is sensible that we do not get an equation for the evolution of the arc angle in this region anymore.

4.2.1 The contact point (Weierstrass-Erdmann conditions)

We acquire some additional equations at the contact point. Those equations are exactly the manifestations of the additional terms appearing at the discontinuous transition between the contacting and the non-contacting region. They are produced by the partial integrations of the terms $\propto \delta r'$ and $\propto \delta z'$ or $\propto \delta n'$ and $\propto \delta t'$ during the variation of the free energy respectively. When the variation is performed explicitly, those terms need to be carefully collected. A visual schematic of this is provided as Fig. 4.3, where the left-sided and right-sided variations at the contact point are visualized. Here, however, we can use the Weierstrass-Erdmann formalism (as detailed in the Appendix A.1.3) to attain the first Weierstrass-Erdmann condition

$$0 = \frac{\partial \mathcal{L}^c}{\partial z'}(l_{0,-})\delta z(l_{0,-}) - \frac{\partial \mathcal{L}^f}{\partial z'}(l_{0,+})\delta z(l_{0,+}) + \frac{\partial \mathcal{L}^c}{\partial r'}(l_{0,-})\delta r(l_{0,-}) - \frac{\partial \mathcal{L}^f}{\partial r'}(l_{0,+})\delta r(l_{0,+})\,, \tag{4.6}$$

[2] While the force makes an appearance in Eqn. (4.2), it is immediately eliminated by the derivative, as it is a constant factor.

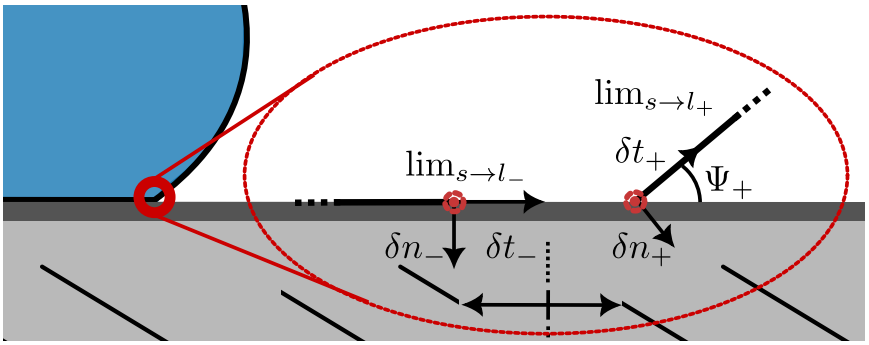

Figure 4.3: Schematic of the variation at the contact point. The functional is broken at the contact point, hence the variation at the contact point needs to account for the left-sided limit $\lim_{s\to l_-}$ and the right-sided limit $\lim_{s\to l_+}$ respectively, as the variations no longer need to be continuous at this specific point.

where we have to make sure that the variations do not violate properties of our solution. In this case the properties we must protect are continuity of the shape, i.e. $\delta r(l_{0,-}) = \delta r(l_{0,+})$ and $\delta z(l_{0,-}) = \delta z(l_{0,+})$, and contact with the wall. We can assure contact with the wall by again expressing the variations in terms of the normal and tangential variations, such that

$$\delta r_- = \sin\Psi_-\delta n_- + \cos\Psi_-\delta t_- \tag{4.7}$$
$$\delta z_- = -\cos\Psi_-\delta n_- + \sin\Psi_-\delta t_-\,, \tag{4.8}$$

where we set the normal variations left of the contact point δn_- to zero, such that the contact point may only slide along the wall. The first Weierstrass-Erdmann condition then reduces to

$$\cos\left(\Psi(l_+) - \Psi(l_-)\right) = \frac{\tau_s(l_-) - \Delta\gamma_{\text{wall}}}{\tau_s(l_+)}\,, \tag{4.9}$$

which produces an expression for the contact angle of the capsule with the wall as a function of the change in internal stresses across the contact point.

For a liquid interface, this would be the change in surface tension, i.e. the surface stress in the contact region would be the surface tension between capsule and wall $\tau_{s,-} = \gamma_{cw}$, while the surface stress in the non-contacting region would be the surface tension between the capsule and the surrounding ambient medium $\tau_{s,+} = \gamma_{ca}$, finally the difference in wall surface tension is given as the tension between the wall and the ambient medium $\Delta\gamma_{\text{wall}} = \gamma_{wa}$, such that the relationship for the contact arc angle $\Psi(l_+) - \Psi(l_-)$ reduces to the well known Young-Equation as first discussed by Thomas Young already in his 1805 work "cohesion of fluids", and appearing in many fields of study [117]:

$$\cos(\Psi(l_+) - \Psi(l_-)) = \frac{\gamma_{cw} - \gamma_{wa}}{\gamma_{ca}}\,. \tag{4.10}$$

From the formalism discussed in the Appendix A.1.3, we encour a second equation due to the variation of the contact point itself. Since the position of the contact point along the wall is not fixed, we incur a transversality condition, referred to as the second Weierstrass-Erdmann corner condition in the formalism we use and it is given as

$$0 = \mathcal{L}^c(l_-) - \mathcal{L}^f(l_+) - z'(l_-)\frac{\partial\mathcal{L}^c}{\partial z'}(l_-) + z'(l_+)\frac{\partial\mathcal{L}^f}{\partial z'}(l_+) - r'(l_-)\frac{\partial\mathcal{L}^c}{\partial r'}(l_-) + r'(l_+)\frac{\partial\mathcal{L}^f}{\partial r'}(l_+)\,, \tag{4.11}$$

and produces the equation

$$w^c_{S_0}(l_-) - w_{S_0}(l_+) = \lambda_s(l_-)\lambda_\phi(l)\tau_s(l_-) - \lambda_s(l_+)\lambda_\phi(l)\tau_s(l_+) \tag{4.12}$$

from which the meridional stretch ratio $\lambda_s(l_+)$ (or equivalently the meridional stress $\tau_s(l_+)$) is determined. As long as the constitutive change is constrained to stresses independent of the stretches, e.g. a change in surface tension, this equation forces continuity of the stretch ratio $\lambda_s(l_+) = \lambda_s(l_-)$ across the contact point. If the contact changes e.g. the elastic moduli, then Eqn. (4.12) must be solved for $\lambda_s(l_+)$. Here, we will only discuss changes in the constant stresses, e.g. adhesive terms, such that we always have continuity in the stretch ratio λ_s. Note that the transversality condition Eqn. (4.12) is equivalent to that found for a capsule at a liquid-liquid interface in Ref. [26].

More strictly speaking, all constant stress contributions $\tau^\gamma_{s,\phi} = \text{const.}$ constitute a surface energy density per undeformed unit area proportional to the area stretch ratio $w^\gamma_{S_0} \propto \lambda_s\lambda_\phi$, however, the r.h.s of Eqn. (4.12) exactly scales the stresses by the area stretch ratio, such that the constant stress contributions $\tau^\gamma_{s,\phi} = \text{const.}$ and $w^\gamma_{S_0} = \text{const.}\lambda_s\lambda_\phi$ cancel from Eqn. (4.12). This leads to an equation where the difference of the remaining surface energy density must vanish, i.e. $w_{S_0}(l_-) - w^\gamma_{S_0}(l_-) = w_{S_0}(l_+) - w^\gamma_{S_0}(l_+)$. The resulting residual surface energy density function is purely dependent on the meridional and circumferential stretch ratios and the constitutive parameters of the problem (e.g. Young's modulus and Poisson's ratio). Keeping the constitutive parameters continuous only leaves λ_s as a potentially non-continuous parameter (since $\lambda_\phi = r/r_0$ is always continuous), such that Eqn. (4.12) dictates continuity in λ_s for all constitutive laws that satisfies the construction premise (i.e. a function exclusively of λ_s and λ_ϕ).

4.2.2 Bending energy effects

In the previous section we neglected the influence of bending stiffness. If the interface additionally resists out-of-plane deformations we need to include this degree of freedom as additional variables in our surface energy density, as discussed for a pendant shell in the Appendix A.2.1. If bending effects play a role, the interface will punish small radii of curvature with a large energy penalty. In essence, the bending energy will act to *smooth* sharp corners. The influence on the solution shape by the bending energy is thus greatest in regions of large curvature [3]. Bending stiffness has a profound effect in red blood cells [118] and is thus interesting to include. Without any bending stiffness we find a kink in the solution shape at the contact point, manifesting as $\Psi(l_+) \neq \Psi(l_-)$. This is not possible with the addition of bending energies, as a kink in the shape costs infinite energy. Thus, the shape *must* transition smoothly at the contact point with $\Psi(l_+) = \Psi(l_-)$, however, the same will not be true for other functions of the problem, such that we still have to treat this problem as a broken functional.

Since we still keep the adhesion at the wall, we are confronted with a competition of energies at the contact point: while the change in surface tension energy would like to produce a sharp corner at the contact point, the bending energy can not allow this, we thus expect to see this competition manifest in the equations generated at the contact point.

The energy functional we want to subject to extremization changes only in the surface energy density w_{S_0}, since we account for the additional bending energy there. The bending energy contributions are dependent on the bending strains $K_s = \Psi' - \Psi'_0$ and $K_\phi = (\sin\Psi - \sin\Psi_0)/r_0$ as detailed in the Appendix A.2.1.

[3] Inverse radius of curvature.

We want to neglect gravity for the discussion of the bending-stiff-capsule-wall contact for simplicity, such that we are able to express the entire energy functional as a function of r, r', Ψ and Ψ', when using $\lambda_s = r'/\cos\Psi$ and $z' = r'\tan\Psi$:

$$\begin{aligned} F =& \pi \int_0^{l_0} \mathrm{d}s_0 \underbrace{\left\{ 2r_0(w^c_{S_0} - \lambda_s \lambda_\phi \Delta\gamma_{\text{wall}}) - \left(pr^2 - \frac{f}{\pi}\right) r' \tan\Psi \right\}}_{\mathcal{L}^c} \\ &+ \pi \int_{l_0}^{L_0} \mathrm{d}s_0 \underbrace{\left\{ 2r_0 w_{S_0} - \left(pr^2 - \frac{f}{\pi}\right) r' \tan\Psi \right\}}_{\mathcal{L}^f} . \end{aligned} \tag{4.13}$$

Following the formalism introduced in the Appendix A.1.3, the Euler-Lagrange equations in the free region are given by

$$\frac{\mathrm{d}}{\mathrm{d}s_0}\frac{\partial \mathcal{L}^f}{\partial r'} = \frac{\mathrm{d}}{\mathrm{d}s_0}\left(2r\frac{\tau_s}{\cos\Psi} - \left(pr^2 - \frac{f}{\pi}\right)\tan\Psi\right) = \frac{\partial \mathcal{L}^f}{\partial r} = 2\lambda_s\tau_\phi - 2pr\lambda_s\sin\Psi \tag{4.14}$$

$$\frac{\mathrm{d}}{\mathrm{d}s_0}\frac{\partial \mathcal{L}^f}{\partial \Psi'} = \frac{\mathrm{d}}{\mathrm{d}s_0}(2rm_s) = \frac{\partial \mathcal{L}^f}{\partial \Psi} = \lambda_s\left(2r\left(\tau_s\tan\Psi - m_\phi\frac{\cos\Psi}{r}\right) - \left(pr^2 - \frac{f}{\pi}\right)\frac{1}{\cos\Psi}\right) , \tag{4.15}$$

where it is important to note that the force f now appears in all equations, as it acts against the bending resistance of the shell. Contrary, without bending stiffness we only had *in-plane* force balances, where the external force did not appear at all. The two equations Eqn. (4.14) and Eqn. (4.15) are thus not entirely equivalent to the force-free equations found as Eqn. (A.26) and Eqn. (A.27), or in the literature [15]. Rather the modified shape equations for the force loaded free region are given as:

$$\frac{m_s'}{\lambda_s} = \frac{\cos\Psi}{r}(m_\phi - m_s) + \tau_s\tan\Psi - \left(\frac{pr}{2} - \frac{f}{2\pi r}\right)\frac{1}{\cos\Psi} . \tag{4.16}$$

$$\frac{\tau_s'}{\lambda_s} = \frac{\cos\Psi}{r}(\tau_\phi - \tau_s) + \kappa_s\left(\left(\frac{pr}{2} - \frac{f}{2\pi r}\right)\frac{1}{\cos\Psi} - \tau_s\tan\Psi\right) . \tag{4.17}$$

The equations Eqn. (4.16) and Eqn. (4.17) can be used along with the trivial geometric shape equations to solve for the entire non-contacting region.

The transverse shear stress

A common quantity arises in both Euler-Lagrange equations (4.16) and (4.17), which we can identify as

$$q \equiv \frac{\cos\Psi}{r}(m_\phi - m_s) - \frac{m_s'}{\lambda_s} . \tag{4.18}$$

This is the same common factor that appears when performing the normal and tangential variations of the bending energy of the free shell, as detailed in the Appendix A.2.1. The interpretation of q is revealed when considering the force balance in z-direction, where q has the role of a transverse shear stress [18], i.e. it captures an out-of-plane stress resultant acting normal to the surface. In the non-contacting region the resulting transverse shear stress can be read off of Eqn. (4.16) and is given as

$$q = -\tau_s\tan\Psi + \left(\frac{pr}{2} - \frac{f}{2\pi r}\right)\frac{1}{\cos\Psi} , \tag{4.19}$$

where the external force f appears additionally to the algebraic relation for q found for free shells in Ref. [18]. If the bending modulus vanishes $E_B \equiv 0$, so do the bending moments $m_\phi \propto E_B$,

$m_s \propto E_B$ and its derivatives $m_s' \propto E_B$, such that Eqn. (4.18) demands $q = 0$, which results the force balance in z-direction for a capsule without bending stiffness Eqn. (4.4) from Eqn. (4.19).

Note that the solution of the shape equations does not require knowledge about the interpretation of Eqn. (4.18) and Eqn. (4.19) at all, it merely acts to help to understand the resulting equations on a more intuitive level.

Contacting region

In the contacting region, the variations need to again be restricted to only include variations tangential to the wall. From the calculation in Sec. 1.2 in combination with the bending terms from the Appendix A.2.1 we are thus able to conclude that in the contacting region we only get Eqn. (4.14) and lack an explicit equation for the evolution of the bending moment, i.e. we are missing Eqn. (4.16). This can again be easily understood, since the wall now dictates the curvatures κ_s and κ_ϕ, and as such it also dictates the bending strains K_s and K_ϕ as well as the bending moments m_s and m_ϕ and their respective derivatives m_s' and m_ϕ' along the contact contour. The information dictated by the wall are thus enough to determine the bending moments m_s and m_ϕ along with their derivatives m_s' from its definition and no further evolution equation is required for it. For a flat wall, we have $\mathrm{d}^n\Psi/\mathrm{d}s_0^n = 0$ and thus the bending strains in the contact region are given by $K_s = -\kappa_{s,0} = \text{const.}$ and $K_\phi = -\kappa_{\phi,0} = \text{const.}$ [4], such that the transverse shear stress in the contact region may be calculated as:

$$q = \frac{\cos\Psi}{r}(m_\phi - m_s) - \frac{\mathrm{d}m_s}{\mathrm{d}s} = \frac{\cos\Psi}{r}\left(m_\phi - m_s\frac{\lambda_\phi}{\lambda_s}\frac{\cos\Psi_0}{\cos\Psi}\right). \tag{4.20}$$

To calculate Eqn. (4.20), we used the defining equation for the meridional bending moments $m_s \equiv \frac{1}{\lambda_\phi}\partial w_{S_0}/\partial K_s$, where the later part $g(K_s, K_\phi) \equiv \partial w_{S_0}/\partial K_s$ is a function purely of K_s and K_ϕ, which are constant along the entire contact region if the reference shape is spherical, such that

$$\frac{m_s'}{\lambda_s} = \frac{\mathrm{d}m_s}{\mathrm{d}s} = \frac{\mathrm{d}}{\mathrm{d}s}\frac{g(K_s,K_\phi)}{\lambda_\phi} = -\frac{m_s}{\lambda_\phi}\frac{\mathrm{d}\lambda_\phi}{\mathrm{d}s} = -\frac{m_s}{r}\left(\cos\Psi - \frac{\lambda_\phi}{\lambda_s}\cos\Psi_0\right). \tag{4.21}$$

Note that Eqn. (4.20) differs from the transverse shear stress found by Ref. [100] (who find that it is always zero), because they did not account for the geometric non-linearities in the definition of the bending moments, i.e. they are missing the non-linear factors $1/\lambda_{s,\phi}$ in $m_{\phi,s}$ respectively. Additionally, the equation produced here holds for arbitrary constitutive laws complying with our construction premises. We can calculate the value of q at the center of the contact region at $r = 0$ with the rule of l'Hôspital and symmetry considerations. At $s = 0$ we have isotropy, such that $m_s = m_\phi$ and $\lambda_s = \lambda_\phi$, finally $(\cos\Psi - \cos\Psi_0)/r \to 0$ as $s \to 0$, such that $q(0) = 0$. The transverse shear stress must vanish at $s = 0$ due to symmetry already [18], such that this finding is not surprising.

Finally, the only non-geometric shape equation found in the contacting region is given as

$$\frac{\tau_s'}{\lambda_s} = \frac{\cos\Psi}{r}\left(\tau_\phi - \tau_s\right) + \kappa_s q\,, \tag{4.22}$$

where the term $\kappa_s q$ will not appear for a flat wall, simply because $\kappa_s \equiv 0$ in the contact region if the wall is flat. Conversely, for a flat wall, this is the same evolution equation found for the meridional stress of a capsule without any bending stiffness. The evolution of the meridional stress

[4] For a spherical reference geometry.

is thus not influenced by the addition of bending stiffness and, with equal initial conditions, will give the exact same contact region behaviour.

Together with Eqn. (4.22) we are now able to solve the entire contacting region of the problem. We are still not able to traverse the contact point with our solution. The additional equations required for this are, again, the Weierstrass-Erdmann conditions.

Weierstrass-Erdmann corner conditions

The equations required at the contact point – the Weierstrass-Erdmann conditions – are again determined from the formalism introduced in the Appendix A.1.3. The first Weierstrass-Erdmann condition in this case is given by

$$0 = \frac{\partial \mathcal{L}^c}{\partial r'}(l_{0,-})\delta r(l_{0,-}) - \frac{\partial \mathcal{L}^f}{\partial r'}(l_{0,+})\delta r(l_{0,+}) + \frac{\partial \mathcal{L}^c}{\partial \Psi'}(l_{0,-})\delta \Psi(l_{0,-}) - \frac{\partial \mathcal{L}^f}{\partial \Psi'}(l_{0,+})\delta \Psi(l_{0,+})\,, \tag{4.23}$$

where we enforce geometric continuity and contact with the wall by expressing the variations $\delta r(l_{0,-}) \equiv \delta r_- = r(l_{0,+}) \equiv \delta r_+$ and $\delta \Psi(l_{0,-}) \equiv \delta \Psi_- = \delta \Psi(l_{0,+}) \equiv \delta \Psi_+$ by their respective normal and tangential contributions. We find

$$\delta r_- = \sin \Psi_- \delta n_- + \cos \Psi_- \delta t_- \tag{4.24}$$

$$\delta \Psi_- = \kappa_{s,-} \delta t_- - \frac{1}{\lambda_{s,-}} \delta n'_-\,, \tag{4.25}$$

where we set $\delta n_- = \delta n'_- = 0$ and recover the first Weierstrass-Erdmann condition

$$m_{s,-}\kappa_{s,-} - m_{s,+}\kappa_{s,+} = \tau_{s,+} - (\tau_{s,-} - \Delta\gamma_{\text{wall}})\,, \tag{4.26}$$

which is exactly the in-plane force balance between the meridional stresses and bending moments. For a flat wall the curvature in the contact region $\kappa_{s,-}$ vanishes, such that $m_{s,+}\kappa_{s,+} = \tau_{s,-} - \Delta\gamma_{\text{wall}} - \tau_{s,+}$.

Forcing δn_- to be zero makes the wall act as a bearing that supports external forces acting upon it, the same is true for $\delta n'_-$, which allows the wall to counter bending moments.

The second Weierstrass-Erdmann corner condition is given as

$$0 = \mathcal{L}^c(l_-) - \mathcal{L}^f(l_+) - r'(l_-)\frac{\partial \mathcal{L}^c}{\partial r'}(l_-) + r'(l_+)\frac{\partial \mathcal{L}^f}{\partial r'}(l_+) - \Psi'(l_-)\frac{\partial \mathcal{L}^c}{\partial \Psi'}(l_-) + \Psi'(l_+)\frac{\partial \mathcal{L}^f}{\partial \Psi'}(l_+)\,, \tag{4.27}$$

and produces the equation

$$\begin{aligned} w_{S_0,-} - w_{S_0,+} &= \lambda_\phi \lambda_{s,-} m_{s,-}\kappa_{s,-} - \lambda_\phi \lambda_{s,+} m_{s,+}\kappa_{s,+} + \lambda_\phi \lambda_{s,-}\tau_{s,-} - \lambda_\phi \lambda_{s,+}\tau_{s,+} \\ &= \lambda_\phi (m_{s,-}\kappa_{s,-} + \tau_{s,-})(\lambda_{s,-} - \lambda_{s,+}) + \Delta\gamma_{\text{wall}}\lambda_\phi \lambda_{s,+}\,. \end{aligned} \tag{4.28}$$

The equations Eqn. (4.26) and Eqn. (4.28) determine the meridional curvature after the contact point $\kappa_{s,+}$ and the meridional stretch ratio after the contact point $\lambda_{s,+}$ [5]. Solving these equations for the relevant quantities is not straight forward, since the constitutive law might contain several non-linear relationships between all the involved quantities. An important distinction between the

[5] Or equivalently the meridional stress $\tau_{s,+}$ and bending moment $m_{s,+}$.

contact with bending stiffness and the one without must be made: while the second Weierstrass-Erdmann condition for the purely elastic capsule imposes continuity in the stresses if the changes in the constitutive model due to the contact are limited to constant stress terms, it no longer implies this when including bending terms. We can understand this intuitively by realizing that the bending terms disallow kinks in the shape, such that the force balance is achieved through the bending moments counteracting the stress difference across the contact point (see Eqn. (4.26)). However, the energetically optimal solution no longer needs to be the one with continuous stretch ratios λ_s, it rather depends on the relative importance of the stretching energies and the bending energies, ultimately controlled by their respective moduli, this is exactly the meaning of Eqn. (4.28).

If we use a simple quadratic surface energy density (as discussed previously in Sec. 1.2.1) such as

$$\begin{aligned} w_{S_0} =& \frac{Y_{2D}}{2(1-\nu^2)}\left((\lambda_s-1)^2+2\nu(\lambda_s-1)(\lambda_\phi-1)+(\lambda_\phi-1)^2\right) \\ &+\frac{E_B}{2}\left(K_s^2+2\nu K_s K_\phi+K_\phi^2\right)+\lambda_s\lambda_\phi\gamma \end{aligned} \tag{4.29}$$

we can progress further and rewrite the surface energy densities on the l.h.s of Eqn. (4.28) in terms of the stresses and bending moments such that

$$w_{S_0} = \frac{1}{2}\left(\lambda_\phi(\tau_s-\gamma)(\lambda_s-1)+\lambda_s(\tau_\phi-\gamma)(\lambda_\phi-1)+\lambda_\phi m_s K_s+\lambda_s m_\phi K_\phi\right)+\lambda_s\lambda_\phi\gamma\,, \tag{4.30}$$

which allows us to reduce Eqn. (4.28) for a flat wall to

$$m_{s,-}(K_{s,+}-K_{s,-}) = \lambda_{s,-}(\tau_{s,+}-\gamma_+-(\tau_{s,-}-\gamma_-))-\lambda_{s,+}(\gamma_+-\gamma_--\Delta\gamma_{\text{wall}}) \tag{4.31}$$

which is an explicit equation for $K_{s,+}$ as a function of $\lambda_{s,+}$ (or vice versa) and describes exactly the balance between stretching and bending, as the l.h.s only considers bending contributions and the r.h.s only considers stretching contributions.

The only situation where the meridional curvature κ_s and the meridional stretch ratio λ_s is continuous at the contact point is the case where the wall consists of the same material as the shell and as such $\gamma_- = 0$ and $\gamma_+ = \Delta\gamma_{\text{wall}}$, which implies that the meridional stretch ratio and the meridional curvature are continuous at the contact point. In all other cases the two conditions must be solved for $\lambda_{s,+}$ and $\kappa_{s,+}$ respectively.

The initial meridional bending moment $m_s(s=0)$ is determined by the geometry of the wall and can not be chosen arbitrarily, such that only $\tau_s(s=0)$ can be chosen to control the volume of the shell. The pressure p must be chosen, such that the boundary condition at $s=L$ is fulfilled. Additionally, however, we must choose $m_s'(s=l_+)$ in a way such that the boundary condition for the clamped angle at the capillary, i.e. $\Psi(L)$ is met. This produces a discontinuity in the transverse shear stresses across the contact point, as we will see in the following.

Note that the situation is different when bending is involved compared to the discussion for the contact without bending stiffness – without bending we are allowed to choose the contact length as a parameter and the contact force would be a resultant of the solution in the non-contacting region, as the force enters the shape equations at no point. If the contact length is chosen here, we need to determine the contact force at the contact point, because it is needed to calculate the transverse shear stresses in the non-contacting region.

The question then becomes: how are the length of the contact region l and the external force f related? To resolve this question we need an additional equation which gives a constraint to the discontinuity in the transverse shear stress q. This equation is subtle and turns out to be hidden in one of the boundary conditions for the arc-angle, e.g. for a closed shell we necessarily have

$\Psi(L) = r(L) = q(L) = 0$, such that $m_s'(l_+)$ has to be chosen such that the boundary conditions at $s = L$ are fulfilled. Alternatively, for a shell suspended from a capillary, we have $m_s(s = L) = 0$. By choosing $m_{s,+}'$ in a way that fulfills the boundary condition at $s = L$ we generate an additional equation for q_+, since q_+ can then directly be calculated from its definition. Finally, the external force can then be calculated from the Euler-Lagrange equations just right of the contact point.

The force exerted from the wall onto the shell is the counter-force to the external force f and thus has the same magnitude. Just like in the case without bending stiffness, the force f is the conserved quantity generated by translational invariance in the $z-$axis (without gravity), where

$$f = \pi p r^2 - 2\pi r(\tau_s \sin\Psi + q\cos\Psi)\,, \tag{4.32}$$

which is particularly easy to evaluate at the positive side of the contact point, where $\Psi_+ = 0$ for a flat wall, such that

$$f = \pi p r^2 - 2\pi r q_+\,. \tag{4.33}$$

This enables us to calculate the external force f from a given contact length configuration, by choosing q_+ to fulfill all boundary conditions at $s = L$ and inputting it in Eqn. (4.33). Because we know that this quantity is conserved along the entire remaining shape, we can then use it to calculate the transverse shear stresses along all remaining points of the solution.

4.3 Contact shape equations for capsule-capsule contacts

The schematic setup for this problem is shown in Fig. 4.4. We consider two independent capsules, which are affected by a gravitational pull g and a compressing force f along the axis of axi-symmetry [6]. We are interested in the contact behaviour of this system, i.e. what are the solution shapes, how is the stress distributed in the interface material and how does the force affect the region of contact.

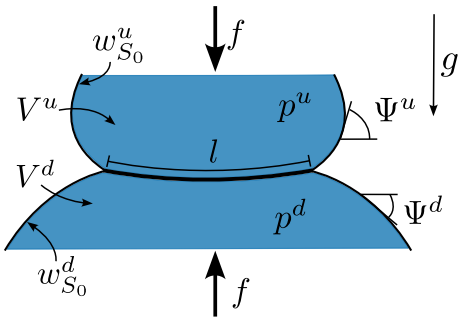

Figure 4.4: Parametrization of the capsule-capsule contact problem. Each capsule has their own surface energy density $w^{u,d}_{S_0}$, volume $V^{u,d}$ and internal pressure $p^{u,d}$. The shape and stress evolution for such a configuration follows from the shape equations of the problem, we derive from variational calculus. The external force f is the relevant control parameter for the compression of the capsules.

For these considerations we want to assume two elastic capsules, which we will distinguish by superscribing them with their respective identifier, which we choose as u and d. This choice is motivated by u and d being mnemonics for "up" and "down", which will be the parametrization we want to consider for this problem. The "up" capsule u and the "down" capsule d are pressed together by the force f, such that they come in contact over a length l.

We parametrize the upper capsule u exactly as we did for the single capsule before and analogous to [14], [15], [18], [24], such that it has the coordinates r^u, z^u, arc-angle Ψ^u, total arc-length L^u, stretches $\lambda^u_s, \lambda^u_\phi$, volume V^u and pressure difference p^u.

The same is true for the lower capsule d, such that all superscripts for u are replaced by d. An important note is that we choose to mirror the z-axis of the upper and lower shape, i.e. the shapes are both parametrized such that the apex is at height $z^u(s=0) = z^d(s=0) = 0$ and the boundary where they are suspended is $z^{u,d}(s = L^{u,d}) > 0$ [7].

Again, we start by neglecting bending energy terms, such that the solution may have kinks along its shape and discuss how to add the bending terms in a later section. We expect a kink in the solution to appear exactly at the contact point between the two capsules (yellow region 2 in Fig. 4.5), just as it is for purely liquid interface contacts with an imposed contact angle of $2\pi/3$, only that the contact angle here will depend on the internal stress states of both capsules at the contact point.

We are thus searching for a broken extremal of the combined energy functional, which we combine from the energies of both individual capsules with an additional force term, such that we acquire:

$$F = \int \mathrm{d}A^u_0\, w^u_{S_0} - \int \mathrm{d}V^u\, p^u + \int \mathrm{d}A^d_0\, w^d_{S_0} - \int \mathrm{d}V^d\, p^d + f\int_0^{L^u} \mathrm{d}z^u + f\int_0^{L^d} \mathrm{d}z^d\,. \tag{4.34}$$

The terms appearing in Eqn. (4.34) are the surface energies of the upper and lower shape, parametrized by their respective surface energy density $w^{u,d}_{S_0}$, the respective volumetric energies scaled by the Lagrange multipliers $p^{u,d}$, which are the respective pressure differences between the inside and outside of the respective capsules. Finally, the work done by the external force is exactly $f(H^u + H^d)$, where $H^{u,d}$ is the projection of the height of the respective capsule onto the force axis. Additional energetic contributions like gravity are easy to include, as shown in the Appendix A.4.1. The resulting shape must be split into four distinct regions (see Fig. 4.5):

[6] Without loss of generality we choose the z-axis.
[7] Where the superscript u, d indicates that these are actually two equations for u and d respectively.

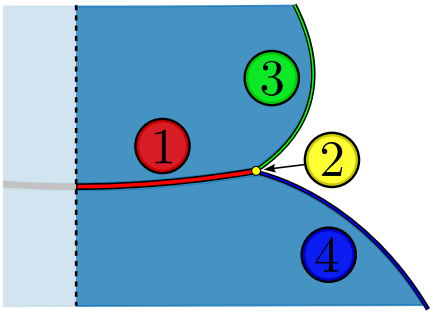

Figure 4.5: The four distinct regions of the capsule-capsule contact problem. All of these regions must be treated individually in our variational approach in order to obtain all required equations to solve this problem. Region 1 is the contact-region. Region 2 is the splitting-point and regions 3 and 4 are the free-regions.

1. The region where the upper and lower capsule are in contact.
2. The "splitting point", where the solutions of the upper and lower shapes separate
3. The region of the upper capsule u where it is not in contact with the lower capsule.
4. The region of the lower capsule d where it is not in contact with the upper capsule.

The region of contact between the capsules shall be between $s = 0$ [8] and $s = l$, where l is the position along the *deformed* arc where the capsules loose their contact. It is important to realize that the coordinate l is the same for both the upper and the lower shape, since they share the same deformed arc length coordinate up to this point, simply due to their contact with each other.

Another important realization is that the contact between both capsules directly imposes

$$\frac{\mathrm{d}\Psi^u}{\mathrm{d}s} = -\frac{\mathrm{d}\Psi^d}{\mathrm{d}s} \;,\; \forall s \in [0, l) \,. \tag{4.35}$$

In a sense, Eqn. (4.35) is a trivial contact condition, which we enforce in the following by using it during the variation. Note that the negative sign appears because the coordinate systems of the upper and lower capsule are mirrored at the r-axis.

Finally, we write the target functional:

$$\begin{aligned} F =& \pi \int_0^l \mathrm{d}s \left\{ 2r^u \frac{w^u_{S_0}}{\lambda^u_s \lambda^u_\phi} + 2r^d \frac{w^d_{S_0}}{\lambda^d_s \lambda^d_\phi} - p^u {r^u}^2 \sin\psi^u - p^d {r^d}^2 \sin\psi^d + \frac{f}{\pi} \left[\sin\Psi^u + \sin\Psi^d \right] \right\} \\ &+ \pi \int_l^{L^u} \mathrm{d}s \left\{ 2r^u \frac{w^u_{S_0}}{\lambda^u_s \lambda^u_\phi} - p^u {r^u}^2 \sin\Psi^u + \frac{f}{\pi} \sin\Psi^u \right\} \\ &+ \pi \int_l^{L^d} \mathrm{d}s \left\{ 2r^d \frac{w^d_{S_0}}{\lambda^d_s \lambda^d_\phi} - p^d {r^d}^2 \sin\Psi^d + \frac{f}{\pi} \sin\Psi^d \right\} \end{aligned} \tag{4.36}$$

Where we will denote the first integral by F_c, the second by F_u and the third by F_d. At this point it is crucial to realize that applying normal and tangential variations directly to Eqn. (4.36) is not expedient, since it results unwieldy expressions and will potentially miss one equation.

Instead, the proper procedure is to introduce normal and tangential shape variations for the upper and lower shape separately, i.e. $\delta n^u, \delta t^u$ and $\delta n^d, \delta t^d$, and couple them with the appropriate conditions in the contact region. Doing it this way forces us to explicitly state the coupling between the capsules in the contact region, which will be similar to the slip and no-slip discussion for the contact with a wall.

This insight allows us to perform the variations of the upper and lower shape independently up to the point where we enforce the contact conditions for the variations, which makes the calculation

[8] Which is at the center of the contact region with $r(s = 0) = 0$.

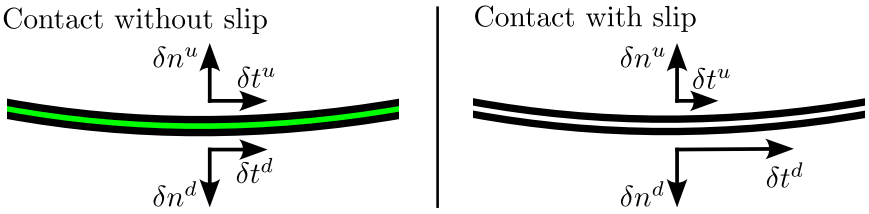

Figure 4.6: Schematic coupling of the variations in the contact region. We discuss the two cases of no-slip (left) coupling and free-slip (right) coupling. These coupling conditions determine how the respective normal variations $\delta n^{u,d}$ and tangential variations $\delta t^{u,d}$ are coupled in the contact region, influencing the final set of shape equations.

approachable. Since we already know the individual variations of the upper and lower shape from Sec. 1.2 we can directly write the variations of the upper/lower shape functional in the contact domain $\delta F_c^{u,d}$ to be

$$\begin{aligned}\delta F_c^{u,d} = \pi &\left[2\frac{r^{u,d}}{\lambda_\phi^{u,d}} \frac{\partial w_{S_0}^{u,d}}{\partial \lambda_s^{u,d}} \delta t^{u,d} - \left(p^{u,d} r^{u,d\,2} - \frac{f}{\pi} \right) \delta z^{u,d} \right]_0^l \\ &+ \pi \int_0^l \mathrm{d}s \left\{ \delta n^{u,d}\, 2r^{u,d} \left[-p^{u,d} + \frac{1}{\lambda_\phi^{u,d}} \frac{\partial w_{S_0}^{u,d}}{\partial \lambda_s^{u,d}} \frac{\mathrm{d}\Psi^{u,d}}{\mathrm{d}s} + \frac{\sin\Psi^{u,d}}{r} \frac{1}{\lambda_s^{u,d}} \frac{\partial w_{S_0}^{u,d}}{\partial \lambda_\phi^{u,d}} \right] \right. \\ &\left. + \delta t^{u,d}\, 2r^{u,d} \left[-\frac{1}{\lambda_\phi^{u,d}} \frac{\mathrm{d}}{\mathrm{d}s} \frac{\partial w_{S_0}^{u,d}}{\partial \lambda_s^{u,d}} + \frac{\cos\Psi^{u,d}}{r^{u,d}} \frac{1}{\lambda_s^{u,d}} \frac{\partial w_{S_0}^{u,d}}{\partial \lambda_\phi^{u,d}} \right] \right\},\end{aligned} \tag{4.37}$$

where we have used $f\delta \int_0^l \mathrm{d}s \sin\Psi = [f\delta z]_0^l$.

The full variation of the contact region is given as the sum of the upper and lower shape variation $\delta F_c = \delta F_c^u + \delta F_c^d$.

Just as for the contact with the wall, we need to carefully evaluate the contact coupling conditions between the capsules. Again, we want to only consider the both limiting cases of slip and no-slip coupling between the capsules. Obviously, a no-slip coupling is equivalent to coupling both δr^u and δz^u to δr^d and δz^d, such that any point that is in contact must stay in contact during the variation. This makes the exact stress-distribution in the contact region entirely contact history dependent. The no-slip contact coupling of the shape variations is visualized in Fig. 4.6 (left).

For the slip case, instead, it is sufficient to link only the normal variation of both capsules and leave the tangential variations entirely separated (see Fig. 4.6 (right)). This ensures that both capsules can change their internal stress states independently along the shape, while being in contact – we allow the shapes to "slip" over each other while they are in contact. The only connection condition we must impose for the variations in the free-slip case is thus $\delta n^u = -\delta n^d$, which we use to extract the normal and tangential conditions in the contact region from Eqn. (4.37):

$$p^u - p^d = \left(\tau_s^u + \tau_s^d\right) \kappa_s^u + \left(\tau_\phi^u + \tau_\phi^d\right) \kappa_\phi^u \qquad \text{for } s \in [0, l) \text{ (slip)} \tag{4.38}$$

$$\frac{\mathrm{d}\tau_s^{u,d}}{\mathrm{d}s} = \frac{\cos\Psi^{u,d}}{r^{u,d}} \left(\tau_\phi^{u,d} - \tau_s^{u,d}\right) \qquad \text{for } s \in [0, l) \text{ (slip)}\,. \tag{4.39}$$

Note that Eqns. (4.39) are exactly the equations found for an individual capsule [15], [18], [26] and Eqn. (4.38) gives the difference pressure between both contacting shapes as a function of the sum of internal stress states and principal curvatures.

Interestingly, the stronger coupling condition, i.e. the no-slip case with $\delta n^u = -\delta n^d$ and $\delta t^u = \delta t^d$ eliminates one further shape equation

$$p^u - p^d = \left(\tau_s^u + \tau_s^d\right)\kappa_s^u + \left(\tau_\phi^u + \tau_\phi^d\right)\kappa_\phi^u \qquad \text{for } s \in [0, l) \text{ (no-slip)} \tag{4.40}$$

$$\frac{\mathrm{d}(\tau_s^u + \tau_s^d)}{\mathrm{d}s} = \frac{\cos\Psi^u}{r^u}\left(\tau_\phi^u + \tau_\phi^d - \tau_s^u - \tau_s^d\right) \qquad \text{for } s \in [0, l) \text{ (no-slip)} \tag{4.41}$$

which is replaced by a deformation history dependent mapping function $s_0^d(s_0^u)$ to be supplied externally. This function essentially determines how the shapes are glued together. Integrating solutions for the no-slip case is computationally more demanding because it requires to integrate an entire deformation sequence, where the function $s_0^d(s_0^u)$ is incrementally computed from the initial contact at $s_0^d(s_0^u = 0) = 0$ up to the final undeformed contact length of the upper shape $s_0^d(s_0^u = l_0^u)$. The slip and no-slip cases are manifestations of two completely different contact boundary couplings and are the two extreme limits for a more general friction based coupling between the two materials. While the slip case implements the zero friction case, the no-slip case implements a perfect linking (or infinite friction) between the two materials. Notably, the slip and no-slip cases are entirely equivalent in the mirror-symmetric case, where the upper solution is a mirror image of the lower solution, because in this case, the mapping function is trivially given by the additional symmetry $s_0^u = s_0^d$.

4.3.1 The splitting point

Although we now have the set of differential equations at almost all points of the problem, it is still not possible to integrate for a solution, since we lack equations for exactly one point of the problem, namely at the kink at $s = l$. These equations are exactly the Weierstrass-Erdmann conditions. To acquire the Weierstrass-Erdmann corner conditions we need to carefully collect all boundary terms created at the corner and equate them to zero.

Since the kink in the shape results in a discontinuity in some shape variables, it is imperative to distinguish between the left and right sided limits at the discontinuity, i.e. $g(l_{+,-}) \equiv \lim_{s \to l_{+,-}} g(s)$. Select geometric functions are continuous at the kink, simply due to the fact that the shape has to be continuous, such as $r(l_+) = r(l_-) = r(l)$ and $z(l_+) = z(l_-) = z(l)$. The same is not generally true for the arc angle $\Psi(l_-) \neq \Psi(l_+)$ [9], the internal stresses $\tau_s(l_+) \neq \tau_s(l_-)$ and others, such that the distinction becomes important.

Collecting all boundary terms at $s = l$, denoted as R, gives

$$\begin{aligned}\frac{R}{2\pi r(l)} = &\left[\tau_s^u(l_-)\delta t^u(l_-) + \tau_s^d(l_-)\delta t^d(l_-)\ -\tau_s^u(l_+)\delta t^u(l_+) - \tau_s^d(l_+)\delta t^d(l_+)\right] \\ &+ \frac{r(l)}{2}\left[p^u\delta z^u(l_+) + p^d\delta z^d(l_+)\ -p^u\delta z^u(l_-) - p^d\delta z^d(l_-)\right] - \frac{f}{2\pi r l}\left[\delta z^u(l_+) + \delta z^d(l_+)\right] .\end{aligned} \tag{4.42}$$

We demand some continuity conditions at the kink, such that the shape is not ripped apart by the variations:

$$\delta r^u(l_+) = \delta r^u(l_-) = \delta r^d(l_-) = \delta r^d(l_+)\,, \tag{4.43}$$

$$\delta z^u(l_+) = \delta z^u(l_-) = -\delta z^d(l_-) = -\delta z^d(l_+)\,. \tag{4.44}$$

[9] Since we have no bending stiffness here, with bending stiffness this is obviously not the case

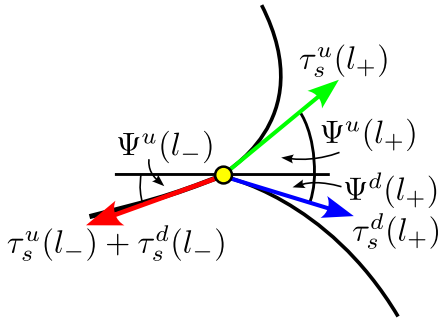

Figure 4.7: The resulting stress triangle at the splitting point is equivalent to the first Weierstrass-Erdmann conditions. The red arrow depicts the stresses pulling on the splitting point (yellow dot) from the contact region where the shapes are still in contact and the green and blue arrows depict the stresses pulling from the respective free regions of the solution.

Note that the condition at the kink is stronger than in the contact region, since the tangential perturbations of the upper and lower shape are not independent anymore, as treating them independently would lead to a unilateral shifting of the contact arc-length variable, which is unphysical. It is clear that only two variations out of the set of eight variations at the contact point are independent. In the following we will choose [10] $\delta n^u(l_-)$ and $\delta t^u(l_-)$ as the independent variations and express the other six variations $\delta n^d(l_-), \delta t^d(l_-), \delta n^d(l_+), \delta t^d(l_+), \delta n^u(l_+)$ and $\delta t^u(l_+)$ in terms of those, by utilising the six continuity conditions Eqns. (4.43) and Eqns. (4.44). We express the continuity conditions Eqns. (4.43) and Eqns. (4.44) in terms of the normal and tangential variations $\delta n^{u,d}$ and $\delta t^{u,d}$ and use the relationship

$$\delta t^{u,d}(l_+) = \delta n^{u,d}(l_-) \sin\left(\Psi^{u,d}(l_-) - \Psi^{u,d}(l_+)\right) + \delta t^{u,d}(l_-) \cos\left(\Psi^{u,d}(l_-) - \Psi^{u,d}(l_+)\right) \tag{4.45}$$

to isolate only our select independent variations at the contact point. Finally, we obtain

$$\begin{aligned}\frac{R}{2\pi r(l)} =& \delta n^u(l_-) \left\{ -\sin\left(\Psi^u(l_-) - \Psi^u(l_+)\right) \tau_s^u(l_+) + \sin\left(\Psi^d(l_-) - \Psi^d(l_+)\right) \tau_s^d(l_+) \right\} \\ & \delta t^u(l_-) \left\{ \tau_s^d(l_-) + \tau_s^u(l_-) - \cos\left(\Psi^u(l_-) - \Psi^u(l_+)\right) \tau_s^u(l_+) - \cos\left(\Psi^d(l_-) - \Psi^d(l_+)\right) \tau_s^d(l_+) \right\}\end{aligned} \tag{4.46}$$

which can be unwrapped by allowing $\delta n^u(l_-)$ and $\delta t^u(l_-)$ to be arbitrary and forcing that $R = 0$, finally giving the two Weierstrass-Erdmann corner conditions at the contact point:

$$\sin\left(\Psi^u(l_-) - \Psi^u(l_+)\right) \tau_s^u(l_+) = \sin\left(\Psi^d(l_-) - \Psi^d(l_+)\right) \tau_s^d(l_+) \tag{4.47}$$

$$\tau_s^u(l_-) + \tau_s^d(l_-) = \cos\left(\Psi^u(l_-) - \Psi^u(l_+)\right) \tau_s^u(l_+) + \cos\left(\Psi^d(l_-) - \Psi^d(l_+)\right) \tau_s^d(l_+) \,. \tag{4.48}$$

The two conditions found in Eqn. (4.47) and Eqn. (4.48) are precisely the stress balance at the contact point which can also be derived from a simple geometric argument as depicted in Fig. 4.7. The two conditions can be solved for the arc angle differences $\Delta\Psi^{u,d} \equiv \Psi^{u,d}(l_+) - \Psi^{u,d}(l_-)$ as functions of the stresses.

One way to do it is to solve the first contact condition Eqn. (4.47) for the arc angle difference $\Delta\Psi^d$, input this result into Eqn. (4.48) and solve the result for $\Delta\Psi^u$, which gives:

$$\Delta\Psi^u = \arccos\left(1 + \frac{(\tau_s^u(l_-) + \tau_s^d(l_-) - \tau_s^d(l_+))^2 - (\tau_s^d(l_+)^2)}{2(\tau_s^u(l_-) + \tau_s^d(l_-))\tau_s^u(l_+)}\right) . \tag{4.49}$$

Finally, we use this result and input it into Eqn. (4.47) to solve for $\Delta\Psi^d$ and arrive at:

$$\Delta\Psi^d = \arcsin\left(\sin(\Delta\Psi^u)\frac{\tau_s^u(l_+)}{\tau_s^d(l_+)}\right) . \tag{4.50}$$

[10] Without loss of generality.

4.3.2 Determining contact forces

The compression force f did not appear in any equations yet. This is to be expected, since all equations we calculated so far are manifestations of *changes* in forces. To calculate the forces at any point along the problem we need a first integral of one of our equations. Since the force is directed along the z-axis, variations in the z-coordinate will unveil this force. The forces applied to the capillaries can then be found just as discussed in the previous section. Both non-contacting regions of the problem at hand produce the Euler-Lagrange equations

$$\frac{\mathrm{d}}{\mathrm{d}s_0^{u,d}}\frac{\partial \mathcal{L}^{u,d}}{\partial (z^{u,d})'} = \frac{\mathrm{d}}{\mathrm{d}s_0^{u,d}}\left(2r^{u,d}\tau_s^{u,d}\sin\Psi^{u,d} - p^{u,d}(r^{u,d})^2 + \frac{f}{\pi}\right) = \frac{\partial \mathcal{L}^{u,d}}{\partial z^{u,d}} = \pm (z^{u,d})'(r^{u,d})^2 \Delta\rho^{u,d} g \tag{4.51}$$

such that integration yields an equation for the forces at the respective height [11]

$$f^{u,d}(z) = \pi p^{u,d}(r^{u,d})^2 - 2\pi r^{u,d}\tau_s^{u,d}\sin\Psi^{u,d} \pm \pi\Delta\rho g\int_l^{L^{u,d}} \mathrm{d}z\,(r^{u,d})^2\,. \tag{4.52}$$

The force may be evaluated at any point along the non-contacting shapes. A particular point, which gives the compression force f without the corrections made by the self-weight of the system is the positive side of the splitting point:

$$f = \pi p^{u,d} r(l)^2 - 2\pi r(l)\tau_s^{u,d}(l_+)\sin\Psi^{u,d}(l_+)\,. \tag{4.53}$$

We can verify that the forces of the upper and lower regions after the splitting point are equal by utilizing the Weierstrass-Erdmann conditions. The equation we have found as Eqn. (4.52) combines the upper and lower shape force balance in z-direction with the requirement of a net zero force in the contact region.

4.3.3 The mirror-symmetric special case

If the contact is between two identical capsule systems we have $p^u = p^d = p$ and because of Eqn. (4.38) $\kappa_s = \kappa_\phi = 0$ in the contact region. This enforces $\Psi^u = -\Psi^d = 0\,, \forall s \in [0, l)$. We are thus investigating a contact between two systems in a mirror-symmetric configuration, with respect to a reflection at the radial axis at $z = 0$. The contacting region is hence completely flat. Additionally, simply because of mirror-symmetry we can deduce that $\Psi^u(l_+) = \Psi^d(l_+)$. Applying these conditions to the first Weierstrass-Erdmann condition Eqn. (4.47) yields $\tau_s^u(l_+) = \tau_s^d(l_+)$, which complies with the assumption of mirror-symmetry. Furthermore, the second Weierstrass-Erdmann condition Eqn. (4.48) reduces significantly to $\tau_s(l_-) = \cos\Psi(l_+)\tau_s(l_+)$, where no distinction between the upper and lower shape is made, since their properties are exactly equal.

In the mirror-symmetric case the contact angle is thus given by $\Omega = 2\Psi(l_+) = 2\arccos(\tau_s(l_-)/\tau_s(l_+))$ where a first trivial observation can be made – the meridional stress at l_+ must always be larger than the meridional stress at l_-, otherwise a stress balance is impossible in a rotationally-symmetric configuration. Additionally, the relationship between contact region length and force applied to push the system together is given as

$$f = \pi p l^2 - 2\pi l\sqrt{\tau_s^2(l_+) - \tau_s^2(l_-)}\,. \tag{4.54}$$

[11] Without gravity, this equation is a conserved quantity along the entire shape.

If additional assumptions are made regarding the surface energy density w_{S_0} the analytical treatment can progress a bit further.

In the case of a pure liquid we have $w_{S_0}^{u,d} = \gamma\lambda_s^{u,d}\lambda_\phi^{u,d}\,, s \in (l, L^{u,d}]$, which gives $\tau_s^{u,d}(s) = \tau_\phi^{u,d}(s) = \gamma\,, s \in (l, L^{u,d}]$. Where it is instructive to distinguish between the surface tension of the interface with the outer phase γ_o and the surface tension of the interface with the inner phase γ_i, where $\gamma = \gamma_o + \gamma_i$.

The contacting region then has surface tension $\tau_s^u + \tau_s^d = 2\gamma_i + \gamma_{ud}\,, s \in [0, l)$, as the interface is exposed to the inner liquid on both sides. The additional tension γ_{ud} arises if there is additional surface interaction between both contacting interfaces (e.g. adhesion). Here we will disable such effects $\gamma_{ud} = 0$ such that the surface energy density can be expressed as $w_{S_0} = \gamma_i\lambda_s\lambda_\phi\,, s \in [0, l)$. The contact angle is thus given by $\Omega = 2\arccos(\gamma_i/\gamma)$. It is worth noting that if inner and outer phase are the same $\gamma_i = \gamma_o = \gamma/2$ we get a contact angle of $2\pi/3$, which is what is expected in e.g. liquid foams and directly follows from the von-Neumann triangle force balance condition.

The force required to create a contact region of arc-length l is then given by

$$f = \pi l^2 p - 2\pi l\sqrt{\gamma_o^2 + 2\gamma_i\gamma_o}\,.$$

Interestingly, the force changes its sign at $l_s = 2\sqrt{\gamma_o^2 + 2\gamma_i\gamma_o}/p$, up to this point the reduction of surface energy through the shared interface outweighs the penalty created by loss of volume (when controlling pressure). Extending the contact length beyond l_s finally requires an external force that compresses the system with a force pointing inwards. For $l < l_s$ a force is required which pulls the system apart, with forces pointing outwards. In the case where inner and outer phase are the same we have $\gamma_i = \gamma_o = \gamma/2$ and thus $f = \pi l^2 p - \pi\sqrt{3}l\gamma$ such that the contact length at $f = 0$ is given by $l_s = \sqrt{3}\gamma/p$. Obviously, a second solution for $f = 0$ is given as $l_s = 0$. We will discuss this hysteresis in more detail in the next sections.

4.3.4 Bending energy corrections

We will now discuss how bending stiffness can be accounted for during the variational calculus performed in the derivation of the contact problem. Fortunately, the bending energy contributions can be added to the problem via linear superposition, because we assume bending terms to be independent of stretching terms, as we have demonstrated for the free elastic capsule in Appendix A.2.1. The resulting variation of the bending energy is Eqn. (A.25), which we can reuse for the contact problem, such that the total bending energy contribution to the first variation is given by:

$$\begin{aligned}\frac{\delta E_B^{u,d}}{2\pi} =& -\left[r^{u,d} m_s^{u,d}\delta\Psi^{u,d}\right]_{l_-}^{l_+} + \left[r^{u,d} q^{u,d}\delta n^{u,d}\right]_{l_-}^{l_+} \\ &+ \int_0^{l_-} \mathrm{d}s\, \left[\delta t^{u,d}\,\frac{\mathrm{d}\Psi^{u,d}}{\mathrm{d}s} + \delta n^{u,d}\,\frac{\mathrm{d}}{\mathrm{d}s}\right]\left(r^{u,d} q^{u,d}\right) \\ &+ \int_{l_+}^{L^{u,d}} \mathrm{d}s\, \left[\delta t^{u,d}\,\frac{\mathrm{d}\Psi^{u,d}}{\mathrm{d}s} + \delta n^{u,d}\,\frac{\mathrm{d}}{\mathrm{d}s}\right]\left(r^{u,d} q^{u,d}\right)\,.\end{aligned} \tag{4.55}$$

Combining this extra term with the one we have found in the previous calculation without bending energy as Eqn. (4.37), isolating the terms relevant for the contact region, and employing the slip contact coupling condition for the normal variations $\delta n^u = -\delta n^d$ reduces the first variation only to the independent contributions from which we can directly read off the five non-geometric shape equations in the contact region:

$$\frac{\mathrm{d}(q^d - q^u)}{\mathrm{d}s} = p^d - p^u + (\tau_s^u + \tau_s^d)\kappa_s^u + \kappa_\phi^u(\tau_\phi^u + \tau_\phi^d) + \frac{\cos\Psi^u}{r^u}(q^u - q^d) \quad \text{for } s \in [0, l) \text{ (slip)} \tag{4.56}$$

$$\frac{\mathrm{d}\tau_s^{u,d}}{\mathrm{d}s} = \frac{\cos\Psi^u}{r^{u,d}}(\tau_\phi^{u,d} - \tau_s^{u,d}) + \kappa_s^{u,d} q^{u,d} \quad \text{for } s \in [0, l) \text{ (slip)} \tag{4.57}$$

$$\frac{\mathrm{d}m_s^{u,d}}{\mathrm{d}s} = \frac{\cos\Psi^{u,d}}{r^{u,d}}(m_\phi^{u,d} - m_s^{u,d}) - q^{u,d} \quad \text{for } s \in [0, l) \text{ (slip)} \tag{4.58}$$

A first integral of Eqn. (4.56) may be found simply by grouping the differentiation with respect to the arc length coordinate until we find

$$\frac{\mathrm{d}}{\mathrm{d}s}\left(r^u \cos\Psi^u \left(q^u - q^d + \tan\Psi^u(\tau_s^u + \tau_s^d) - \frac{(p_a^u - p_a^d)r^u}{2\cos\Psi^u}\right)\right) + (\Delta\rho^u - \Delta\rho^d) g z^u r^u \cos\Psi^u = 0\,, \tag{4.59}$$

such that an explicit equation for the difference in transverse shear stresses is recovered

$$q^u - q^d = -(\tau_s^u + \tau_s^d)\tan\Psi^u + r^u \frac{p_a^u - p_a^d}{2\cos\Psi} - \frac{g(\Delta\rho^u - \Delta\rho^d)}{r^u \cos\Psi^u}\int \mathrm{d}s\, z^u r^u \cos\Psi^u + \frac{\mathcal{C}}{r\cos\Psi^u}\,, \tag{4.60}$$

where the constant of integration $\mathcal{C}$ appears, which captures additional external forces in the contact region and is hence zero here. In the case where gravitational effects can be neglected, we find an algebraic equation for the difference in transverse shear stresses.

One observation we can directly make is that the bending strains K_s and K_ϕ *must* stay finite. Otherwise, the bending energy contribution goes off to infinity as well, which can at no time be the energetic minimum of the functional. Due to the definition of the bending strain $K_s = \mathrm{d}(\Psi - \Psi_0)/\mathrm{d}s_0$ there may be no kinks in the solution shape, i.e. $\Psi(l_+) = \Psi(l_-)$, such that the arc angle derivative stays finite. This implies that $K_\phi = (\sin\Psi - \sin\Psi_0)/r_0$ is not only bounded but also continuous. This argument does not, however, constrain K_s to be continuous, such that step changes in the meridional curvature are not disallowed and thus step changes in the bending moments $m_{s,\phi}$ are possible. As we will show in the following derivation, these observations are highly relevant for the correct treatment of the problem.

For the terms $\propto \delta\Psi^{u,d}$, we can thus mandate $\delta\Psi^u(l_+) = \delta\Psi^u(l_-) = -\delta\Psi^d(l_-) = -\delta\Psi^d(l_+)$. Because of the definition of $\lambda_s^{u,d}\delta\Psi^{u,d} = \mathrm{d}\Psi^{u,d}/\mathrm{d}s_0^{u,d}\delta t - \mathrm{d}\delta^{u,d} n/\mathrm{d}s_0^{u,d}$ we are able to extract an additional equation for the terms $\propto \mathrm{d}\delta^{u,d} n/\mathrm{d}s_0^{u,d}$, which must hold at the splitting point, as $0 = m_s^u(l_-) + m_s^d(l_+) - m_s^u(l_+) - m_s^d(l_-)$, which is precisely the meridional moment balance around the splitting point.

The remaining terms constitute the corrections to the shape and splitting point equations of the previously discussed contact problem without bending stiffness. Notably, however, due to the hard constraint the bending stiffness demands from the arc angle, i.e. $\Psi^{u,d}(l_-) = \Psi^{u,d}(l_+)$, the prior contributions to the splitting point equations simplify tremendously. Collecting the boundary terms, as before, allows us to read off the new contact conditions at the splitting point

$$\begin{aligned} \tau_s^u(l_-) - \tau_s^u(l_+) + \tau_s^d(l_-) - \tau_s^d(l_+) =& m_s^u(l_+)\kappa_s^u(l_+) - m_s^u(l_-)\kappa_s^u(l_-) \\ &+ m_s^d(l_+)\kappa_s^d(l_+) - m_s^d(l_-)\kappa_s^d(l_-)\,, \end{aligned} \tag{4.61}$$

$$q^u(l_-) - q^u(l_+) = q^d(l_-) - q^d(l_+)\,, \tag{4.62}$$

$$m_s^u(l_-) + m_s^d(l_+) = m_s^u(l_+) + m_s^d(l_-)\,. \tag{4.63}$$

The interpretation of these equations is immediately obvious when considering the force and moment balances at the splitting point. Where Eqn. (4.61) is the force balance tangential to the contact line, Eqn. (4.62) is the force balance normal to the contact line, while, finally, Eqn. (4.63) is the moment balance of all moments attacking the splitting point.

It is important to realize that if $E_B \to 0$ but still $E_B > 0$, we have $\Psi(l_-) = \Psi(l_+)$ on the length-scale implied by the relative importance of the bending energy, however, on a macro-scale, we can use the results from the discussion without any bending stiffness as *effective* contact angles observed over an (experimentally accessible) macro length-scale.

These are all the corrections necessary to include the bending energy terms. Note, however, that solving the shape equations with bending energy included is *much* more difficult than solving the shape equations without bending stiffness. This is simply due to the fact that all available equations need to be used in order to determine the individual quantities q^u and q^d, as implied by geometry, in the contact region. We will thus limit our numerical treatment to the case without bending energy contributions.

4.4 Numerical integration of the shape equations

The integration of the shape equations is more involved than the integration of a single free capsule, both in terms of the conceptual integration routine and the technical aspects of generating solution shapes. The following steps are required to qualitatively solve the shape equations. On a quantitative level, many more steps are needed. Those additional steps are described in the next sections.

We start the integration at $s = 0$ with $\Psi^{u,d}(s = 0) = r^{u,d}(s = 0) = z^{u,d}(s = 0) = 0$ and with a given $\tau_s^{u,d}(s = 0)$, which represents a certain volume. The pressures p^u and p^d are *not* free parameters, rather they need to be adjusted such that the solution satisfies the boundary conditions at $s = L^{u,d}$. In our case, we will connect the shape to a capillary of fixed diameters $a^{u,d}$, such that $r^{u,d}(s = L^{u,d}) = a^{u,d}/2$. Both shapes are integrated in the undeformed arc-length coordinates of the upper shape s_0^u, purely by arbitrary choice. It would be equally possible to integrate in terms of any other fixed parameter, however, we note the simplicity of choosing an undeformed coordinate of the system.

Since we choose to integrate in the undeformed coordinates of the upper shape we have direct access to the upper circumferential stretch ratio $\lambda_\phi^u = r/r_0^u(s_0^u)$. Additionally, the circumferential stretch ratio of the lower shape is required to proceed, which can be accessed by $\lambda_\phi^d = r/r_0^d(s_0^d(s_0^u))$, where the function $s_0^d(s_0^u)$ appears for the first time. It connects the undeformed coordinate of the upper and lower shapes. The defining property of this function is the coincidence of deformed arc lengths at the respective undeformed shape coordinates s_0^u and s_0^d:

$$\int_0^s \mathrm{d}s' = \int_0^{s_0^u} \mathrm{d}s_0^{u\prime} \lambda_s^u(s_0^{u\prime}) = \int_0^{s_0^d} \mathrm{d}s_0^{d\prime} \lambda_s^d(s_0^{d\prime})\,. \tag{4.64}$$

This function must hold for any s, such that the evolution of the undeformed coordinate of the lower shape, as a function of the undeformed coordinate of the upper shape is simply given by $\mathrm{d}s_0^d/\mathrm{d}s_0^u = \lambda_s^d/\lambda_s^u$. In the no-slip case, the function $s_0^d(s_0^u)$ is prescribed by the deformation history of the contact, where in the free-slip case it can be integrated along with the other shape equations. This gives access to $s_0^d(s_0^u)$ and, conversely, gives access to λ_ϕ^d.

The meridional stresses τ_s^u and τ_s^d are known at integration time, since they are generated by their derivatives contained in the shape equations. This makes $\lambda_s^u(s_0^u)$ and $\lambda_s^d(s_0^d(s_0^u))$ available

by rearranging the constitutive equations of τ_s^u and τ_s^d for the respective meridional stretch ratio $\lambda_s^{u,d}$. With all stretches being known, the circumferential stresses can be calculated by utilizing the respective constitutive equations for $\tau_\phi^u(s_0^u)$ and $\tau_\phi^d(s_0^d(s_0^u))$.

These are all the properties needed to calculate the derivatives $\mathrm{d}\tau_s^u/\mathrm{d}s$, $\mathrm{d}\tau_s^d/\mathrm{d}s$ and $\mathrm{d}\Psi^u/\mathrm{d}s = -\mathrm{d}\Psi^d/\mathrm{d}s$ with the shape equations (4.38) and (4.39), such that we are able to extrapolate to the next integration step. The solution can be integrated up to an arbitrary l, where we need to then satisfy the Weierstrass-Erdmann conditions to continue the integration.

The conditions at the splitting point Eqn. (4.47) and Eqn. (4.48) contain four unknown quantities: $\Psi^u(l_+), \Psi^d(l_+)$ and the meridional stresses after the splitting point $\tau_s^{u,d}(l_+)$. To integrate across the contact point, we need access to all of them. However, not all of these four quantities can be chosen arbitrarily. The surface stresses need to additionally satisfy the transversality conditions Eqn. (4.12), such that the meridional stretch ratio is prescribed and the meridional stresses are entirely determined a priori. This leaves the two unknown quantities $\Psi^u(l_+)$ and $\Psi^d(l_+)$ to be determined by the two equations Eqn. (4.47) and Eqn. (4.48).

The rest of the shape can be integrated in a straightforward manner, since the solution is equivalent to that of two free capsules with initial conditions at $s = l$ being $\tau_s^{u,d}(l_+)$, $\Psi^{u,d}(l_+)$, $r^{u,d}(l_-)$ and $z^{u,d}(l_-)$.

4.4.1 Non-dimensionalization

Of course, one crucial step to take before actually integrating the shape equations is to bring them into a dimensionless form. By doing so we reduce the problem to its minimum set of control parameters and make the resulting numeric values unambiguous.

Some care has to be taken when performing the non-dimensionalization of this problem, because there are numerous dimensional quantities involved. It is imperative to choose the length and stress scales uniquely for *all* involved equations. This begins with the liquid reference shapes.

For instance, we now have two liquid reference shapes, an upper and a lower shape. Without loss of generality, we choose the upper shape to be the scale defining shape. This means, that the length scale for our problem is the diameter of the capillary of the upper system a^u and the stress scale is the surface tension of the upper systems reference shape γ^u. This gives rise to the definition of the dimensionless length quantities:

$$\tilde{r}_0^{u,d} \equiv r_0^{u,d}/a^u\,, \qquad \tilde{r}^{u,d} \equiv r^{u,d}/a^u\,, \tag{4.65}$$

$$\tilde{z}_0^{u,d} \equiv z_0^{u,d}/a^u\,, \qquad \tilde{z}^{u,d} \equiv z^{u,d}/a^u\,, \tag{4.66}$$

$$\tilde{s}_0^{u,d} \equiv s_0^{u,d}/a^u\,, \qquad \tilde{s} \equiv s/a^u\,. \tag{4.67}$$

The shape equations for the upper reference shape are thus obviously the exact same ones as derived in Sec. 1.1. However, the lower reference shape must now also utilize the length and stress scales found in the upper shape, which leads to the appearance of the new non-dimensional parameters $\Gamma \equiv \gamma^d/\gamma^u$ and $\alpha \equiv a^d/a^u$, which quantifies the ratios of surface tensions and capillary diameters between upper and lower reference systems. The resulting modified shape equations for the lower reference shape are thus given by

$$\frac{\mathrm{d}\tilde{r}_0^d}{\mathrm{d}\tilde{s}_0^d} = \cos(\Psi_0^d)\,, \qquad \frac{\mathrm{d}\tilde{z}_0^d}{\mathrm{d}\tilde{s}_0^d} = \sin(\Psi_0^d)\,, \qquad \frac{\mathrm{d}\Psi_0^d}{\mathrm{d}\tilde{s}_0^d} = \frac{\tilde{p}_L^d}{\Gamma} + \frac{\Delta\tilde{\rho}^d}{\Gamma}\tilde{z}_0^d\,. \tag{4.68}$$

The dimensionless control parameters for the lower shape are defined with respect to the same scales as the upper shape $\tilde{p}_L^d \equiv p_L^d a^u/\gamma^u$ and $\Delta\tilde{\rho}^d \equiv \Delta\rho^d g(a^u)^2/\gamma^u$. The additional scale Γ appears

in the shape equations (4.68) simply because the surface tension γ^u does not arise naturally in the Young-Laplace equation of the lower shape, while γ^d does. The initial and boundary conditions for the lower reference shape are then given by $\tilde{r}_0^d(\tilde{s}_0^d = 0) = \tilde{z}_0^d(\tilde{s}_0^d = 0) = \Psi_0^d(\tilde{s}_0^d = 0) = 0$ and $\tilde{r}_0^d(\tilde{s}_0^d = L_0^d) = \alpha/2$.

Progressing to the elastic shape, we use that the tension scale for both deformed shapes is set by the surface tension of the upper shape γ^u, such that the non-dimensional tensions are defined as $\tilde{\tau}_{s,\phi}^{u,d} \equiv \tau_{s,\phi}^{u,d}/\gamma^u$. Utilizing this, the previous definitions of the non-dimensional quantities and expressing the shape equations in the contact region Eqn. (4.38) and Eqns. (4.39) in terms of s_0^u gives the seven non-dimensional shape equations for the free-slip problem [12]

$$\frac{\mathrm{d}\tilde{s}}{\mathrm{d}\tilde{s}_0^u} = \lambda_s^u \tag{4.69}$$

$$\frac{\mathrm{d}\tilde{s}_0^d}{\mathrm{d}\tilde{s}_0^u} = \frac{\lambda_s^u}{\lambda_s^d} \tag{4.70}$$

$$\frac{\mathrm{d}\tilde{r}^u}{\mathrm{d}\tilde{s}_0^u} = \lambda_s^u \cos\Psi^u \tag{4.71}$$

$$\frac{\mathrm{d}\tilde{z}^u}{\mathrm{d}\tilde{s}_0^u} = \lambda_s^u \sin\Psi^u \tag{4.72}$$

$$\frac{\mathrm{d}\Psi^u}{\mathrm{d}\tilde{s}_0^u} = \lambda_s^u \frac{1}{\tilde{\tau}_s^u + \tilde{\tau}_s^d}(\tilde{p}_a^u - \tilde{p}_a^d - (\Delta\tilde{\rho}^u - \Delta\tilde{\rho}^d)\tilde{z}^u - (\tilde{\tau}_\phi^u + \tilde{\tau}_\phi^d)\frac{\sin\Psi^u}{\tilde{r}^u}) \tag{4.73}$$

$$\frac{\mathrm{d}\tilde{\tau}_s^{u,d}}{\mathrm{d}\tilde{s}_0^u} = \lambda_s^u \cos\Psi^u \frac{\tilde{\tau}_\phi^{u,d} - \tilde{\tau}_s^{u,d}}{\tilde{r}^u} \tag{4.74}$$

where we define the dimensionless pressure $\tilde{p}_a^{u,d}$ at $s = 0$ as $\tilde{p}_a^{u,d} \equiv p_a^{u,d} a^u/\gamma^u$ and recognize the dimensionless density contrasts $\Delta\tilde{\rho}^{u,d}$, which are the same as for the liquid reference shapes.

Already at $s = 0$ we encounter a numerical problem we have to carefully solve. Namely, since $s = 0$ coincides [13] with $r^{u,d} \equiv 0$, several equations develop numerical singularities. All of those are of the kind "0/0" where L'Hôspital's rule is applicable. At $s = 0$ shape equations Eqn. (4.73) and Eqn. (4.74) are thus replaced by

$$\frac{\mathrm{d}\Psi^u}{\mathrm{d}\tilde{s}_0^u} = \lambda_s^u \frac{1}{2(\tilde{\tau}_s^u + \tilde{\tau}_s^d)}\left(\tilde{p}_a^u - \tilde{p}_a^d - (\Delta\tilde{\rho}^u - \Delta\tilde{\rho}^d)\tilde{z}^u\right), \qquad \frac{\mathrm{d}\tilde{\tau}_s^{u,d}}{\mathrm{d}\tilde{s}_0^u} = 0, \tag{4.75}$$

which we employ in a radius $\epsilon = 10^{-8}$ around $s = 0$ in order to solve the equations.

In order to integrate the shape equations we still need to specify a constitutive material model, which connects the surface stresses with the stretch ratios. For this, we choose the non-linear Hookean constitutive law, as detailed in Sec. 1.2.1. Other choices are possible, however, this choice is the simplest model, with a surface energy density accurate up to quadratic order in the strains, while still retaining the geometric non-linearities [15].

The surface tension contribution to the stresses is split into the contribution $\gamma_i^{u,d}$ made by the contact of the interface to the inner phase and the contribution $\gamma_o^{u,d}$ due to the contact to the outer phase. Additionally, we include a tension due to the contact of the upper and lower interface γ_{ud}, which captures additional adhesive effects. This distinction is important, because only the inner contributions play a role in the contact region, while the sum of the inner and outer contributions

[12] In the no-slip problem the two equations Eqn. (4.74) reduce to the sum of the equations.
[13] By choice of our initial conditions.

play a role outside of the contact region. The total surface tension of the reference liquid drop is thus $\gamma^{u,d} \equiv \gamma_i^{u,d} + \gamma_o^{u,d}$.

The resulting non-dimensional stresses in the contact region are thus given by

$$\tilde{\tau}_{s,\phi}^{u,d} = \frac{\tilde{Y}_{2D}^{u,d}}{1-(\nu_{2\mathrm{D}}^{u,d})^2} \frac{1}{\lambda_{\phi,s}^{u,d}} \left(\lambda_{s,\phi}^{u,d} - 1 + \nu_{2\mathrm{D}}^{u,d}(\lambda_{\phi,s}^{u,d} - 1)\right) + \underbrace{\frac{\gamma_i^{u,d} + \gamma_{ud}}{\gamma^u}}_{\tilde{\gamma}_c^{u,d}} \text{ for } s \in [0, l)\,, \tag{4.76}$$

where we find the two additional non-dimensional parameters $\tilde{\gamma}_c^{u,d}$, which quantify the magnitude of the surface tension in the contact region in relation to the total surface tension of the upper shape outside the contact region.

4.4.2 Quantitative Integration Routine

The integration is implemented using C++ in the same numerical framework presented in Chap. 2. We are able to combine the data structure of two individual capsules and implement the new shape equations only for the contact region and the splitting point. The solution of the shape for $s > l$ can then be generated with the routine used for the single pendant capsules, eliminating the need for code duplication and again highlighting the modularity of the framework.

The integration is started in the center of the contact region, from where we progress with a Runge-Kutta method of order four to integrate the dimensionless shape equations (4.69), (4.70), (4.71), (4.72) (4.73) and (4.74) together with the constitutive equations (4.76). Here we additionally discriminate between the shape equations for $s < \epsilon = 10^{-8}$ and $s > \epsilon$ to avoid numerical singularities. The shape equations for $s < \epsilon$ are thus only used for the very first integration step to kick off the integration. For $s > \epsilon$ we need access to $r_0^{u,d}(s_0^u)$, which is granted by evaluating a spline of the reference shape at the current undeformed arc length. For access to $r_0^d(s_0^u)$ we use the property $s_0^d(s_0^u)$, which we integrate together with the other shape equations as Eqn. (4.70). Due to the dimensionless constitutive equations (4.76) we gain access to $\lambda_s^{u,d}$ and $\tau_\phi^{u,d}$, which we finally use to calculate the derivatives on the l.h.s of the shape equations (4.69), (4.70), (4.71), (4.72), (4.73), (4.74), and start to propagate to the next integration step.

Due to the fact that we integrate $s(s_0^u)$ along with the other shape equations as Eqn. (4.69), we are able to access the deformed arc length at any integration step and use it to determine when to switch the shape equations from the contact region shape equations to the splitting point shape equations and the shape equations of the free capsule afterwards. We thus set a contact length l as our control parameter rather than a contact force f, simply because it is easier to handle from a technical perspective. Conversely, the contact force is calculated as a by-product at the splitting point via Eqn. (4.53) once the splitting point equations Eqn. (4.47) and Eqn. (4.48) are evaluated to determine the contact angles. At this point we fall back to the integration routine for a free pendant capsule and integrate the shape equations up to the respective total undeformed arc length.

The solutions generated in this way are a super class of the solutions we are interested in, simply because they do not necessarily reach the respective attachment boundary conditions. Searching for the solutions that *do* satisfy the additional boundary condition requires the use of two coupled shooting methods.

We can not choose both the apex stresses $\tau_s^{u,d}(s = 0)$ and the pressures $p^{u,d}$ if we want to reach an attachment boundary condition. This is similar to the shooting problem encountered for the free pendant capsule in Sec. 2.2 and literature [14], only that we now have a significantly more

complex problem. As already discussed for the free pendant capsule in Sec. 3.1 and Ref. [13] – choosing a pressure and searching for the accompanying apex stress is ambiguous. Thus an apex stress must be chosen for which we determine the relevant pressure in a shooting method. The additional complexity over the free capsule stems from the fact that changing the pressure of the upper shape influences the solution shape for the lower shape and vice versa, because they are linked in the contact region. Ultimately, this is a problem where we search for two coupled zero crossings as a function of two parameters.

Analysing the problem reveals that it is accessible to a simple iterative method. Changing p^u while searching for the zero crossing of $d^u = r(L^u) - a^u/2$, will influence the contact region solution of the lower shape, simply because the pressure difference changes, such that $d^d = r(L^d) - a^d/2$ also changes. However, if the pressures of the upper and lower shape are in the same order of magnitude, the pressure difference will be small and the radius of curvature in the contact region will be large compared to the total height of the droplet, such that the change in $d^{u,d}$ is small compared to the attachment radius $a^{u,d}/2$ when changing $p^{d,u}$. This makes the problem suitable for a fix-point iteration scheme, where we search for the pressures $p^{u,d}$ sequentially and iteratively to eventually satisfy both equations $|d^{u,d}| < \epsilon$ to a given acceptable uncertainty ϵ.

We employ a hybrid between a multi-section method and a secant method to solve both of the shooting problems. While a shooting method certainly introduces computational overhead, we are able to robustly generate solutions in acceptable time due to an optimized integration code implemented in C++.

On top of the shooting method performed for the pressures, we can search for the relevant apex stresses $\tau_s^{u,d}(s = 0)$ which lead to a given volume $V^{u,d}$. The application for this might be that the volume is controlled in an experiment and thus the deformation will not happen at a given apex stress but rather at a given volume. For example, the volume of the reference liquid droplets could be a conserved quantitiy due to the upper and lower shape not allowing any volume exchange [14].

The same methodology applied for the double pressure shooting problem can be applied here as well. We thus search for the apex stresses $\tau_s^{u,d}(s = 0)$ seperately and iteratively to eventually converge to a set of $\tau_s^{u,d}(s = 0)$ for which the appropriate volume is achieved by both shapes.

Since we are stacking complexity, this method is severely slower than the double pressure shooting method alone. However, this method is not needed to study the parameter space of the system, or in an eventual shape fitting routine.

[14] Due to the shape being closed, or attached to a capillary with closed valves.

4.5 Analysis of the shape space

The shape space of the present problem is severely high-dimensional. For the convenience of the reader, we will now rehearse all the involved control parameters. The two liquid reference shapes already provides us with a range of control parameters. They encompass the dimensionless apex pressures $\tilde{p}_L^{u,d}$, the respective dimensionless density contrasts $\Delta\tilde{\rho}^{u,d}$, the ratio of capillary widths $\alpha \equiv a^d/a^u$, the ratio of surface tensions $\Gamma \equiv \gamma^d/\gamma^u$ and the surface tension contributions generated by the contact of the inner and outer phases respectively, i.e. $\gamma^{u,d} = \gamma_i^{u,d} + \gamma_o^{u,d}$ which gives two additional parameters in total. The reference configuration thus already constitutes 8 entirely independent continuous control parameters. As shown previously in Sec. 1.1 and in more detail in Ref. [24], there are two additional discrete control parameters for the reference shapes, which control the shape class $\Omega^{u,d}$ of the reference shape solution.

Furthermore, the control parameters for the elastic constitutive equation are expressed by two elastic moduli per shape, e.g. $Y_{2D}^{u,d}/\gamma^u$ and $\nu_{2D}^{u,d}$. Additionally, the constitutive material equations provide a surface tension contribution, which captures an additional adhesive contribution in the contact region γ_{ud}/γ^u. The elastic material properties add a total of 5 independent continuous control parameters to the shape space.

Moreover, the shape equations of the problem expose the dimensionless apex stresses $\tilde{\tau}_s^{u,d}(s=0)$ and the dimensionless contact length l/a^u as control parameters, which adds an additional 3 continuous control parameters to the problem. All other properties are implied by utilising the set of equations generated from the variational calculation in Sec. 4.3, such as the external force, pressures, local stresses and stretches, as well as the full geometry of the solution.

Finally, we arrive at a set of 16 continuous control parameters, which present a 16-dimensional shape-parameter space. Consequently, we need to limit our investigation of the shape space to a well motivated slice of the shape space. As

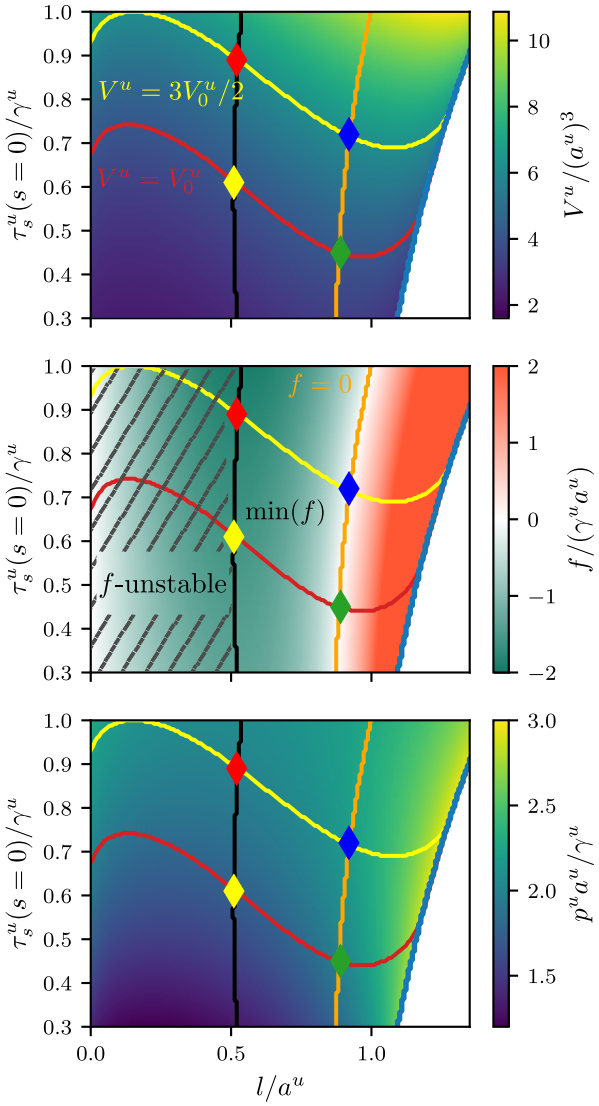

Figure 4.8: We generate a slice of the shape space for the elastic contact problem. Here we choose $K_{2D} = \gamma$. The lines of constant volume (contour lines of the upper plot) are shown for the deformed volumes equaling the reference volume $V^{u,d} = V_0^{u,d}$ (red line) and for a 50% inflated reference volume (yellow line). Additionally, the lines of minimum forces (black lines) and zero forces (orange line) are shown. The intersections between the volume and force lines are highlighted with colored diamonds and mark the respective characteristic points in the deformation sequences of fixed volume. In a certain region, no solutions can be found for a given contact length and apex stress (blue line), i.e. there does not exist a pressure for which the capillary boundary condition may be fulfilled. The area marked as f-unstable is always unstable under force control.

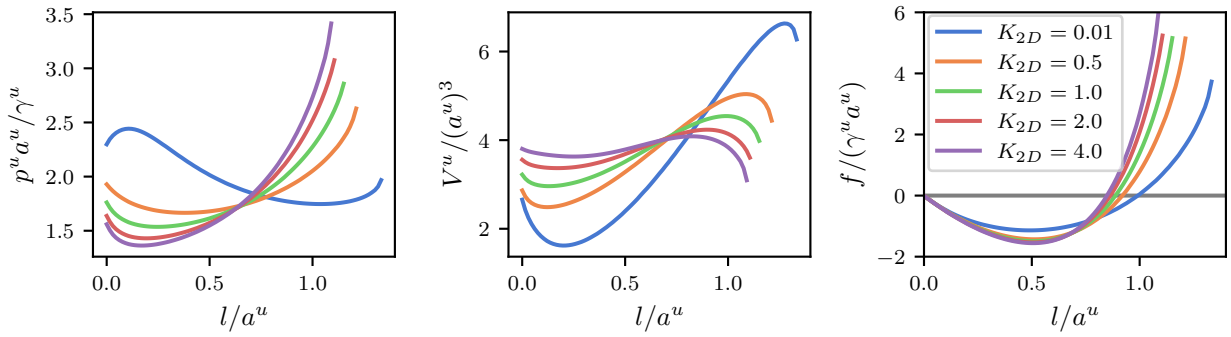

Figure 4.9: Evolution of the pressure, volume and external force during a contact deformation at fixed apex stress. Additionally, we show the difference between five elastic compression moduli K_{2D}. The fixed apex stress we subject the elastic shape to is chosen, such that we are able to compare with the liquid case, which only allows $\tau_s^u/\gamma = 0.5$.

evident from the above listing of control parameters, they can be categorised based on their origin of appearance.

An especially easy choice, which conveys a certain conceptual simplification, is the case of mirror-symmetric reference shapes. Mirror-symmetry of the reference shapes mandates that gravitational effects can be neglected and $\Delta\tilde{\rho}^{u,d} = 0$ as well as $\tilde{p}_L^u = \tilde{p}_L^d$ and $\gamma^u = \gamma^d = \gamma$, reducing the control parameter count for the reference shapes to only 2. Additionally, we choose the reference shapes to have a shape class of $\Omega^{u,d} = 2$, leaving only a single control parameter for the reference shapes, which is e.g. $\tilde{p}_L^u$. Propagating the assumption of mirror-symmetry to the deformed shapes additionally forces equality for the respective constitutive parameters, e.g. $\tilde{Y}_{2D}^u = \tilde{Y}_{2D}^d$, $\nu_{2D}^u = \nu_{2D}^d$, and apex stresses $\tilde{\tau}_s^u(s=0) = \tilde{\tau}_s^d(s=0)$.

Since the parameter space is still too large to properly visualize, we eliminate further insensitive control parameters by fixing them to arbitrary [15] values. Two of such parameters are the Poisson's ratios $\nu_{2D}^{u,d}$, which we fix to a value of $\nu_{2D}^{u,d} = 0.5$ [16]. Additionally, we fix the reference shape apex pressure to $\tilde{p}_L^{u,d} = 2$ and provide quantitative arguments how the fixed parameters influence the recovered results.

We can further reduce the complexity of the parameter space by eliminating γ_i^u/γ. The assumption needed for this is that the respective inner and outer phase are equal, e.g. both air, giving $\gamma_i^u/\gamma = 1/2$. Initially, we disable additional adhesive effects by setting $\gamma_{ud} = 0$. We include these parameters in the quantitative description of the characteristics found in the shape space, enabling the reader to infer the influence of this parameter on the presented figures.

These simplifications reduce the set of control parameters to $\tilde{l}, \tilde{Y}_{2D}^u = \tilde{K}_{2D}^u, \tilde{\tau}_s^u(s=0)$.

We sample the apex stress $\tau_s^u(s=0)$ and contact length l parameters and find volume, force and apex pressure dependencies for $K_{2D} = \gamma$ in Fig. 4.8. Interestingly, the control over the apex stress $\tau_s^u(s=0)$ is something that only arises due to the elastic skin. A liquid droplet does *not* have this degree of freedom, on the contrary, for the purely liquid contact, the apex stress is dictated entirely by the surface tension of the interface to the inner liquid $\tau_s^{u,d}(s=0) = \gamma_i^{u,d} = \gamma^{u,d} - \gamma_o^{u,d}$ and the pressure dictates the volume. The purely liquid contact exhibit different shapes than any elastic

[15] But experimentally typical.
[16] The choice is typical and motivated because this value implies 3D isotropy and incompressibility of the skin. Furthermore, this choice mandates $K_{2D} = Y_{2D}$.

interface would have. This is simply due to the reference shape of the elastic problem being a non-contacting liquid configuration. This can not be neglected, even for very small contact lengths $l/a \ll 1$, because the mere existence of a contact introduces the necessity for a specific contact angle at the splitting point. For very small l/a this essentially imposes a change in the initial condition of the arc-angle. Thus, achieving the reference liquid volume for the elastic contact problem requires an apex stress $\tau_s^u(s=0) \neq \gamma_i^u + \gamma_{ud}$.

The volume evolution in Fig. 4.8 (top) gives an insight into how volume controlled deformation sequences move through the parameter space. Two fixed volume curves are shown as the red and yellow lines ($V^u = 3V_0^u/2$ and $V^u = V_0^u$ respectively). The evolution of external force and pressure at constant volume can be seen by tracing the red line in Fig. 4.8 through the respective figures. We additionally show this evolution for a shape that is inflated 50% in volume throughout the entire contact (yellow line). After a specific contact length for a given apex stress, no further solutions are found (blue solid line in Fig. 4.8). All of the shapes along this line have an arc angle of $\Psi^{\text{cap}} = 3\pi/2$ at the capillary and thus meet the capillary from above with a vertical tangent. No further solutions exist because they would penetrate the capillary walls.

In Fig. 4.9, we show horizontal slices through the shape space, color coded in Fig. 4.8. These slices reveal the modifications made by the elastic skin at a fixed apex stress. The pressure (see Fig. 4.9(left)) variations are amplified with increasing elastic modulus, while the volume variations (see Fig. 4.9(center)) are supressed. Note that the crossing of all lines at $l/a^u \sim 3/4$ is only present for $\tau_s^u/\gamma = 1/2$ and is the point where elastic stresses are approximately isotropic and homogeneous (i.e. the shape is liquid-like).

During such contact evolution the external force required to stabilize the shape changes drastically. When the force is negative, the shapes need to be pulled apart from each other to keep them from increasing the contact length. If the force is positive, the shapes need to be pressed against each other to increase the contact length. We can thus use the external force to make statements about the stability of certain regions in the shape space.

From our previous theoretical discussion of the symmetric case we acquire the external force in the limit $l/a \ll 1$ from Eqn. (4.54), by recognizing that the pressure term is a contribution of second order in the contact length [17]. Additionally, the stress in the contact region will not vary by much in the limit of short contact lengths $\tau_s(s = l_-) \sim \tau_s(s=0)$, such that we finally arrive at

$$f(l/a \ll 1) \approx -2\pi l(\gamma_o - \gamma^{ud})\sqrt{1 + \frac{2\tau_s(s=0)}{\gamma_o - \gamma^{ud}}}\,, \tag{4.77}$$

As discussed previously, for the purely liquid case with $\gamma_o = \gamma_i = \gamma/2$ this reduces to $f_{\text{liquid}}(l/a \ll 1) \approx -\pi l\gamma\sqrt{3}$.

Thus, for contact lengths $l/a \ll 1$, the force is small and negative, however, this configuration is not stable at constant external force. A slight perturbation that causes the contact to increase slightly, also increases the force required to keep the shapes separated from each other, so $\mathrm{d}f/\mathrm{d}l < 0$. As long as this is true, the shapes will dynamically increase their contact length until they eventually reach a steady state where $\mathrm{d}f/\mathrm{d}l > 0$ and a force balance is restored. The black line in Fig. 4.8 symbolizes the line of minimum force [18]. All shapes to the left of this black line are dynamically unstable if subjected to a constant external force and transition to the corresponding contact length of equal external contact force to the right of the black line. A contact with external force $f \equiv 0$ will thus instantaneously [19] transition from $l/a = 0$ to $l/a > 0$ onto the orange line in

[17] Because the apex pressure corrections due to the change in contact length are of higher order.
[18] The maximum absolute force required to keep the shapes apart.
[19] In an idealized sense. Experimentally, this will not happen instantaneously due to inertial effects.

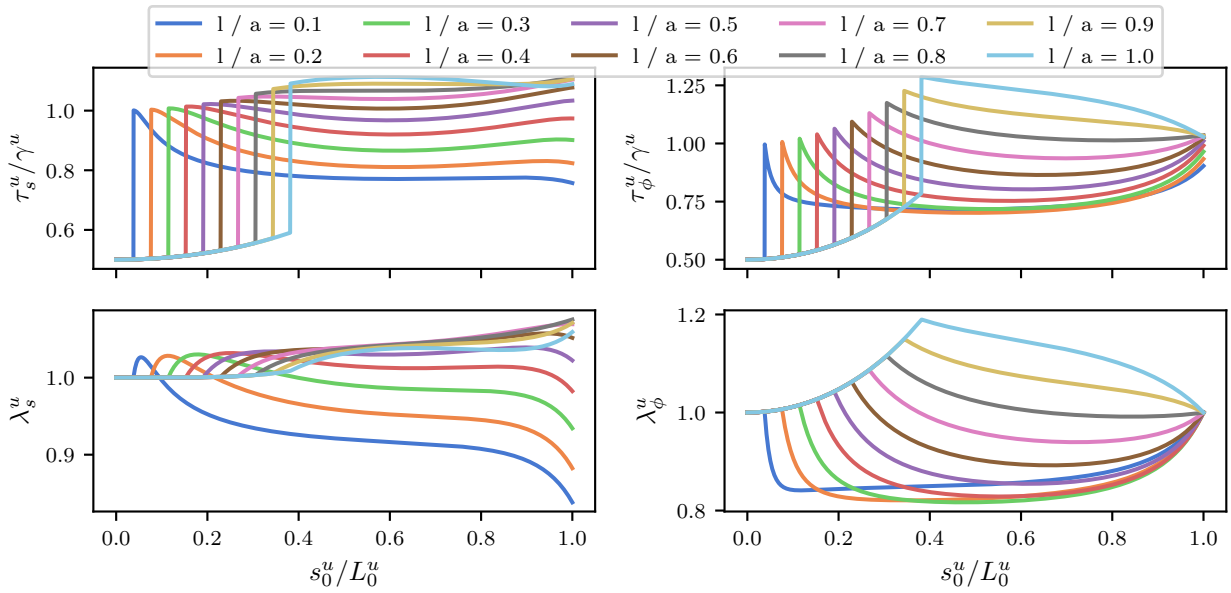

Figure 4.10: The evolution of the meridional and circumferential stretch ratios and surface stresses along a set of solution shapes. The contacting region is enlarged by the choice of l, however, since we are considering a mirror-symmetric system, the difference pressure in the contact region is always the same and thus we find a universal contact region behaviour. As soon as the mirror-symmetry is broken, the contact region behaviour will be influenced by the choice of l as well. The shapes shown here have constant apex stresses $\tau_s^u = \tau_s^d = \gamma/2$, with the other parameters set to the characteristic values chosen for this section.

Fig. 4.8. This orange line is characterised by setting Eqn. (4.53) to zero, which gives a functional connection between the stress at the splitting point, the pressure p and the contact length l:

$$l_{\text{orange}} p = 2(\gamma_o - \gamma^{ud}) \sqrt{1 + \frac{2\tau_s(l_-)}{\gamma_o - \gamma^{ud}}} \,. \tag{4.78}$$

Unfortunately, the contact length is no longer small at the orange line, where $l/a \sim 1$. Thus, the corrections in the pressure p and the difference between apex stress $\tau_s(s=0)$ and splitting point stress $\tau_s(l_-)$ need to be carefully considered to arrive at usable results. As we show in Fig. 4.8 (lower) the pressure changes substantially while traversing the shape space. This effect is amplified with larger compression moduli, as can be seen in the Appendix Fig. A.2.

We have no immediate access to the pressure difference, as the shape equations in the contact region only include apex pressure differences $p^u - p^d$, which are trivially zero in the symmetric case. The first occurrence of the relevant pressures is right after the splitting point, where the shapes come into contact with the external medium for the first time. We thus have $p = \kappa_s(l_+)\tau_s(l_+) + \kappa_\phi(l_+)\tau_\phi(l_+)$, where p can not be determined from, since it needs to be chosen such that the connection boundary condition is fulfilled.

Separating the contacting shapes again is prevented by an energy barrier corresponding with the black line of minimum forces. This energy/force barrier must be overcome by the external force in order to separate the shapes. As soon as the external force is strong enough to overcome the barrier, the shapes separate. The shapes to the left of the black line are, again, unreachable in an experiment where the force is controlled.

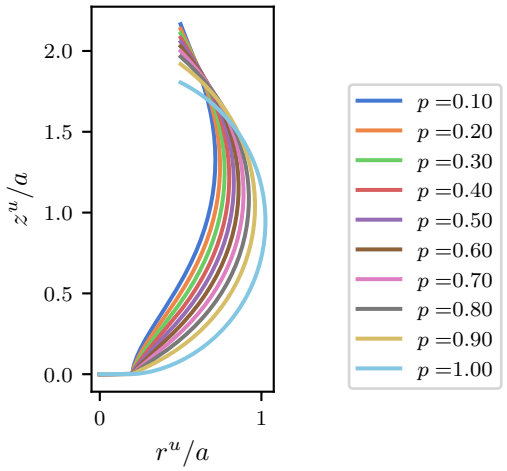

Figure 4.11: All of the displayed shapes have the same total surface tension γ in the non-contacting region. Depending on how the total effective surface tension in the non-contacting region is composed from the inner and outer phase contributions, the partitioning p in the contact region changes necessarily, changing the contact angle at the contact point. Here we still disable additional adhesive surface tension terms $\gamma^{\mathrm{ud}} = 0$.

We can approximate the black line in Fig. 4.8 by using Eqn. (4.53). The black line corresponds to the minimum of the function. Again, the simplest approximation can be found when assuming $p \sim p_0 = \text{const.}$ and $\tau_s(s = l_-) \sim \tau_s(s = 0)$, which gives $l_{\text{black}} \sim l_{\text{orange}}/2$ and qualitatively captures the behaviour seen in Fig. 4.8.

The force required to separate the shapes f_{rip} then approximates to

$$f_{\text{rip}} \sim -\frac{\pi}{p_0}((\gamma_o - \gamma^{ud})^2 + 2(\gamma_o - \gamma^{ud})\tau_s(s = 0))\,. \tag{4.79}$$

For Fig. 4.9 the force required to separate the shapes is approximated by Eqn. (4.79) to be $f_{\text{rip}}/(\gamma a) \approx -3\pi/8$ encountered at a contact length $l_{\text{rip}}/a \approx \sqrt{3}/4$, which is a solid approximation for $K_{2D} \leq \gamma$.

We can inspect the properties of a single solution in more detail by evaluating the evolution of the stretch ratios λ_s^u and λ_ϕ^u together with the surface stresses τ_s^u and τ_ϕ^u along the solution shape. We find that in the mirror-symmetric case, all contact regions for different values of the contact length l collapse onto each other (see Fig. 4.10). This fact can be understood by realizing that the only parameters allowed to change in a response to a change in contact length l is the upper and lower pressure p^u and p^d. Since, however, the contact region only depends on the *difference* $p^u - p^d = 0$, we do not actually see a change in the contact region solutions. At the splitting point, the absolute value of the pressures enters and the solution in the non-contacting region depends on the choice of the contact length l, as can be seen in Fig. 4.10.

Short contact lengths lead to a short-ranged extensive stretching in meridional direction and compressive stretching in circumferential direction just right of the contact point (see Fig. 4.10). This is exactly the manifestation of the effective adhesion due to the combined surface tension in the contact region being only half that of the two individual capsules in the non-contacting region [20]. In this immediate contact region, elastic stretching energy is traded for adhesive surface energy. If it where not for the external force f, the shapes would continue trading stretching energy for surface energy until an equilibrium is reached exactly at the orange line in Fig. 4.8.

The pinning at the capillary demands $\lambda_\phi^u(s_0^u = L_0^u) = 1$, which we can confirm is respected by all of our solutions in Fig. 4.10.

Another set of mirror-symmetric solutions is obtained if the inner and outer phases – relative to the skin – are not the same and thus do not contribute the same amount to the total effective

[20] Or the discontinuity in τ_s^u and τ_ϕ^u as seen in Fig. 4.10

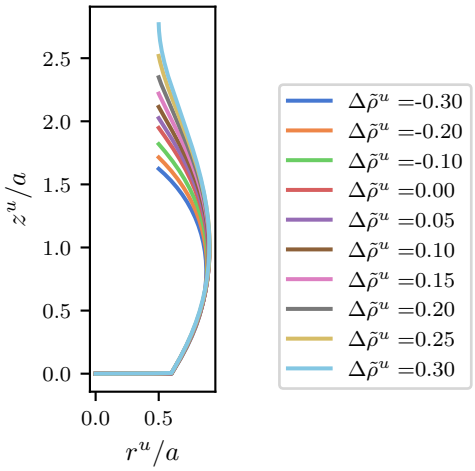

Figure 4.12: Exemplary upper contact shapes with varying gravitational influence (parameter $\Delta\tilde{\rho}^u$). The shapes are additionally compressed/stretched by gravity. For all of these shapes we choose a contact length of $l/a = 0.6$ and an apex stress of $\tau_s^u(s = 0)/\gamma = 0.5$ (i.e. we select a specific point in Fig. 4.8 and only vary the gravitational influence). The accompanying lower shape is not shown explicitly, but is equivalent to that of the upper shape with a flipped sign in $\Delta\tilde{\rho}^u$, while the upper shape is stretched by gravity, the lower shape is compressed by it.

surface tension in the non-contacting region $\gamma = \gamma_i + \gamma_o$, the partitioning $p \in [0, 1]$ between $\gamma_i = p\gamma$ and $\gamma_o = (1 - p)\gamma$ would control the contact angle in the purely liquid case. These configurations are still mirror-symmetric as long as all other control parameters still are mirror-symmetric. Here it controls the effective adhesive energy contribution in the contact region. Both shapes trade stretching energy in the contact region against surface tension energy because of the difference in surface tension in the non-contacting versus the contacting region $2\gamma \leftrightarrow 2\gamma_i + \gamma^{ud}$ by elongating the contact length l. The result is a change in the contact angle as described by the Weierstrass-Erdmann conditions

$$\Omega = 2 \arccos \frac{\tau_s^{\mathrm{el}}(l) + p\gamma + \gamma^{\mathrm{ud}}}{\tau_s^{\mathrm{el}}(l) + \gamma} \tag{4.80}$$

however, we can assume $\tau_s^{\mathrm{el}}(l) \ll p\gamma < \gamma$ if the contact length is sufficiently small. This gives $\Omega \sim 2 \arccos(p + \gamma^{\mathrm{ud}}/\gamma)$. In a sense, the partitioning p creates a "trivial" adhesion of the two skins, with "trivial" in the sense that it is an inherent adhesion due to the inner and outer fluid phases, which is entirely independent of the inter-material interactions. The inter-material interactions leading to additional adhesive effects are captured in the entirely separate parameter γ^{ud}. Some shape examples are given in Fig. 4.11, where only the partitioning p is varied. As expected $p = 1$ gives a contact angle $\Omega = 0$.

Up to this point we did not include any additional adhesive effects, i.e. $\gamma^{\mathrm{ud}} = 0$. The term γ^{ud} scales additional energetic contributions in the contact region, where it is the proportionality constant between the additional contact energy and the contact surface area. It can be used to modify the total effective surface tension energy in the contact region. If the contact between the capsules leaves a wetted liquid film between the individual capsules, due to it not being drained fast enough, the additional surface tension is exactly equal to the sum of the outer liquid surface tension contributions $\gamma^{\mathrm{ud}} = \gamma_o^u + \gamma_o^d$.

In the case, where the contact between the two materials causes an effective attraction between the two, due to adsorbtion or other surface processes, the additional effective surface tension would be negative $\gamma^{\mathrm{ud}} < 0$, acting to further increase the contact length in exchange for elastic energy.

Gravity induced mirror-asymmetry

Up to this point we have disabled gravitational effects by explicitly choosing $\Delta\tilde{\rho}^{u,d} = 0$ as an assumption in our analysis. This assumption is well suited if the capsules are sufficiently small,

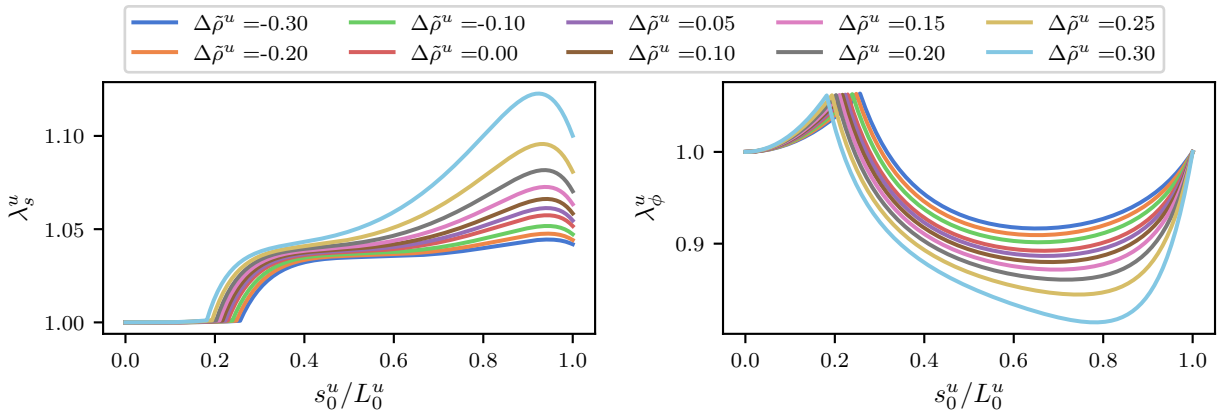

Figure 4.13: Gravitational effects change the solution shapes by modifying the reference shapes and the local stretch ratios. The stretch ratios λ_s^u and λ_ϕ^u are defined relative to the liquid reference shape. We identify the region where gravitational effects influence the solution shapes most drastically to be close to the capillary.

or if the density between inner and outer phase are negligible [32]. We will now discuss what happens to a configuration that is symmetric in every parameter but gravity is introduced into the problem by choosing $\Delta\tilde{\rho}^u = \Delta\tilde{\rho}^d \neq 0$. Most obviously, introducing gravity changes the shapes to be longer/shorter if gravity stretches/compresses the shape additionally. We always have both deformation modes in our contact problem, because if the upper shape is stretched by gravity, the lower shape is compressed by gravity and vice versa. This is simply because their respective orientation exactly mirrors the gravitational influence. Since we have axisymmetry as a fundamental assumption for all of our derivations, we are not able to access solutions where gravity leads to a non-axisymmetric configuration.

In Fig. 4.12 we only show the upper solution shapes, however, the lower shape needs to be calculated as well to arrive at this solution, as the contact pressure is dependent on both solutions, as discussed previously. By sampling the gravitational influence $\Delta\tilde{\rho}$ from negative to positive, we essentially flip the role of upper and lower shapes during our sampling, because a negative value for $\Delta\tilde{\rho}^u$ gives the same shape solution as the lower solution shape would have for a positive $\Delta\tilde{\rho}^u$. In a sense, the shape for $\Delta\tilde{\rho}^u = -0.3$ in Fig. 4.12 is the same shape as the lower solution for $\Delta\tilde{\rho}^u = 0.3$, such that these are intimately connected.

The visual intuition is that the shapes do not change significantly in and around the contact region when gravity is activated. We can quantify this intuition by evaluating the internal stretch states of the respective shapes in Fig. 4.13. Furthermore, Fig. 4.13 gives an insight into how the shapes redistribute the surface area stretches when gravity is enabled. As intuitively expected, the local stretches are amplified in the vicinity of the capillary with increased gravitational pull. This is simply because a large meridional stretch lengthens the region of the capsule, where it is comparatively slender and transfers a larger body of volume to the lower parts of the capsule, as preferred by the gravitational potential energy. The total arc-length of the capsule thus increases, trading stretching energy against gravitational potential energy. For negative gravitational pull, the effect is inverted, since the gravitational potential energy prefers having as much volume as possible close to the capillary.

4.6 Capsule contact at constant volume

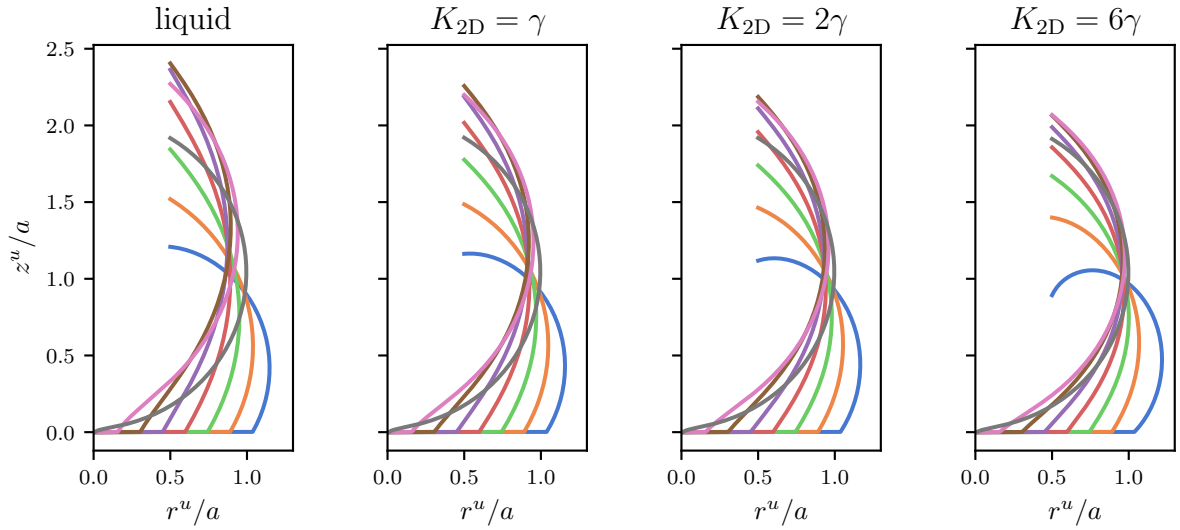

Figure 4.14: A deformation sequence at constant enclosed volume $V^u = V_0$ and with a mirror-symmetric contact. Shown is only the first quadrant of the shape, where the full shape is recovered by symmetry. The shape sequences have varying elastic moduli and the visual appearance of the deformation sequence only differs in details, such as the total height, or the angle at the capillary at $s = L$. A more detailed investigation reveals that the external forces required to achieve the respective shapes vary distinctively, leading to a modified adhesion behavior and a hysteresis.

The convenient parameters to control from the theory point-of-view are the apex stresses $\tau_s^{u,d}(s = 0)$ and the contact length l, since they are immediately used in the integration routine. Unfortunately, they are not the parameters usually controlled during an experiment. Instead, an easily accessible control parameter is the respective volume of the configuration $V^{u,d}$. Controlling the volume during a contact sequence is experimentally more accessible than controlling the apex stress $\tau_s^{u,d}(s = 0)$. From the theoretical point-of-view this is an unpleasant control parameter, because in order to control it, we must iteratively search for the proper initial meridional stresses, which generate the prescribed volumes. This adds another layer of complexity on top of our numerical approach. As already shown in Fig. 4.8, the path of constant volume snakes through the $\tau_s^{u,d}(s = 0)$-l shape space along a sine-like curve. The numerically demanding task is to iteratively search for exactly these curves through the shape space at given control parameters and volumes $V^{u,d}$. Finally, we choose to use a bisection algorithm [21] in order to find the shapes with appropriate volume.

In Fig. 4.14 we fix the volume to that of the reference liquid droplet $V = V_0$ for all deformed shapes and progressively increase the contact length l. Additionally, we show the changes to the shapes caused by the elastic modification of the interface from left to right. Note, that the liquid shapes are integrated with a different solver than the elastic shapes, simply because the notion of stretch and reference shape get lost, which our elastic solver relies on. Essentially, when setting $K_{2D} = 0$, we are dividing by zero when inverting Eqn. (4.74). This is of course only a numerical problem and is solved by integrating the shape equations of the liquid contact problem separately which is simple such that we will not discuss it here [22].

At $K_{2D} \sim \gamma$, the visual difference between the deformed shapes is not immediately obvious but starts to become more pronounced for $K_{2D} \geq 4\gamma$. The difference in the deformed shapes is caused by the additional force required to deform the elastic interface. During this deformation sequence

[21] Similar to the one used in the shooting process for the respective pressures.
[22] Similar to the integration used in Sec. 1.1 and Ref. [24] with the appropriate initial conditions.

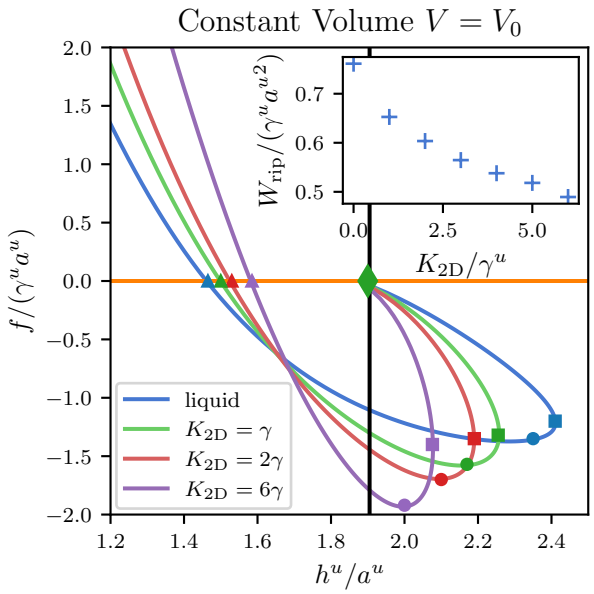

Figure 4.15: The total height of the capsule h^u and the external force required to achieve the specific configuration are shown for the deformation sequences in Fig. 4.14. A change in the two dimensional compression modulus reveals the distinct differences introduced by the elastic skin. The force required to rip the capsules apart rises with the elastic modulus, while the work required to do so W_{rip} decreases. Additionally, the colored markers indicate several distinct regions along a contact hysteresis. The shapes come into contact first at the green diamond, then immediately transfer to the colored triangles (with force control) from which they need to progress towards the colored circles in order to separate again. If, instead, the separation distance is controlled, the shapes only separate at the colored squares. The ripping work is exactly the area under the respective force-height lines.

we prescribe the contact length l and let the required external force f and the total height $h^{u,d}$ settle in. The forces and total heights required to achieve a given contact length are modified by the elastic skin, as shown in Fig. 4.15. Following the deformation sequence along the colored lines in Fig. 4.15 reveals that the shapes come into contact first at the green diamond, where, if the external force is zero $f = 0$, they instantaneously slip along the orange horizontal line at $f = 0$ to the corresponding triangle, where a stable force balance is achieved. The stable point differs not only in total height, but also in contact length l. Increasing the compression modulus at zero external force, leads to a decrease in the contact length and a decrease in the total height h^u compared to the reference shape. This makes intuitive sense, since the elastic skin additionally resists a deformation away from the reference shape and thus decreases the energy advantage obtained from the adhesion in the contact zone due to an increase in elastic energy.

In order to separate the shapes again, starting at the colored triangles in Fig. 4.15, we need to trace through the negative forces along the respective colored lines up to the colored circles [23]. At the circles, the biggest separating force is required. If we control the pulling force, the shapes will separate at the colored circles, as an increase in the pulling force will yield no stable solution anymore. The detachment following from here is a complex dynamic process not captured by the present theory. Ultimately, however, the shapes will separate at this point, simply because there is no configuration beyond this pulling force which satisfies a force balance.

The magnitude of the maximal separating force f_{rip} is increased by an increase in K_{2D}. Counterintuitively, this does not mean that the shapes stick together more strongly. Instead, the height of the energy barrier locking the shapes together is a better measure of how strongly the shapes stick together. The height of this energy barrier is exactly the work required to rip the shapes apart W_{rip} and is obtained by integrating over the colored curves from the colored triangles up to the colored circles. The ripping energy barrier height is shown in the inset of Fig. 4.15 and shows a decrease of the energy barrier with increasing K_{2D}. The elastic shapes thus stick together with greater force, but the work required to separate them is decreased with increasing K_{2D}. In a sense, the compound could be considered as being increasingly brittle with increasing K_{2D}.

If, instead of the pulling force, the separation of the shapes h^u is controlled, the contact sequence

[23] Along increasing h^u.

behaves distinctly different. The shapes still come into contact first at the green diamond at zero external force, then, however, they instantaneously slide along the black vertical line to the corresponding intersection point on the respective colored line with negative external forces. Bringing the shapes closer together, by decreasing the separation of the capsules, increases the external force from here on [24]. Separating the shapes again requires an increase in the separation, beyond the original contact separation up to the colored squares along the colored lines. Increasing the separation any further does not yield stable configurations anymore, such that the shapes must separate after this point.

Both for force and for separation control, we see a hysteresis in the contact behavior, induced entirely by the adhesion between the two capsules. Deactivating the adhesive effects by setting $\gamma^{u,d} = \gamma^{i}$ and $\gamma_{\mathrm{ud}} = 0$ [25] eliminates the hysteresis entirely.

4.7 Elastic meta-materials and the elastic capsule unit cell

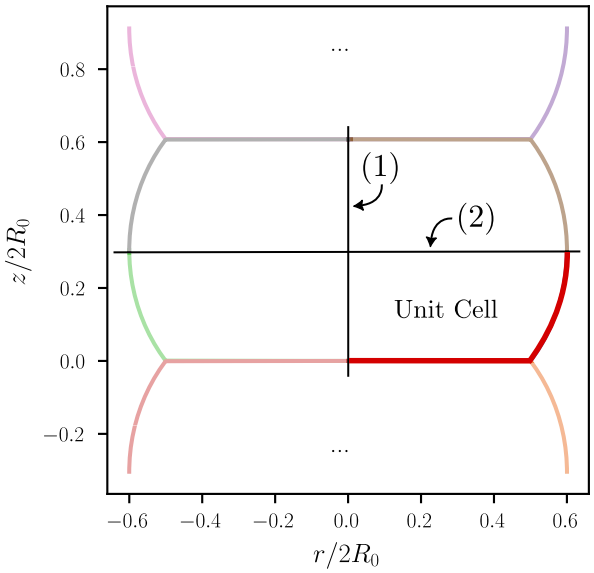

Figure 4.16: We are able to solve an entire column of stacked elastic capsules by exploiting certain symmetries. The unit cell of the column is only one quadrant of the actual full solution of a single capsule from the column, since we are able to construct the remaining quadrants by reflections at the symmetry lines indicated as (1) and (2). The full solution of a capsule column can be constructed by additionally translating the unit cell solution along the z-axis. Using the elastic unit cell to characterize an entire stack of capsules is only possible if gravitational effects are negligible and if all capsules share the exact same control parameters. Otherwise, the entire stack needs to be solved, by explicitly integrating all contributing (coupled, through the contact pressure) capsules.

Determining the macroscopic elastic properties of materials is important to properly characterise the acoustic and mechanical response functions of the material. Ultimately, the material constants allow to precisely manufacture sound absorbtion, thermal insulation or structural mechanical properties [119], [120]. We would thus like to discuss how we can apply the present theory to improve the understanding of a particular meta-material geometry.

In all of our considerations, we are limited by our initial assumption of axi-symmetry. So far we have discussed a single contact between two capsules. Increasing the number of contacts to beyond two is not possible, as it would require at least one of the contacts to not be on the symmetry axis. We can however investigate one further contact scenario. Here, we have three capsules stacked on top of each other, as seen in Fig. 4.16. This stack of elastic capsules could be considered as a column in an elastic meta material. However, because of the limitations axi-symmetry entails, this column does not interact with any other material column. While the present theory allows for a multitude of scenarios (e.g. gravitational effects, different elastic properties for all capsules etc.) we want to focus on the most simple scenario first. The most simple scenario is that where

[24] Lowering the separating force up to the colored triangles, then requiring a compressive external force to bring the capsules closer together.
[25] I.e. the contact angle vanishes.

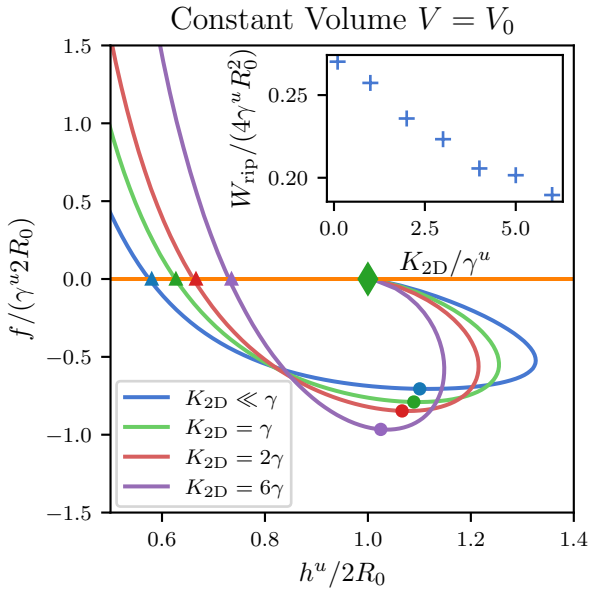

Figure 4.17: The total height of a single capsule h^u in a column of similar capsules against the external force required to achieve the configuration. The qualitative behavior is similar to that seen in Fig. 4.15 but shows qualitative differences because the boundary conditions and reference shapes differ conceptually. Here, mirror-symmetry must be enforced such that there is a vertical tangent at exactly half the total undeformed length, where the boundary condition in Fig. 4.15 is to reach the capillary. Note that the length scale is now set by the size of the reference spherical liquid droplet, such that this figure is universal for all contact unit cells.

all capsules of the column have the same fully spherical liquid reference shape and have identical elastic constitutive properties. Additionally, we want to disable gravity.

In this scenario, we have a multitude of symmetries. First, all of the capsules in the column have the same deformed shape. Second, the solution of a single capsule in the column is mirror-symmetric with respect to a horizontal plane at half the total height of the capsule.

Similar to the approaches in foam mechanics [121], [122], we can define an elastic unit cell of the capsule column. The unit cell of the capsule column is a capsule which has a reference shape with the parameters $\tilde{p}_L = 4$ and $\Delta\tilde{\rho} = 0$ [26]. This sets the natural length scale as the diameter of the reference liquid sphere and eliminates the dimensionless pressure of the reference shape as a control parameter. All of the deformed unit cell capsule solutions must satisfy $\Psi(s_0 = L_0) = \pi/2$, which ensures mirror-symmetry (see the red line in Fig. 4.16). The full solution of a single capsule in the column can then be generated by reflecting the solution of the unit cell at the horizontal plane at $z(s_0 = L_0)$.

To find the appropriate deformed unit cell shape, we search for the pressure of the deformed configuration, such that the boundary condition $\Psi(s_0 = L_0) = \pi/2$ is satisfied. This still leaves us with two further control parameters, i.e. the contact length l or force f, and the meridional apex stress $\tau_s(s = 0)$ or the volume V. If we control the enclosed volume, such that it is constant, as detailed before, we are left with only one control parameter, which is the contact length l or the contact force f. This elastic unit cell behaves qualitatively similar to the elastic capsule on a capillary, as can be seen in Fig. 4.17. The beauty of this unit cell is however, that its properties can be exactly extended to the entire column. All intensive variables, such as the external force stay the same for all capsules [27]. The extensive variables scale by the number of capsules in the column, such as the total height of the column and by extension the ripping work W_{rip}.

Furthermore, we are able to deduce the macroscopic elastic moduli from Fig. 4.17. The contacting system is in a force balance with no external force $f = 0$ exactly at the colored triangles in Fig. 4.17. The region around this point is approximately linear for a certain range of displacement heights h^u.

[26] Which is a perfect half sphere.
[27] Because they are in series.

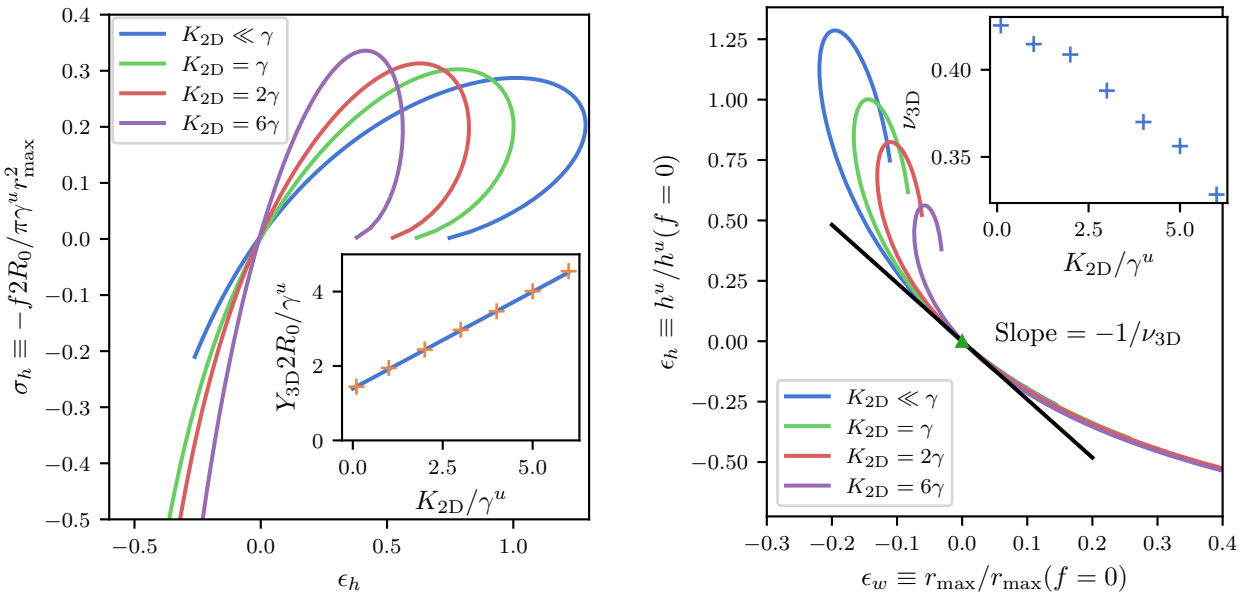

Figure 4.18: The effective three dimensional stress-strain curves of a column of stacked elastic adhesive capsules reveals the effective elastic properties. The slope of the stress-strain curve around the reference (external force free) state at $\epsilon_h = 0$ determines the three dimensional Young's modulus of the entire capsule column (left). We show in the inset (left) that the three dimensional Young's modulus scales linearly with the two dimensional Young's modulus, while it has an offset at $K_{2D} = 0$ caused by the adhesion, which is also present in the purely liquid case. Similarly, we apply a uni-axial force to the capsule column along the z-axis and investigate its strain response in the axial direction ϵ_h as a function of the strain in the radial direction ϵ_w (right). The slope of this curve around the reference configuration (external force free) at $\epsilon_h = \epsilon_w = 0$ reveals the three dimensional Poisson's ratio ν_{3D} of the capsule column. We find that the three dimensional Poisson's ratio decreases with an increase of the two dimensional compression modulus K_{2D}, as can be seen in the inset figure (right).

We can imagine an arrangement where multiple columns of this kind are placed in a grid, such that they are immediately neighboring, but not contacting the other columns. This creates a scenario, where we are able to pull on the macroscopic three dimensional material in the direction of the column orientation and measure its effective elastic moduli. The three dimensional Young's modulus is defined as the force per area exerted on the material faces divided by the relative extension of the material. In our case this means that the three dimensional Young's modulus is calculated as

$$Y_{3D} = \frac{f h^u(f=0)}{\pi r_{max}^2 (h^u(f=0) - h^u(f))}, \tag{4.81}$$

where the relative change in the height h^u is exactly the strain ϵ_h induced by the uni-axial force f that acts on the capsule stack over its surface πr_{max}^2. The Young's modulus given in Eqn. (4.81) results from a linearization around $f = 0$, but in principle, we are able to determine Y_{3D} as the slope of the deformation sequences in a stress-strain (σ_h- ϵ_h) diagram. This is exactly what we show in Fig. 4.18 (left). With increasing two dimensional compression modulus K_{2D}, or equivalently increasing two dimensional Young's modulus $Y_{2D} = 2(1 - \nu_{2D})K_{2D}$ (with fixed $\nu_{2D} = 1/3$), we find an increase in the slope of the effective three dimensional stress-strain curve (see Fig. 4.18 (left)). We quantify this increase in the slope by showing the relationship between the three dimensional modulus Y_{3D} and K_{2D} in the inset of Fig. 4.18(left). We find a linear relationship $2R_0 Y_{3D} = \alpha K_{2D} + \beta\gamma^u$ with the coefficients $\alpha \approx 0.52$ and $\beta \approx 1.39$. We have $\beta \neq 0$ because the adhesion between the capsules is also present if there is no elastic skin and introduces a quasi-elastic response to the uni-axial force.

The three dimensional Poisson's ratio ν_{3D} quantifies the deformation of the normal directions (with respect to the axis of loading) when a uni-axial loading is applied. When pulling on the capsule column, the maximum radius of the capsules changes. The proper definition of the Poisson's ratio is given as

$$\nu_{3D} = -\frac{\mathrm{d}\epsilon_w}{\mathrm{d}\epsilon_h} \,. \tag{4.82}$$

We thus determine the three dimensional Poisson's ratio from Eqn. (4.82), or via the slope of the ϵ_w-ϵ_h diagram as we show in Fig. 4.18(right). We find that ν_{3D} decreases with increasing capsule compression modulus K_{2D}. This means that a stiffer capsule material inhibits the contraction of the radial component more strongly than a softer capsule material. This makes sense, since the stretching energy required to pull the capsule into a cylindrical shape (with larger ϵ_w) increases, and it will be energetically favourable to trade-in some adhesion energy at the contact sites to avoid the larger stretching energy penalty incurred alternatively to provide the same axial strain.

4.8 Discussion

We provide a detailed discussion of the contact between two elastic capsules and the contact of a single elastic capsule and a solid wall. The present discussion enables the design of experiments and novel shape fitting methods to deduce adhesive properties of thin walled elastic capsules. We show that the coupling of both contacting shapes is important to generate the appropriate solutions and discuss the shape equations of the free-slip and no-slip contact coupling case. The differences in the contact coupling are subtle but fundamentally change the problem from being history independent (free-slip) to being entirely history dependent (no-slip). The main result of the theoretical investigation is the set of shape and contact equations, which we derive formally from a variational method and motivate the results with simple force and moment balances. We additionally show that an effective contact angle for small bending length scales may be derived from the variational problem by allowing step angle changes over length scales longer than the bending length scale. These effective contact angles may be used for visual analysis of contacting elastic skins.

We show that gravity has a profound influence on the deformation behaviour. The gravitational effects enter as a hydrostatic pressure contribution into the shape equations, thereby modifying the resulting shapes distinctively. We find that gravitational effects may only be neglected if $\Delta\tilde{\rho}^{u,d} \ll 1$.

Additionally, we parametrize the severely high-dimensional parameter-shape space of this problem and derive approximate relationships for characteristic points in the shape space, possibly to be utilized by experimentalists in the future. One of the main result of the shape space investigation is the detailed analysis of the contact hysteresis created by adhesion effects. Importantly, having force control versus separation control distinctly changes the contact hysteresis and the accessible solutions. In an experiment, both of those control mechanisms could be employed. In the future, experiments could measure both separation and exerted force at known elastic constitutive parameters [28] to determine the adhesive properties of the capsule-capsule system.

Finally, the source code is openly available at `https://www.github.com/FelixKratz/CapSol`, where we provide an interactive Python frontend to easily explore the parameter-shape space.

[28] Determined, e.g. by capsule elastometry (see Chap. 2).

5 Machine learning applications in ill-posed inverse problems

Because the computing power evolved exponentially in the past decades, it has become possible to exploit learning capabilities of machines. The idea of machine learning is as old as computers (or even older) and can be marked as one of the most important technological advances in the 21th century. Creating a machine, which learns to exploit and act on arbitrary correlations found in an appropriately designed set of training data has the potential to shift a multitude of paradigms. Certainly one of them is the solution of ill-posed inverse problems, as we will discuss in this section.

A remarkable application of machine learning is an approach to the problem of protein folding called *AlphaFold* developed at Google DeepMind, which significantly outperforms conventional methods and allows for entirely new design processes [123]–[125]. Of course, in the recent past, capable and powerful transformer networks demonstrate the capabilities of machine learning in the context of natural language processing. A prominent example of such transformer network is *ChatGPT* [126], poised to challenge several paradigms in text processing, text production and more [1]. Further prominent examples of machine learning include image and video generating networks such as *DALLE* and *Sora* [127], where images or entire videos are created from simple natural language text prompts. *AlphaZero/AlphaGo* is an AI playing Chess/Go, able to beat even the most sophisticated conventional algorithms such as *Stockfish* and – of course – the best human players [128]. The aforementioned examples are popular examples, however, the fields of application for machine learning are essentially endless. It is fair to say that the concepts of machine learning currently drive a full grown revolution in several fields of science. For example, in medicine and diagnostics machine learning is able to confidently identify pathological patterns from highly limited data and provide information otherwise unattainable [129]–[131].

Generally, whenever an algorithmic approach to a certain problem is convoluted [2] and sufficient example data is available, a machine learning approach seems to regularly outperform the algorithmic approach [24]. Here, we will discuss applications of machine learning in ill-posed inverse problems. The steps required to create a successful machine learning approach to an inverse problem include but are not limited to:

- Find a suitable parametrization for the problem.
- Understand the intrinsic accuracy limitations of the problem.
- Create a training data set which contains labeled samples for the inverse problem and respects the physics of the problem, e.g. covers the parameter space appropriately.
- Design a network architecture capable of learning the appropriate correlation from the training data set.
- Probe the resulting network and compare it to other methods.

This will be the general recipe for the following sections, where we will investigate several inverse problems and accelerate their solution with the help of machine learning.

[1] This thesis text is created without use of any neural network or AI. Possibly being one of the last of this kind.

[2] E.g. by having many edge cases, being ill-conditioned, having many hyperparameters or using phenomenological assumptions.

5.1 Liquid droplet machine learning tensiometry

> **Notice** – This section is a continuation of the author's publication [24] and master thesis [45].

We can intuitively understand that we should be able to provide a more efficient and severely faster method for determining the control parameters of the Young-Laplace equation from a single image than the previously detailed numerical fitting approach (see Sec. 2.1). A fundamental shortcoming of the numerical inverse approach is that it has no *memory* or deeper *understanding* of the problem [3]. Rather, every shape is fitted without any use of the information about previously fitted shapes – this is a history agnostic algorithmic approach. While this approach has a certain elegance because it is entirely deterministic, it is simply inefficient. The major overhead with the algorithmic approach stems from the necessity to sample the residual gradient landscape anew for every individual shape fit. While this problem itself may not be considered ill-posed, as we have shown that a stable algorithm exists for its solution (see Sec. 2.1), we will use it as a first introductory problem. Later problems will indeed be ill-posed in the mathematical sense.

On the contrary to an algorithmic approach would be a lookup table, where several fitted shapes are characterized in a suitable way [63], [64], [67] and the appropriate values are provided essentially for free from any computational effort – as long as some similar shape is already in the lookup list. Ultimately, we do not want to create a large lookup table because it is too inflexible, but rather a highly compressed representation of that lookup table, where functional correlations are exploited to reduce the amount of storage needed. Because we have severely limited knowledge about the correlations in shape-parameter space, implementing these heuristics on an algorithmic level ourselves is unreasonable. However, we are able to generate $\sim 1000\,\text{shapes/s}$ as solutions to the purely liquid shape equations on a single laptop CPU core. This enables us to easily sample the parameter space in reasonable time to generate a large sample data set. This brings us into a position where we have essentially *unlimited* sample data available. The only part missing to the puzzle is a clever – and in the best case autonomous – way to use this data set to extract the relevant information. Finally, we can realize that a fully connected deep neural network is exactly what can do this job for us. Without us supplying any bias, we can simply provide the sample data set – essentially an uncompressed lookup table – to the network and let it find a sufficient compression for it. This compression is found in terms of a set of correlations, implementing a mapping function from shape space to parameter space by use of the trainable weights and biases of the network. Furthermore, because the network learns to exploit the fundamental correlations of the problem, it does more than learning a simple compression, it rather learns to generalize the problem to data never seen before. A naïve upper bound for the compression ratio [4] may be found simply by comparing the information contained in the training data set and the weights and biases. While the training data set contains data of size $\sim 10^{10}\,\text{Bytes}$, the final weights and biases only contain data of size $\sim 10^{7}\,\text{Bytes}$, which sets an upper bound for the compression ratio at $\sim 10^{3}$. The elegance of this approach is its independence of any human bias [5] and its generalization potential, where it fails to provide us with any insight about its exact inner workings. In essence, we create a highly capable black box [6]. Retroactively, we can of course verify that this black box does what we expect it to do, which is exactly what we will discuss in the following. Once the

[3] Altough some understanding is coded into the algorithm, the algorithm still requires an iterative approach, manifesting that deeper knowledge about the inverse problem solution space is lacking. In a sense, we use "deeper understanding" as a way to describe the fact that a solution to the problem is created ad-hoc, witout need for initial guesses and iterations.

[4] This is only a bound because we did not show that the training data set is minimal.

[5] Under the assumption that the training data set sufficiently characterizes the problem.

[6] Similar to the human brain, which is also essentially a highly capable black box.

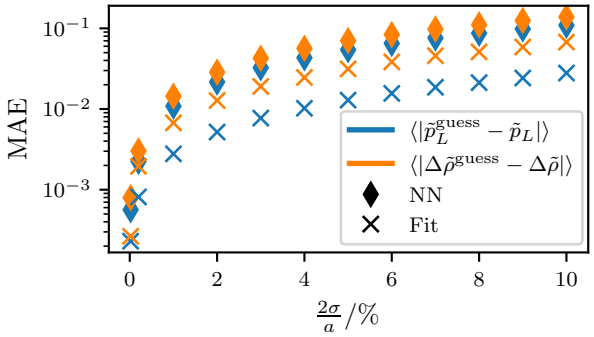

Figure 5.1: The performance of our adapted neural network (NN) as compared to the highly optimized numerical solver. The NN provides its guess three orders of magnitude faster than the numerical fit. The precision of the NN is consistently lower than that of our numerical shape fit. This would not be true if both methods are only allowed to take the same amount of time. We additionally quantify the resistance to noise by applying a Gaussian noise with standard deviation σ to numerically generated shapes and only then feed them back to the respective inverse solver.

black box is trained, evaluating shape data never seen before will cut out any numerical fitting overhead and only include trivial GPU accelerated matrix multiplications to find a proper result.

As we showed previously in Ref. [24] such approach can compete with a numerical fitting algorithm in all metrics and severely beats it in terms of computational cost. While we used a fixed arc-length sampling ($\Delta\tilde{s}_0 = 10^{-2}$) in Ref. [24] for the input shape data with a maximum of 226 coordinates, we now want to always provide 250 equidistantly spaced ($\Delta\tilde{s} = \tilde{L}_0/250$) points to the input layer of the network. The problem with the prior sampling approach is that small shapes only have few data points and large shapes do not entirely fit into the 226 coordinate slots available, leaving out information towards the capillary. Both of these problems are efficiently countered by adapting the input data format of the network. Additionally, since computing the benchmark with the numerical fit in Ref. [24] many improvements to it are implemented (as detailed in Sec. 2.1), such that the numerical benchmark now is consitently lower than that presented in Ref. [24].

An updated performance comparison is provided as Fig. 5.1. The NN is able to accurately solve the inverse problem and has generalized well, as indicated by the low MAE in Fig. 5.1. However, the numerical solver outperforms the NN across all noise levels σ, which is reasonable when considering that it uses three orders of magnitude more time to do so. Additionally, the numerical shape fit is able to continuously probe the shape equations to find the actual minimum of residual shape error, where the NN has no feedback and essentially creates an ad-hoc one-shot guess [7]. Still, the NN is capable of solving the inverse problem in high precision, while presenting high throughput capabilities. This makes the NN approach interesting for real-time or ad-hoc data analysis, e.g. for rapid feedback during experiments. Additionally, this approach marks a proof-of-concept, where we show that machine learning approaches are well versed to solve intricate numerical inverse problems efficiently. We will built on-top of the knowledge acquired here in order to extend the conceptual approach to more involved problems in the following sections.

[7] If the numerical solver only had one iteration available, the performance would be significantly worse.

5.2 Elastic capsule machine learning elastometry

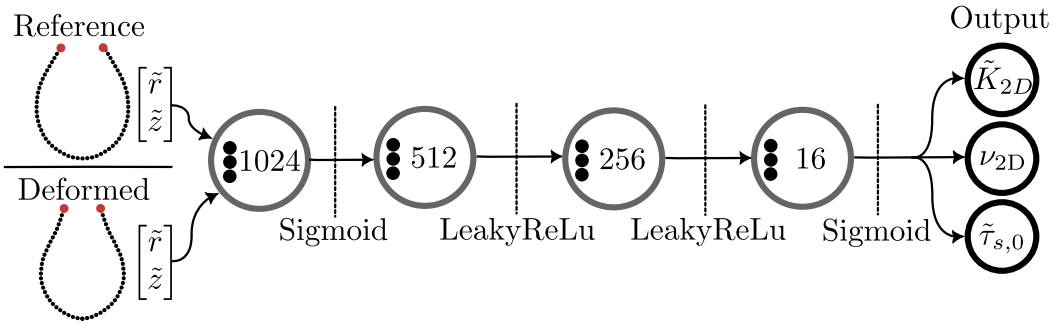

Figure 5.2: The neural network we employ for capsule elastometry has a simple feed-forward architecture. We provide discretized shape information of the elastic reference shape, along with shape information of a sufficiently elastically stressed shape as an input. The input is passed through a number of hidden layers, until finally, the output of the network provides information about the non-dimensional control parmameters of the elastic capsule.

As we showed in the previous section and Ref. [24], it is possible to determine the control parameters of pendant droplets (i.e. no elastic or viscoelastic stress contributions) with high precision via a neural network. Here, we want to adapt this approach to elastic capsules. The task at hand is thus to create and train a set of weights and biases which solve the inverse problem of determining the constitutive elastic parameters from deformed capsule shapes. We have shown in Sec. 2.2 that finding a stable algorithmic approach is highly challenging, where the proper choice of the shooting parameter is imperative for the success of the numerical approach. A distinction between an ill-conditioned and an ill-posed problem can be made, where ill-conditioned problems are sensitive to noise, ill-posed problems have parameter space regions where the inverse problem, even under ideal circumstances will not converge. We discuss the ill-posedness of the elastic shape fitting problem in Sec. 2.2.

The merits of using a machine learning approach for an inverse problem of this kind is an orders of magnitude faster execution time once the machine has been trained. Because the training has to be performed only once, the performance benefits always pay off in the long run. However, improvements in performance should not come with significant loss in precision or traceability. Conveniently, we are not depending on experimental training data, since we can generate the training data from the numerical realization of the forwards problem. This eliminates a possible bias introduced when labeling experiment training data and makes this approach bias-free as long as the sampling of the training data set is cautiously performed. Furthermore, we do not depend blindly on the guess of the machine but are able to feed the reconstructed parameters back into our numerical solver and thereby calculate a true shape residual. This allows us to keep traceability of our networks in check. Whether precision can be retained by our machine learning approach can only be evaluated once the networks are trained.

We already discussed the problem in detail for the numerical approach to the inverse problem (see Sec. 2.2) and can reuse the gathered knowledge for the machine learning approach. Furthermore, similarly to the tensiometry problem discussed in Sec. 5.1, we have access to essentially unlimited sample data. Our numerical forwards solver is able to produce up to 67 shapes/s on an M1 Pro CPU, using 10 CPU cores. Thus, we are again able to generate a labeled training data set with our numerical solver, where we solve the forward problem (i.e. solving the shape equations) for a given, randomly sampled, set of control parameters.

Again, we use a deep neural network to extract the fundamental correlations from the training data set, allowing the trained network to generalize to data never seen before and hence provide

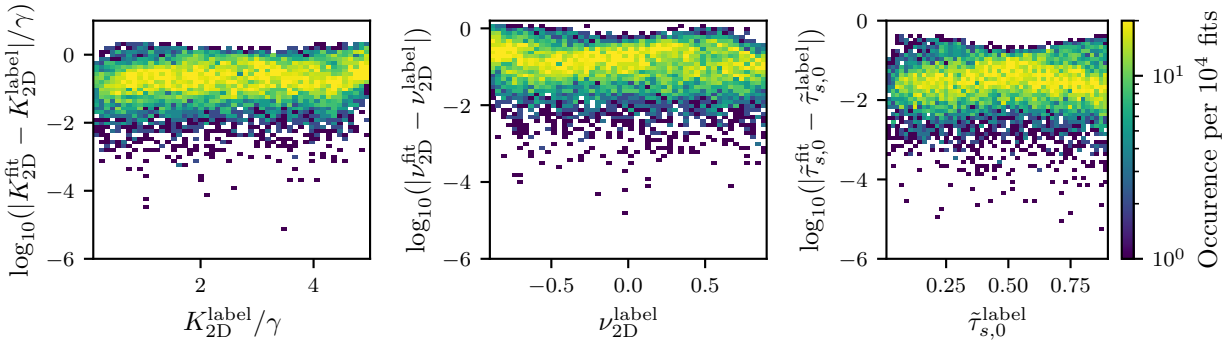

Figure 5.3: The precision of our trained neural network is within a drastically narrower band than the numerical fit (compare to Fig. 2.4). This means the best case performance of the NN is worse than the best case performance of the numerical solver, while the worst case performance is better for the NN. On average, the NN beats the numerical shape fitting approach in precision roughly by a factor two, while being six orders of magnitude faster.

an appropriate estimate for the control parameter set from experimental image input. We start our discussion by detailing the architecture of the neural network we employ.

5.2.1 Architecture

We choose an architecture similar to that used in the liquid droplet problem in Ref. [24], where some important modifications are made. The input for our neural network will be a set of shape coordinates of the undeformed reference shape (i.e. a liquid droplet) and a set of shape coordinates from the deformed elastic shape. This is the same input that our numerical inverse solver requires. While it would theoretically be possible to only provide a single deformed image and fit the accompanying reference parameters along with the constitutive parameters, the resolution of the shape needed for this to reliably work would be unrealistic. Additionally, in the future, a systematic approach for infering the "true" reference shape could be made available. Of course, we could also provide any number of deformed shapes from a deformation sequence to the machine to improve precision. For this work, we will focus on the most simple case first, where we provide a reference shape and a single deformed shape. A schematic of the network architecture is provided as Fig. 5.2.

We need to take some care to consider which information is actually available in an experiment and choose the training data such that we are able to apply the neural network to experiment data as well. In the numerical implementation, we integrate the shape equations in terms of the undeformed arc-length coordinate s_0. Creating a set of shape coordinates sampled naively, e.g. equidistantly spaced along the undeformed arc coordinate s_0, will provide the network with information implausible to obtain experimentally, since in an experimental image the shape is always obtained as a function of the deformed, geometric, coordinate s at first. This is a very important observation, as a sampling in the undeformed arc coordinate implicitly provides information about the local stretches λ_s and λ_ϕ. We thus sample our numerical solutions equidistantly in terms of the *deformed* arc length coordinate s, such that we acquire 250 pairs of shape coordinates $(r(s), z(s))$. We flatten the shape coordinates of both the reference and the deformed shape, and supply them to the neural network as a list with 500 entries. This is the only information the neural network shall receive.

The shape coordinates are propagated through a fully connected feed-forward neural network with

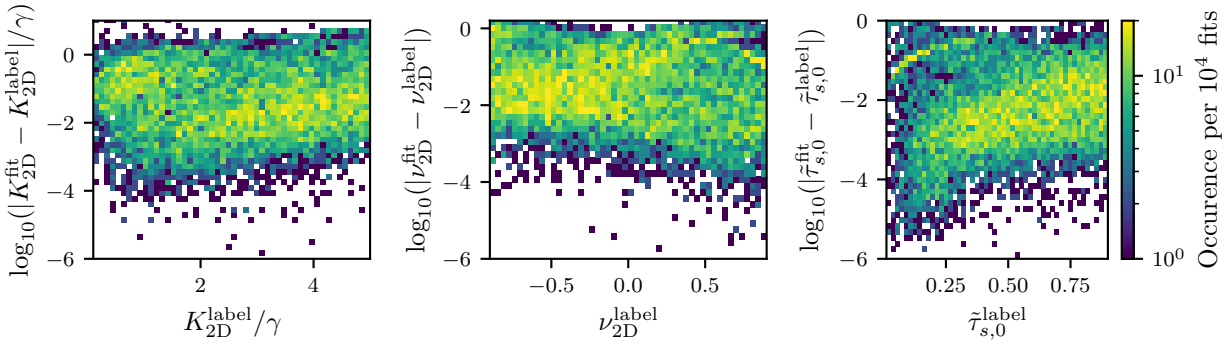

Figure 5.4: We employ a hybrid shape fitting technique, where we provide an informed initial guess for the control parameters by evaluating the shapes with our NN first and only then starting the numerical shape fit. This allows us to combine the strengths of both approaches, significantly reduce computational cost and improve overall precision.

four hidden layers (see Fig. 5.2). The first layer has 1024 neurons and is activated with a *sigmoid* function. This is done to normalize the input. The second layer has 512 neurons and is activated with a *LeakyReLu* function. The third layer has 256 neurons and is activated with a *LeakyReLu* function as well. A motivation why to use *LeakyReLu* instead of *ReLu* functions is given by the vanishing gradient problem [132]. Finally, we have a layer with 16 neurons directly connected to the output layer with 3 neurons and a *sigmoid* activation. The final layer is passed through a sigmoid function, such that the outputs map to the target domain of $[0, 1]$. This means that the training labels must be normalized to the range $[0, 1]$ before supplying them to the training process. Since K_{2D} is unbounded, we artificially choose an upper bound for the sampling process of $K_{2D} = 5\gamma$.

We are able to generate up to 67 shapes/s, utilizing up to 10 M1 Pro CPU cores for the numeric solution of the shape equations. This allows us to generate a large training set, consisting of 500.000 individual pairs of deformed and undeformed elastic shapes. 90% of these are used in training, while the remaining 50.000 shape pairs are used for evaluation at the end of each training epoch to detect over-fitting. Generally, over-fitting can be a problem when the capacity of the network is on the same order of magnitude as the training data sets size, this is not the case here, hence we do not expect or see over-fitting.

5.2.2 Hybrid Shape Fitting

Generally, the best-case precision of the network is not as good as the best-case precision of the numerical fit, as can be seen by comparing Fig. 5.3 and Fig. 2.4. However, the worst-case precision of the network is better than that of the numerical shape fit and most importantly, the network produces guesses close to the actual control parameters more frequently than the numerical fit. This manifests in the average precision (MAE) of the network being roughly a factor two more precise when averaging over all 10.000 fitted shapes. We also have to keep in mind the drastically different computational costs of those evaluations. While a numerical fit on a modern 10-core CPU takes on average 5 s, the network produces its guess in 10 μs – the NN is roughly six orders of magnitude faster.

We realize that the numerical fit has stability problems produced by the nature of the parameter space minimum search, which are most pronounced if the initial guess for the shape fitting is too far away from the global minimum. Conversely, the machine learning approach has problems

achieving precision in the vicinity of the global minimum but can predict the approximate vicinity of the global minimum reliably. Hence, we are able to *combine* both approaches to achieve an overall superior fitting performance. In extent, we first create a rough approximation of the control parameters using the neural network. This rough approximation brings us in the vicinity of the global minimum in the parameters-error landscape. We then use this approximation as the initial guess for the numerical fit. Since the numerical fit now already starts in the vicinity of the global minimum, we not only circumvent the numerical instabilities of the parameter space search, but also accelerate the numerical fits drastically, since the search is slowest far from the actual minimum. The precision of the hybrid-fitting approach is shown in Fig. 5.4

The first approximation of the control parameters by the ML approach can be created at effectively no additional computational cost compared to the numerical fitting algorithm and leads to at worst the same precision as the numerical fit with a randomly selected initial shape. We can however show that the worst case precision is drastically improved by the hybrid fitting approach. We also note that using the NN to provide an initial guess close to the minimum reduces the computational cost by a factor of ~ 3 on average.

5.3 Machine learning traction force microscopy

Published material – This section is reproduced with modifications and permission from the author's publication [133], © 2023 Biophysical Society. It is a continuation of the work by Lars Möllerherm described in his master thesis [134].

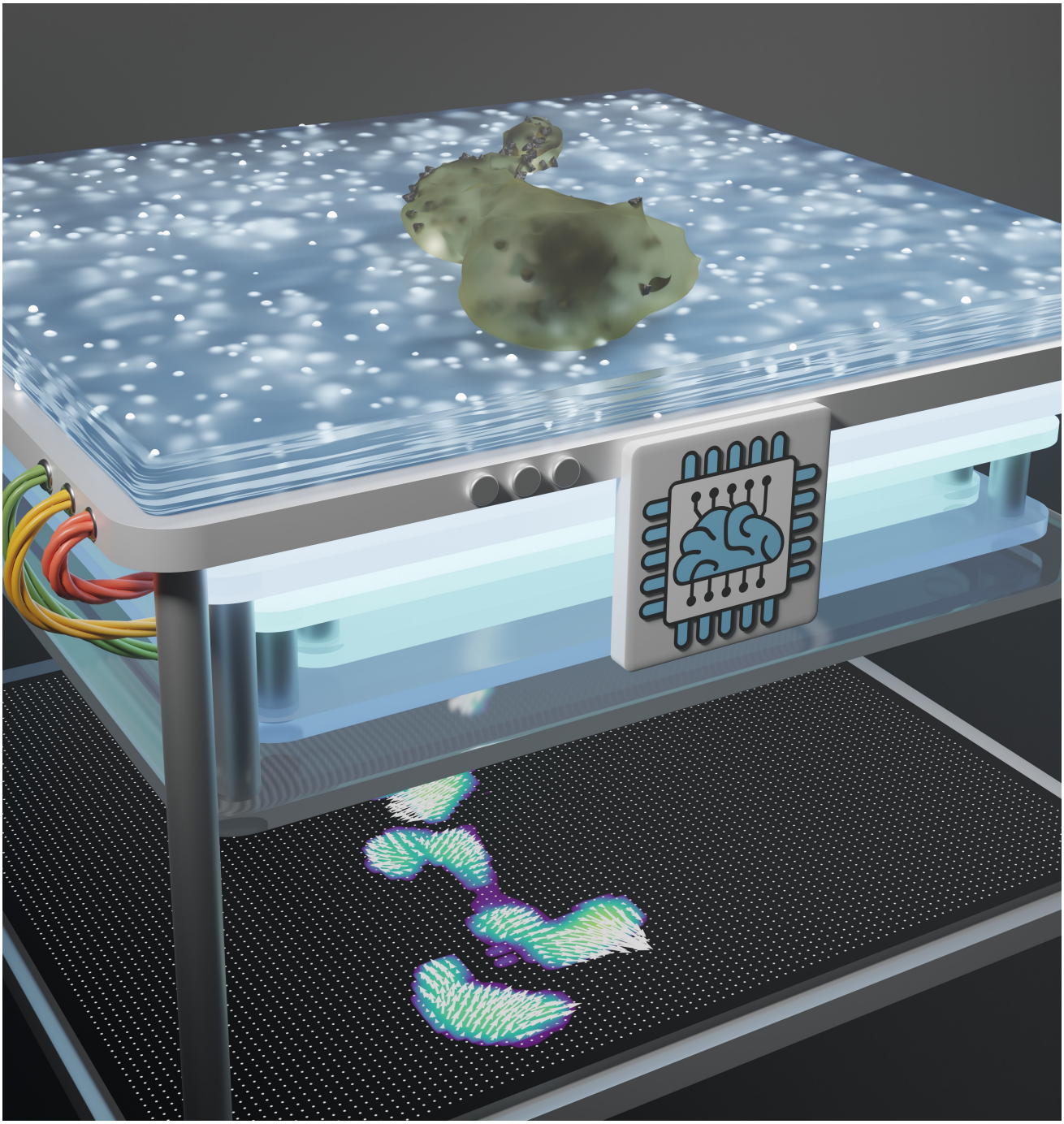

Figure 5.5: An artistic visualization of traction force microscopy. The cell is resting on an elastic substrate with embedded light emitting marker beads. Our machine learning approach (as indicated by the brain-chip) translates the observed marker bead displacements into an accurate cell traction reconstruction (shown as the projection onto the black surface).

Many cellular processes are intrinsically connected to mechanical interactions of the cell with its surroundings. Mechanical surface forces control the shape of single cells or groups of cells in tissue patterns and morphogenesis [135]. Forces alter cell behavior via mechanotransduction [136] and affect cell migration and adhesion. Gaining access to the forces [8] exerted by the cell during critical processes like migration or proliferation can give insight into biophysical processes underlying force-generation and aid the development of novel medication and treatment, e.g. by identifying changes of cellular forces in diseased states. Altered cell behavior is present in diseases [137] like atherosclerosis [138], deafness [139], or tumor metastasis [140].

*T*raction *F*orce *M*icroscopy (TFM) is a modern method designed to measure tractions exerted by an adherent cell. The tractions are deduced from the cell-induced deformations of an engineered external substrate with known elastic properties [141]–[143]. Beyond adherent cells it has applications to a broader range of biological and physical systems where interfacial forces are of interest [144]. TFM thus constitutes a classic inverse problem in elasticity, where tractions or forces are calculated from displacements and given external material properties. This inverse problem turns out to be ill-posed, i.e., noise or slight changes in displacement input data induce large deviations in traction output data because of singular components of the elastic Green's tensor. This technical problem has been addressed by different regularization schemes that have been developed over the last two decades [145]–[149]. As discussed in the previous sections, machine learning can be an elegant alternative to numerical schemes when the inverse problem to a bounded problem is ill-posed in the context of elasticity or rheology. ML-aided traction force determination can thus provide an elegant way to improve TFM as a method, as recent studies have already begun to show [150], [151]. A systematic investigation of ML-aided TFM with respect to an optimal general purpose training set that allows the machine to predict tractions accurately across many experimental situations as well as a systematic investigation of accuracy and of robustness with respect to noise, which is present in any experimental realization, are still lacking.

The first implementation of TFM was achieved by Harris and coworkers in the early 1980s, where thin silicone films are wrinkled by compressive surface stresses, inflicted by the traction field of the cell [152]. Due to the inherent non-linearity of wrinkling and the connected difficulties solving the inverse elastic problem, this method has been superseded by linear elastic hydrogel marker based TFM introduced by Dembo et al. [153]. Due to the simplicity of the hydrogel marker based approach, it is the most commonly used and most evolved method. Alternative techniques and extensions include micro-needle deformations [154], force microscopy with molecular tension probes [155], and 3D techniques [156]. Wrinkling based TFM has recently been re-explored with generative adversarial neural networks with promising results [151].

In this work, we focus on the hydrogel marker based technique and train a deep *C*onvolutional *N*eural *N*etwork (CNN), which has the capabilities to solve the inverse elastic problem reliably, giving fast and robust access to the traction pattern exerted by the cell onto a substrate. Specifically, we do this by numerically solving the elastic forward problem, where we prescribe generic traction fields and solve the governing elastic equations to generate an associated displacement field. The "synthetic" displacement field generated this way is used as a training input for our NN, while we use the prescribed traction field as the labels for our training set. This way, the network learns the mapping between displacement and traction fields and is able to generate traction fields for displacement fields never seen before, while still respecting the relevant governing elastic equations. Complete knowledge of the prescribed tractions for the synthetic training data enables a training process that directly minimizes deviations in the predicted tractions. This contrasts conventional TFM techniques which determine traction forces indirectly by minimizing deviations in the resulting displacement field. We use traction force distributions generated from collections

[8] We are interested in tractions – forces per area.

of circular force patches as training data, which seems a natural general choice to allow the NN to predict generic force distributions in cell adhesion but should also cover other future applications. We show that the proper, physics-informed choice of training data and inclusion of artificial noise is a similarly important step in the ML solution of the inverse problem as the proper choice of regularization in conventional TFM techniques, in order to achieve the best compromise between accuracy and robustness.

5.3.1 Hydrogel Marker Based TFM

The hydrogel marker approach to TFM can be described as follows. First, a cross-linked gel substrate, often Polydimethylsiloxane (PDSM) or Polyacrylamide substrates (PAA) [157], is cultivated. The cross-linked gel can be classified as an elastic substrate with long linkage lifetimes compared to the imaging process [158].

Second, the substrate is coated with proteins prevalent in the extracellular matrix like collagen type I, gelatin, laminin, or fibronectin, allowing the cell to adhere to the substrate. Fluorescent marker beads embedded in the gel substrate aid the determination of cell-induced substrate deformations. The reference and stressed positions of the marker beads can be determined via various microscopy techniques, ranging from confocal to optical microscopy [152].

Third, to infer the displacement field from the marker bead positions, a particle tracking velocimetry (PTV) algorithm, a particle image velocimetry (PIV) algorithm or a CNN particle tracker [159] is used, which calculates the discrete displacement field. The information about the displacement field, combined with the predetermined constitutive properties of the hydrogel substrate gives access to the traction field of the cell via the inverse solution of the elastic deformation problem. For homogeneous, isotropic, and linear elastic solids the displacement field $\vec{u}$ satisfies the equations of equilibrium in the bulk [37]

$$(1-2\nu_{3D})\Delta\vec{u} + \vec{\nabla}(\vec{\nabla}\cdot\vec{u}) = 0\,, \tag{5.1}$$

while the force balance at the surface is modified to account for external tractions $\vec{t}$ [9]

$$\underline{\underline{\sigma}}\vec{n} = \vec{t}\,, \tag{5.2}$$

where $\vec{n}$ is the surface normal vector and $\underline{\underline{\sigma}}$ the stress tensor.

The TFM gel substrate can be considered sufficiently thick to be modelled as an elastic half-space ($z > 0$), bounded by the x-y-plane, at which traction forces $\vec{t} = \vec{t}(x,y)$ are applied. The displacements are a solution of the boundary problem given as Eqn. (5.1) and Eqn. (5.2). Its solution is given by the spatial convolution of the external traction field $\vec{t}(x,y)$ with the Green's tensor $\mathbf{G}$ over the boundary of the surface S [37]:

$$\vec{u}(x,y,z) = \iint_S \mathbf{G}(x-x', y-y', z)\vec{t}(x',y')\mathrm{d}x'\mathrm{d}y'\,. \tag{5.3}$$

The relevant Green's tensor is given by [37], [153]:

$$\mathbf{G}(x,y,z) = \frac{1+\nu_{3D}}{2\pi E}\begin{pmatrix} \frac{2(1-\nu_{3D})r+z}{r(r+z)} + \frac{(2r(\nu_{3D}r+z)+z^2)x^2}{r^3(r+z)^2} & \frac{(2r(\nu_{3D}r+z)+z^2)xy}{r^3(r+z)^2} & \frac{xz}{r^3} - \frac{(1-2\nu_{3D})x}{r(r+z)} \\ \frac{(2r(\nu_{3D}r+z)+z^2)xy^2}{r^3(r+z)^2} & \frac{2(1-\nu_{3D})r+z}{r(r+z)} + \frac{(2r(\nu_{3D}r+z)+z^2)y^2}{r^3(r+z)^2} & \frac{yz}{r^3} - \frac{(1-2\nu_{3D})y}{r(r+z)} \\ \frac{xz}{r^3} + \frac{(1-2\nu_{3D})x}{r(r+z)} & \frac{yz}{r^3} + \frac{(1-2\nu_{3D})y}{r(r+z)} & \frac{2(1-\nu_{3D})}{r} + \frac{z^2}{r^3} \end{pmatrix}. \tag{5.4}$$

[9] Forces per area applied to the surface.

On the surface $z = 0$, this becomes

$$\mathbf{G}(x, y, 0) = \frac{1 + \nu_{3D}}{\pi E r^3} \begin{pmatrix} (1-\nu_{3D})r^2 + \nu_{3D}x^2 & \nu_{3D}xy & -\frac{1}{2}(1-2\nu_{3D})xr \\ \nu_{3D}xy & (1-\nu_{3D})r^2 + \nu_{3D}y^2 & -\frac{1}{2}(1-2\nu_{3D})yr \\ \frac{1}{2}(1-2\nu_{3D})xr & \frac{1}{2}(1-2\nu_{3D})yr & (1-\nu_{3D})r^2 \end{pmatrix}. \quad (5.5)$$

If we have an incompressible polymer material with $\nu_{3D} \sim 1/2$, the coupling between in-plane tractions and out-of-plane displacements is small, such that it is sensible to separate the treatment of deformations into the tangential and normal components relative to the surface of the half-space.

In TFM, it can be assumed that adherent cells exert *in-plane* surface tractions ($t_z = 0$), and we are interested in *in-plane* displacement $\vec{u} = (u_x, u_y)$ only because out-of-plane z-displacements are hard to quantify by microscopy. The approximate problem given in Eqn. (5.3) is now quasi-two-dimensional in the plane $z = 0$, such that the Green's tensor is given by the 2x2 matrix [153]

$$\mathbf{G}(x, y) = \frac{1 + \nu_{3D}}{\pi E r^3} \begin{pmatrix} (1-\nu_{3D})r^2 + \nu_{3D}x^2 & \nu_{3D}xy \\ \nu_{3D}xy & (1-\nu_{3D})r^2 + \nu_{3D}y^2 \end{pmatrix}. \quad (5.6)$$

It solves the elastic boundary problem for in-plane tractions and displacements if the tractions vanish at infinity.

TFM is essentially a technique to provide a numerical solution for the inverse elastic problem posed by asking to recover the traction field $\vec{t} = (t_x, t_y)$ from Eqn. (5.3) via a deconvolution of the right hand side surface integral. This can be done in real space [145], [146], [153] or in Fourier space [160].

Employing the convolution theorem for the Fourier-transform $\mathcal{FT}$ of a convolutional integral, the deconvolution problem encountered in Eqn. (5.3) can equivalently be stated as performing two Fourier-transforms and one inverse Fourier-transform

$$\mathcal{FT}\left(\vec{u}\right)(u, v) = \mathcal{FT}\left(\mathbf{G}\right)(u, v)\ \ \mathcal{FT}\left(\vec{t}\right)(u, v) \quad (5.7)$$

$$\vec{t}(x, y) = \mathcal{FT}^{-1}\left\{\left(\mathcal{FT}\left(\mathbf{G}\right)\right)^{-1}\mathcal{FT}\left(\vec{u}\right)\right\}(x, y), \quad (5.8)$$

which is named *F*ourier-*T*ransform-*T*raction-*F*orce-*C*ytometry (FTTC) [160] and recovers the traction field exactly for perfect displacement data.

Common iterative techniques used for numerical deconvolution can become unstable when subjected to noisy data, which is why conventional approaches to the ill-posed inverse elastic problem rely on regularization techniques (e.g. Tikhonov(L2)- or Lasso(L1)-regularization) coupled with iterative minimization schemes [145]–[148], [161]. This applies both to real space and Fourier space methods. These methods minimize deviations in the resulting displacement field subject to suitable regularization constraints for the traction forces. Regularization improves stability while accuracy might suffer. The optimal choice of regularization parameters is important, but ultimately subjective. In *B*ayesian *F*ourier *T*ransform *T*raction *C*ytometry (BFTTC) the regularization parameters need not be picked manually and heuristically, but they are inferred from probability theory, making it an easy to use and objective FTTC method [149], [162].

The shortcomings of most conventional approaches are systematic under-predictions and edge smoothing of the constructed traction field, caused by the regularization [163], as well as elevated computational effort, inflicted by the computationally demanding iterative deconvolution techniques and transformations at play.

A recent trend in many fields, including the natural sciences, has shown the capabilities of ML-based approaches in such ill-posed and ill-conditioned scenarios [164], [165], often outperforming complex algorithms by orders of magnitude in computing time and precision, and thus allowing for new

and more accessible workflows with reduced computational overhead. ML based approaches to TFM [150] and wrinkle force microscopy [151] have recently been discussed and find that deep CNNs can perform the deconvolution of Eqn. (5.3), by learning the mapping from strain-space to surface traction-space in training. The existing NN approaches show a promising proof-of-concept which we want to extend further in the present work by performing systematic studies of accuracy and robustness to noise. While regularization is particularly important in conventional TFM approaches for accuracy and stability, accuracy and robustness to noise of deep CNNs crucially depend on the choice of training data.

Physics-informed ML methods have also been applied to directly solve general partial differential equations with boundary conditions, such as Eqn. (5.1) and Eqn. (5.2) that are underlying TFM [166]–[168]. In TFM we can solve the elastic problem analytically up to the point that the Green's tensor Eqn. (5.6) is exactly known but proper inversion is difficult. We want to solve this inversion problem by deep CNNs with a physics-informed choice of training data and learning metric.

5.3.2 Machine Learning the Inverse Problem

If we want to teach a machine to solve an inverse problem for us, counter-intuitively, we do not need to know how to solve the inverse problem itself. We only need to know how to solve the corresponding forward problem i.e., we only need to know how to precisely formulate the learning task for the network and provide sample data that characterizes the problem well enough.

We will adhere to the steps outlined in the introduction of the present chapter to produce a capable machine learning approach. The first step is thus to understand the forward problem, including a discussion of the parametrization and limitations of the problem. Additionally, we need to design an appropriate method to generate traction fields akin to those seen in the actual experimental realization of the problem, i.e. we need to understand how real cells anchor to the substrate and find a protocol to create displacement fields for physiologically relevant traction fields.

An additional constraint for our effort is set by the computational time. We should be able to generate an abundance of training data in a computationally traceable time frame. Hence, we will need to employ approximations at the proper place in order to trade-off accuracy of the model for computational speed. As we will discuss in the following, the intrinsic linearity of the problem allows us to employ severe simplifications.

Understanding the forward problem for traction patches

The forward problem we are trying to solve involves cell tractions on elastic substrates. Thus, essential to the performance of our NN is the accurate interpretation of cell-characteristic deformations of the substrate. Cells generate forces exerted onto the substrate via focal adhesion complexes with sizes in the µm-range and tractions in the range $\mathrm{nN\,\mu m^{-2}} = \mathrm{kPa}$ [169]. Forces are generated by tensing acto-myosin stress-fibers that attach to the focal adhesions and, therefore, have a well-defined direction over a focal adhesion complex. Therefore, typical cellular traction patterns consist of localized *patches*, which can comprise single or several focal adhesion complexes and are anchored to the substrate at positions $\vec{r}_i = (x_i, y_i)^{\mathrm{T}}$. Within these patches, tractions have a well-defined in-plane angle γ_i with the x-axis, resulting in a traction pattern

$$\vec{t}_i(\vec{r}) = t_i(|\vec{r} - \vec{r}_i|) \begin{pmatrix} \cos\gamma_i \\ \sin\gamma_i \end{pmatrix}. \tag{5.9}$$

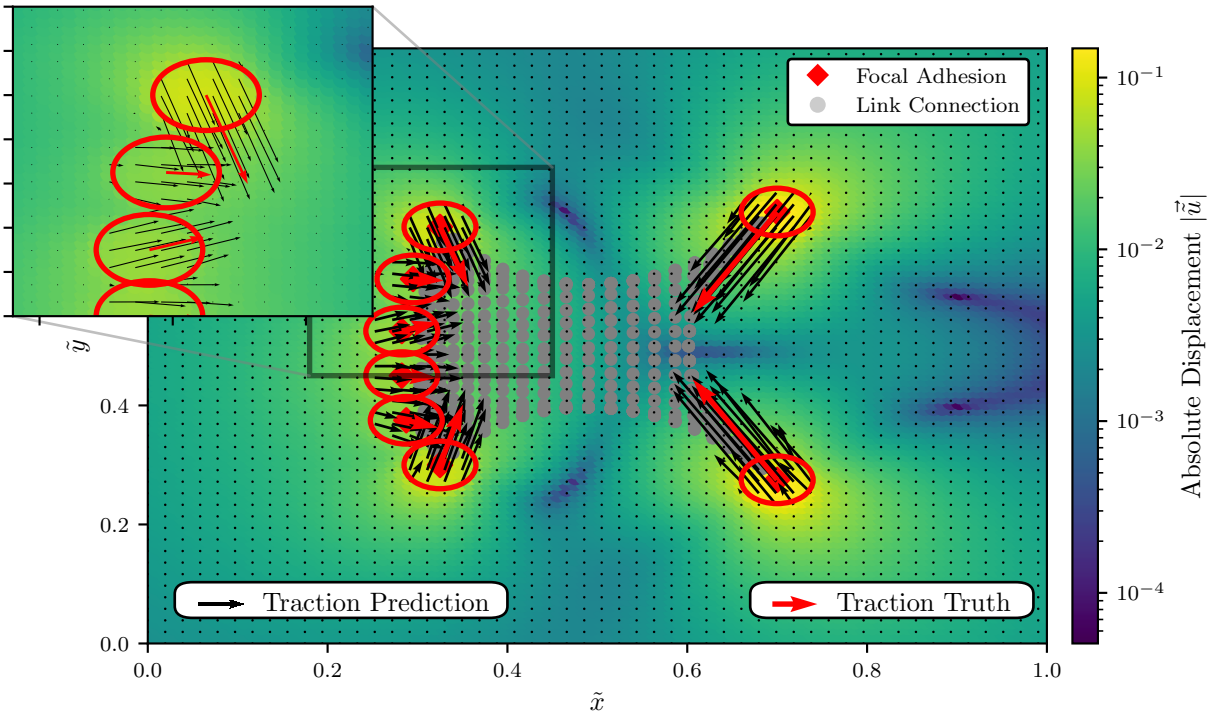

Figure 5.6: A model cell with circular focal adhesion points. The model cell perturbs the elastic substrate it is resting on by generating tractions (red arrows) at the focal adhesion spots (red circles), resulting in the color coded displacement field; tractions (red arrows) are generated based on a contractile network model. Red arrows are the ground-truth average tractions generated by the cell model over the red circles, while the black arrows indicate the local tractions that the $\mathrm{NN}_{\mathrm{low}}$ network predicts at the discrete grid spots.

These tractions are applied to circular patches of variable radius R_i at the anchored nodes (see Fig. 5.6), such that $t_i(|\vec{r}-\vec{r}_i|) = t_{0,i}$, for $|\vec{r}-\vec{r}_i| < R_i$ and $t_i(|\vec{r}-\vec{r}_i|) = 0$ otherwise.

We model typical traction patterns as a linear superposition of traction patches of the type given in Eqn. (5.9), localized at different anchoring points. Within linear elasticity, the resulting displacement pattern is also a linear superposition of all the displacement patterns $\vec{u}_i$ caused by all traction patches i.

For a single traction patch, we solve the forward elastic problem by exploiting the convolution theorem $\mathcal{FT}\{\vec{u}_i\} = \mathcal{FT}\{G\}\mathcal{FT}\{\vec{t}_i\}$ where the Fourier transform of the Green's kernel in polar coordinates ρ and ϕ is known [160]

$$\tilde{G}(\rho,\phi) \equiv \mathcal{FT}\{G\}(\rho,\phi) = \frac{2(1+\nu_{3D})}{E\rho}\begin{pmatrix}(1-\nu_{3D})+\nu_{3D}\sin^2(\phi) & -\nu_{3D}\sin(\phi)\cos(\phi)\\ -\nu_{3D}\sin(\phi)\cos(\phi) & (1-\nu_{3D})+\nu_{3D}\cos^2(\phi)\end{pmatrix}, \tag{5.10}$$

and the Fourier transform of the traction spot is given by $\mathcal{FT}\{t_i\}(\rho) = 2\pi t_{0,i}R_i J_1(\rho R_i)/\rho$, where J_n are the Bessel functions of the first kind.

The Fourier transformed displacement field $\mathcal{FT}\{\vec{u}\}$ is now accessible and can be converted back to the displacement field by performing the inverse Fourier transform $\vec{u}_i(x,y) = \mathcal{FT}^{-1}\{\mathcal{FT}\{\vec{u}_i\}(\rho,\phi)\}$. This can be performed analytically in polar coordinates centered around the corresponding anchored

node with a scaled radial component $\tilde{r}_i \equiv |\vec{r} - \vec{r}_i|/R_i$ and an angle θ with the x-axis,

$$u_x^i = \frac{R_i t_{0,i}(1+\nu)}{\pi E}\left[((1-\nu)N_1(\tilde{r}_i) + \nu N_2(\tilde{r}_i,\theta))\cos(\gamma_i) \; -\nu N_3(\tilde{r}_i,\theta)\sin(\gamma_i)\right] \tag{5.11}$$

$$u_y^i = \frac{R_i t_{0,i}(1+\nu)}{\pi E}\left[((1-\nu)N_1(\tilde{r}_i) + \nu N_4(\tilde{r}_i,\theta))\sin(\gamma_i) \; -\nu N_3(\tilde{r}_i,\theta)\cos(\gamma_i)\right] \tag{5.12}$$

where $N_{1,2,3,4}(\tilde{r}_i,\theta)$ are specific functions, that describe the geometric dependence of the displacement field, and are obtained by explicitly solving the occurring inverse Fourier transforms, as detailed in the Appendix A.5.1. Strictly speaking, this analytical solution of the forward elastic problem for a single traction patch anchored at R_i is valid on an infinite substrate. We will neglect finite size effects in the following, and use this analytical solution also on finite substrates. The solution for many traction patches anchored at different points is obtained by linear superposition.

Numerically solving the forward problem

We consider a square substrate of size $L \times L$, in which displacements are analyzed [10]. Typical sizes are in the range $L \sim 10 - 100\,\mu\text{m}$. We use the size L to non-dimensionalize all length scales: $\bar{u} \equiv u/L$, $\bar{r} \equiv r/L$ and $\bar{R}_i \equiv R_i/L$, such that the substrate in which displacements are observed always is a square which has unit side lengths. Typical focal adhesion patch sizes R_i are in the range of several µm [149], [169]; in dimensionless units, we take $\bar{R}_i \sim 0.05$ as a typical value. The above dimensionless coordinate $\tilde{r}$ remains unchanged by non-dimensionalization.

Furthermore, we use the elastic constant E as a traction scale: $\bar{t} \equiv t/E$. Typical hydrogel substrate elastic moduli of $E \sim 10\text{kPa}$ [149] and tractions in the range up to 5kPa [169] imply typical dimensionless tractions up to $\bar{t} \sim 0.5$. We note that this choice of typical dimensionless tractions does *not* limit our approach to substrates of stiffness $E \sim 10\text{kPa}$, it rather sets an upper bound for the dimensional tractions we allow on a substrate of given stiffness. For example, a substrate of stiffness $E \sim 15\text{kPa}$ would allow dimensional tractions, corresponding to our upper bound $\bar{t} \sim 0.5$, of 7.5kPa. The dimensionless quantities and dimensionless equations are obviously entirely equivalent for a substrate with stiffness $E \sim 10\text{kPa}$ and tractions of 5kPa and a substrate with stiffness $E \sim 15\text{kPa}$ and tractions of 7.5kPa. In addition, we show that our approach is able to correctly predict dimensionless tractions of up to $\bar{t} \sim 3/2$, increasing the available range of dimensional tractions to $3E/2$ (see Appendix A.5.5 for details).

We create a $N \times N$ square grid, on which we discretize the solution of Eqn. (5.11) and Eqn. (5.12) for a supplied traction patch $\bar{t}_{0,i}$ with direction γ_i and use a superposition of the individual patch solutions for all anchored nodes, such that we get the full displacement field for a number of n circular traction patches of variable radius $R_{1,\ldots,n}$.

We discretize both displacement and traction fields on the same $N \times N$ square grid. While generating the displacements in Eqn. (5.11) and Eqn. (5.12) on a discrete grid is simple, we note that the discretization of the traction field needs to be performed with great care. A naive approach for the discretization of the circular traction patches onto a square pixel grid with indices $i, j \in \{1, ..., N\}$ would be the direct discretization of Eqn. (5.9), i.e., to check whether any square segment center point $\vec{c}_{ij}$ is contained in the circular traction patch of radius R_t and center point $\vec{c}_t$. If the center point is contained, the grid segment i, j is assigned the traction $\tilde{t}_0$ of the circular patch. This naive discretization suffers from a critical artifact: it is not force conserving, i.e., does

[10] The total substrate size can be larger.

not conserve the total traction force exerted by the patch, which is given by the area-integrated tractions. This violates the fundamental physical requirement of force balance.

Rather, we present an exactly force conserving traction discretization procedure by calculating the *exact* overlap area A_{ov} of each square grid segment (with side lengths $a = L/N$) and the circular traction spots. Then we assign a corresponding fraction $\tilde{t}_0 A_{\text{ov}}/a^2$ of the traction to each square grid segment. A detailed derivation and discussion of the force-conserving traction discretization we employ is given in the Appendix A.5.2. Finally, we quantify the accuracy gain by the force conserving traction discretization method by computing the errors in the displacement field of a large circular patch that is discretized.

We want to emphasize the relevance of these findings to our approach: As the NN will be trained with the discretized traction fields and we are ultimately interested in an accurate *discretized* traction prediction by our machine, we are forced to deliver as accurate discrete traction field representations as ground-truths for training as possible.

We integrate this force balance conserving discretization algorithm in a solver to generate the displacement fields from arbitrary superpositions of circular traction patches. The solver is implemented in a C/C++ package with a Python binary interface to combine the speed of native byte code with the simplicity of an interpreted language.

Generating arbitrary traction fields via superposition

Because of the underlying linearity of the elastic problem at hand we are able to construct displacements for *arbitrary* traction patterns via superpositions of the circular traction patch solutions. While this might seem obvious, it has far reaching implications for our approach and implies that a solver with the ability to reconstruct traction fields constructed from circular traction patches will also be able to reconstruct *arbitrary* traction fields if the solver preserves the linearity of the elastic problem.

Because we will present our NNs with an arbitrary superposition of circular traction spots, discretized to a finite grid, it is trained to exploit the linearity of the problem explicitly, and we thus expect the networks to be able to solve the more general problem of predicting an arbitrary superposition of traction patches. In a sense, generating superpositions of the analytical circular traction patch solutions is an optimization we employ to reduce the computational effort for generating displacement fields for training, while retaining the relevant properties of the problem, as we will show.

Another implication of this observation is that we are able to check the predicted discretized traction fields for consistency with a supplied displacement field by constructing a superposition of displacement fields for circular traction spots with radius $R_t = a/\sqrt{\pi}$ for each grid point, where a is the distance between grid points. The choice $R_t = a/\sqrt{\pi}$ assures conservation of the total traction force. We implement this method along with our solver to generate the displacement fields from arbitrary superpositions of circular traction patches.

Architecture of the deep convolutional neural network

We choose to employ a *Unet* structure [170] consisting of an *input* encoder, which extracts and compresses the relevant information from the high-dimensional *input* displacement field into a lower-dimensional representation. From the lower-dimensional and compressed displacement information we inflate the dimensionality again with a decoder, such that we finally receive the

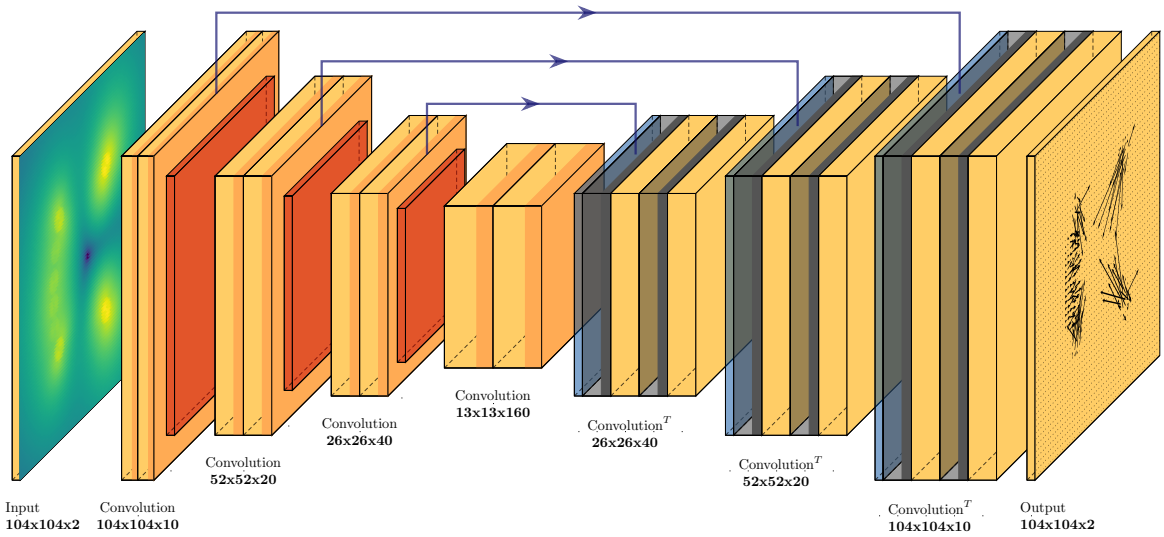

Figure 5.7: The network we employ is a *Unet* Convolutional Neural Network with a discretized displacement field as an input and a discretized traction field as an output. The mapping from input to output is learned in training by adapting the parameters of the convolutional and transposed convolutional layers of the network. Eventually the network will be able to reconstruct the traction field for displacement fields never seen before. We do not enforce a strict bottleneck, rather we allow for skip connections from the encoding process to the decoding process (blue arrows). The skip connections thus offer a way for the network to manipulate the decoding process with selected information gathered during encoding, increasing the capacity of the network.

representation of a traction field in the *output* of the network, as shown in Fig. 5.7. The motivation for this choice is the conceptual similarity of image procession tasks such as segmentation, which involve local classification of an image, to the assignment of local "traction labels" to each grid point of the "displacement image". Furthermore, the elastic problem has long range interactions, where a localized traction spot causes large scale displacements. The layered structure of a Unet is well suited to handle this problem, as the high-dimensional layers process short scale information and the increasingly lower-dimensional layers will be able to handle longer range correlations. Finally, through the process of compressing and reinflating dimensionality we might loose spatial precision and, thus, use the skip connections to provide the upsampling layers with additional spatial information. Additionally, skip connections have been demonstrated to improve generalization potential and stability when used in combination with batch normalization [11] [171].

Our network (as shown in Fig. 5.7) is a fully convolutional NN, where the encoding part is a stack of convolutional blocks, and max-pooling layers, while the symmetric decoding part consists of transposed convolutional layers, skip connections and convolutional blocks. Each convolutional block consist of two convolutional layers, with one *Dropout* layer and *LeakyReLU* activation functions, which introduce non-linearity. Specially, the last layer uses a linear activation function, ensuring that the output maps to the domain of a traction field. The encoding part uses size 3 kernels and size 1 strides, while the decoding part uses size 4 kernels and size 2 strides to avoid checkerboard effects that would otherwise negatively impact performance.

[11] Which is also used in our networks.

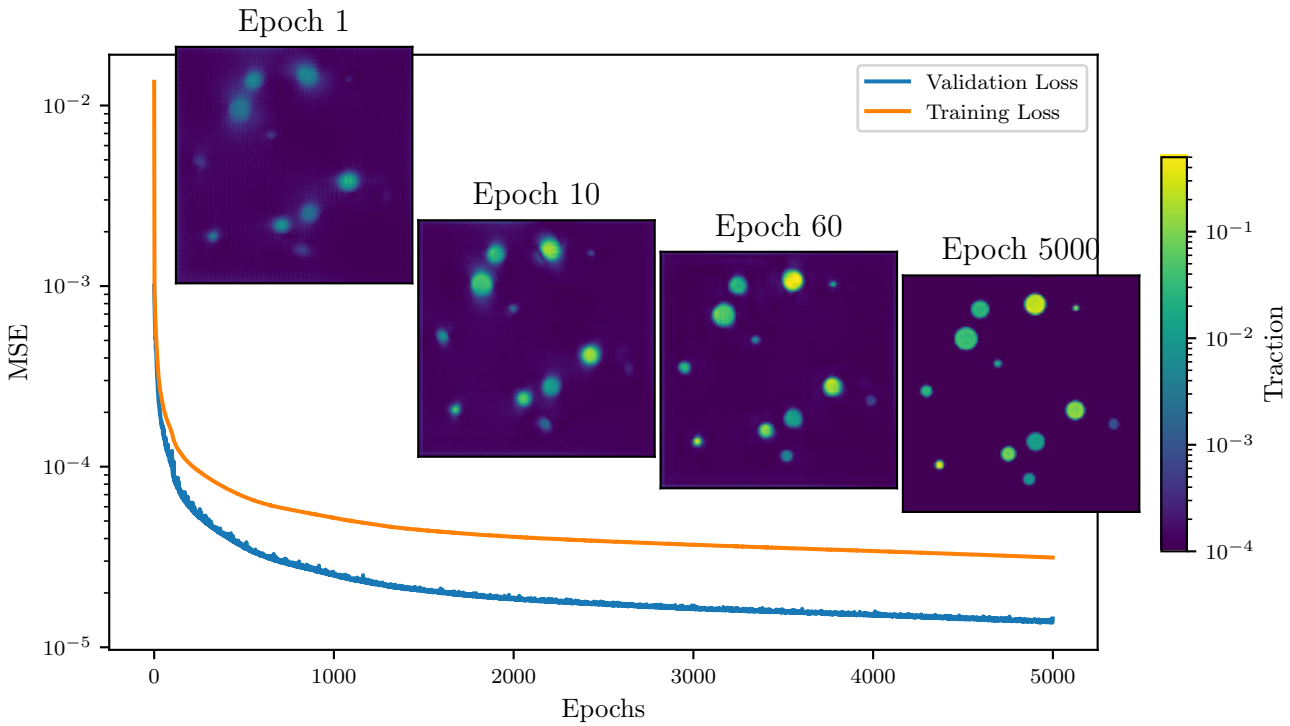

Figure 5.8: The time evolution of training and validation MSE during training of the neural network $\mathrm{NN}_{\mathrm{low}}$. Already after the first epoch a rough traction reconstruction is achieved. After 10 Epochs the reconstruction gains significantly in terms of visual sharpness, which is further increased in the following epochs. We stop the training process after 5000 epochs, because longer training yields diminishing returns.

Training data sampling and the training process

To train our NN we choose a 104×104-grid ($N = 104$) which holds the discrete representation of the dimensionless displacement and traction fields. We will later show that our networks are still able to work on arbitrary grid sizes (with proper scaling of the input), since they are fully convolutional. The training data is generated by numerically solving the explicit forward problem in dimensionless form as outlined in Sec. 5.3.2.

The traction distribution $\vec{\bar{t}}(x, y)$ is generated by a random number (uniformly sampled in $[10, 50]$) of traction spots $\bar{t}_i(x, y)$, where the radius $\bar{R}_i$ is drawn uniformly in the range $[0.01, 0.05]$ with a random center point $\{x_i, y_i\} \in [\bar{R}_i + 0.05, 1 - \bar{R}_i - 0.05]^2$. The traction magnitude $\bar{t}_{0,i}$ is uniformly distributed in the range $[0, 0.5]$ and the polar angle γ_i is uniformly distributed in $[0, 2\pi]$.

While traction values and patch sizes are typical for adherent cells, our training data is more general in the sense that other important characteristics of cellular force patterns, such as the occurrence of force dipoles at the end of stress fibers, are *not* contained in our training data. This makes our approach more general compared to Ref. [150], where training was performed on traction patterns typical for migrating cells. In combination with non-dimensionalization, this will allow us to easily adapt the training process to other applications of TFM in interfacial physics [144] in future applications. Below, we will demonstrate the ability of the CNN to specialize from our general patch-based training set to artificial and real cell data. As a convenient model to generate realistic cell traction data artificially we use the contractile network model of Ref. [172].

We expect a NN trained with noisy data to also perform better when confronted with noisy data.

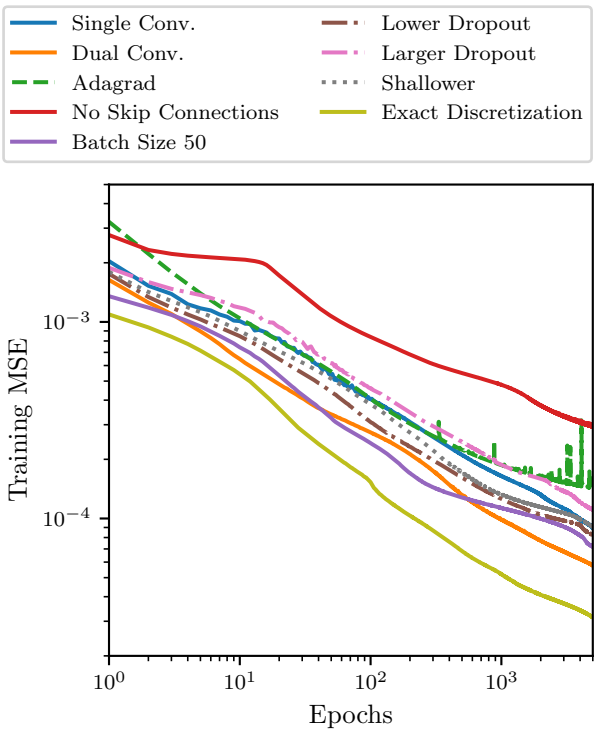

Figure 5.9: The learning processes of different networks where we sweep the hyper-parameter space by changing one property at a time to search for well performing networks. Generally, training follows a power law and we cut off training at 5.000 epochs. It is evident that some networks train and perform significantly better than others. The most striking improvement over the base line (Single Conv, blue) is the network which is trained on training data sampled using the force conserving discretization scheme derived in the Appendix A.5.2 (Exact Discretization, yellow). On the other side, we directly see that disabling the skip connections yields a far worse performing network (No Skip Connections, red). Other modifications yield more subtle changes in performance and are examined in the main text.

To test this hypothesis, we add different levels of background noise to the displacement field $\bar{u}$ in our training data. In order to evaluate the effects on robustness we train two types of NN:

- A network $\mathrm{NN}_{\mathrm{low}}$ is trained with a low level of background noise: To each dimensionless training displacement field value $\vec{\bar{u}}$ a spatially uncorrelated Gaussian noise with a variance $\bar{\sigma}$ that is 0.5% of the average variance of the dimensionless displacement field over all training samples: $\bar{\sigma} = 0.005\langle\sigma_{\bar{u}}\rangle$, where $\langle ...\rangle$ is an average over all training samples.
- A network $\mathrm{NN}_{\mathrm{high}}$ is trained with a high level of background noise which is 5% of the average variance of the dimensionless displacement field over all training samples: $\bar{\sigma} = 0.05\langle\sigma_{\bar{u}}\rangle$.

We want to emphasize that we use *uniform* Gaussian noise for the training. The assumption of uniform Gaussian noise is used as the central assumption in BFTTC to evaluate the likelihood. The training data can easily be adapted to contain different types of noise if there is a concrete experimental motivation to do so.

As a loss, or performance, metric we use the mean-square error (MSE) calculated from the output guess of the tractions and the corresponding labels of the input traction data, averaged over M training batches

$$\mathrm{MSE} = \frac{1}{M}\sum_{m=1}^{M}\sum_{(x,y)\in\mathrm{grid}} |\vec{\bar{t}}_{\mathrm{in,m}}(x,y) - \vec{\bar{t}}_{\mathrm{out,m}}(x,y)|^2. \tag{5.13}$$

We train in batches of 50 samples by backpropagation using the Adadelta algorithm. The number of training steps per epoch consists of 900 training batches or 45.000 samples.

A traction-based objective function comparing the residual of the force balance that generates the displacements is the proper physics-informed error metric, since we are interested in correct traction forces in TFM. Training for correct traction forces is enabled by using synthetic training data based on traction patches, where we know the true tractions. Alternatively, one could use the residual between the input displacement field and a displacement field generated from the predicted traction field as a training metric, but this approach has an obvious problem: to do

the backpropagation during training we would have to compute *all* predictions of the network for the displacement field in each step of the training, which slows down training several *orders of magnitude* [12]. Implicitly, conventional TFM techniques such as the BFTTC algorithm follow this strategy as they minimize deviations in the resulting displacement field [13] [149]. Therefore, we expect networks trained according to this strategy to perform qualitatively similar to the BFTTC algorithm. We will investigate in detail the resulting differences in accuracy of the traction and displacement predictions in Sec. 5.3.3.

During training, we evaluate the loss MSE given as Eqn. (5.13) for the training data and a validation MSE for unknown displacement data of the same type. The validation and training errors in Fig. 5.8 show constant learning and generalization of the model without over-fitting. We note that a valuation loss lower than the training loss is common when using dropout layers, which are active in training but inactive during inference. In total, the training is performed for 5.000 epochs, which we chose as an arbitrary training limit to truncate the power law tail seen in training, took $\sim 100\,\mathrm{h}$ on an *NVIDIA QUADRO RTX 8000* GPU, with the main learning advancements occurring in the first 5 h. Each epoch consists of 50.000 randomly chosen traction patch distributions of which 45.000 samples are used in training and 5.000 are used for validation.

Sampling the hyper-parameter space of networks

We sample the hyper-parameter space to detect which network traits are important for its performance, i.e., we train a number of different networks on the same data for the same duration and compare their learning progress. The findings of this sampling are contained in Fig. 5.9, where the baseline (solid blue, label "Single Conv.") is a network with a single convolutional layer per block, skip connections, a dropout of 10% and a batch size of 132, using the *Adadelta* optimizer. For this figure we use data generated with the "naive" traction patch discretization and switch to the force conserving method for one of the trials (see the yellow line in Fig. 5.9).

In Fig. 5.9 we vary only one parameter at a time, i.e., we disable the skip connections, vary the batch size, change the optimizer, change the dropout rate, change the number of convolutional layers in a block or change the traction discretization method, this allows us to get an understanding of the hyper-parameter space and its implications on predictive performance:

1. The base line configuration "Single Conv." (solid blue) with a single convolutional layer and trained with the Adadelta optimizer performs better compared to training with the Adagrad optimizer ("Adagrad", dashed green).
2. The training performance is improved when using two convolutional layers per block ("Dual Conv.", solid orange), but, because of the increased complexity, training and inference is computationally significantly more expensive.
3. We observe that the network without skip connections ("No Skip Connections", solid red) performs significantly worse than all other networks.
4. We are able to improve learning by using a lower batch size of 50 ("Batch Size 50", solid purple).
5. Changing dropout affects training as one would expect – a larger dropout decreases and a lower dropout increases training precision ("Larger/Lower Dropout", dashed dotted magenta/brown).

[12] In a first approximation by a factor of N^2.
[13] Which is then subjected to additional regularization.

6. When employing a shallower network obtained by removing one encoder and one decoder block ("Shallower", dotted grey) the learning is faster initially, but seems to plateau earlier before improving again.

7. Finally, when using the exact force conserving discretization for the traction grid ("Exact Discretization", solid yellow) we are able to drastically improve training performance, supporting our above claim that conserving the force balance exactly is of great importance.

For all network variants, the training progress shown in Fig. 5.8 and Fig. 5.9 follows a power law MSE $\propto$ epochs$^{-\alpha}$ with exponents $\alpha \sim 0.4$.

We finally settle on a network architecture with one convolutional layer per block, skip connections, a dropout of 10% and a batch size of 50, while using the *Adadelta* optimizer. This network architecture has also been used for the training process shown in Fig. 5.8 and has been used to produce all results shown in the following. The entire network structure is implemented using the Keras Python API [173].

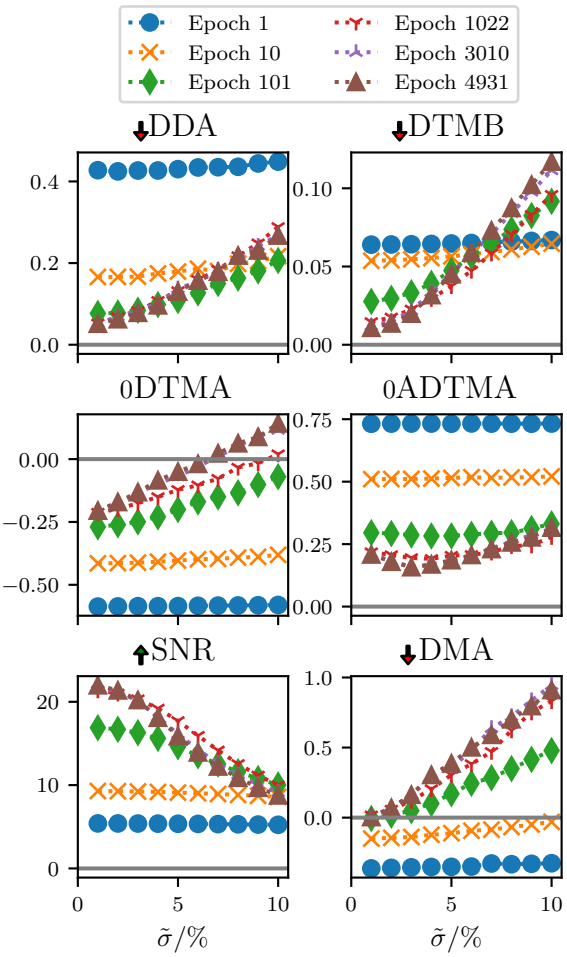

Figure 5.10: We evaluate the final low noise network NN_{low} during training by computing six precision metrics at intermediate points during training. We use the metrics to quantify the performance of the traction reconstruction during training of the network. This evaluation is performed with new data drawn from the same distribution and problem class as the training data. We clearly observe drastic improvements in predictive precision in the first 100 epochs, after which the improvement of the metrics is drastically slower. For the metrics DDA, DTMB and DMA a lower score is better (as indicated by the red arrow), while the SNR is better for larger values. Finally, the DTMA and ADTMA scores are better when they are closer to zero.

BFTTC algorithm

In order to evaluate the performance of our CNN in comparison to conventional TFM methods, we employ the Bayesian Fourier Transform Traction Cytometry (BFTTC) algorithm as a standard to compare with. The algorithm is described in Refs. [149], [162] and has been made publicly available by the authors.

5.3.3 Results

We analyze the performance of our ML approach on a set of error metrics. Additionally, we compare the performance to the BFTTC algorithm [149], [162] as a state-of-the-art conventional TFM method. Importantly, we want to discriminate between background noise and signal while also evaluating magnitude and angle reconstruction precision to infer whether our network generalizes to data never seen before. This will be done for synthetic displacement data first, which is generated in the same way as the training data and contains an additional varying level of noise. Subsequently, we can evaluate the performance of the CNN on artificial cell data using the same error metrics, on completely random displacement fields and, finally, we apply the CNN to real cell data.

Evaluation metrics and application to synthetic patch-based data

We employ six evaluation metrics (see Fig. 5.11 and Fig. 5.12). Their definition is based on a comparison of traction predictions $\vec{t}^{\,\mathrm{pre,s}}(x,y)$ in sample s compared to "true" tractions $\vec{t}^{\,\mathrm{tru,s}}(x,y)$, which are known for the artificial data for random circular traction patches. We evaluate all six metrics by averaging over $S = 100$ samples; the sample average is denoted by $\langle ... \rangle$. All traction vectors $\vec{t}_{i,v}$ in patch i ($i = 1, ..., n$) are indexed by v. All traction vectors $\vec{t}_{b,w}$ outside patches are considered as belonging to the background b and indexed by w.

In Fig. 5.10 we evaluate these metrics for varying noise levels during training of the network NN_{low} and in Fig. 5.11 we evaluate these metrics for varying noise levels $\tilde{\sigma}$ on our synthetic patch-based data.

The noise applied to the displacement field data is uncorrelated between pixels and randomly chosen from a Gaussian distribution centered around zero, with standard deviation σ. Let the dimensionless displacement field standard deviation be $\mathrm{std}\,\bar{u}$, then we define our noise levels $\tilde{\sigma} = \sigma/\mathrm{std}\,\bar{u}$, such that $\tilde{\sigma}$ is the relative noise applied to the displacement field. In the following considerations we vary $\tilde{\sigma}$ between 1 % and 10 %.

We pass the exact noise standard deviation to the BFTTC method for the noise evaluations, such that the BFTTC method has optimal conditions. Our networks do not get any additional information about standard deviation of the noise floor.

First, we introduce a measure to more precisely quantify the orientation resolution via the Deviation of Traction Direction at Adhesions (DDA)

$$\mathrm{DDA} = \langle p(\gamma^{\mathrm{pre}}, \gamma^{\mathrm{tru}})^2 \rangle \qquad (5.14)$$

between predicted and true traction angles γ; $p(\alpha, \beta)$ measures the *periodic* distance between two angles α and β. A small DDA indicates precise traction direction reconstruction. For both of our networks the direction reconstruction is more precise than the BFTTC method across the range of tested noise levels.

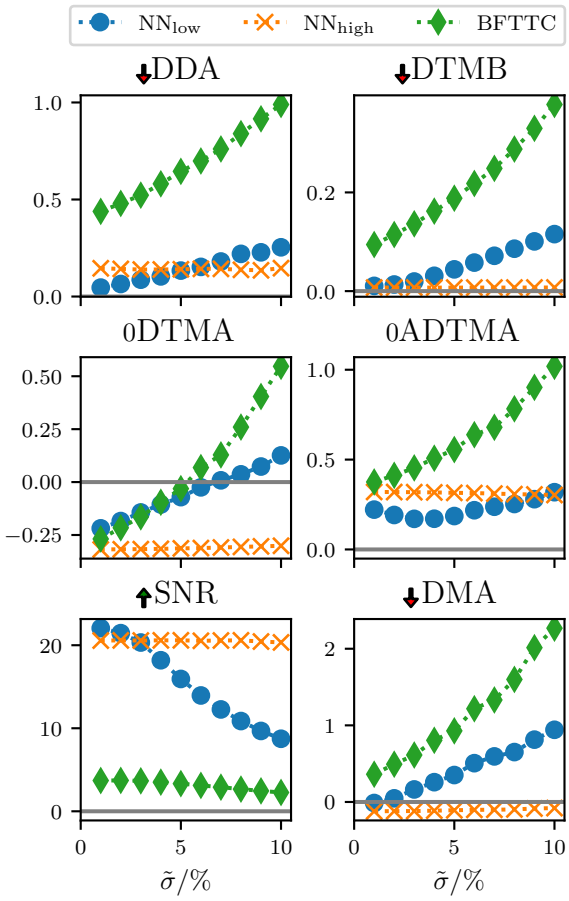

Figure 5.11: The comparison of our networks $\mathrm{NN}_{\mathrm{low}}$ (trained with low noise background) and $\mathrm{NN}_{\mathrm{high}}$ (trained with high noise background) with a state of the art conventional BFTTC approach shows the precision across the six evaluation metrics for varying noise levels $\tilde{\sigma}$ on synthetic patch-based data. This test is performed with an ensemble of traction spots randomly chosen in count, size, magnitude and orientation, testing our networks performance on data similar to the training data. The arrows next to the metric name indicate whether higher or lower is better; "0" indicates that the metric has a sign and a value of zero is optimal. Both of our networks outperform the BFTTC method in most metrics. With the high noise network $\mathrm{NN}_{\mathrm{high}}$ we trade low noise fidelity for elevated noise handling capabilities.

Second, we evaluate the Deviation of Traction Magnitude in the Background (DTMB) [149]:

$$\mathrm{DTMB} = \left\langle \frac{\mathrm{mean}_w \left(|\vec{t}^{\,\mathrm{pre,s}}_{b,w}| - |\vec{t}^{\,\mathrm{tru,s}}_{b,w}| \right)}{\mathrm{mean}_i \mathrm{mean}_v \left(|\vec{t}^{\,\mathrm{tru,s}}_{i,v}| \right)} \right\rangle . \tag{5.15}$$

Note that $|\vec{t}^{\,\mathrm{tru,s}}_{b,w}| = 0$ because artificial traction data exactly vanishes outside patches. This metric quantifies how accurate the traction magnitude reconstruction works in the background, thus, if there is no prediction of an underground noise floor, not associated with any focal adhesion point, the DTMB score will be zero. Both of our NNs have a significantly lower DTMB score in than the BFTTC method in the limit $\tilde{\sigma} \to 0$, which should manifest in a less noisy traction force reconstruction. While the low noise network again departs from that score linearly, the high noise network stays comparatively constant. During training we see that precision in low noise scenarios is traded for less robustness as evident from the increasing slope in Fig. 5.10. The high noise network again does not show this tendency.

Third, we discuss the Deviation of Traction Magnitude at Adhesions (DTMA) [147], [149]:

$$\mathrm{DTMA} = \left\langle \mathrm{mean}_i \frac{\mathrm{mean}_v \left(|\vec{t}^{\,\mathrm{pre,s}}_{i,v}| - |\vec{t}^{\,\mathrm{tru,s}}_{i,v}| \right)}{\mathrm{mean}_v \left(|\vec{t}^{\,\mathrm{tru,s}}_{i,v}| \right)} \right\rangle . \tag{5.16}$$

Note that $\mathrm{mean}_v \left(|\vec{t}^{\,\mathrm{tru,s}}_{i,v}| \right) = |\vec{t}^{\,\mathrm{tru,s}}_{i,v}|$ because artificial traction data is piecewise constant in traction patches. This metric evaluates the precision of traction magnitude reconstruction at the focal adhesion points, thus the DTMA is zero for a perfect reconstruction, negative for an underestimation and positive for an overestimation of traction magnitudes. During training (see Fig. 5.10) this quantity consistently improves but trades precision in low noise scenarios for an increasing slope of the DTMA as a function of background noise. This is a first evidence that this network might perform poorly on high noise experimental data. We do not see the increase in slope for the high noise network (see Fig. 5.11). In Fig. 5.11 we see similar DTMA scores for all approaches in the limit $\tilde{\sigma} \to 0$, with a systematic under-prediction of tractions. For increasing noise floors both the BFTTC and the low noise network ($\mathrm{NN_{low}}$) depart from this common score and start to overestimate tractions. While the DTMA score for the high noise network barely changes, the low noise network DTMA score rises linearly with the noise floor $\tilde{\sigma}$, while the BFTTCs DTMA rises faster than linearly. The high noise network ($\mathrm{NN_{high}}$) retains a comparatively constant DTMA score and always under-predicts the traction magnitude.

Fourth, we introduce the Absolute Deviation of Traction Magnitude at Adhesions (ADTMA) that is similar to the DTMA, but evaluates the absolute deviations, capturing the actual reliability of reconstructions more precisely than DTMA, since alternating under- and over-predictions do not cancel out in this score:

$$\mathrm{ADTMA} = \left\langle \mathrm{mean}_i \left| \frac{\mathrm{mean}_v \left(|\vec{t}^{\,\mathrm{pre,s}}_{i,v}| - |\vec{t}^{\,\mathrm{tru,s}}_{i,v}| \right)}{\mathrm{mean}_v \left(|\vec{t}^{\,\mathrm{tru,s}}_{i,v}| \right)} \right| \right\rangle . \tag{5.17}$$

We can again see the same qualitative behavior as in most of the other metrics: Both networks are more precise in the low noise region, but the low noise network seems to perform best at a noise level of $\sim 3\%$, while the high noise network is robust against increases in background noise.

Fifth, the Signal to Noise Ratio (SNR) [149]:

$$\mathrm{SNR} = \left\langle \frac{\mathrm{mean}_i \mathrm{mean}_v \left(|\vec{t}^{\,\mathrm{pre,s}}_{i,v}| \right)}{\mathrm{std}_w \left(\vec{t}^{\,\mathrm{tru,s}}_{b,w} \right)} \right\rangle , \tag{5.18}$$

where std is the standard deviation. This metric gives an insight into the noise floor of predictions, it is high for a precise distinction between background noise and actual focal adhesion induced deformation and goes to zero for an increasingly noisy reconstruction. Both of our networks have a consistently higher SNR than the BFTTC method, undermining the assumption that the networks will yield a less noisy reconstruction overall. The low noise network SNR decays quickly with increasing noise levels, while the high noise network is more resilient against the increases in noise floor.

Finally, the Deviation of the Maximum traction at Adhesions (DMA) [149]:

$$\mathrm{DMA} = \left\langle \mathrm{mean}_i \frac{\max_v \left(|\vec{t}^{\,\mathrm{pre,s}}_{i,v}| \right) - \max_v \left(|\vec{t}^{\,\mathrm{tru,s}}_{i,v}| \right)}{\mathrm{mean}_v \left(|\vec{t}^{\,\mathrm{tru,s}}_{i,v}| \right)} \right\rangle . \tag{5.19}$$

Note that $\max_v \left(|\vec{t}^{\,\mathrm{tru,s}}_{i,v}| \right) = |\vec{t}^{\,\mathrm{tru,s}}_{i,v}|$ because artificial traction data is piecewise constant in traction patches. This metric gives a more detailed insight into the consistency for high amplitude tractions within a focal adhesion point. A perfect reconstruction would yield a DMA score of zero, while under-predictions give negative scores and over-predictions positive scores. We can again observe that both of our networks give similar scores for low noise scenarios, which are both lower than the score of the BFTTC method. The low noise network again departs linearly from this common value, while the high noise network DMA score stays at a consistent level.

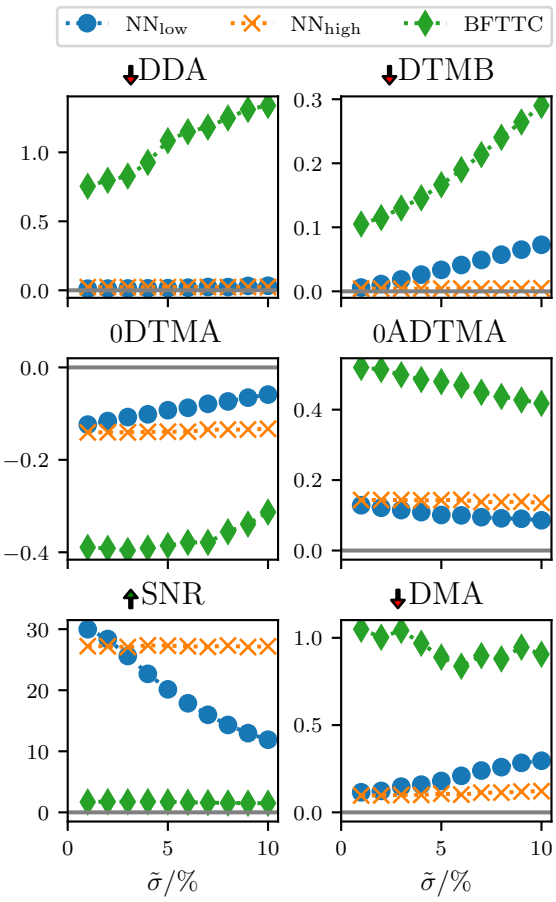

Figure 5.12: We compare our networks $\mathrm{NN}_{\mathrm{low}}$ and $\mathrm{NN}_{\mathrm{high}}$ with the BFTTC method for data generated from an artificial cell model using the same six evaluation metrics for varying noise levels $\tilde{\sigma}$ as in Fig. 5.11. Since the method of generating the data is now different from the training process, we expect to see the generalization potential of our networks more clearly than in Fig. 5.11. The BFTTC method works considerably worse on this data compared to Fig. 5.11. Additionally, we see an amplified underestimation of the traction magnitudes for the BFTTC method. With respect to noise, the high noise network seems to give the best compromise between precision and regularization of the output traction fields.

Across all six measures we observe the following trends for network $\mathrm{NN}_{\mathrm{low}}$ trained with a low level of background noise as compared to network $\mathrm{NN}_{\mathrm{high}}$ trained with a high level of background noise: $\mathrm{NN}_{\mathrm{low}}$ perform superior to the BFTTC-standard *and* $\mathrm{NN}_{\mathrm{high}}$ for low-noise data, because they are trained on low noise data. Their performance deteriorates, however, for higher noise levels $\tilde{\sigma}$, where their performance drops below $\mathrm{NN}_{\mathrm{high}}$ but also below the BFTTC-standard. $\mathrm{NN}_{\mathrm{high}}$ finds a better compromise between robustness and accuracy such that it outperforms the BFTTC-standard across *all* noise levels. Remarkably, the performance of the $\mathrm{NN}_{\mathrm{high}}$ only deteriorates above noise levels $\tilde{\sigma} \sim 100\%$.

Tractions of artificial cells

In order to test the ability of the CNN to specialize from our general patch-based training set to realistic cell data, we first test the model on artificial cell data. The advantage of artificial cell data is that the *"true"* tractions are precisely known. A convenient model to generate realistic cell traction data artificially is the contractile network model [172]. In this model, the stress fibers are active cable links with specific nodes anchored to the substrate at positions $\vec{r}_i = (x_i, y_i)^{\mathrm{T}}$. To construct a typical cell shape with lamellipodium and tail focal adhesions the tractions $\vec{t}_i(\vec{r})$ generated at each anchor point are generated by minimizing the total energy of the cable network. These tractions are then applied to circular patches of radius $\tilde{R} = 0.04$ under an angle γ_i given by the stress fiber orientation at the anchored nodes (see Fig. 5.6).

In addition to Fig. 5.11, we want to evaluate the aforementioned metrics (DDA, ADTMA, DTMB, DMA, DTMA, SNR) on a displacement field generated by an artificial cell as shown in Fig. 5.6. Again, we add Gaussian noise to the displacement field with varying noise levels $\tilde{\sigma}$ and evaluate the behavior of our networks $\mathrm{NN}_{\mathrm{low}}$, $\mathrm{NN}_{\mathrm{high}}$, and the BFTTC method in Fig. 5.12. We average all our results over 10 artificial cells.

We see qualitatively similar results to Fig. 5.11 in the SNR and DTMB metrics, while the absolute performance in those metrics is better [14] for the artificial cell data. This is likely due to the lower number of traction patches in total and the equal radii of all traction patches. Both networks, are able to reconstruct the traction fields more reliably and with greater precision. This is true across all observed metrics.

The artificial cell data show a clear tendency towards a traction magnitude underestimation (DTMA, ADTMA) for all approaches. Since we are generating tractions in strongly bounded range due to the cable network, the traction spots tend to be in close proximity to each other, which can increase smearing of sharply separated traction spots.

Reconstruction of random traction fields

In order to prove that our networks indeed have learned to exploit the linearity of the problem and that they have learned a general solution for the problem, we probe them on entirely random traction fields. To achive this, we generate a completely random traction field, compute the corresponding displacement field [15] and pass it to our high noise network and the BFTTC method for reconstruction. The advantage of this reconstruction setting is that we have the exact ground-truth for the tractions, while not using traction fields similar to the training data.

We generate these random traction fields such that they resemble traction fields that my be encountered in reality. We first generate Gaussian noise with vanishing mean and a standard deviation of 10^{-2}. We then convolve the substrate field with a proximity filter $\exp(-|\vec{r} - \vec{r}'|^4/0.1^4)$ corresponding to a characteristic correlation length of 0.1 in dimensionless units of the image size, which induces correlations over ~ 10 pixels for $N = 104$.

The result of this is a traction field and an associated displacement field which can be seen in Fig. 5.13 (first column). The traction field we have generated here has an entirely different character than the circular training samples the network has seen in training. The displacement field generated from the random traction field is passed to our high noise network and the BFTTC method without further altering it (e.g. by adding noise). The reconstructed traction fields for both methods are shown in Fig. 5.13 (bottom row). We then pass these reconstructed traction

[14] Higher SNR and lower DTMB scores respectively.
[15] Via the superposition of grid-sized circular patches, as detailed previously.

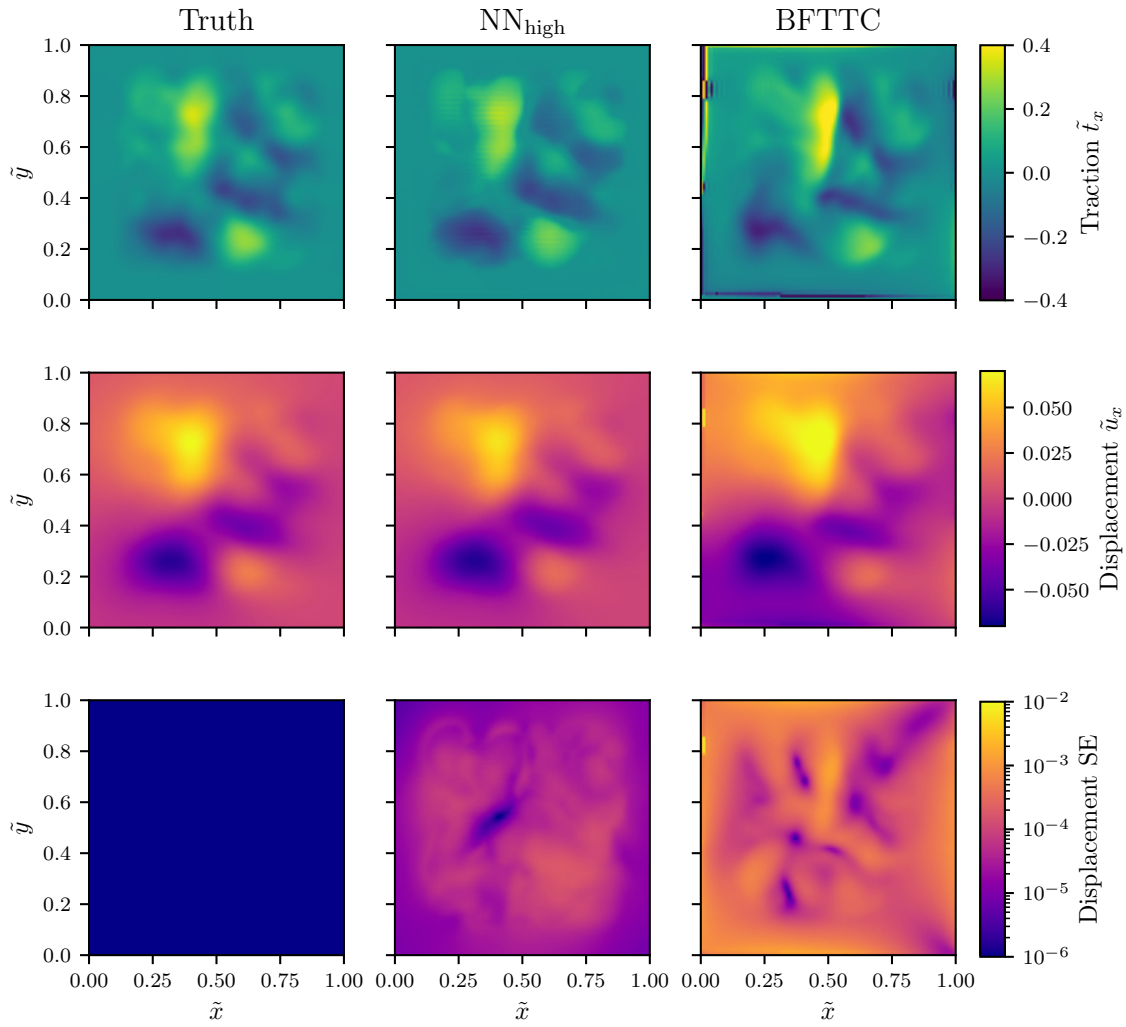

Figure 5.13: We construct a completely random traction field, generated by an entirely different method compared to the training data. From the random traction field (upper left) we generate the accompanying displacement field (middle left), which we feed to our high noise network and the BFTTC method. Both methods generate a traction field reconstruction (top row), from which we can compute the reconstructed displacement field (middle row) and the corresponding displacement errors (bottom row).

traction fields back into our traction solver, which generates the associated displacement field. The resulting reconstructed displacement fields are shown in Fig. 5.13 (top row).

Some observations are possible from visual comparison alone. First, our network is able to reconstruct the traction field accurately and the resulting reconstructed displacement field is visually similar to the ground-truth. Second, the BFTTC method achieves a reconstruction, which at first glance seems similar, but on closer inspection clearly shows stronger deviations from the ground-truth than our network. Third, the BFTTC method suffers from strong reconstruction artifacts at the perimeter of the substrate. These visual findings are supported by the RMSE we

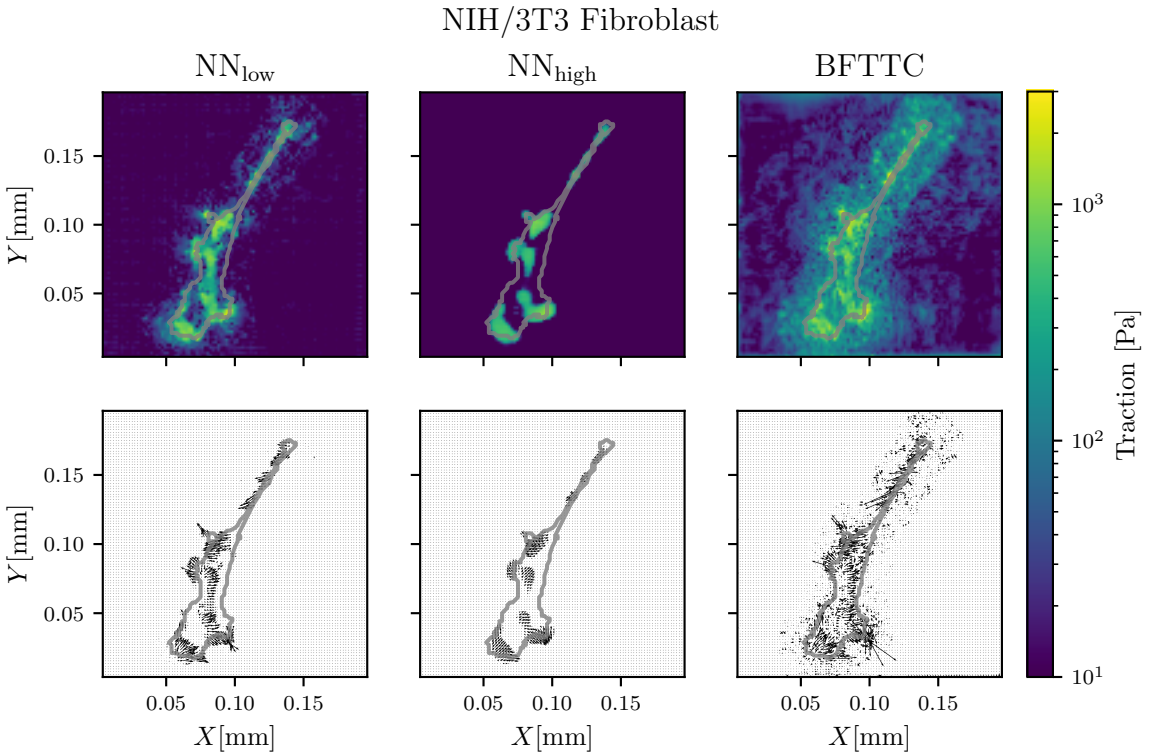

Figure 5.14: Comparison of traction reconstruction for a real Fibroblast between our networks $\mathrm{NN}_{\mathrm{low}}$ and $\mathrm{NN}_{\mathrm{high}}$ and the BFTTC method (top and middle row). Although we do not have the "true" traction field at hand for a quantitative evaluation of precision across the methods, we see compatible results across the board, while both networks have a significantly reduced noise floor. The top row shows traction magnitude reconstruction, while the bottom row shows angle reconstruction.

calculate between the ground-truth displacement field and the reconstructed displacement fields. While the network has an RMSE $\sim 6.5 \cdot 10^{-2}$ the BFTTC method achieves an RMSE $\sim 1.8 \cdot 10^{-1}$, as seen in the displacement error (bottom row of Fig. 5.13). We generate 50 random force fields and determine the RMSE for the BFTTC method and our NN_{high} network between the input displacement field and the reconstructed displacement field (generated from the reconstructed traction field). The BFTTC method achieves on average RMSE ~ 0.04, while our network achieves on average RMSE ~ 0.01. Our network thus predicts traction fields that are more consistent with the input displacement fields.

We have thus shown two things here – our network is able to reconstruct arbitrary traction fields, and it does so with high precision.

Tractions of real cells

Finally, we want to test our ML approach on real cell images. Of course, we do not have access to the *"true"* traction field for those images, however, we can qualitatively compare the results obtained from our ML approach with those obtained by the well tested BFTTC method. The example cell results shown in Fig. 5.14 are for a NIH/3T3 (National Institutes of Health 3T3 cultivated) Fibroblast on a substrate with length $L = 200.2\,\mu\mathrm{m}$ and elastic modulus $E = 10670\,\mathrm{Pa}$ [16]. Additional results for all 14 cells provided in Ref. [150] are similar with further select examples presented in the Appendix A.5.6.

[16]The data was made available in Ref. [150]

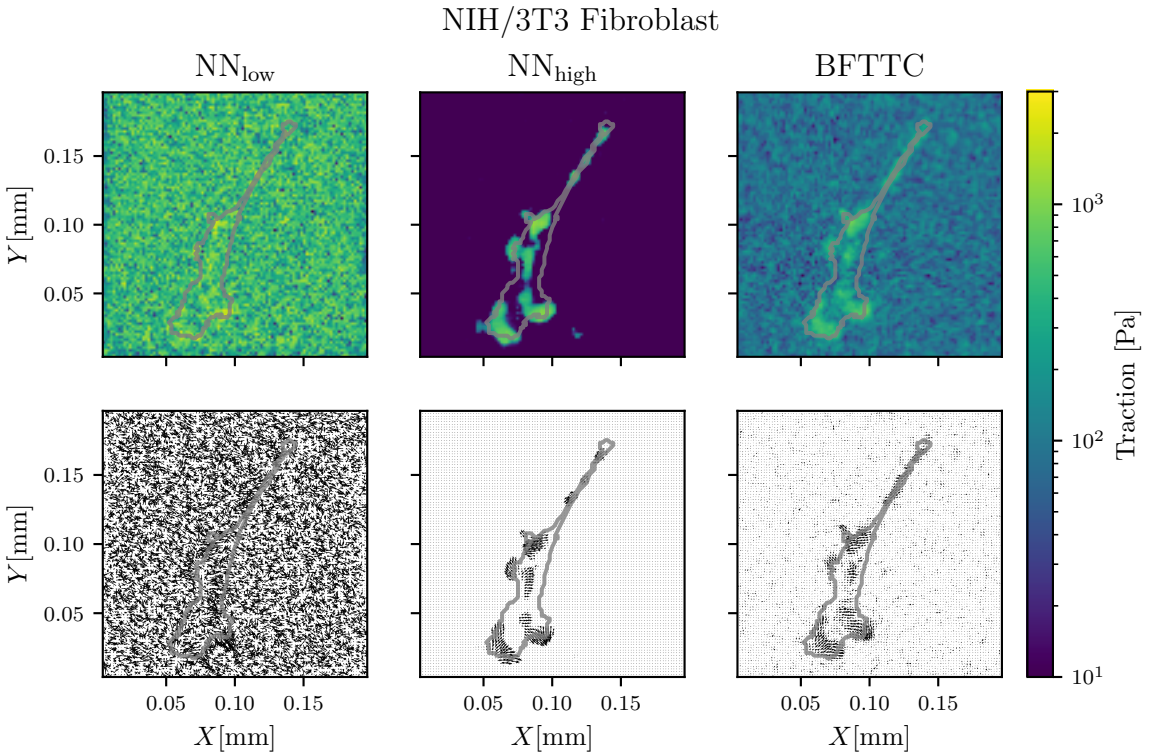

Figure 5.15: Adding noise to the Fibroblast displacement field shows strong noise robustness of our network NN$_{\text{high}}$, which has been trained for high noise scenarios, in traction reconstruction. The low noise network NN$_{\text{low}}$ fails to compensate for the high noise and the BFTTC method yields qualitatively similar results to the high noise network, but exhibits strong noise artifacts in the reconstructed traction fields. The BFTTC method has an unfair advantage, since we pass the *exact* standard deviation of the perfectly uniform Gaussian noise to it for its regularization, while our networks do not get this information.

It is apparent that the network trained with low noise reconstructs a traction field, which is similar to that of the BFTTC method, while the noise in the vicinity of the cell is significantly reduced. The network trained with a high noise floor gives a more regular traction pattern and cuts off lower amplitude tractions.

The reason for these results is that the network trained with low noise exhibits a SNR superior both to BFTTC and the network trained with high noise levels if noise in the experimental data is low (see Fig. 5.11 and Fig. 5.12); for artificial cell data the DTMA and ADTMA of the network trained with low noise is superior for low experimental noise levels (see Fig. 5.12). A low noise in experimental data seems to be realized here. We can thus infer that the tractions reconstructed by the high noise network systematically under-predict the real tractions for this particular data.

As expected from our prior analysis, the resistance to additional noise is much better for the network which saw high noise levels during training, where the low noise network fails completely when subjected to very high noise. The robustness of the high noise network is highlighted in Fig. 5.15, where the cell data is superposed with significant background noise of $\tilde{\sigma} = 100\,\%$. Both our low noise network and the BFTTC method produce a noisy traction field in this case, while the high noise network still displays a similar traction pattern in both of these cases. The noise seen in the BFTTC method is significantly reduced, as we pass the *exact* standard deviation of the applied noise to the method.

Overall, the result from the high noise network and the BFTTC method is qualitatively similar

in the high noise scenario, while the high noise network reconstruction is more regular and fits the circular focal adhesion point model more consistently and stays invariant for a wide range of background noise levels. Apparently, the noise the network sees in training directly controls the effective regularization of the reconstruction and it would be possible to create intermediate networks with higher sensitivity, but lower noise invariance.

Finally, we compute the residual error between the experimental (already noisy) input image and the reconstructed displacement field, by solving the reconstructed traction field for the displacement field. We do this for all the 14 cells provided in Ref. [150]. For the low noise network we achieve a mean RMSE $\sim 10^{-3}$, while the high noise network performs slightly better at an RMSE $\sim 9 \cdot 10^{-4}$. The BFTTC method performs significantly better with an average RMSE $\sim 5 \cdot 10^{-5}$. While the residual errors are low for all approaches we can conclude that the BFTTC method reconstructs the input displacement field more accurately. This seems surprising in light of the higher traction background noise outside the cell shape that the BFTTC clearly produces. The reasons are discussed in the next section in more detail.

We can additionally quantify the contribution of tractions that lie outside the cell contour, which can be considered unphysical. For this we subtract all tractions inside of the contour from the full traction fields and are left with tractions that lie outside the cell contour. When calculating the rooted mean square of these outside tractions we are left with a metric that quantifies physical consistency. We perform this analysis for the cell in Fig. 5.14 and find that the mean background traction for the BFTTC method is ~ 0.013, while it is ~ 0.009 for $\mathrm{NN}_{\mathrm{low}}$ and ~ 0.008 for $\mathrm{NN}_{\mathrm{high}}$. Since the cell segmentation is only an approximation this metric is only a proxy for physical consistency.

We conclude that the high noise network is the better choice for a traction field where the noise is not known, or might be inhomogeneous. If the experimental error is high, or the displacement field reconstruction is imprecise the high noise network provides a robust way of extracting the traction field, while conventional methods are plagued by high background noise in the reconstructed traction fields in this case.

Evaluating a traction field with our networks takes 1 ms, while evaluation an image with the BFTTC method takes 1.5 s [17]. This is a performance improvement of more than three orders of magnitude. Because of the non-dimensionalization we perform it is only necessary to train one network for a large range of experimental realizations. Thus, when the same network is reused for a number of different experiments the long training time will eventually be outweighed by the significant performance advantage at inference.

Displacement versus traction error

We train our NNs for correct tractions by using the MSE of tractions from Eqn. (5.13) as an objective function. This is only possible with synthetic data, where the "truth" for tractions is known. Within this approach we optimize accuracy in tractions but concede errors in the displacement which are not of primary interest in TFM.

Alternatively, one could base training on the MSE of displacements with the drawback of slowing down the training process by orders of magnitude but with the advantage that training could also be performed with actual experimental data. Networks trained with displacement-based metrics will minimize the displacement error in order to obtain correct tractions, which is a more indirect approach. The BFTTC algorithm also minimizes the deviations in displacements in order to

[17] With a discretized substrate of size 104×104.

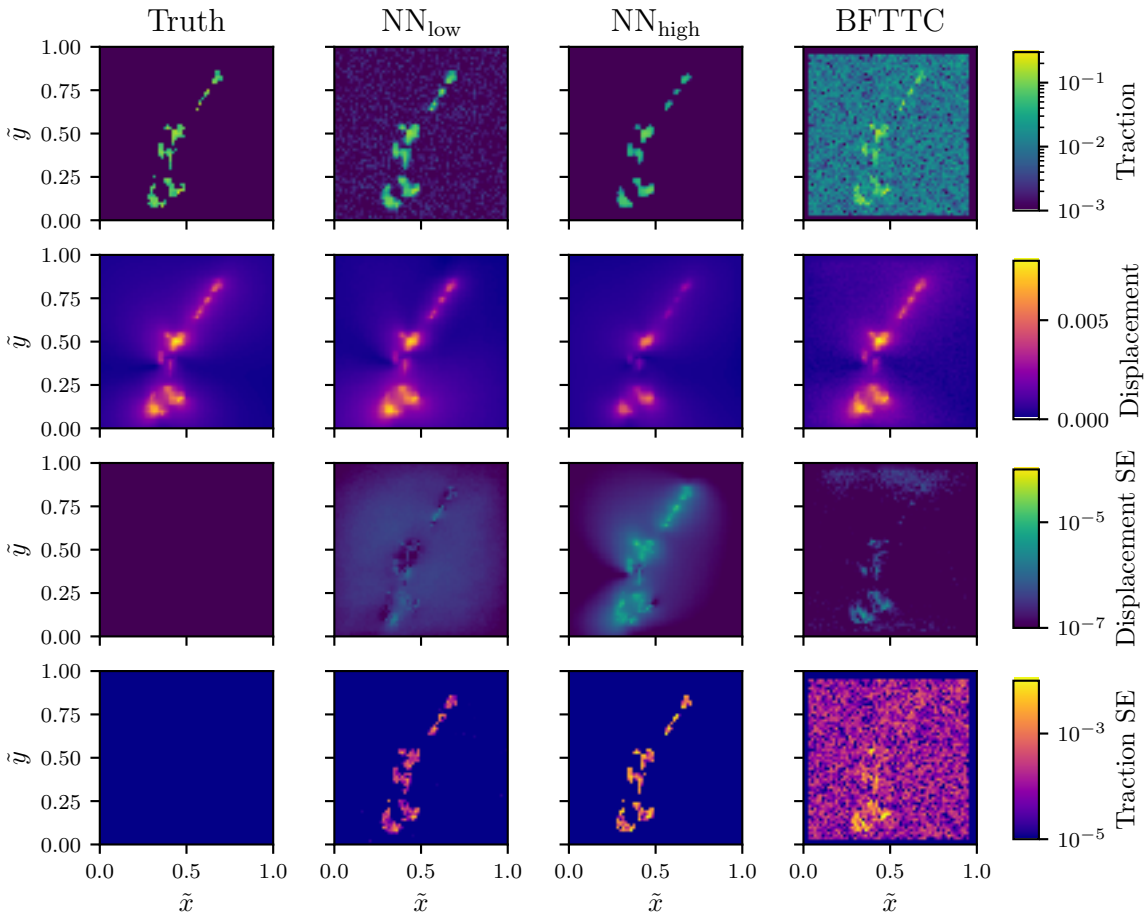

Figure 5.16: Comparison of traction and displacement error between our networks NN_{low} and NN_{high} and the BFTTC method for a synthetic Fibroblast-like traction field and corresponding calculated displacements. The two top rows show the reconstructed traction and displacement fields as compared to the "truth" (first column), which is at hand in this comparison. The two bottom rows display the square error calculated between the "true" and reconstructed displacement and traction fields. We see that both NNs give better traction reconstruction with reduced noise outside the cell as compared to BFTTC, while displacement errors are slightly higher.

determine an optimal traction field [149]. We show that this causes deviations in tractions by applying both strategies to situations where we know the "true" tractions.

Figure 5.16 shows a comparison for a synthetic traction field that we generate from the NIH/3T3 traction data (see Fig. 5.14) by suppressing tractions outside the cell shape (which should be artifacts). This provides the traction "truth" for the comparison. The corresponding displacement field is computed and spatially uncorrelated low amplitude Gaussian noise is added. This displacement field is analyzed by the low and high noise networks and the BFTTC algorithm. Fig. 5.16 clearly shows that, on the one hand, both low and high noise network give a significantly better traction reconstruction, in particular outside the cell shape where the BFTTC method tends to generate background traction noise. On the other hand, this background traction noise obviously enables the BFTTC method to lower the displacement errors, in particular inside the cell shape. As we are interested in correct traction reconstruction in TFM, this comparison clearly pinpoints the advantages of the CNN reconstruction when trained with the traction MSE as objective function.

Input resolution scaling

So far we used a fixed size of $N \times N = 104 \times 104$ for input images. Since our networks are exclusively composed of input size independent layers (fully convolutional layers), we are able to feed arbitrary input sizes [18] to the networks.

It is, however, important to realize that we provide no spatial information to the network apart from the size $N \times N$ of the input array. Because the total input size is not visible to our convolutional layers the network has no means to adapt to changes of the input size N. It is possible to circumvent this limitation by scaling the input displacements properly, such that the input is locally equivalent to that of a 104×104 grid. A local 104×104 section of a $N \times N$ image of a substrate of length L corresponds to a section of smaller length $(104/N)L$ such that the dimensionless displacement $\bar{u}$ for a resolution $N \times N$ corresponds to a larger dimensionless displacement $(N/104)\bar{u}$ for a 104×104 section of the same substrate. Or, in other words, the displacement scale must be coupled to the pixel scale, since our networks directly operate on the pixel level with dimensionless displacements. The scale factor for the input displacements for an image of size $N \times N$ is thus $N/104$.

Applying these transformations yields good performance across all of the six metrics and even improves the SNR for a higher resolution and allows us to provide *arbitrary* image resolutions to our networks. The results for this investigation are contained in the Appendix A.5.3.

5.3.4 Discussion

We present a ML approach to TFM via a deep convolutional NN trained on a general set of synthetic displacement-traction data derived from the analytic solution of the elastic forward problem for random ensembles of circular traction patches. This follows the general strategy that NNs trained with easy-to-generate data of representative forward solutions can serve as a regressor to solve the inverse problem with high accuracy and robustness.

Our approach to TFM uses synthetic training data derived from superpositions of known and representative traction patches. This allows us to employ an objective training function that directly measures traction errors. This contrasts conventional TFM approaches such as BFTTC, where the tractions are adjusted to match the displacement field [19], such that low displacement errors are the implicit objective. We show that a force conserving discretization is crucial for high performance networks and we find a significant enhancement of the robustness of the NN if the training data is subjected to an appropriate level of additional noise.

In conventional TFM approaches the inverse elastic problem is ill-posed and the suitable choice of regularization in the inversion procedure is crucial and has been a topic of active research over the last twenty years. ML approaches circumvent the need for explicit regularization and provide an implicit regularization by a proper choice of the network architecture, i.e., convolutional NNs for TFM, and after proper training. Our work shows that the suitable choice of physics-informed training data and, moreover, the suitable choice of noise on the training data governs the applicability of the NN and the compromise between accuracy and robustness in ML approaches, somewhat analogous to the role of the regularization procedure in conventional TFM approaches.

We employ a sufficiently general patch-based training set and show that this allows the CNN to successfully specialize to artificial cell data and real cell data. Moreover, training with an additional background noise that is 5% of the average variance of the dimensionless displacement field (the NN_{high} network), gives a robustness against noise in the NN performance that is superior

[18] I.e., arbitrary image resolutions.
[19] Eventually subject to additional regularizing constraints on the tractions.

to state-of-the-art conventional TFM approaches without significantly compromising accuracy. We can systematically back these claims by characterizing both the NN performance and the performance of state-of-the-art conventional TFM (the BFTTC method) via six error metrics both for the patch-based training set (Fig. 5.11) and the artificial cell data set (Fig. 5.12), which are two data sets where we can compare the prediction to the true traction labels. We also test the NN performance on random traction fields and traction fields derived from real cell data (Fig. 5.16). Whenever the true tractions are known, we find that our NNs, which were trained to minimize traction errors, give more accurate traction reconstruction with a reduced background traction noise outside the cell shape, although the NNs tend to concede higher errors in the corresponding displacement fields.

For real cell data, we find that a NN trained with low noise (0.5%) gives the best performance if the experimental data is of high quality with low noise levels (see Fig. 5.14). For noisy experimental data, on the other hand, the NN trained with high levels of noise (5%) clearly performs best (see Fig. 5.15). This suggests that it might be beneficial to first employ the high noise network on experimental data and only switch to the low noise network if the background noise level is below 1% of the displacement standard deviation.

Overall, we provide a computationally efficient way to accelerate TFM as a method and improve both on accuracy and noise resilience of conventional approaches, while reducing the computational complexity, and thus execution time by multiple orders of magnitude compared to state-of-the-art conventional approaches. It is apparent from our analysis that ML approaches have the potential to shift the paradigm in solving inverse problems away from conventional iterative methods, towards educated regressors which are trained on a well understood and numerically simple to solve forward problem.

We make all NNs discussed in this work freely available for further use in TFM. We use a 104×104-grid for the displacement data, but show that our networks are able to handle arbitrary displacement data resolutions. Experimental data can easily be adapted to comply with the network input shape by properly scaling the displacements or, alternatively, by interpolating or downsampling to a 104×104-grid, which will, however, decrease the traction resolution.

By using non-dimensionalized units, the NNs made available with this work are widely applicable across different problems and can also be easily further adapted, for example, to problems where typical tractions are not limited to the range traction ranges discussed here by repeating the training process. In the Appendix (see A.5.5), we show that the present networks are able to generalize to larger dimensionless traction magnitudes than trained for, with $\tilde{t}$ ranging up to 1.5, without re-training. Another potential problem to be addressed in future work is the effect of spatial noise correlations, for example, from optical aberration or from the displacement tracking routine that is applied to generate the displacement input data. In Appendix A.5.4, we consider uncorrelated Gaussian noise with a standard deviation that decreases with the distance from the image center and find a robust performance of the high noise network. Robustness to noise with genuine spatial correlations over characteristic distances significantly larger than the pixel size will presumably require re-training of the networks. All necessary routines to re-train a NN to new traction levels, new characteristic patch sizes, or other noise levels are made freely available with this work at `https://gitlab.tu-dortmund.de/cmt/kierfeld/mltfm`. This will also allow to easily adapt the training to other types of noise correlations.

Discussion and outlook

In this thesis, we discuss the properties of complex interfaces in detail. Starting from simple liquid-liquid interfaces in Sec. 1.1, where we discuss the rich parameter-shape space of the problem, we progress to elastic interfaces and discuss their anisotropic and inhomogenous surface stress contributions in Sec. 1.2, where we find a suitable non-dimensional parameter Q to quantify the importance of anisotropic and inhomogenous surface stress contributions. To arrive at the parameter Q, we analyse the anisotropic region at the capillary, where the anisotropy is accumulated. The maximal anisotropy is encountered at the capilary and roughly scales as $\max(\lambda_s/\lambda_\phi) \propto \tilde{p}_L^{-1/3}$. We show that $Q \propto \tilde{p}_L^{2/3}/\lambda_A^{1/2}$ if $\lambda_A > \lambda_A^\dagger$ and provide a more involved scaling law for all other cases.

Additionally, we discuss time-dependent constitutive laws with the ability to dissipate energy during deformation. For this purpose we derive a generalized constitutive law from first principles while carefully stating the assumptions. The resulting viscoelastic constitutive law respects the geometric non-linearities of the problem and may be used to more accurately describe temporal shape sequences, where dissipative effects play a role. Additionally, we provide an alternative derivation of the capsule shape equations appropriate for non-conservative forces, including inertial terms. These derivations may be used as a starting point to include hydrodynamic corrections generated by the fluid-flow on the inside and outside of the skin.

A novel shape fitting software is created for the purpose of making elastic and viscoelastic capsule shape fitting generally available (see Chap. 2). We highlight several intricasies in the shape fit for capsules and advance the method severely – both in terms of performance and reliablity. The main conceptual insight we attain during this discussion is that the apex pressure p_a is *not* a suitable control parameter of the elastic capsule problem and may thus not be used as a fitting parameter of the problem. We use the implicit function theorem to determine, that instead of the apex pressure, the apex stress $\tau_s(s = 0)$ is to be used as a control parameter. Additionally, we detail several technical improvements to the method, which ultimately accelerates its precision and reliability by several orders of magnitude compared to state-of-the-art methods.

Ultimately, we unleash the new method on experiment data and are able to give insight into the complex behavior of crude oil interfaces (see Sec. 3.1), where we detect a phase transition in the composition of the interfacial layer and are able to provide a novel interpretation of it. We are able to systematically – for the first time – show that a solidification of the interfacial layer takes place at a specific volumetric deflation. These insights are enabled only by the new shape fitting software. Additionally, we are able to quantify the scaling law for a polyelectrolyte multilayer system, comprised of NaPSS and PAH, between the compression modulus $K_{2\mathrm{D}}$ and the number of layers n, where we find $K_{2\mathrm{D}} \propto 1.85^n$ (see Sec. 3.2). The experiment data consists of several deflation sequences, which we analyse with our novel viscoelstic shape sequence fit in order to properly account for the viscous losses during the deformation. Only by including the viscous term, we arrive at a consistent scaling law.

Additionally, we derive the shape equations together with all relevant additional contact conditions for a pressurized, adhesive, bending-stiff, elastic capsule in contact with a wall and another such capsule under an external force (see Chap. 4). This is the first time in literature that this problem is tackled in such generality (to the best of the author's knowledge). A numerical solver is developed which is able to solve the numerous shape equations for the contact problem in a timely manner,

allowing us to perform a detailed investigation into the shape-parameter space of the problem. The shape-parameter space of the problem reveals a hysteresis induced by the adhesive properties of the capsule, which we are able to quantitatively understand by providing approximations for the ripping force f_{rip} (with force control) at which the system disconnects after initially being in contact. While the ripping force increases with K_{2D}, the same is not true for the work required to rip the capsules apart W_{rip}, as it decreases with K_{2D}. Thus, the contact holds larger force, but fails at a smaller displacement, making the contact more brittle with increasing compression modulus.

Furthermore, we use the contact shape equations to manufacture (theoretically) a macroscopic meta-material of capsules. We are able to do this, by identifying an elastic capsule unit cell, which generates entire capsule columns. We study the effective three dimensional material properties of the system, such as the three dimensional Young's modulus Y_{3D}. We find a linear scaling law between the three dimensional modulus and the two dimensional modulus $Y_{\mathrm{3D}} \propto K_{\mathrm{2D}}$ with an offset generated by the adhesive properties of the system.

Finally, we investigate several problems that could be considered ill-conditioned and ill-posed and try to accelerate their solution with machine learning (see Chap. 5). We show that tensiometry of liquid droplets can be tackled by a suitable neural network such that the precision of the control parameter estimate is sufficent and the speed is three orders of magnitude faster than conventional shape fitting methods. We show that the same is true for the elastic shape fitting problem and provide a hybrid shape-fitting approach, where the strengths of the machine learning approach is combined with the strengths of the conventional shape fitting approach, to give an overall superior method.

Lastly, we discuss the problem of traction force microscopy in terms of machine learning. We provide a novel approach to generate a suitable training data set by explicitly exploiting the linearity of the problem and presenting the networks we train with superpositions of traction patches, for which we can analytically calculate the accompanying displacement fields from linear elasticity theory. We show that from a superposition of sufficiently small traction patches arbitrary displacement fields can be created, making the methodology sufficiently general, as we show by demonstrating our networks capabilities in terms of several benchmarks in Sec. 5.3. Additionally, we show that while we train our networks on a finite sized grid of input/output data, the networks do work on arbitrary resolution data once scaled appropriately. Our method severely outperforms conventional methods, with BFTTC as a benchmark, across the board. Future investigations could generalize our approach for quasi-two-dimensional traction force microscopy to 2.5 dimensional, or even fully three dimensional traction force microscopy to better capture the cell forces in physiological conditions.

The methods and theories discussed and derived in this thesis have a high generality, which makes them available to extensive further investigation. For example, the contact problem might benefit from a shape fitting routine if suitable experiment data is available in order to determine adhesive properties of capsules, not available to classic pendant capsule shape fits. Future work could accelerate the shape sequence fit performed numerically for viscoelastic capsules with an appropriate machine learning approach, should throughput and reliability be a substantial problem in the future.

A Appendix

A.1 Calculus of Variations

Many problems in physics can be phrased as a search for an extremum of some kind. For example, all conservative problems, i.e. all problems that have a potential for its forces, naturally tend to the minimum of said potential. Being at a minimum of the potential of the forces is equivalent to being in a stable balance of forces. We will discuss several problems in the present work where calculus of variations is an appropriate way to derive identities at the extremal points of an energy functional. We will discuss how the extremization of an energy functional gives rise to force balances at variation boundaries and how the resulting extremal identities can be used to integrate the solution of a problem.

First, however, we will discuss the basic principles of calculus of variations and define the nomenclature.

Similar to single or multi variable calculus we need a necessary and a sufficient condition in order to identify an extremum of a functional. Most different from single or multi variable calculus, however, we do not search for an extremal point, but rather for an extremal function.

A function ξ extremizes a functional $E(\xi)$ if the functional derivative of E with respect to ξ is zero, or in other terms, if the first variation of E vanishes:

$$\xi \text{ extremizes } E(\xi) \Leftrightarrow \delta E = 0\,. \tag{A.1}$$

This is the necessary condition for an extremal function ξ.

We will now define the meaning of δE. To search for an extremal function ξ, which extremizes $E(\xi)$, suppose we allow changes at every point of the function, such that we replace $\xi \to \xi + \delta\xi$. If we analyse what effect replacing ξ with $\xi + \delta\xi$ has on the target functional E, we gain an expression which captures the change of the functional value with $\delta\xi$. At an extremal point of the functional, changing the function ξ by an infinitesimal, but arbitrary, amount everywhere along the contour should not result in any change, simply due to the fact that an extremum of a smooth function is insensitive to small changes. The variation of the functional E is thus given by:

$$\delta E \equiv E(\xi + \delta\xi) - E(\xi)\,, \tag{A.2}$$

however, for all of our purposes, this is equivalent to the first derivative of the functional E with respect to the symbol ξ:

$$\delta E = \frac{\partial E}{\partial \xi}(\xi)\delta\xi\,, \tag{A.3}$$

where we treat the functional E as a regular function depending on the variable ξ.

Keeping the variations $\delta\xi$ is important, because the constraints and boundary conditions of our problem might produce additional conditions for $\delta\xi$. For example, if a solution shall be clamped at a specific point, e.g. a rope attached to a wall, the variation $\delta\xi$ must respect this condition. In many cases, this means that $\delta\xi$ must be zero at specific points along the solution.

A.1.1 The Euler-Lagrange equations

A particularly simple first variation can be performed for a functional which can be expressed as a parametric integral over another functional $\mathcal{L}$ in the variable t, for which the solution functions $\{x_n\}$ are differentiable at least once with respect to t. The integrand can then be expressed as a function of the solution functions and their first derivatives $\mathcal{L} = \mathcal{L}(\{x_n\}, \{x'_n\})$, where the prime denotes derivation with respect to t:

$$\delta E = \delta \int_a^b \mathrm{d}t\, \mathcal{L}(\{x_n\}, \{x'_n\}) \,. \tag{A.4}$$

Let the parametrization t be independent of the solution functions such that we can swap the variation and differentiation, such that we can apply the chain rule to perform the variation of $\mathcal{L}$

$$\delta\mathcal{L} = \sum_n \frac{\partial\mathcal{L}}{\partial x_n}\delta x_n + \sum_n \frac{\partial\mathcal{L}}{\partial x'_n}\delta x'_n \,, \tag{A.5}$$

where we can perform a partial integration to promote $\delta x'_n$ to the variation of the solution function itself. The resulting variation of the functional then yields

$$\delta E = \left[\sum_n \frac{\partial\mathcal{L}}{\partial x'_n}\delta x_n\right]_a^b + \int_a^b \mathrm{d}t \sum_n \left\{\frac{\partial\mathcal{L}}{\partial x_n} - \frac{\mathrm{d}}{\mathrm{d}t}\frac{\partial\mathcal{L}}{\partial x'_n}\right\}\delta x_n \,, \tag{A.6}$$

where the variation of the solution functions δx_n can be chosen arbitrarily, except at an external clamping.

Since the first variation shall vanish for *arbitrary* choices of δx_n it is mandatory to impose

$$\frac{\partial\mathcal{L}}{\partial x_n} - \frac{\mathrm{d}}{\mathrm{d}t}\frac{\partial\mathcal{L}}{\partial x'_n} = 0 \;,\; \forall n, t \tag{A.7}$$

and

$$\sum_n \left[\frac{\partial\mathcal{L}}{\partial x'_n}(b)\delta x_n(b) - \frac{\partial\mathcal{L}}{\partial x'_n}(a)\delta x_n(a)\right] = 0 \,, \tag{A.8}$$

which may be trivially fulfilled if the solution is clamped at both a and b, as then $\delta x_n(a) = \delta x_n(b) = 0$. Note that Eqn. (A.7) are exactly the Euler-Lagrange equations.

A.1.2 Variation of free endpoints

In a variational problem, the endpoints of the integration might not always be fixed, i.e. a and b in Eqn. (A.4) might not be known a priori. In this case, the endpoints need to be subjected to a variation as well. We will consider here that the endpoint a is fixed and only b is allowed to vary, because this will be the only case needed in the present work.

Because b no longer commutes with the variation, we need to apply Leibniz' rule of integration, such that

$$\delta E = \delta b\mathcal{L}(\{x_n\}, \{x'_n\}) + \left[\sum_n \frac{\partial\mathcal{L}}{\partial x'_n}\delta x_n\right]_a^b + \int_a^b \mathrm{d}t \sum_n \left\{\frac{\partial\mathcal{L}}{\partial x_n} - \frac{\mathrm{d}}{\mathrm{d}t}\frac{\partial\mathcal{L}}{\partial x'_n}\right\}\delta x_n \,. \tag{A.9}$$

Furthermore, we need to exchange the variations at b with those at $b + \delta b$, as this is the proper new endpoint. Using an expansion to first order yields

$$\delta x_n(b + \delta b) = \delta x_n(b) + x_n'(b)\delta b + \mathcal{O}(\delta b^2)\,, \tag{A.10}$$

such that the final variation with a free endpoint at b is given as

$$\begin{aligned}\delta E =& \delta b \left\{ \mathcal{L}\left(\{x_n\}, \{x_n'\}\right) - \sum_n \frac{\partial \mathcal{L}}{\partial x_n'} x_n'(b) \right\} \\ &+ \sum_n \frac{\partial \mathcal{L}}{\partial x_n'} \delta x_n(b + \delta b) - \sum_n \frac{\partial \mathcal{L}}{\partial x_n'} \delta x_n(a) + \int_a^b \mathrm{d}t \sum_n \left\{ \frac{\partial \mathcal{L}}{\partial x_n} - \frac{\mathrm{d}}{\mathrm{d}t} \frac{\partial \mathcal{L}}{\partial x_n'} \right\} \delta x_n\,.\end{aligned} \tag{A.11}$$

The additional equation we acquire due to the the free endpoint is a transversality condition and imposes that the value of the Lagrangian at the endpoint is equal to the sum of its derivatives with respect to the primed coordinates times the primed coordinates:

$$\mathcal{L}\left(\{x_n\}, \{x_n'\}\right)(b) = \sum_n \frac{\partial \mathcal{L}}{\partial x_n'}(b) x_n'(b) \tag{A.12}$$

A.1.3 Broken functionals

One of the main assumptions for the derivation of Eqn. (A.7) in Sec. A.1.1 is that the solution functions x_n are differentiable on the entire domain. This assumption is broken in many cases, e.g. when the shape of a capsule without bending stiffness has a kink along the shape [1]. These broken parts of the solution need to be handled explicitly. For the context of this thesis it is sufficient to discuss broken extremals with only a single kink along the solution, however, multiple kinks in the solution can be handled fully analogously.

The solution x_n shall have a kink at $t = l$, such that

$$\lim_{t \to l_+} x_n'(t) \neq \lim_{t \to l_-} x_n'(t) \text{ , but still } \lim_{t \to l_+} x_n(t) = \lim_{t \to l_-} x_n(t)\,, \tag{A.13}$$

where we will use the notation $f(l_{+,-}) \equiv \lim_{t \to l_{+,-}} f(t)$ in the following.

We handle the broken extremal at $t = l$ by splitting the integration at the kink, such that

$$E = \int_a^{l_-} \mathrm{d}t\, \mathcal{L}\left(\{x_n\}, \{x_n'\}\right) + \int_{l_+}^b \mathrm{d}t\, \mathcal{L}\left(\{x_n\}, \{x_n'\}\right) \tag{A.14}$$

note that the derivatives x_n' are defined over the entire respective integration domain, since the domains are defined from a to l_- and l_+ to b respectively. The integration misses exactly one point at $t = l$, this is, however, a zero measure set [2].

There are two ways l may be controlled, either it is imposed externally, e.g. a hanging chain being supported at a fixed point along its shape, or it is controlled by the functional and thus free to move.

[1] This is exactly the case for Pogorelov mirror-inversion buckling at zero bending stiffness.
[2] The same is true if there is an arbitrary countable number of kinks in the shape.

First, consider the case where l is fixed. We perform the individual variations of both integrals exactly as shown in Sec. A.1.1, such that

$$\begin{aligned}\delta E = &\left[\sum_n \frac{\partial \mathcal{L}}{\partial x_n'}\delta x_n\right]_a^{l_-} + \left[\sum_n \frac{\partial \mathcal{L}}{\partial x_n'}\delta x_n\right]_{l_+}^{b} \\ &+ \int_a^{l_-} \mathrm{d}t \sum_n \left\{\frac{\partial \mathcal{L}}{\partial x_n} - \frac{\mathrm{d}}{\mathrm{d}t}\frac{\partial \mathcal{L}}{\partial x_n'}\right\}\delta x_n + \int_{l_+}^{b} \mathrm{d}t \sum_n \left\{\frac{\partial \mathcal{L}}{\partial x_n} - \frac{\mathrm{d}}{\mathrm{d}t}\frac{\partial \mathcal{L}}{\partial x_n'}\right\}\delta x_n \,,\end{aligned} \tag{A.15}$$

which results in the same Euler-Lagrange equations as derived in Sec. A.1.1 with the important distinction that these equations are defined on the domain $[a,l) \cup (l,b] \equiv [a,b] \setminus \{l\}$, where an additional equation arises at l, which is the first Weierstrass-Erdmann corner condition

$$0 = \sum_n \frac{\partial \mathcal{L}}{\partial x_n'}(l_-)\delta x_n(l_-) - \sum_n \frac{\partial \mathcal{L}}{\partial x_n'}(l_+)\delta x_n(l_+) \tag{A.16}$$

and has to be fulfilled by any solution of the problem. Some caution has to be applied when evaluating the variations δx_n, they may be subject to additional constraints and thus not allowed to vary freely.

Second, consider the kink does not have a fixed position. Since the coordinate l is no longer imposed externally, it must be allowed to vary. Thus, instead of simply swapping the integration and variation in Eqn. (A.4) we need to apply Leibniz' integration rule:

$$\begin{aligned}\delta E = &\delta l_- \frac{\mathrm{d}}{\mathrm{d}l_-}\int_a^{l_-} \mathrm{d}t\, \mathcal{L}\left(\{x_n\},\{x_n'\}\right) + \delta l_+ \frac{\mathrm{d}}{\mathrm{d}l_+}\int_{l_+}^{b} \mathrm{d}t\, \mathcal{L}\left(\{x_n\},\{x_n'\}\right) \\ &+ \int_a^{l_-} \mathrm{d}t\, \delta\mathcal{L}\left(\{x_n\},\{x_n'\}\right) + \int_{l_+}^{b} \mathrm{d}t\, \delta\mathcal{L}\left(\{x_n\},\{x_n'\}\right) \,.\end{aligned} \tag{A.17}$$

It is obvious that $\delta l_- = \delta l_+$, such that we can simplify the variation to:

$$\begin{aligned}\delta E = &\delta l \left[\mathcal{L}\left(\{x_n\},\{x_n'\}\right)(l_-) - \mathcal{L}\left(\{x_n\},\{x_n'\}\right)(l_+)\right] \\ &+ \sum_n \frac{\partial \mathcal{L}}{\partial x_n'}(l_-)\delta x_n(l_-) - \sum_n \frac{\partial \mathcal{L}}{\partial x_n'}(l_+)\delta x_n(l_+) \\ &+ \sum_n \frac{\partial \mathcal{L}}{\partial x_n'}(b)\delta x_n(b) - \sum_n \frac{\partial \mathcal{L}}{\partial x_n'}(a)\delta x_n(a) \\ &+ \int_a^{l_-} \mathrm{d}t \sum_n \left\{\frac{\partial \mathcal{L}}{\partial x_n} - \frac{\mathrm{d}}{\mathrm{d}t}\frac{\partial \mathcal{L}}{\partial x_n'}\right\}\delta x_n + \int_{l_+}^{b} \mathrm{d}t \sum_n \left\{\frac{\partial \mathcal{L}}{\partial x_n} - \frac{\mathrm{d}}{\mathrm{d}t}\frac{\partial \mathcal{L}}{\partial x_n'}\right\}\delta x_n \,.\end{aligned} \tag{A.18}$$

At this step some caution has to be applied: The variation of the solution function at the kink $\delta x_n(l_{+,-})$ is *not* independent of the variation of the kink location δl itself. The independent variation of the solution function at the kink needs to be expressed in terms of the varied length $l + \delta l$ instead.

This complication can be fixed by considering the Taylor expansion to first order around the unperturbed kink location, such that

$$\delta x_n(l+\delta l) = \delta x_n(l) + \frac{\partial x_n}{\partial t}(l)\delta l + \mathcal{O}(\delta l^2)\,, \tag{A.19}$$

which we use to express the $\delta x_n(l)$ terms in Eqn. (A.18) in terms of the perturbed kink location, such that the final variation states

$$\begin{aligned}\delta E =& \delta l \left[\mathcal{L}(l_-) - \sum_n \frac{\partial \mathcal{L}}{\partial x_n'}(l_-) x_n'(l_-) - \mathcal{L}(l_+) + \sum_n \frac{\partial \mathcal{L}}{\partial x_n'}(l_+) x_n'(l_+) \right] \\ &+ \sum_n \frac{\partial \mathcal{L}}{\partial x_n'}((l+\delta l)_-)\delta x_n((l+\delta l)_-) - \sum_n \frac{\partial \mathcal{L}}{\partial x_n'}((l+\delta l)_+)\delta x_n((l+\delta l)_+) \\ &+ \sum_n \frac{\partial \mathcal{L}}{\partial x_n'}(b)\delta x_n(b) - \sum_n \frac{\partial \mathcal{L}}{\partial x_n'}(a)\delta x_n(a) \\ &+ \int_a^{l_-} \mathrm{d}t \sum_n \left\{ \frac{\partial \mathcal{L}}{\partial x_n} - \frac{\mathrm{d}}{\mathrm{d}t}\frac{\partial \mathcal{L}}{\partial x_n'} \right\} \delta x_n + \int_{l_+}^{b} \mathrm{d}t \sum_n \left\{ \frac{\partial \mathcal{L}}{\partial x_n} - \frac{\mathrm{d}}{\mathrm{d}t}\frac{\partial \mathcal{L}}{\partial x_n'} \right\} \delta x_n \,,\end{aligned} \tag{A.20}$$

which gives all equations obtained in the case where the kink position was fixed plus an additional condition the solution functions must satisfy, namely the condition obtained when imposing that the pre-factor of δl shall vanish

$$0 = \mathcal{L}(l_-) - \sum_n \frac{\partial \mathcal{L}}{\partial x_n'}(l_-) x_n'(l_-) - \mathcal{L}(l_+) + \sum_n \frac{\partial \mathcal{L}}{\partial x_n'}(l_+) x_n'(l_+) \,, \tag{A.21}$$

which is the second Weierstrass-Erdmann corner condition.

A.1.4 Noether's Theorem

The theorem found by Emmy Noether states that each continuous symmetry transformation has an associated conserved quantity. A prominent example is the conservation of energy, which is the conserved quantity to gauge invariance of the energy. As soon as this gauge invariance is broken, e.g. due to the coupling to another system, the conservation of the subsystems energy is violated along with the gauge invariance. Note that the energy of the combined system is again conserved, since the total systems energy is gauge invariant. The implications of Noethers Theorem are far fetching and it can be used in almost all physics problems.

We can understand the theorem on the level of calculus of variations, since all continuous symmetries ξ entail a variation that does not change the value of the functional, such that $\partial\mathcal{L}/\partial\xi = 0$. This means that the Euler-Lagrange equation for ξ reveals a conserved quantity, since

$$0 = \frac{\mathrm{d}}{\mathrm{d}t}\frac{\partial \mathcal{L}}{\partial \xi'} \Leftrightarrow \frac{\partial L}{\partial \xi'} = \text{const.} \tag{A.22}$$

It is thus enough to analyse the systems symmetries to eventually produce all conservation laws. We will make use of this theorem in several derivations in order to find important conserved quantities.

A.2 Axisymmetric interfaces attached to capillaries

A.2.1 Interfaces with bending stiffness

Bending energy contributions can be added to the problem formulation by allowing the surface energy density w_{S_0} to have out of plane displacement dependencies, in addition to the in-plane displacements λ_s and λ_ϕ. For bending contributions in particular, the additional parametric dependencies encountered are exactly the bending strains $K_s = \mathrm{d}(\Psi - \Psi_0)/\mathrm{d}s_0$ and $K_\phi = (\sin\Psi - \sin\Psi_0)/r_0$, which are related to changes in the principal curvatures [18]. Thus the surface energy density is given as $w_{S_0} = w_{S_0}(\lambda_s, \lambda_\phi, K_s, K_\phi)$ and the variation is

$$\delta w_{S_0} = \left(\delta\lambda_s \frac{\partial}{\partial \lambda_s} + \delta\lambda_\phi \frac{\partial}{\partial \lambda_\phi} + \delta K_s \frac{\partial}{\partial K_s} + \delta K_\phi \frac{\partial}{\partial K_\phi} \right) w_{S_0} \,. \tag{A.23}$$

The two last terms mark the only difference to the elastic case discussed in Sec. 1.2 and are exactly the variations of the new bending energy contribution:

$$\delta E_B = \pi \int_0^{L_0} \mathrm{d}s_0 2r_0 \left\{ \delta K_s \frac{\partial w_{S_0}}{\partial K_s} + \delta K_\phi \frac{\partial w_{S_0}}{\partial K_\phi} \right\} . \tag{A.24}$$

The variation of the bending strains is straight forward to calculate such that the variation of the bending energy terms is immediately recovered as

$$\begin{aligned} \delta E_B = &\left[2\pi \frac{r}{\lambda_\phi} \frac{\partial w_{S_0}}{\partial K_s} \delta\Psi \right]_0^L - 2\pi \left[\left(\frac{1}{\lambda_s} \frac{\partial w_{S_0}}{\partial K_\phi} \cos\Psi - \frac{\mathrm{d}}{\mathrm{d}s} \left(\frac{r}{\lambda_\phi} \frac{\partial w_{S_0}}{\partial K_s} \right) \right) \delta n \right]_0^L \\ &+ 2\pi \int_0^L \mathrm{d}s \left[\delta t \frac{\mathrm{d}\Psi}{\mathrm{d}s} + \delta n \frac{\mathrm{d}}{\mathrm{d}s} \right] \left\{ \frac{1}{\lambda_s} \frac{\partial w_{S_0}}{\partial K_\phi} \cos\Psi - \frac{\mathrm{d}}{\mathrm{d}s} \left(\frac{r}{\lambda_\phi} \frac{\partial w_{S_0}}{\partial K_s} \right) \right\} . \end{aligned} \tag{A.25}$$

The terms appearing as pre-factors to the normal and tangential variations δn and δt modify the two shape equations generated previously in Sec. 1.2 respectively.

The shape equations for the interface with bending stiffness can be obtained by combining the terms produced from the variation without any bending stiffness Eqn. (1.13) and the corrections Eqn. (A.25) as [18]

$$\frac{\mathrm{d}\tau_s}{\mathrm{d}s} = \frac{\cos\Psi}{r}(\tau_\phi - \tau_s) + \kappa_s \left(\frac{\cos\Psi}{r}(m_\phi - m_s) - \frac{\mathrm{d}m_s}{\mathrm{d}s} \right) \tag{A.26}$$

$$\frac{\mathrm{d}m_s}{\mathrm{d}s} = \frac{\cos\Psi}{r}(m_\phi - m_s) + \tau_s \tan\Psi - \frac{1}{2}\frac{pr}{\cos\Psi} \,. \tag{A.27}$$

We use the definition of the meridional and circumferential bending moments

$$m_s \equiv \frac{1}{\lambda_\phi} \frac{\partial w_{S_0}}{\partial K_s} \text{ , and } m_\phi \equiv \frac{1}{\lambda_s} \frac{\partial w_{S_0}}{\partial K_\phi} \tag{A.28}$$

to realize that the resulting shape equations are again equivalent to a force and bending moment balance [18].

Again, we need to properly discuss the resulting boundary terms from Eqn. (A.25). Here we find terms scaled by the normal variations δn at the endpoint $s = 0$ and $s = L$, and terms scaled by a variation in the arc-angle $\delta\Psi$. As we discussed for elastic capsules in Sec. 1.2, these are the only

resulting boundary terms from the combined variation. We can immediately state two trivial things: First, the variation of the arc-angle at the apex $s = 0$ is disallowed, because it would create a kink in the shape and thus incur infinite bending energy, so $\delta\Psi(s = 0) = 0$. Second, the normal variation at the capillary is disallowed, because the shell is clamped there, such that $\delta n(s = L) = 0$. This leaves us with one equation for each endpoint:

$$0 = r(s = L)m_s(s = L)\delta\Psi(s = L) \tag{A.29}$$

$$0 = q(s = 0)r(s = 0)\delta n(s = 0)\,. \tag{A.30}$$

The implications of Eqn. (A.30) are obviously void, because $r(s = 0) = 0$ by parametrization. The implications of Eqn. (A.29) depend on a subtle detail at the capillary. If the shell is clamped at the capillary, such that the attachment angle $\Psi(s = L)$ is fixed (like a beam slotted into an inset) we trivially find $\delta\Psi(s = L) = 0$ and thus no additional equation, however, if the attachment angle can arrange freely, we find the additional condition $m_s(s = L) = 0$, which mandates that there may not be any bending moments in meridional direction at the capillary.

A.3 Numerically solving and fitting shape equations

A.3.1 Fitting Parameter Considerations

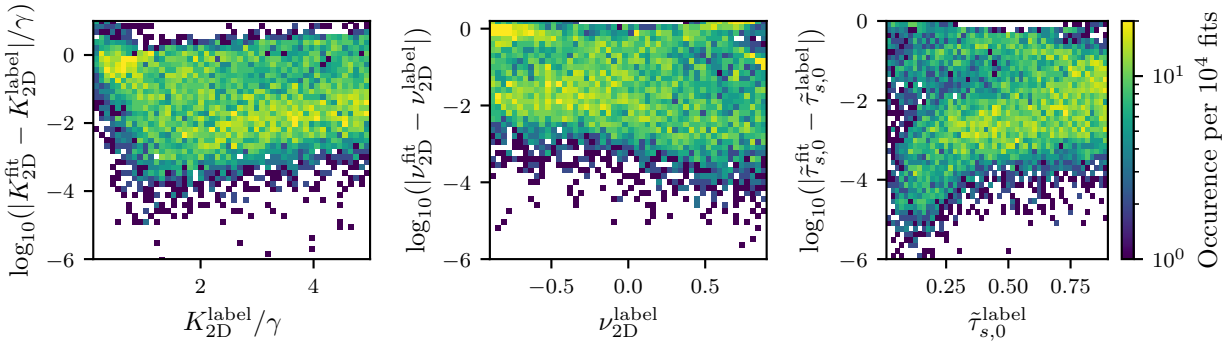

Figure A.1: We determine the performance of the numerical fit with a different set of elastic moduli. The algorithm seems to be more robust when exchanging ν_{2D} as a parameter for G_{2D}. This is evident by comparing to Fig. 2.4

Obviously, the choice of the constitutive fit parameters as K_{2D} and ν_{2D} is entirely arbitrary. The elastic constitutive parameters are an interchangeable set of two parameters, which means that we could, for example, choose to exchange the problematic Poisson's ratio for another parameter, which is better conditioned for the fit. As we discover in a later section (see Sec. 3.2), the fit of experimental shape sequences is better conditioned if the Poisson's ratio is exchanged for the shear modulus $G_{2D} = K_{2D}(1 - \nu_{2D})/(1 + \nu_{2D})$ during the fit. In essence, this means that internally the fitting algorithm will work with G_{2D}, where externally, the Poisson's ratio is retrieved as previously. We can understand why Poisons ratio is ill-versed for a shape fit by analysing the poles of the constitutive law. If ν_{2D} gets close to -1 or 1, we see a real divergence in the constitutive law. Additionally, the sensitivity close to the boundaries of the admissible range for ν_{2D} is amplified significantly. Since the fitting algorithm (i.e. least-squares) uses a linearization to update the parameter set, the algorithm is ill-conditioned in this region. The shear modulus has the algorithmic benefit, that one of the poles in the constitutive law coincides with $G_{2D} \to \infty$ and the other with $G_{2D} \to 0^+$. Appropriately, G_{2D} has no upper bound for its admissible range, which is advantageous – in an algorithmic sense – as well.

We fit another 10.000 generated and noised shapes, internally using this new parametrization of the constitutive law and indeed find a superior fitting performance (see Fig. A.1). In Fig. A.1 we can see a subtle, but qualitatively noticeable improvement in fitting performance compared to Fig. 2.4, i.e. the bands of high error promptly visible in Fig. 2.4 are entirely absent from the improved fit in Fig. A.1.

A.4 Contact phenomena of complex interfaces

A.4.1 Gravitational Effects

Up to this point the gravitational effects where not included in the calculations, however, they are trivial to include.

To show this, consider the potential energy of both capsules

$$E_{\text{pot}} = g \int \mathrm{d}V^u \, \Delta\rho^u z^u - g \int \mathrm{d}V^d \, \Delta\rho^d z^d \,, \tag{A.31}$$

where g is the gravitational acceleration and $\Delta\rho^{u,d}$ the respective density difference between the inside and the outside of the volumes $V^{u,d}$ enclosed by the capsules. This potential energy term can be absorbed into a hydro-static pressure difference, where we introduce a height dependent pressure function $p^{u,d} = p_a^{u,d} \mp \Delta\rho^{u,d} g z^{u,d}$ with a negative sign for the upper shape and a positive sign for the lower shape, simply because the axis of gravity is flipped for the lower shape.

Writing Eqn. (A.31) in terms of the arc length s yields:

$$\begin{aligned} \frac{E_{\text{pot}}}{\pi g} = &\int_0^{l_-} \mathrm{d}s \, (\Delta\rho^u - \Delta\rho^d)(r^u)^2 \sin\Psi^u z^u \\ &+ \int_{l_+}^{L^u} \mathrm{d}s \, \Delta\rho^u (r^u)^2 \sin\Psi^u z^u - \int_{l_+}^{L^d} \mathrm{d}s \, \Delta\rho^d (r^d)^2 \sin\Psi^d z^d \,. \end{aligned} \tag{A.32}$$

The first variation of Eqn. (A.32) reveals

$$\begin{aligned} \frac{\delta E_{\text{pot}}}{\pi g} = &\left[(\Delta\rho^u - \Delta\rho^d) z^u (r^u)^2 \delta z^u\right]_0^{l_-} + \left[\Delta\rho^u z^u (r^u)^2 \delta z^u\right]_{l_+}^{L^u} - \left[\Delta\rho^d z^d (r^d)^2 \delta z^d\right]_{l_+}^{L^d} \\ &+ \int_0^{l_-} \mathrm{d}s \, (\Delta\rho^u - \Delta\rho^d) 2 r^u z^u \delta n^u + \int_{l_+}^{L^u} \mathrm{d}s \, \Delta\rho^u 2 r^u z^u \delta n^u - \int_{l_+}^{L^d} \mathrm{d}s \, \Delta\rho^d 2 r^d z^d \delta n^d \,, \end{aligned} \tag{A.33}$$

where the boundary terms vanish in sum because they are composed from continuous geometric properties. This observation makes it obvious that the gravitational contributions may be accounted for, simply by performing the substitution

$$p^{u,d} \to p_a^{u,d} \mp \Delta\rho^{u,d} g z^{u,d} \tag{A.34}$$

in all prior calculations. The static pressure $p^{u,d}$ is thus replaced with the pressure at the apex of the drop $p_a^{u,d}$ and a height dependent hydro-static pressure contribution.

A.4.2 Shape space for $K_{2D} = 2\gamma$

We show the parameter space slice from the main text (see Fig. 4.8) with a modified compression modulus, i.e. $K_{2D} = 2\gamma$ in Fig. A.2. The modifications to the shape space due to the change in compression modulus are subtle and include a slight increase in apex stress required for the $V^u = V_0^u$ configuration. Furthermore, the orange line of zero force is slightly rotated into a more vertical orientation. The same is true for the blue line, after which no further solutions exist. Qualitatively, however, the parameter space does not change significantly with the increase in compression modulus.

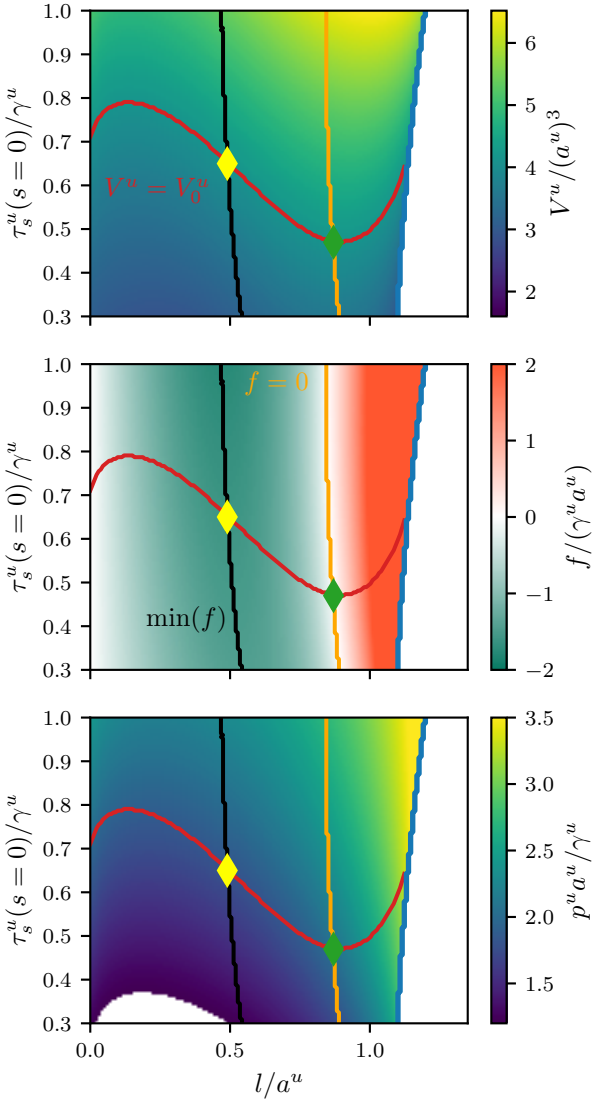

Figure A.2: Slice of the shape space for the elastic contact problem. Here we choose $K_{2D} = 2\gamma$. The lines of constant volume (contour lines of the upper plot) are shown for the deformed volumes equaling the reference volume $V^{u,d} = V_0^{u,d}$ (red line). Additionally, the lines of minimum forces (black lines) and zero forces (orange line) are shown. The intersections between the volume and force lines are highlighted with colored diamonds and mark the respective characteristic points in the deformation sequences of fixed volume. In a certain region, no solutions can be found for a given contact length and apex stress (blue line), i.e. there does not exist a pressure for which the capillary boundary condition may be fulfilled.

A.5 Machine learning applications in ill-posed inverse problems

Published material – This appendix is reproduced with modifications and permission from the author's publication [133], © 2023 Biophysical Society..

A.5.1 Details of the solution of the forward problem for traction patches

For the solution of the forward problem for a tractions patch of size R_i, we obtained the functions $N_j(\tilde{r}_i, \theta)$ in Eqn. (5.11) and Eqn. (5.12). They are defined as

$$N_j(\tilde{r}_i, \theta) \equiv \int_0^{2\pi} d\phi \int_0^{\infty} d\rho \frac{J_1(\rho R_i)}{\rho} f_j(\phi) e^{-i\rho R_i \tilde{r}_i \cos(\phi-\theta)} \tag{A.35}$$

with

$$\begin{aligned} f_1(\phi) &\equiv 1 \\ f_2(\phi) &\equiv \sin^2\phi \\ f_3(\phi) &\equiv \sin\phi\cos\phi \\ f_4(\phi) &\equiv \cos^2\phi. \end{aligned}$$

By definition, $N_2 + N_4 = N_1$.

The remaining integrals in the functions $N_j(\tilde{r}_i, \theta)$ can be performed analytically:

$$\begin{aligned} N_1(\tilde{r}_i) &= 2\pi \int_0^{\infty} dx \frac{J_1(x) J_0(x\tilde{r}_i)}{x} \\ &= \begin{cases} 4E\left(\tilde{r}_i^2\right) & \tilde{r}_i < 1 \\ 4\left[\tilde{r}_i E\left(\tilde{r}_i^{-2}\right) - (\tilde{r}_i - \tilde{r}_i^{-1}) K\left(\tilde{r}_i^{-2}\right)\right] & \tilde{r}_i > 1 \end{cases} \end{aligned} \tag{A.36}$$

with the complete elliptic integrals $E(m) = \int_0^{\pi/2} (1 - m\sin^2\theta)^{1/2} d\theta$ and $K(m) = \int_0^{\pi/2} (1 - m\sin^2\theta)^{-1/2} d\theta$;

$$\begin{aligned} N_2(\tilde{r}_i, \theta) &= 2\pi \int_0^{\infty} dx \left(\frac{J_1(x) J_1(x\tilde{r}_i)}{x^2 \tilde{r}_i} - \sin^2\theta \frac{J_1(x) J_2(x\tilde{r}_i)}{x} \right) \\ &= \begin{cases} 4\sin^2\theta E\left(\tilde{r}_i^2\right) + \frac{4}{3\tilde{r}_i^2}\cos(2\theta)\left[(1+\tilde{r}_i^2) E\left(\tilde{r}_i^2\right) + (\tilde{r}_i^2 - 1) K\left(\tilde{r}_i^2\right)\right] & \tilde{r}_i < 1 \\ \frac{2}{3\tilde{r}_i}\left[(3\tilde{r}_i^2 + (2-\tilde{r}_i^2)\cos(2\theta)) E\left(\tilde{r}_i^{-2}\right) + (1-\tilde{r}_i^2)(3-\cos(2\theta)) K\left(\tilde{r}_i^{-2}\right)\right] & \tilde{r}_i > 1 \end{cases}; \end{aligned} \tag{A.37}$$

$$\begin{aligned} N_3(\tilde{r}_i, \theta) &= -2\pi \sin\theta\cos\theta \int_0^{\infty} dx \frac{J_1(x) J_2(x\tilde{r}_i)}{x} \\ &= \begin{cases} \frac{2}{3\tilde{r}_i^2}\sin(2\theta)\left[(\tilde{r}_i^2 - 2) E\left(\tilde{r}_i^2\right) + 2(1-\tilde{r}_i^2) K\left(\tilde{r}_i^2\right)\right] & \tilde{r}_i < 1 \\ \frac{2}{3\tilde{r}_i}\sin(2\theta)\left[(\tilde{r}_i^2 - 2) E\left(\tilde{r}_i^{-2}\right) + (1-\tilde{r}_i^2) K\left(\tilde{r}_i^{-2}\right)\right] & \tilde{r}_i > 1 \end{cases}; \end{aligned} \tag{A.38}$$

$$N_4(\tilde{r}_i, \theta) = N_1(\tilde{r}_i) - N_2(\tilde{r}_i, \theta). \tag{A.39}$$

A.5.2 Discretization of traction patches

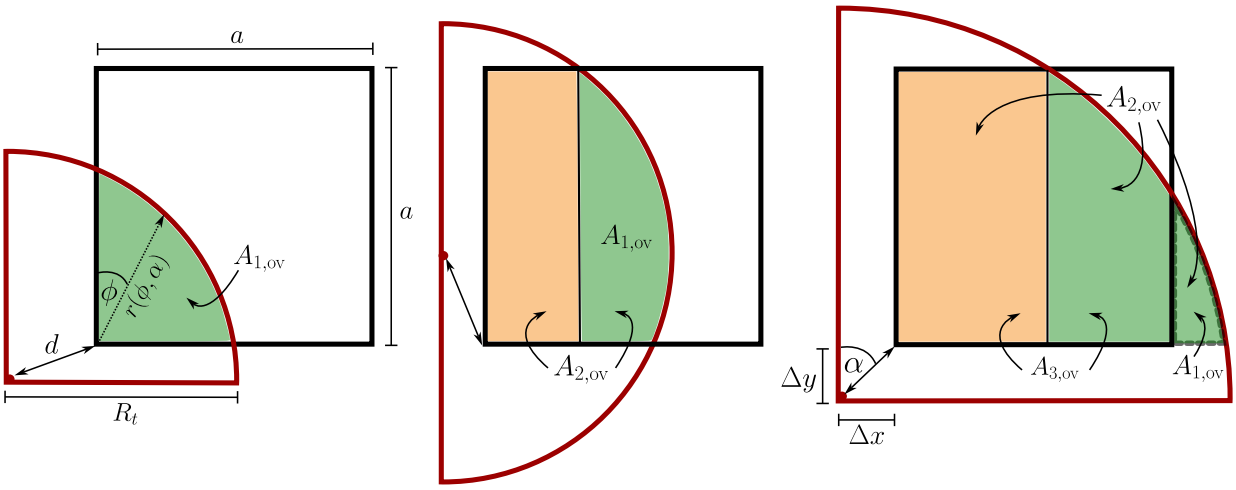

Figure A.3: Calculation of overlap areas $A_{k,\mathrm{ov}}$ for circular patches containing $k = 1, 2, 3$ corners of square grid segments.

A naive approach for the discretization of the circular traction patches onto a square pixel grid with indices $i, j \in \{1, ..., N\}$ and square side lengths $a = L/N$ is to check whether any square segment center point $\vec{c}_{ij}$ is contained in the circular traction patch of radius R_t and center point $\vec{c}_t$. If the center point is contained, the grid segment ij is assigned the traction $\tilde{t}_0$ of the circular patch:

$$\tilde{t}_{ij} = \begin{cases} \tilde{t}_0, & \text{for } |\vec{c}_{ij} - \vec{c}_t| < R_t \\ 0, & \text{else.} \end{cases} \tag{A.40}$$

This naive discretization suffers from a critical artifact: it does not conserve the total traction force F_t exerted by the patch, $\sum_{i,j} a^2 \tilde{t}_{ij} \neq \tilde{t}_0 \pi R_t^2 = F_t$.

One step towards improving the force conservation is to check for all four corners of the square grid segment whether they are contained in the traction circle. If we assign equal weights to any of the corners

$$\tilde{t}_{ij} = t_0 \frac{\#\text{corners contained}}{4}, \tag{A.41}$$

the naive optimization is improved, but still not force conserving.

Ultimately, we construct a force conserving discretization by explicitly calculating the *exact* area occupation ratio of each square grid segment and the circular traction spots (see Fig. A.3).

We start with the case where exactly one corner of the grid square is contained in the traction circle. We only need to consider the case where only the bottom left corner of the grid segment is contained in the traction circle; all remaining cases can be constructed by mirror or rotational symmetries. We denote the vector from the center of the circle to the bottom left corner of the grid segment by $(\Delta x, \Delta y)$, its length by d and the angle with the y-axis by α such that $(\Delta x, \Delta y) = d(\sin\alpha, \cos\alpha)$. The overlap area of traction circle and grid square is given by the polar integral

$$A_{1,\mathrm{ov}} = \frac{1}{2} \int_0^{\pi/2} \mathrm{d}\phi r^2(\phi, \alpha) \tag{A.42}$$

with

$$r(\phi, \alpha) = \sqrt{R_t^2 - d^2 \sin(\phi - \alpha)} - d\cos(\phi - \alpha)\,. \tag{A.43}$$

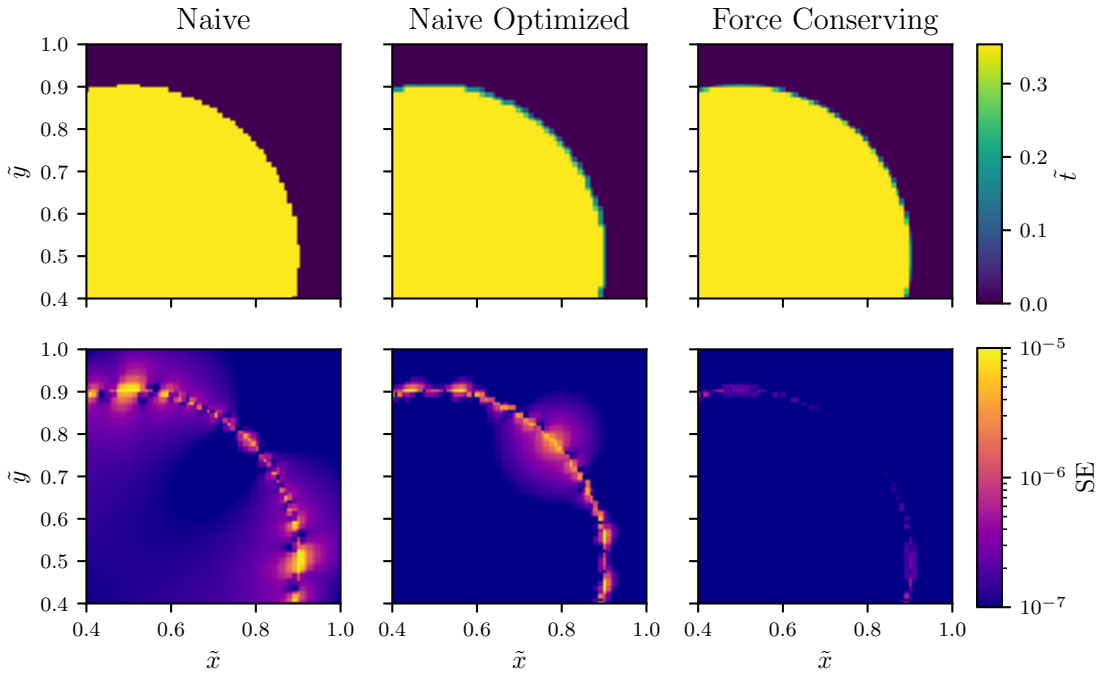

Figure A.4: The discretization of circular traction patches onto a pixel grid (top row) with a naive discretization, an improved discretization and a force conserving discretization (left to right). The resulting residual displacement errors (bottom row) are generated by feeding the discretized traction field back to the solver to generate a residual of the input displacement field and the displacement field obtained from resolving the discretized traction field. The residual error decreases drastically if the total traction force is conserved by the discretization method.

This integral can be solved via basic calculus:

$$A_{1,\mathrm{ov}}(\Delta x, \Delta y) = \frac{1}{4}R_t^2 + \Delta x \Delta y - \frac{1}{2}\left(\sqrt{R_t^2 - \Delta y^2}\Delta y + \sqrt{R_t^2 - \Delta x^2}\Delta x + R^2 \arcsin(\Delta y / R_t) + R^2 \arcsin(\Delta x / R_t)\right). \tag{A.44}$$

We are able to construct all other cases from this result. For the other cases where only one corner of the grid segment is contained we simply exploit the rotational symmetry, e.g. if the top right corner is contained, we rotate the traction patch around the center of the grid segment by π radians and recover a scenario where we can apply Eqn. (A.44).

If two corners of the grid square are contained in the traction patch it suffices to consider the case where the bottom left and the top left corner are contained because of rotational symmetries. Additionally, we can concentrate on the case where the center point of the traction patch is *below* (smaller y-component) the grid square center point because of the mirror symmetries of the problem. The two corner overlap can be viewed as a one corner overlap with a shifted Δx and an additional rectangular overlap (see Fig. A.3) resulting in

$$A_{2,\mathrm{ov}}(\Delta x, \Delta y) = A_{1,\mathrm{ov}}\left(\sqrt{R_t^2 - (\Delta y + a)^2}, \Delta y\right) + a\left(\sqrt{R_t^2 - (\Delta y + a)^2} - \Delta x\right). \tag{A.45}$$

Similarly, the three corner overlap decays into a two corner overlap minus a shifted one corner overlap (see Fig. A.3). Again, for symmetry reasons, we only need to consider one configuration,

where the top left, bottom left and bottom right corner of the grid square are contained in the circular traction patch:

$$A_{3,\mathrm{ov}}(\Delta x, \Delta y) = A_{2,\mathrm{ov}}(\Delta x, \Delta y) - A_{1,\mathrm{ov}}(\Delta x + a, \Delta y) \ . \tag{A.46}$$

Finally, in order to conserve the total force exerted by the traction patch, the tractions assigned to a grid square must then be weighted by their area occupation percentage,

$$\tilde{t}_{ij} = \tilde{t}_0 \frac{A_{\mathrm{ov},ij}}{a^2} \ , \tag{A.47}$$

where $A_{\mathrm{ov},ij}$ is calculated from Eqn. (A.44), Eqn. (A.45), or Eqn. (A.46) depending on the number of corners of square ij contained in the circular traction patch.

The fundamental error of this method can be computed by generating a large exact circular solution and feeding the discretized traction grid back into our solver. With the force conserving implementation we are able to reproduce the displacement field of a large circular traction patch of radius $R_t = 0.4$ to a precision of RMSE $\sim 1.2 \cdot 10^{-4}$. This also allows us to probe the difference between the three traction discretization methods in Fig. A.4. The naive discretization gives a residual error RMSE $\sim 5.1 \cdot 10^{-4}$ for the displacement field, the optimized naive discretization is already able to lower the residual error drastically to RMSE $\sim 4.4 \cdot 10^{-4}$. The force conserving method finally lowers the residual error to RMSE $\sim 1.2 \cdot 10^{-4}$, which is significantly better than both the naive and the improved naive method.

A.5.3 Input resolution scaling

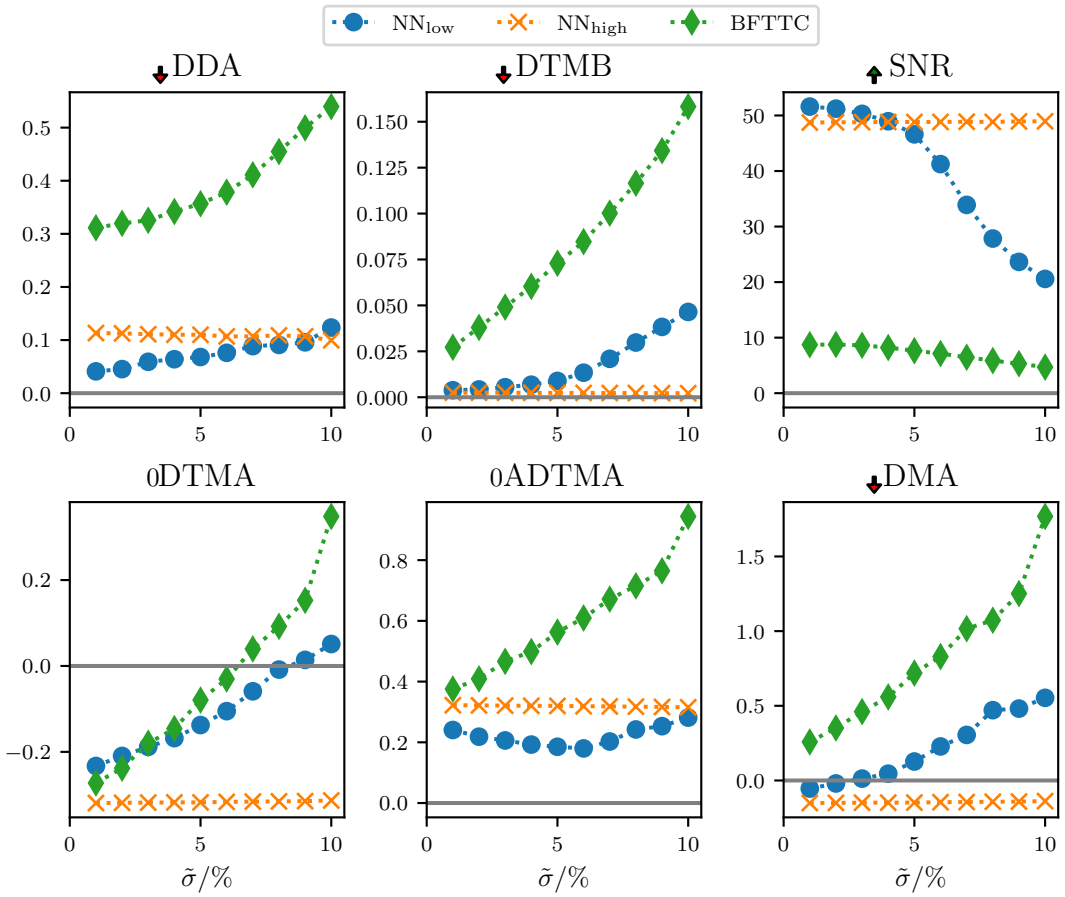

Figure A.5: We generate traction patches on a larger grid of size 256×256 to verify that our networks are able to adapt to input resolution changes. We compare our six precision metrics with the BFTTC method and find similar results compared to the findings for 104×104 grids (see Fig. 5.11).

To quantify the performance of our networks for higher input resolutions we generate data on a significantly larger grid ($N \times N = 256 \times 256$) and scale the input displacements by 256/104. We compare the traction reconstruction performance with the BFTTC method in Fig. A.5. In our implementation (using TensorFlow), the execution time scales $\propto N^2$ for the BFTTC method, while it remains linear $\propto N$ for network inference.

A.5.4 Gaussian noise with amplitude correlated with position

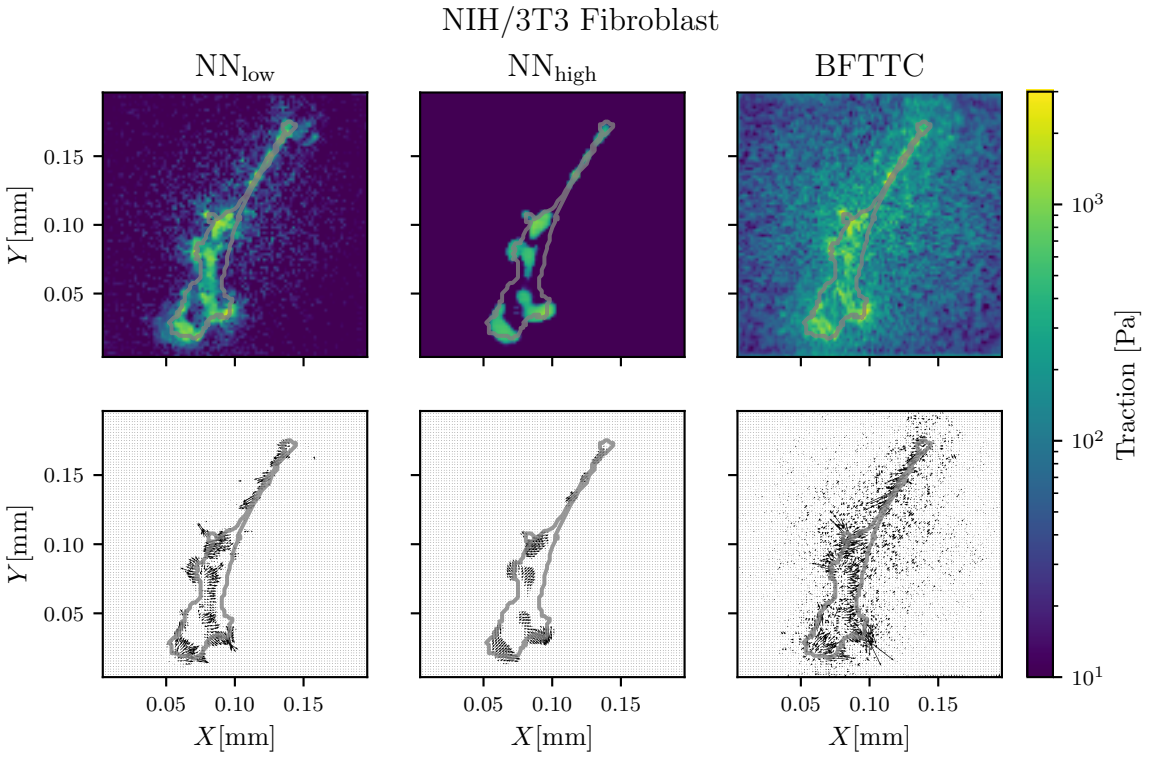

Figure A.6: Results for Gaussian noise with a standard deviation decreasing with the distance to the center of the experimental images. It is evident, that the high noise network returns an invariant prediction even under these circumstances. The BFTTC method produces a significantly elevated traction background noise.

In this work, we focused on uncorrelated Gaussian noise. Experimental noise might contain correlations, for example, from optical aberration that gives rise to a non-uniform noise amplitude. As an example, we consider effects from uncorrelated Gaussian noise with a standard deviation that decreases with the distance from the center of the experimental image in Fig. A.6. In this example, the standard deviation decreases with a factor $(1 - r/\sqrt{2})^4$, where r is the dimensionless distance from the center.

A.5.5 Higher traction magnitudes

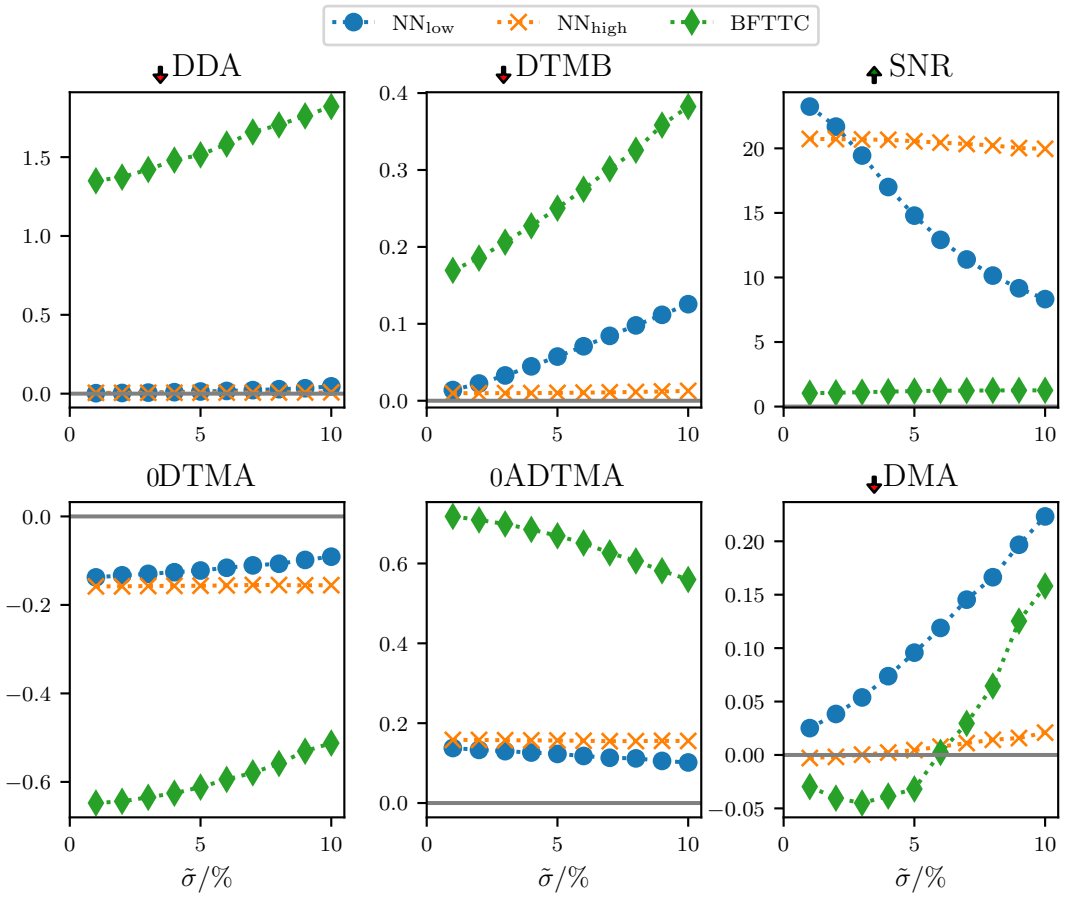

Figure A.7: We generate traction patches with magnitudes uniformly varying from 0.5 to 1.5, which is well outside our training range. We observe that the networks are still able to provide highly accurate predictions, even in this traction magnitude regime.

We trained our networks on traction patches with dimensionless traction magnitudes $\tilde{t}$ uniformly distributed between 0.0 and 0.5. In Fig. A.7, we show that the networks are able to generalize to larger traction magnitudes by evaluating all six metrics for synthetic patch-based data with dimensionless traction magnitudes $\tilde{t}$ uniformly distributed between 0.5 and 1.5.

A.5.6 Further analysis of experimental data

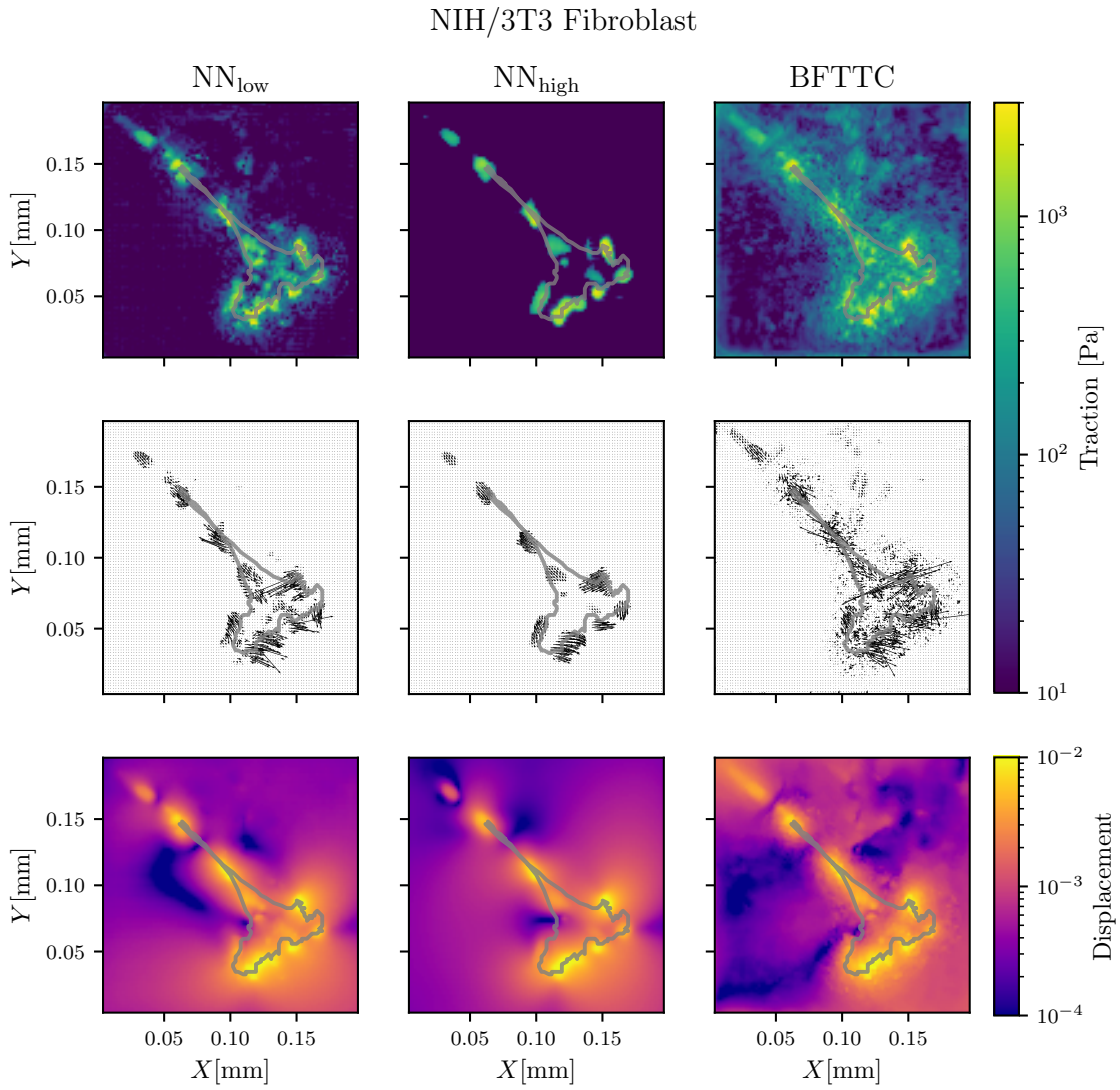

Figure A.8: Comparison of traction and displacement reconstruction for a real Fibroblast between our networks NN_{low} and NN_{high} and the BFTTC method for cell 1 of Ref. [150].

We present additional results for one of the 14 cells provided in Ref. [150]. We compare the traction reconstruction for an additional real Fibroblast between our networks NN_{low} and NN_{high} and the BFTTC method (top and middle rows of Fig. A.8). Although we do not have the "true" traction field at hand for a quantitative evaluation of precision across the methods, we see compatible results, while both networks have a significantly reduced noise level. The top row shows the traction magnitude reconstruction, while the center row shows the angle reconstruction. In addition, the bottom row displays the displacement field computed from the reconstructed traction fields. We see that deviations in the displacement field between all three methods are small.

A.5.7 Manual regularization of the traction reconstruction

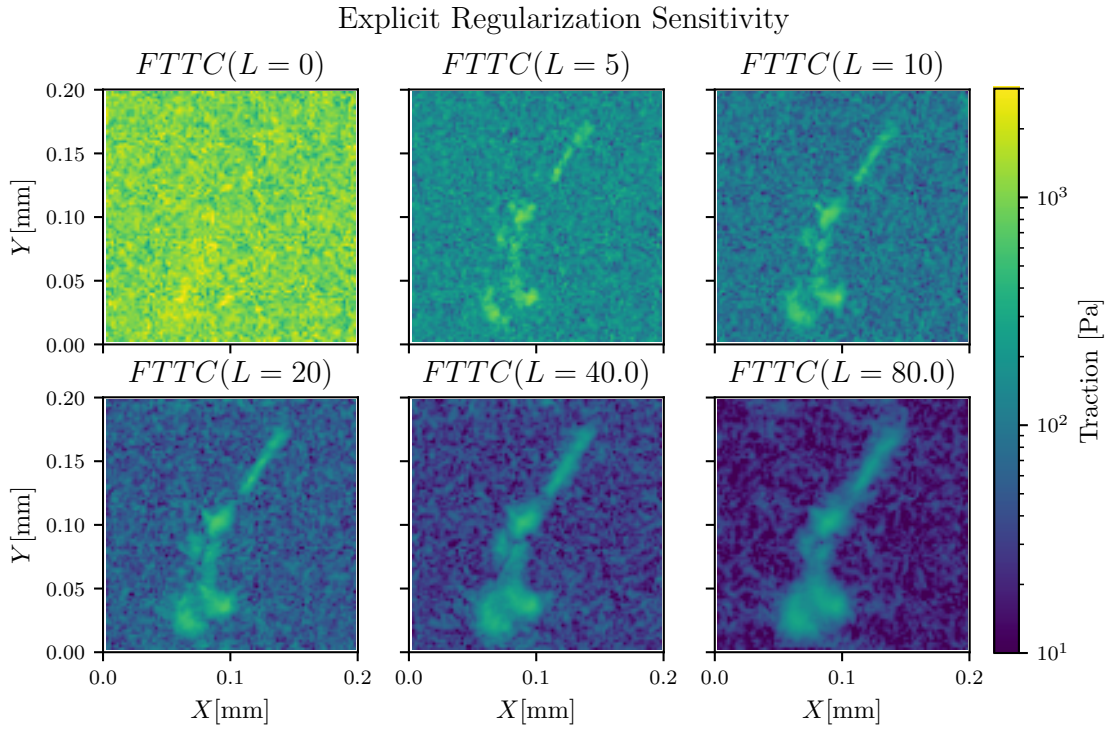

Figure A.9: Comparison of the traction reconstruction for different manually chosen regularization parameters. The BFTTC method automatically chooses $L = 10$.

To show that the tractions produced by the BFTTC method are indeed a fair benchmark for our method we provide additional traction reconstructions, where we choose the regularization parameter L manually to show that lower regularization parameters than that chosen by the BFTTC method lead to excessive noise and higher regularization parameters lead to highly blurred reconstructions. The automatically chosen regularization parameter of the BFTTC method is $L \sim 10$.

Bibliography

[1] Y. Bu, L. Li, Y. Chendong, R. Li, and J. Wang, "Measuring Viscoelastic Properties of Living Cells," *Acta Mech. Solida Sin.*, 2019. DOI: 10.1007/s10338-019-00113-7.

[2] E. Fischer-Friedrich, A. A. Hyman, F. Jülicher, D. J. Müller, and J. Helenius, "Quantification of surface tension and internal pressure generated by single mitotic cells," *Sci. Rep.*, vol. 4, 2014. DOI: 10.1038/srep06213.

[3] H. Brenner, *Interfacial Transport Processes and Rheology*. Elsevier Science, 2013. DOI: 10.1016/C2009-0-26916-9.

[4] T. Bhattacharjee, D. B. Amchin, J. A. Ott, F. S. Kratz, and S. S. Datta, "Chemotactic migration of bacteria in porous media," *Biophys. J.*, vol. 120, 2021. DOI: 10.1016/j.bpj.2021.05.012.

[5] J. Mead, J. L. Whittenberger, and E. P. Radford, "Surface Tension as a Factor in Pulmonary Volume-Pressure Hysteresis," *J. Appl. Physiol.*, vol. 10, 1957. DOI: 10.1152/jappl.1957.10.2.191.

[6] J.-F. Louf, F. S. Kratz, and S. S. Datta, "Elastocapillary network model of inhalation," *Phys. Rev. Res.*, vol. 2, 2020. DOI: 10.1103/PhysRevResearch.2.043382.

[7] T. Young, "Iii. an essay on the cohesion of fluids," *Phil. Trans. R. Soc.*, vol. 95, 1805. DOI: 10.1098/rstl.1805.0005.

[8] J. C. Maxwell, "Principia generalia theoriae figurae fluidorum in statu aequilibrii," 1830. DOI: 10.1007/978-3-642-49319-5_3.

[9] N. Jyothi, P. Prasanna, S. Sakarkar, K. Prabha, P. Ramaiah, and G. Srawan, "Microencapsulation techniques, factors influencing encapsulation efficiency," *J. Microencapsul.*, vol. 27, 2010. DOI: 10.3109/02652040903131301.

[10] D. Barthes-Biesel and H. Sgaier, "Role of membrane viscosity in the orientation and deformation of a spherical capsule suspended in shear flow," *J. Fluid Mech.*, vol. 160, pp. 119–135, 1985. DOI: 10.1017/S002211208500341X.

[11] T. W. Secomb and R. Skalak, "Surface flow of viscoelastic membranes in viscous fluids," *Q. J. Mech. Appl. Math.*, vol. 35, 1982. DOI: 10.1093/qjmam/35.2.233.

[12] S. Pivard, L. Jacomine, F. S. Kratz, *et al.*, "Interfacial rheology of linearly growing polyelectrolyte multilayers at the water–air interface: From liquid to solid viscoelasticity," *Soft Matter*, vol. 20, 2024. DOI: 10.1039/d3sm01161e.

[13] A. Z. Stetten, F. S. Kratz, N. Schilderink, *et al.*, "Elastometry of complex fluid pendant capsules," *Langmuir*, vol. 39, 2023. DOI: 10.1021/acs.langmuir.3c01845.

[14] J. Hegemann, S. Knoche, S. Egger, *et al.*, "Pendant capsule elastometry," *J. Colloid Interface Sci.*, vol. 513, 2018. DOI: 10.1016/j.jcis.2017.11.048.

[15] S. Knoche, D. Vella, E. Aumaitre, *et al.*, "Elastometry of Deflated Capsules: Elastic Moduli from Shape and Wrinkle Analysis," *Langmuir*, vol. 29, 2013. DOI: 10.1021/la402322g.

[16] H. Rehage, M. Husmann, and A. Walter, "From two-dimensional model networks to microcapsules," *Rheologica Acta*, vol. 41, 2002. DOI: 10.1007/s00397-002-0233-3.

[17] J. D. Berry, M. J. Neeson, R. R. Dagastine, D. Y. C. Chan, and R. F. Tabor, "Measurement of surface and interfacial tension using pendant drop tensiometry," *J. Colloid Interface Sci.*, vol. 454, 2015. DOI: 10.1016/j.jcis.2015.05.012.

[18] S. Knoche and J. Kierfeld, "Buckling of spherical capsules," *Phys. Rev. E*, vol. 84, 2011. DOI: 10.1103/PhysRevE.84.046608.

[19] C. Wischnewski and J. Kierfeld, "Spheroidal and conical shapes of ferrofluid-filled capsules in magnetic fields," *Phys. Rev. Fluids*, vol. 3, 2018. DOI: 10.1103/PhysRevFluids.3.043603.

[20] D. Kwok, D. Vollhardt, R. Miller, D. Li, and A. Neumann, "Axisymmetric drop shape analysis as a film balance," *Colloids Surf. A Physicochem. Eng. Asp.*, vol. 88, 1994. DOI: 10.1016/0927-7757(94)80085-5.

[21] M. Hoorfar, M. Kurz, and A. Neumann, "Evaluation of the surface tension measurement of axisymmetric drop shape analysis (adsa) using a shape parameter," *Colloids Surf. A Physicochem. Eng. Asp.*, vol. 260, 2005. DOI: 10.1016/j.colsurfa.2004.08.080.

[22] S. M. Saad, Z. Policova, and A. W. Neumann, "Design and accuracy of pendant drop methods for surface tension measurement," *Colloids Surf. A Physicochem. Eng. Asp.*, vol. 384, 2011. DOI: 10.1016/j.colsurfa.2011.05.002.

[23] A. Libai and J. G. Simmonds, *The Nonlinear Theory of Elastic Shells*. Cambridge University Press, 1998. DOI: 10.1017/CBO9780511574511.

[24] F. S. Kratz and J. Kierfeld, "Pendant Drop Tensiometry: A Machine Learning Approach," *J. Chem. Phys*, vol. 153, 2020. DOI: 10.1063/5.0018814.

[25] E. H. Lucassen-Reynders, A. Cagna, and J. Lucassen, "Gibbs elasticity, surface dilational modulus and diffusional relaxation in nonionic surfactant monolayers," *Colloids Surf. A Physicochem. Eng. Asp.*, vol. 186, 2001. DOI: 10.1016/S0927-7757(01)00483-6.

[26] J. Hegemann, H.-H. Boltz, and J. Kierfeld, "Elastic capsules at liquid–liquid interfaces," *Soft Matter*, vol. 14, 2018. DOI: 10.1039/C8SM00316E.

[27] S. Knoche, "Instabilities and shape analyses of elastic shells," *Dissertation*, 2014. DOI: 10.17877/DE290R-6596.

[28] A. C. Pipkin, "The Relaxed Energy Density for Isotropic Elastic Membranes," *IMA J. Appl. Math.*, vol. 36, 1986. DOI: 10.1093/imamat/36.1.85.

[29] J. H. Weiner, "Entropic versus kinetic viewpoints in rubber elasticity," *Am. J. Phys.*, vol. 55, 1987. DOI: 10.1119/1.15034.

[30] H. M. James and E. Guth, "Theory of the elastic properties of rubber," *J. Chem. Phys.*, vol. 11, 1943. DOI: 10.1063/1.1723785.

[31] W. L. Vandoolaeghe and E. M. Terentjev, "Constrained Rouse model of rubber viscoelasticity," *J. Chem. Phys.*, vol. 123, no. 3, 2005. DOI: 10.1063/1.1955445.

[32] G. Ginot, F. S. Kratz, F. Walzel, *et al.*, "Pressure–deformation relations of elasto-capillary drops (droploons) on capillaries," *Soft Matter*, 2021. DOI: 10.1039/D1SM01109J.

[33] U. Seifert, "Configurations of fluid membranes and vesicles," *Adv. Phys.*, vol. 46, 1997. DOI: 10.1080/00018739700101488.

[34] J. W. Gibbs, "On the equilibrium of heterogeneous substances," *Am. J. Sci.*, 1878. DOI: 10.2475/ajs.s3-16.96.441.

[35] Y. Fung, "On pseudo-elasticity of living tissues," S. Nemat-Nasser, Ed., 1980. DOI: 10.1016/B978-0-08-024249-1.50014-5.

[36] D. Barthès-Biesel, A. Diaz, and E. Dhenin, "Effect of constitutive laws for two-dimensional membranes on flow-induced capsule deformation," *J. Fluid Mech.*, vol. 460, 2002. DOI: 10.1017/S0022112002008352.

[37] Landau, L.D. and Lifshitz, E.M. and Kosevitch, A.M. and Pitaevski ĭ, L.P., *Theory of Elasticity* (Course of theoretical physics). Pergamon Press, New York, 1986. DOI: 10.1016/C2009-0-25521-8.

[38] F. S. Wong and R. T. Shield, "Large plane deformations of thin elastic sheets of neo-Hookean material," *Zeitschrift für Angew. Math. und Phys. ZAMP*, vol. 20, 1969. DOI: 10.1007/BF01595559.

[39] C. Raufaste, G. R. Chagas, T. Darmanin, C. Claudet, F. Guittard, and F. Celestini, "Superpropulsion of droplets and soft elastic solids.," *Phys. Rev. Lett.*, vol. 119 10, 2017. DOI: 10.1103/PhysRevLett.119.108001.

[40] R. G. Cox, "The deformation of a drop in a general time-dependent fluid flow," *J. Fluid Mech.*, vol. 37, 1969. DOI: 10.1017/S0022112069000759.

[41] D. Barthès-Biesel, "Motion of a spherical microcapsule freely suspended in a linear shear flow," *J. Fluid Mech.*, vol. 100, 1980. DOI: 10.1017/S0022112080001449.

[42] O. A. Basaran and D. Depaoli, "Nonlinear oscillations of pendant drops," *Phys. Fluids*, vol. 6, 1994. DOI: 10.1063/1.868120.

[43] D. Barthès-Biesel, "Modeling the motion of capsules in flow," *Curr. Opin. Colloid Interface Sci.*, vol. 16, 2011. DOI: 10.1016/j.cocis.2010.07.001.

[44] B. S. Neo and E. S. Shaqfeh, "The effects of suspending fluid viscoelasticity on the mechanical properties of capsules and red blood cells in flow," *J. Nonnewton Fluid Mech.*, vol. 326, 2024. DOI: 10.1016/j.jnnfm.2024.105215.

[45] F. S. Kratz, *Pendant Drops and Capsules: Solving the Inverse Problem by Numerical Shape Fitting and Machine Learning*, Master Thesis, 2020.

[46] Y. Pan and Z. Zhong, "A viscoelastic constitutive modeling of rubber-like materials with the payne effect," *Appl. Math. Model.*, 2017. DOI: 10.1016/j.apm.2017.06.018.

[47] C. Drapaca, S. Sivaloganathan, and G. Tenti, "Nonlinear Constitutive Laws in Viscoelasticity," *Math. Mech. of Solids*, vol. 12, 2007. DOI: 10.1177/1081286506062450.

[48] A. Wineman, "Nonlinear viscoelastic membranes," *Comput. Math. with Appl.*, vol. 53, 2007. DOI: 10.1016/j.camwa.2006.02.017.

[49] D. Gutierrez-Lemini, *Engineering Viscoelasticity*. 2014. DOI: 10.1007/978-1-4614-8139-3.

[50] R. M. Christensen, "A nonlinear theory of viscoelasticity for application to elastomers," *J. Appl. Mech.*, vol. 47, 1980. DOI: 10.1115/1.3153787.

[51] J. Lubliner, "A model of rubber viscoelasticity," *Mech. Res. Commun.*, vol. 12, 1985. DOI: 10.1016/0093-6413(85)90075-8.

[52] E. Evans and R. Hochmuth, "Membrane viscoelasticity," *Biophys. J.*, vol. 16, 1976. DOI: 10.1016/S0006-3495(76)85658-5.

[53] T. Verwijlen, L. Imperiali, and J. Vermant, "Separating viscoelastic and compressibility contributions in pressure-area isotherm measurements," *Adv. Colloid Interface Sci.*, vol. 206, 2014. DOI: 10.1016/j.cis.2013.09.005.

[54] H. Khajehsaeid, J. Arghavani, R. Naghdabadi, and S. Sohrabpour, "A visco-hyperelastic constitutive model for rubber-like materials: A rate-dependent relaxation time scheme," *Int. J. Eng. Sci.*, vol. 79, 2014. DOI: 10.1016/j.ijengsci.2014.03.001.

[55] W. Findley, J. S. Lai, and K. Onaran, *Creep and Relaxation of Nonlinear Viscoelastic Materials*. 1976. DOI: 10.1016/b978-0-7204-2369-3.x5001-2.

[56] L. M. Sagis, "Dynamic properties of interfaces in soft matter: Experiments and theory," *Rev. Mod. Phys.*, vol. 83, 2011. DOI: 10.1103/RevModPhys.83.1367.

[57] J. J. Skrzypek and A. W. Ganczarski, *Mechanics of Anisotropic Materials*. 2015. DOI: 10.1007/978-3-319-17160-9.

[58] H. Banks, S. Hu, and Z. Kenz, "A Brief Review of Elasticity and Viscoelasticity," *Adv. Appl. Math. Mech.*, vol. 3, 2011. DOI: 10.4208/aamm.10-m1030.

[59] M. Karbaschi, M. Lotfi, J. Krägel, A. Javadi, D. Bastani, and R. Miller, "Rheology of interfacial layers," *Curr. Opin. Colloid Interface Sci.*, vol. 19, 2014. DOI: 10.1016/j.cocis.2014.08.003.

[60] J. Hegemann, "Deformation behavior of elastic shells and biological cells," *Dissertation*, 2018. DOI: 10.17877/DE290R-18797.

[61] N. O. Jaensson, P. D. Anderson, and J. Vermant, "Computational interfacial rheology," *J. Nonnewton Fluid Mech.*, vol. 290, 2021. DOI: 10.1016/j.jnnfm.2021.104507.

[62] N. Nguyen, A. Wineman, and A. Waas, "Compression of fluid-filled polymeric capsules and inverse analysis to determine nonlinear viscoelastic properties," *Int. J. Solids Struct.*, vol. 62, 2015. DOI: 10.1016/j.ijsolstr.2014.12.001.

[63] J. M. Andreas, E. A. Hauser, and W. B. Tucker, "Boundary tension by pendant drops," *J. Phys. Chem.*, vol. 42, 1938. DOI: 10.1021/j100903a002.

[64] C. E. Stauffer, "The measurement of surface tension by the pendant drop technique," *J. Phys. Chem.*, vol. 69, 1965. DOI: 10.1021/J100890A024.

[65] Y. Rotenberg, L. Boruvka, and A. Neumann, "Determination of surface tension and contact angle from the shapes of axisymmetric fluid interfaces," *J. Colloid Interface Sci.*, vol. 93, 1983. DOI: 10.1016/0021-9797(83)90396-X.

[66] Y. Touhami, G. H. Neale, V. Hornof, and H. Khalfalah, "Design and accuracy of pendant drop methods for surface tension measurement," *Colloids Surf. A*, vol. 384, 1996. DOI: 10.1016/0927-7757(96)03551-0.

[67] J. Jůza, "The pendant drop method of surface tension measurement: Equation interpolating the shape factor tables for several selected planes," *Czechoslov. J. Phys.*, vol. 47, 1997. DOI: 10.1023/A:1022808017830.

[68] W. H. Press, S. A. Teukolsky, W. T. Vetterling, and B. P. Flannery, *Numerical Recipes in C: The Art of Scientific Computing*. 1992. DOI: 10.1111/j.1539-6924.1989.tb01007.x.

[69] O. S. Deshmukh, A. Maestro, M. H. G. Duits, D. v. d. Ende, M. C. Stuart, and F. Mugele, "Equation of state and adsorption dynamics of soft microgel particles at an air–water interface," *Soft Matter*, vol. 10, 2014. DOI: 10.1039/c4sm00566j.

[70] S. C. Ayirala, A. A. Al-Yousef, Z. Li, and Z. Xu, "Water Ion Interactions at Crude-Oil/Water Interface and Their Implications for Smart Waterflooding in Carbonates," *SPE J.*, vol. 23, 2018. DOI: 10.2118/183894-pa.

[71] R. d. Ruiter, R. W. Tjerkstra, M. H. G. Duits, and F. Mugele, "Influence of Cationic Composition and pH on the Formation of Metal Stearates at Oil–Water Interfaces," *Langmuir*, vol. 27, 2011. DOI: 10.1021/la2010562.

[72] J. J. Adams, "Asphaltene Adsorption, a Literature Review," *Energy & Fuels*, vol. 28, 2014. DOI: 10.1021/ef500282p.

[73] J.-B. Boussingault, "Mémoire sur l'influence des défrichements dans la diminution des cours d'eau," *Annales de chimie*, vol. 64, 1837.

[74] E. M. Freer and C. J. Radke, "Relaxation of Asphaltenes at the toluene/water interface: Diffusion exchange and surface rearrangement," *J. Adhes.*, vol. 80, 2004. DOI: 10.1080/00218460490477143.

[75] C. G. Dodd, "The rheological properties of films at crude petroleum-water interfaces," *J. Phys. Chem.*, vol. 64, 1960. DOI: 10.1021/j100834a008.

[76] A. A. Moud, "Asphaltene induced changes in rheological properties: A review," *Fuel*, vol. 316, 2022. DOI: 10.1016/j.fuel.2022.123372.

[77] H. Yarranton, D. Sztukowski, and P. Urrutia, "Effect of interfacial rheology on model emulsion coalescence I. Interfacial rheology," *J. Colloid Interface Sci.*, vol. 310, 2007. DOI: 10.1016/j.jcis.2007.01.071.

[78] C. B. Kabbach and R. G. d. Santos, "Effects of pH and Temperature on the Phase Behavior and Properties of Asphaltene Liquid Films," *Energy & Fuels*, vol. 32, 2018. DOI: 10.1021/acs.energyfuels.7b03098.

[79] D. M. Sztukowski, M. Jafari, H. Alboudwarej, and H. W. Yarranton, "Asphaltene self-association and water-in-hydrocarbon emulsions," *J. Colloid Interface Sci.*, vol. 265, 2003. DOI: 10.1016/s0021-9797(03)00189-9.

[80] R. K. Moghaddam, H. Yarranton, and G. Natale, "Interfacial micro and macro rheology of fractionated asphaltenes," *Colloids Surf. A: Physicochem. Eng.*, vol. 651, p. 129 659, 2022, ISSN: 0927-7757. DOI: 10.1016/j.colsurfa.2022.129659.

[81] J. P. Rane, D. Harbottle, V. Pauchard, A. Couzis, and S. Banerjee, "Adsorption Kinetics of Asphaltenes at the Oil–Water Interface and Nanoaggregation in the Bulk," *Langmuir*, vol. 28, no. 26, pp. 9986–9995, 2012, ISSN: 0743-7463. DOI: 10.1021/la301423c.

[82] J. P. Rane, V. Pauchard, A. Couzis, and S. Banerjee, "Interfacial Rheology of Asphaltenes at Oil–Water Interfaces and Interpretation of the Equation of State," *Langmuir*, vol. 29, 2013. DOI: 10.1021/la304873n.

[83] M. Mohammadi, M. Zirrahi, and H. Hassanzadeh, "Adsorption Kinetics of Asphaltenes at the Heptol–Water Interface," *Energy & Fuels*, vol. 34, 2020. DOI: 10.1021/acs.energyfuels.0c00019.

[84] V. Pauchard, J. P. Rane, S. Zarkar, A. Couzis, and S. Banerjee, "Long-Term Adsorption Kinetics of Asphaltenes at the Oil–Water Interface: A Random Sequential Adsorption Perspective," *Langmuir*, vol. 30, 2014. DOI: 10.1021/la500384r.

[85] W. J. S. Morais, E. Franceschi, C. Dariva, G. R. Borges, A. F. Santos, and C. C. Santana, "Dilatational Rheological Properties of Asphaltenes in Oil–Water Interfaces: Langmuir Isotherm and Influence of Time, Concentration, and Heptol Ratios," *Energy & Fuels*, vol. 31, 2017. DOI: 10.1021/acs.energyfuels.7b01633.

[86] A. Alicke, S. Simon, J. Sjöblom, and J. Vermant, "Assessing the Interfacial Activity of Insoluble Asphaltene Layers: Interfacial Rheology versus Interfacial Tension," *Langmuir*, 2020. DOI: 10.1021/acs.langmuir.0c02234.

[87] T. C. Botti, A. Hutin, E. Quintella, and M. S. Carvalho, "Effect of interfacial rheology on drop coalescence in water–oil emulsion," *Soft Matter*, vol. 18, 2022. DOI: 10.1039/d1sm01382c.

[88] S. Ashoorian, A. Javadi, N. Hosseinpour, and M. Husein, "Evolution of adsorbed layers of asphaltenes at oil-water interfaces: A novel experimental protocol," *J. Colloid Interface Sci.*, vol. 594, 2021. DOI: 10.1016/j.jcis.2021.02.123.

[89] A. Hutin and M. S. Carvalho, "Use of a Geometric Parameter for Characterizing Rigid Films at Oil–Water Interfaces," *Langmuir*, vol. 38, 2022. DOI: 10.1021/acs.langmuir.2c01058.

[90] E. M. Shchukina and D. G. Shchukin, "Layer-by-layer coated emulsion microparticles as storage and delivery tool," *Curr. Opin. Colloid Interface Sci.*, vol. 17, 2012. DOI: 10.1016/j.cocis.2012.06.003.

[91] D. Guzey and D. J. McClements, "Formation, stability and properties of multilayer emulsions for application in the food industry," *Adv. Colloid Interface Sci.*, vol. 128-130, 2006. DOI: 10.1016/j.cis.2006.11.021.

[92] M. Pepicelli, N. Jaensson, C. Tregouët, *et al.*, "Surface viscoelasticity in model polymer multilayers: From planar interfaces to rising bubbles," *J. Rheol.*, vol. 63, 2019. DOI: 10.1122/1.5096887.

[93] H. Hertz, "The contact of elastic solids," *J. Reine Angew. Math.*, vol. 92, 1881.

[94] N. Kumar, U. Vishwakarma, and A. DasGupta, "On the mechanics of inflated hyperelastic membrane–membrane contact problem," *Int. J. Non Linear Mech.*, vol. 137, 2021. DOI: 10.1016/j.ijnonlinmec.2021.103805.

[95] A. Agrawal, "Mechanics of membrane–membrane adhesion," *Math. Mech. Solids*, vol. 16, 2011. DOI: 10.1177/1081286511401364.

[96] X. Yang, L. Yu, and R. Long, "Contact mechanics of inflated circular membrane under large deformation: Analytical solutions," *Int. J. Solids Struct.*, vol. 233, 2021. DOI: 10.1016/j.ijsolstr.2021.111222.

[97] X. Li and D. Steigmann, "Point loads on a hemispherical elastic membrane," *Int. J. Non Linear Mech.*, vol. 30, 1995. DOI: 10.1016/0020-7462(95)00019-K.

[98] L. Baumgarten and J. Kierfeld, "Shallow shell theory of the buckling energy barrier: From the pogorelov state to softening and imperfection sensitivity close to the buckling pressure," *Phys. Rev. E*, vol. 99, 2019. DOI: 10.1103/PhysRevE.99.022803.

[99] Z. Zhou, A. Ngan, B. Tang, and A. Wang, "Reliable measurement of elastic modulus of cells by nanoindentation in an atomic force microscope," *J. Mech. Behav. Biomed. Mater.*, vol. 8, 2012. DOI: 10.1016/j.jmbbm.2011.11.010.

[100] D. P. Updike and A. Kalnins, "Axisymmetric behavior of an elastic spherical shell compressed between rigid plates," *J. Appl. Mech.*, vol. 37, 1969. DOI: 10.1115/1.3408592.

[101] D. P. Updike and A. Kalnins, "Contact Pressure Between an Elastic Spherical Shell and a Rigid Plate," *J. Appl. Mech.*, vol. 39, 1972. DOI: 10.1115/1.3422838.

[102] K. .-. Wan and K. .-. Liu, "Contact mechanics of a thin-walled capsule adhered onto a rigid planar substrate," *Med. Biol. Eng. Comput.*, vol. 39, pp. 605–608, 2001. DOI: 10.1007/BF02345154.

[103] K. K. Liu, V. Chan, and Z. Zhang, "Capsule-substrate contact deformation: Determination of adhesion energy," *Med. Biol. Eng. Comput.*, vol. 40, 2002. DOI: 10.1007/BF02345084.

[104] K. Tamura, S. Komura, and T. Kato, "Adhesion induced buckling of spherical shells," *J. Phys. Condens. Matter*, vol. 16, 2004. DOI: 10.1088/0953-8984/16/39/L01.

[105] L. Pauchard and S. Rica, "Contact and compression of elastic spherical shells: The physics of a 'ping-pong' ball," *Philos. Mag. B*, vol. 78, 1998. DOI: 10.1080/13642819808202945.

[106] N. Nguyen, A. Wineman, and A. Waas, "Contact problem of a non-linear viscoelastic spherical membrane enclosing incompressible fluid between two rigid parallel plates," *Int. J. Non Linear Mech.*, vol. 50, 2013. DOI: 10.1016/j.ijnonlinmec.2012.11.009.

[107] N. Nguyen, A. Wineman, and A. Waas, "Indentation of a nonlinear viscoelastic membrane," *Math. Mech. Solids*, vol. 18, 2013. DOI: 10.1177/1081286511434196.

[108] S. MansoorBaghaei and A. M. Sadegh, "Elastic spherical shell impacted with an elastic barrier: A closed form solution," *Int. J. Solids Struct.*, vol. 48, 2011. DOI: 10.1016/j.ijsolstr.2011.07.016.

[109] M. Rachik, D. Barthes-Biesel, M. Carin, and F. Edwards-Levy, "Identification of the elastic properties of an artificial capsule membrane with the compression test: Effect of thickness," *J. Colloid Interface Sci.*, vol. 301, 2006. DOI: 10.1016/j.jcis.2006.04.062.

[110] A. Fery and R. Weinkamer, "Mechanical properties of micro- and nanocapsules: Single-capsule measurements," *Polymer*, vol. 48, 2007. DOI: 10.1016/j.polymer.2007.07.050.

[111] S. Song, D.-M. Drotlef, J. Paik, C. Majidi, and M. Sitti, "Mechanics of a pressure-controlled adhesive membrane for soft robotic gripping on curved surfaces," *Extreme Mech. Lett.*, vol. 30, p. 100 485, 2019. DOI: 10.1016/j.eml.2019.100485.

[112] W. T. Coakley and D. Gallez, "Membrane-membrane contact: Involvement of interfacial instability in the generation of discrete contacts," *Biosci. Rep.*, vol. 9, Dec. 1989. DOI: 10.1007/BF01114806.

[113] E. Evans, "Detailed mechanics of membrane-membrane adhesion and separation. i. continuum of molecular cross-bridges," *Biophys. J.*, vol. 48, 1985. DOI: 10.1016/S0006-3495(85)83770-X.

[114] A. V. Pogorelov, "Bendings of surfaces and stability of shells," 1988. DOI: 10.1090/mmono/072.

[115] D. C. Morse and T. A. Witten, "Droplet elasticity in weakly compressed emulsions," *EPL*, vol. 22, 1993. DOI: 10.1209/0295-5075/22/7/012.

[116] R. Long, K. R. Shull, and C.-Y. Hui, "Large deformation adhesive contact mechanics of circular membranes with a flat rigid substrate," *J. Mech. Phys. Solids*, 2010. DOI: 10.1016/j.jmps.2010.06.007.

[117] A. Valencia, M. Brinkmann, and R. Lipowsky, "Liquid bridges in chemically structured slit pores," *Langmuir*, vol. 17, 2001. DOI: 10.1021/la001749q.

[118] P. Canham, "The minimum energy of bending as a possible explanation of the biconcave shape of the human red blood cell," *J. Theor. Biol.*, vol. 26, 1970. DOI: 10.1016/S0022-5193(70)80032-7.

[119] L. Jaouen, A. Renault, and M. Deverge, "Elastic and damping characterizations of acoustical porous materials: Available experimental methods and applications to a melamine foam," *Appl. Acoust.*, vol. 69, 2008. DOI: 10.1016/j.apacoust.2007.11.008.

[120] V. Burlayenko and T. Sadowski, "Effective elastic properties of foam-filled honeycomb cores of sandwich panels," *Compos. Struct.*, vol. 92, 2010. DOI: 10.1016/j.compstruct.2010.04.015.

[121] M. Laroussi, K. Sab, and A. Alaoui, "Foam mechanics: Nonlinear response of an elastic 3d-periodic microstructure," *Int. J. Solids Struct.*, vol. 39, 2002. DOI: 10.1016/S0020-7683(02)00172-5.

[122] M. W. D. V. D. Burg, V. Shulmeister, E. V. D. Geissen, and R. Marissen, "On the linear elastic properties of regular and random open-cell foam models," *J. Cell. Plast.*, vol. 33, 1997. DOI: 10.1177/0021955X9703300103.

[123] A. W. Senior, R. Evans, J. Jumper, *et al.*, "Improved protein structure prediction using potentials from deep learning," *Nature*, vol. 577, 2020. DOI: 10.1038/s41586-019-1923-7.

[124] J. Jumper, R. Evans, A. Pritzel, *et al.*, "Highly accurate protein structure prediction with alphafold," *Nature*, vol. 596, 2021. DOI: 10.1038/s41586-021-03819-2.

[125] J. Abramson, J. Adler, J. Dunger, *et al.*, "Accurate structure prediction of biomolecular interactions with alphafold 3," *Nature*, 2024. DOI: 10.1038/s41586-024-07487-w.

[126] OpenAI, *Chatgpt*. [Online]. Available: https://openai.com/index/chatgpt/.

[127] OpenAI, *Sora*. [Online]. Available: https://openai.com/index/sora/.

[128] D. Silver, T. Hubert, J. Schrittwieser, *et al.*, "A general reinforcement learning algorithm that masters chess, shogi, and go through self-play," *Science*, vol. 362, 2018. DOI: 10.1126/science.aar6404.

[129] S. Nigam, E. Gjelaj, R. Wang, G.-W. Wei, and P. Wang, "Machine learning and deep learning applications in magnetic particle imaging," *Magn. Reson. Imaging*, 2024. DOI: 10.1002/jmri.29294.

[130] J. Montalt-Tordera, V. Muthurangu, A. Hauptmann, and J. A. Steeden, "Machine learning in magnetic resonance imaging: Image reconstruction," *Phys. Med.*, vol. 83, 2021. DOI: 10.1016/j.ejmp.2021.02.020.

[131] S. Gassenmaier, T. Küstner, D. Nickel, *et al.*, "Deep learning applications in magnetic resonance imaging: Has the future become present?" *Diagnostics*, vol. 11, 2021. DOI: 10.3390/diagnostics11122181.

[132] B. Xu, N. Wang, T. Chen, and M. Li, "Empirical Evaluation of Rectified Activations in Convolutional Network," *CoRR*, 2015. DOI: 10.48550/arXiv.1505.00853.

[133] F. S. Kratz, L. Möllerherm, and J. Kierfeld, "Enhancing robustness, precision, and speed of traction force microscopy with machine learning," *Biophys. J.*, vol. 122, 2023. DOI: 10.1016/j.bpj.2023.07.025.

[134] L. Möllerherm, "Machine learning traction force microscopy," *Master Thesis*, 2021.

[135] T. Lecuit and P. F. Lenne, "Cell surface mechanics and the control of cell shape, tissue patterns and morphogenesis," *Nat. Rev. Mol. Cell Biol.*, vol. 8, 2007. DOI: 10.1038/nrm2222.

[136] V. Vogel and M. Sheetz, "Local force and geometry sensing regulate cell functions," *Nat. Rev. Mol. Cell Biol.*, vol. 7, 2006. DOI: 10.1038/nrm1890.

[137] D. E. Jaalouk and J. Lammerding, "Mechanotransduction gone awry," *Nat. Rev. Mol. Cell Biol.*, vol. 10, 2009. DOI: 10.1038/nrm2597.

[138] C. Hahn and M. A. Schwartz, "Mechanotransduction in vascular physiology and atherogenesis," *Nat. Rev. Mol. Cell Biol.*, vol. 10, 2009. DOI: 10.1038/nrm2596.

[139] M. A. Vollrath, K. Y. Kwan, and D. P. Corey, "The micromachinery of mechanotransduction in hair cells," *Annu. Rev. Neurosci.*, vol. 30, 2007. DOI: 10.1146/annurev.neuro.29.051605.112917.

[140] H. Yu, J. K. Mouw, and V. M. Weaver, "Forcing form and function: biomechanical regulation of tumor evolution," *Trends Cell Biol.*, vol. 21, 2011. DOI: 10.1016/j.tcb.2010.08.015.

[141] S. V. Plotnikov, B. Sabass, U. S. Schwarz, and C. M. Waterman, "Quantitative imaging in cell biology," in J. C. Waters and T. Wittman, Eds., 2014. DOI: 10.1016/B978-0-12-420138-5.00020-3.

[142] U. S. Schwarz and J. R. Soiné, "Traction force microscopy on soft elastic substrates: A guide to recent computational advances," *Biochim. Biophys. Acta - Mol. Cell Res.*, vol. 1853, 2015. DOI: 10.1016/j.bbamcr.2015.05.028.

[143] M. Lekka, K. Gnanachandran, A. Kubiak, T. Zieliński, and J. Zemła, "Traction force microscopy – Measuring the forces exerted by cells," *Micron*, vol. 150, 2021. DOI: 10.1016/j.micron.2021.103138.

[144] R. W. Style, R. Boltyanskiy, G. K. German, *et al.*, "Traction force microscopy in physics and biology," *Soft Matter*, vol. 10, 2014. DOI: 10.1039/c4sm00264d.

[145] M. Dembo and Y. L. Wang, "Stresses at the cell-to-substrate interface during locomotion of fibroblasts," *Biophys. J.*, vol. 76, 1999. DOI: 10.1016/S0006-3495(99)77386-8.

[146] U. Schwarz, N. Balaban, D. Riveline, A. Bershadsky, B. Geiger, and S. Safran, "Calculation of Forces at Focal Adhesions from Elastic Substrate Data: The Effect of Localized Force and the Need for Regularization," *Biophys. J.*, vol. 83, 2002. DOI: 10.1016/S0006-3495(02)73909-X.

[147] B. Sabass, M. L. Gardel, C. M. Waterman, and U. S. Schwarz, "High resolution traction force microscopy based on experimental and computational advances," *Biophys. J.*, vol. 94, 2008. DOI: 10.1529/biophysj.107.113670.

[148] A. H. Kulkarni, P. Ghosh, A. Seetharaman, P. Kondaiah, and N. Gundiah, "Traction cytometry: regularization in the Fourier approach and comparisons with finite element method," *Soft Matter*, vol. 14, 2018. DOI: 10.1039/C7SM02214J.

[149] Y. Huang, C. Schell, T. B. Huber, *et al.*, "Traction force microscopy with optimized regularization and automated Bayesian parameter selection for comparing cells," *Sci. Rep.*, vol. 9, 2019. DOI: 10.1038/s41598-018-36896-x.

[150] Y.-l. Wang and Y.-C. Lin, "Traction force microscopy by deep learning," *Biophys. J.*, vol. 120, 2021. DOI: 10.1016/j.bpj.2021.06.011.

[151] H. Li, D. Matsunaga, T. S. Matsui, *et al.*, "Wrinkle force microscopy: a machine learning based approach to predict cell mechanics from images," *Commun. Biol.*, vol. 5, 2022. DOI: 10.1038/s42003-022-03288-x.

[152] A. Harris, P. Wild, and D. Stopak, "Silicone rubber substrata: A new wrinkle in the study of cell locomotion," *Science*, vol. 208, 1980. DOI: 10.1126/science.6987736.

[153] M. Dembo, T. Oliver, A. Ishihara, and K. Jacobson, "Imaging the traction stresses exerted by locomoting cells with the elastic substratum method," *Biophys. J.*, vol. 70, 1996. DOI: 10.1016/S0006-3495(96)79767-9.

[154] J. L. Tan, J. Tien, D. M. Pirone, D. S. Gray, K. Bhadriraju, and C. S. Chen, "Cells lying on a bed of microneedles: An approach to isolate mechanical force," *Proc. Natl. Acad. Sci. U. S. A.*, vol. 100, 2003. DOI: 10.1073/pnas.0235407100.

[155] J. M. Brockman, A. T. Blanchard, V. Pui-Yan, *et al.*, "Mapping the 3D orientation of piconewton integrin traction forces," *Nat. Methods*, vol. 15, 2018. DOI: 10.1038/nmeth.4536.

[156] J. Steinwachs, C. Metzner, K. Skodzek, *et al.*, "Three-dimensional force microscopy of cells in biopolymer networks," *Nat. Methods*, vol. 13, 2016. DOI: 10.1038/nmeth.3685.

[157] K. A. Beningo and Y.-L. Wang, "Flexible substrata for the detection of cellular traction forces," *Trends Cell Biol.*, vol. 12, 2002. DOI: 10.1016/S0962-8924(01)02205-X.

[158] U. S. Schwarz and S. A. Safran, "Physics of adherent cells," *Rev. Mod. Phys.*, vol. 85, 2013. DOI: 10.1103/RevModPhys.85.1327.

[159] J. M. Newby, A. M. Schaefer, P. T. Lee, M. G. Forest, and S. K. Lai, "Convolutional neural networks automate detection for tracking of submicron-scale particles in 2D and 3D," *Proc. Natl. Acad. Sci. U. S. A.*, vol. 115, 2018. DOI: 10.1073/pnas.1804420115.

[160] J. P. Butler, I. M. Tolić-Nørrelykke, B. Fabry, and J. J. Fredberg, "Traction fields, moments, and strain energy that cells exert on their surroundings," *Am. J. Physiol. Physiol.*, vol. 282, 2002. DOI: 10.1152/ajpcell.00270.2001.

[161] S. J. Han, Y. Oak, A. Groisman, and G. Danuser, "Traction microscopy to identify force modulation in subresolution adhesions," *Nat. Methods*, vol. 12, 2015. DOI: 10.1038/nmeth.3430.

[162] Y. Huang, G. Gompper, and B. Sabass, "A Bayesian traction force microscopy method with automated denoising in a user-friendly software package," *Comput. Phys. Commun.*, vol. 256, 2020. DOI: 10.1016/j.cpc.2020.107313.

[163] J. R. D. Soiné, N. Hersch, G. Dreissen, *et al.*, "Measuring cellular traction forces on non-planar substrates," *Interface Focus*, vol. 6, 2016. DOI: 10.1098/rsfs.2016.0024.

[164] J. Adler and O. Öktem, "Solving ill-posed inverse problems using iterative deep neural networks," *Inverse Probl.*, vol. 33, 2017. DOI: 10.1088/1361-6420/aa9581.

[165] L. Xu, J. Ren, C. Liu, and J. Jia, "Deep convolutional neural network for image deconvolution," *Adv. Neural Inf. Process. Syst.*, vol. 2, 2014.

[166] M. Raissi, P. Perdikaris, and G. Karniadakis, "Physics-informed neural networks: A deep learning framework for solving forward and inverse problems involving nonlinear partial differential equations," *J. Comput. Phys.*, vol. 378, 2019. DOI: 10.1016/j.jcp.2018.10.045.

[167] Y. Bar-Sinai, S. Hoyer, J. Hickey, and M. P. Brenner, "Learning data-driven discretizations for partial differential equations," *Proc. Natl. Acad. Sci. U. S. A.*, vol. 116, 2019. DOI: 10.1073/pnas.1814058116.

[168] G. E. Karniadakis, I. G. Kevrekidis, L. Lu, P. Perdikaris, S. Wang, and L. Yang, "Physics-informed machine learning," *Nat. Rev. Phys.*, vol. 3, 2021. DOI: 10.1038/s42254-021-00314-5.

[169] N. Q. Balaban, U. S. Schwarz, D. Riveline, *et al.*, "Force and focal adhesion assembly: a close relationship studied using elastic micropatterned substrates," *Nat. Cell Biol.*, vol. 3, 2001. DOI: 10.1038/35074532.

[170] O. Ronneberger, P. Fischer, and T. Brox, "U-net: Convolutional networks for biomedical image segmentation," *LNCS*, 2015. DOI: 10.1007/978-3-319-24574-4_28.

[171] Y. Furusho and K. Ikeda, "Theoretical analysis of skip connections and batch normalization from generalization and optimization perspectives," *APSIPA Trans. Signal Inf. Process.*, vol. 9, e9, 2020. DOI: 10.1017/ATSIP.2020.7.

[172] P. Guthardt Torres, I. B. Bischofs, and U. S. Schwarz, "Contractile network models for adherent cells," *Phys. Rev. E*, vol. 85, 2012. DOI: 10.1103/PhysRevE.85.011913.

[173] F. Chollet *et al.*, *Keras*, https://keras.io, 2015.

Publications with contributions of the author

[4] T. Bhattacharjee, D. B. Amchin, J. A. Ott, F. S. Kratz, and S. S. Datta, "Chemotactic migration of bacteria in porous media," *Biophys. J.*, vol. 120, 2021. DOI: 10.1016/j.bpj.2021.05.012.

[6] J.-F. Louf, F. S. Kratz, and S. S. Datta, "Elastocapillary network model of inhalation," *Phys. Rev. Res.*, vol. 2, 2020. DOI: 10.1103/PhysRevResearch.2.043382.

[12] S. Pivard, L. Jacomine, F. S. Kratz, *et al.*, "Interfacial rheology of linearly growing polyelectrolyte multilayers at the water–air interface: From liquid to solid viscoelasticity," *Soft Matter*, vol. 20, 2024. DOI: 10.1039/d3sm01161e.

[13] A. Z. Stetten, F. S. Kratz, N. Schilderink, *et al.*, "Elastometry of complex fluid pendant capsules," *Langmuir*, vol. 39, 2023. DOI: 10.1021/acs.langmuir.3c01845.

[24] F. S. Kratz and J. Kierfeld, "Pendant Drop Tensiometry: A Machine Learning Approach," *J. Chem. Phys*, vol. 153, 2020. DOI: 10.1063/5.0018814.

[32] G. Ginot, F. S. Kratz, F. Walzel, *et al.*, "Pressure–deformation relations of elasto-capillary drops (droploons) on capillaries," *Soft Matter*, 2021. DOI: 10.1039/D1SM01109J.

[45] F. S. Kratz, *Pendant Drops and Capsules: Solving the Inverse Problem by Numerical Shape Fitting and Machine Learning*, Master Thesis, 2020.

[133] F. S. Kratz, L. Möllerherm, and J. Kierfeld, "Enhancing robustness, precision, and speed of traction force microscopy with machine learning," *Biophys. J.*, vol. 122, 2023. DOI: 10.1016/j.bpj.2023.07.025.

Danksagung

An dieser Stelle möchte ich zunächst Herrn Professor Jan Kierfeld danken für die Betreuung dieser Arbeit. Ich möchte mich bei ihm für die zahlreichen Diskussionen bedanken, diese haben maßgeblich zu dem Gelingen dieser Arbeit beigetragen und haben meine persönliche intelektuelle Entwicklung gefördert. Ich bedanke mich auch für die außerordentliche Föderung die ich durch Herrn Professor Kierfeld erfahren habe, etwa bei der Bewerbung bei der Studienstiftung oder bei der Nobelpreisträgertagung in Lindau.

Außerdem richte ich meinen Dank an Herrn Professor Herre Jelger Risselada für das Zweitgutachten der Arbeit.

Ich bedanke mich sehr herzlich bei Wiebke Drenckhan. Die enge Zusammenarbeit hat zu einem produktiven Wissensaustausch zwischen der Theorie und dem Experiment geführt. Neben den akademischen Bereicherungen möchte ich mich auch für die Gastfreundschaft bedanken. Bei allen meinen Besuchen habe ich mich in Straßburg sehr wohl gefühlt. Außerdem danke ich Stéphane Pivard, Gaël Ginot und Friedrich Walzel für die Zusammenarbeit und auch für den außerfachlichen Austausch.

Ein weiterer Dank gebührt Amy Stetten für die Kooperation und die regen Diskussionen.

Für die Begleitung durch mein Bachelor-, Master- und Promotionsstudium möchte ich der Studienstiftung des deutschen Volkes einen besonderen Dank aussprechen. Besonders für die ideele Förderung die ich durch die Stiftung erfahren habe bin ich ausgesprochen dankbar.

Außerdem danke ich meiner langjährigen Bürokollegin Lina Heydenreich für die zahllosen Unterhaltungen und die mentale Unterstützung. Außerdem danke ich Lukas Weise, Nico Schaffrath und Tobias Kampmann für die vielen Anregungen und Ablenkungen im Arbeitsalltag.

Meiner Familie gilt der größte Dank. Die Unterstützung, das Verständnis, die Geduld, der Zusammenhalt, die Liebe und die Inspiration die ich durch meine Familie in den Jahren dieser Arbeit erfahren habe schätze ich sehr und bin unendlich dankbar und glücklich.